Synthesis and Characterization of Metal-Functionalized Single-Chain Polymer Nanoparticles as Versatile Catalytic Nanoreactors

Zur Erlangung des akademischen Grades eines

DOKTORS DER NATURWISSENSCHAFTEN

(Dr. rer. nat.)

von der KIT-Fakultät für Chemie und Biowissenschaften

des Karlsruher Instituts für Technologie (KIT)

genehmigte

Dissertation

von

M.Sc. Sebastian Gillhuber

1. Referent: Prof. Peter W. Roesky
2. Referent: Prof. Christopher Barner-Kowollik
3. Referent: Prof. Florian Weigend
Tag der mündlichen Prüfung: 05.12.2024

SYNTHESIS AND CHARACTERIZATION OF METAL-FUNCTIONALIZED SINGLE-CHAIN POLYMER NANOPARTICLES AS VERSATILE CATALYTIC NANOREACTORS

Sebastian Gillhuber

MSc(Chem)

Submitted in fulfilment of the requirements for the degree of

Doctor of Philosophy

School of Chemistry and Physics

Faculty of Science

Queensland University of Technology

Karlsruhe Institute of Technology

2024

Keywords

Action plots • Atomic resolution imaging • Catalysis • Flow synthesis • Metal functionalization • Polymers • SCNPs • Single-chain nanoparticles

Abstract

Naturally occurring proteins form nanosized particles with unique, outstanding properties from a linear strand of amino acids via intramolecular interactions. Inspired by this, the field of single-chain nanoparticles (SCNPs) has emerged. SCNPs are constructed from individual synthetic macromolecular chains by intramolecular interactions of complementary functional groups, resulting in more compact morphologies compared to the precursor macromolecules. The combination of the tunable characteristics of polymeric materials with the diverse functionalities of metals and their complexes within SCNPs forms the research area of metal-functionalized SCNPs. The current thesis investigates the synergistic combination of inorganic and polymer chemistry, critically pushing the state-of-the-art limits of the field of metal-functionalized SCNPs, by addressing omnipresent challenges in synthesis and in-depth characterization. Further, introducing advanced functionalities into SCNPs is targeted to broaden the scope of applications, with a particular focus on catalysis.

The first part of the thesis addresses the synthesis of Ba(II)-folded SCNPs, thereby contributing to the currently underexplored field of main group metal SCNPs. The high contrast provided by the heavy barium atoms in transmission electron microscopy experiments is exploited for the imaging of the internal SCNP structure with atomic resolution, providing unprecedented experimental insights into the distribution of metal ions within metal-folded SCNPs. The second part of the thesis aims at exploring the synthesis of copper-functionalized SCNPs in continuous flow to address the omnipresent scalability challenge currently limiting SCNP synthesis. The third part of the thesis is devoted to advancing the field of multimetallic SCNPs by presenting heterobimetallic iron-palladium SCNPs and demonstrating their catalytic abilities. The last part of the thesis is dedicated to demonstrating how metal ions can beneficially alter the properties of purely organic macromolecules. Therefore, the synthesis of polymers functionalized with the organic dye Eosin Y is described and the influence of zinc functionalization on the wavelength-resolved photocatalytic activity explored.

Kurzzusammenfassung

Natürlich vorkommende Proteine bilden durch intramolekulare Wechselwirkungen funktioneller Gruppen innerhalb von linearen, aus Aminosäuren aufgebauten Polypeptidsträngen nanoskalige Partikel mit einzigartigen, bemerkenswerten Eigenschaften. Davon inspiriert entstand das Forschungsfeld der Einzelkettennanopartikel (Single-chain nanoparticles, SCNPs). SCNPs werden durch intramolekulare Interaktionen komplementärer Funktionalitäten innerhalb einzelner synthetischer makromolekularer Ketten geformt, was in einer verglichen mit den Vorläufermakromolekülen kompakteren Morphologie resultiert. Die Kombination der abstimmbaren Eigenschaften polymerer Materialien mit den diversen Funktionalitäten von Metallen sowie deren Komplexen innerhalb von SCNPs bildet das Forschungsgebiet der metallfunktionalisierten SCNPs.

Ziel der vorliegenden Dissertation ist die synergistische Kombination von anorganischer Chemie und Polymerchemie, um die gegenwärtigen Grenzen des Gebiets der metallfunktionalisierten SCNPs zu verschieben. Dies soll durch Adressierung allgegenwärtiger Herausforderungen in den Bereichen Synthese und Charakterisierung sowie die katalytische Anwendung der neu dargestellten metallfunktionalisierten SCNPs erreicht werden.

Der erste Teil der Arbeit befasst sich mit der Synthese Ba(II)-gefalteter SCNPs und trägt damit zum weitgehend unerforschten Gebiet der Hauptgruppenmetall-SCNPs bei. Der durch die Schwermetallionen gegebene hohe Kontrast ermöglichte die Darstellung einzelner Bariumatome innerhalb der SCNPs durch Rastertransmissionselektronenmikroskopie, was beispiellose Einblicke in die Anzahl und Verteilung von Metallionen innerhalb isolierter Makromoleküle gestattete. Der zweite Teil der Arbeit erforscht die Synthese kupferfunktionalisierter SCNPs in kontinuierlichem Durchfluss, um die allgegenwärtige Skalierbarkeitsproblematik von SCNP-Synthesen, die derzeit eine Aufskalierung behindert, zu adressieren. Der dritte Teil der Arbeit ist dem Vorantreiben des Feldes der multimetallischen SCNPs gewidmet und diskutiert die Darstellung heterobimetallischer Eisen-Palladium-SCNPs sowie deren katalytische Aktivität. Der letzte Teil der Arbeit beschreibt die vorteilhafte Beeinflussung rein organischer Makromoleküle durch Metallfunktionalisierung. Dazu wird die Synthese von Eosin Y-funktionalisierten Polymeren beschrieben und der Einfluss von Zinkfunktionalisierung auf die wellenlängenaufgelöste photokatalytische Aktivität betrachtet.

List of Publications

[1] Paramagnetic NMR Shielding Tensors and Ring Currents: Efficient Implementation and Application to Heavy Element Compounds. S. Gillhuber, Y. J. Franzke, F. Weigend, *J. Phys. Chem. A* **2021**, *124*, 9707-9723.

[2] Introduction of plumbole to f-element chemistry. L. Münzfeld, X. Sun, S. Schlittenhardt, C. Schoo, A. Hauser, S. Gillhuber, F. Weigend, M. Ruben, P. W. Roesky, *Chem. Sci.* **2022**, *13*, 945-954.

[3] Fully Tin-Coated Coinage Metal Ions: A Pincer-Type Bis-stannylene Ligand for Exclusive Tetrahedral Complexation. F. Krätschmer, X. Sun, S. Gillhuber, H. Kucher, Y. J. Franzke, F. Weigend, P. W. Roesky, *Chem. Eur. J.* **2023**, *29*, e202203583 (*Cover feature*).

[4] Ferrocene-driven single-chain polymer compaction. S. Gillhuber, J. O. Holloway, H. Frisch, F. Feist, F. Weigend, C. Barner-Kowollik, P. W. Roesky, *Chem. Commun.* **2023**, *59*, 4672-4675.

[5] TURBOMOLE: Today and Tomorrow. Y. J. Franzke, C. Holzer, J. H. Andersen, T. Begušić, F. Bruder, S. Coriani, F. Della Sala, E. Fabiano, D. A. Fedotov, S. Fürst, S. Gillhuber, R. Grotjahn, M. Kaupp, M. Kehry, M. Krstić, F. Mack, S. Majumdar, B. D. Nguyen, S. M. Parker, F. Pauly, A. Pausch, E. Perlt, G. S. Phun, A. Rajabi, D. Rappoport, B. Samal, T. Schrader, M. Sharma, E. Tapavicza, R. S. Treß, V. Voora, A. Wodyński, J. M. Yu, B. Zerulla, F. Furche, C. Hättig, M. Sierka, D. P. Tew, F. Weigend, *J. Chem. Theory Comput.* **2023**, *19*, 6859-6890.

[6] Synthesis and properties of cyclic sandwich compounds. L. Münzfeld, S. Gillhuber, A. Hauser, S. Lebedkin, P. Hädinger, N. D. Knöfel, C. Zovko, M. T. Gamer, F. Weigend, M. M. Kappes, P. W. Roesky, *Nature* **2023**, *620*, 92-96 (Literature coverage in *Synform* **2024**, *1*, 16-20).

[7] Paramagnetic Nuclear Magnetic Resonance Shifts for Triplet Systems and Beyond with Modern Relativistic Density Functional Methods. Y. J. Franzke, F. Bruder, S. Gillhuber, C. Holzer, F. Weigend, *J. Phys. Chem. A* **2024**, *128*, 670-686.

[8] Phospholyl and Arsolyl Triple-Decker Sandwich Complexes of Europium(II) and Strontium(II). N. Schwarz, J. Feye, V. R. Naina, R. Köppe, S. Gillhuber, X. Sun, P. W. Roesky, *JACS Au* **2024**, *4*, 2343-2350.

[9] Visible light photoflow synthesis of a Cu(II) single-chain polymer nanoparticle catalyst. S. Gillhuber, J. O. Holloway, K. Mundsinger, J. A. Kammerer, J. R. Harmer, H. Frisch, C. Barner-Kowollik, P. W. Roesky, *Chem. Sci.* **2024**, *15*, 15280-15290.

[10] Dye induced luminescence properties of gold(I) complexes with near unity quantum efficiency. V. R. Naina, S. Gillhuber, C. Ritschel, D. Jin, Shubham, S. Lebedkin, C. Feldmann, F. Weigend, M. M. Kappes, P. W. Roesky, *Angew. Chem. Int. Ed.* **2025**, *64*, e202414517.

Unpublished work:

[11] Rare Earth Stibolyl and Bismolyl Sandwich Complexes. N. Schwarz, F. Bruder, V. Bayer, E. Moreno-Pineda, S. Gillhuber, X. Sun, J. van Slageren, F. Weigend, P. W. Roesky, *submitted*.

[12] A Novel Synthetic Pathway to Lanthanide Triple-Decker Complexes: Selective Expansion of a Sandwich Complex by an Insertion Reaction. C. Uhlmann, L. Münzfeld, A. Hauser, S. Gillhuber, P. Hädinger, M. Leskov, F. Weigend, P. W. Roesky, *submitted*.

Conference Contributions

[1] Macromolecular Colloquium. 20th February–22nd February 2019, Freiburg, Germany. Conference participation.

[2] Curiosity - A French-German Young Chemists Conference. 30th June–1st July 2022, Mulhouse, France. Organizational committee member and session chair.

[3] 21st Conference on Inorganic Chemistry. 26th September–28th September 2022, Marburg, Germany. Poster presentation.

[4] German Chemical Society Young Chemists Network Herbstorganisationstreffen. 29th September–1st October 2023, Karlsruhe, Germany. Organizational committee member.

[5] 38th Australasian Polymer Symposium. 18th February–21st February 2024, Auckland, New Zealand. Oral presentation.

Table of Contents

List of Figures

List of Schemes

List of Tables

List of Abbreviations

%	Percent
°	Degree
1D	One-dimensional
2D	Two-dimensional
Å	Ångström (10^{-10} m)
AFM	Atomic force microscopy
AIBN	Azobisisobutyronitrile
as/s	Asymmetric/symmetric (IR)
ATR	Attenuated total reflectance
a.u.	Arbitrary units
B_0	External magnetic flux density (EPR)
β-CD	β-Cyclodextrin
c	Speed of light
°C	Degree Celsius
cal.	Calibration (SEC)
CD	Circular dichroism
2CEA	2-Carboxyethyl acrylate
cm	Centimeter
CME	Cellulose mixed esters
cod	Coordinated 1,5-cyclooctadiene
COD	1,5-Cyclooctadiene
Cp	Cyclopentadienyl
CW	Continuous wave
δ	Chemical shift (NMR)
Δ	Difference
D	Diffusion coefficient
$Đ$	Dispersity index
D_s	Solvodynamic diameter
dB	Decibel

DCM	Dichloromethane
DFT	Density functional theory
DLS	Dynamic light scattering
DMAc	*N,N*-Dimethylacetamide
DMF	*N,N*-Dimethylformamide
DOSY	Diffusion-ordered nuclear magnetic resonance spectroscopy
E_{Pulse}	Laser pulse energy
EDX	Energy-dispersive X-ray spectroscopy
EPR	Electron paramagnetic resonance spectroscopy
eq.	Equivalents
et al.	And others
EY	2-(Propionyloxy)ethyl 2-(2,4,5,7-tetrabromo-6-hydroxy-3-oxo-3*H*-xanthen-9-yl)benzoate
EYMA	2-(Methacryloyloxy)ethyl 2-(2,4,5,7-tetrabromo-6-hydroxy-3-oxo-3*H*-xanthen-9-yl)benzoate
f_{rep}	Laser repetition rate
FRET	Förster resonance energy transfer
FT	Fourier transform
g	Gramm
g	g-factor
GHz	Gigahertz
GMA	Glycidyl methacrylate
GPC	Gel permeation chromatography
h	Planck constant
h	hours
HOMO	Highest occupied molecular orbital
ICP-MS	Inductively coupled plasma mass spectrometry
ICP-OES	Inductively coupled plasma optical emission spectroscopy
IR	Infrared Spectroscopy
J	Joule
K	Kelvin
kDa	Kilodalton

kHz	Kilohertz
kV	Kilovolt
λ	Wavelength
λ_{max}	Wavelength of maximum absorption/emission
L	Liter
LCMS	Liquid chromatography-mass spectrometry
LED	Light emitting diode
LUMO	Lowest unoccupied molecular orbital
µJ	Microjoule
µm	Micrometer
m	Meter
M	General abbreviation for metal
M_n	Number-averaged molar mass
M_p	Peak molar mass
MALS	Multi-angle light scattering
mbar	Millibar
MeCN	Acetonitrile
mg	Milligram
min	Minutes
mL	Milliliter
mm	Millimeter
mol%	Mole fraction in percent
MRI	Magnetic resonance imaging
mT	Millitesla
mW	Milliwatt
m/z	Mass-to-charge ratio
v	Stretching vibration
$\tilde{\nu}$	Wavenumber (IR)
N_{Ph}	Number of photons
nA	Nanoampere
n-BuLi	*n*-Butyllithium
nm	Nanometer

NMP	Nitroxide-mediated polymerization
NMR	Nuclear magnetic resonance spectroscopy
NOESY	Nuclear Overhauser effect spectroscopy
NPA	Natural population analysis
NPT	Isothermal-isobaric ensemble
ns	Nanosecond
NVT	Canonical ensemble
Ω	Ohm
*o*NBMA	2-((((2-Nitrobenzyl)oxy)carbonyl)amino)ethyl methacrylate
OTf	Triflate
PEG	Polyethylene glycol
PEGMEMA	Poly(ethylene glycol) methyl ether methacrylate
PMMA	Poly(methyl methacrylate)
ppb	Parts per billion
ppm	Parts per million
ps	Picosecond
PS	Polystyrene
PTFE	Polytetrafluoroethylene
RAFT	Reversible addition-fragmentation chain transfer polymerization
RDRP	Reversible deactivation radical polymerization
RI	Refractive index
s	Second
SANS	Small-angle neutron scattering
SAXS	Small-angle X-ray scattering
SCNP(s)	Single-chain nanoparticle(s)
SEC	Size-exclusion chromatography
SLS	Static light scattering
STEM	Scanning transmission electron microscopy
t	Time
T_2	Transverse/spin-spin relaxation time
$T(\lambda)$	Wavelength-dependent transmission
^{t}Bu	*tert*-Butyl

TDDFT	Time-dependent density functional theory
TEM	Transmission electron microscopy
THF	Tetrahydrofuran
THF-d_8	Completely deuterated tetrahydrofuran
TMEDA	*N,N,N',N'*-Tetramethyl ethylenediamine
TOC	Total organic carbon
u	Unified atomic mass unit
UV	Ultraviolet
UV/Vis	Ultraviolet-visible spectroscopy
vs/s/m/w	Very strong/strong/medium/weak (IR)
VT	Variable temperature
v/v	Volume to volume ratio
W	Watt
wt%	Weight percent
XAS	X-ray absorption spectroscopy
XIC	Extracted ion chromatogram
XPS	X-ray photoelectron spectroscopy

Statement of Original Authorship

The work contained in this joint thesis undertaken between the Queensland University of Technology (QUT) and the Karlsruhe Institute of Technology (KIT) has not been previously submitted to meet requirements for an award at these or any other higher education institution. To the best of my knowledge and belief, the thesis contains no material previously published or written by another person except where due reference is made.

Die vorliegende Arbeit wurde in der Zeit vom 01.09.2021 bis zum 18.10.2024 am Institut für Anorganische Chemie des Karlsruher Instituts für Technologie (KIT) sowie an der School of Chemistry and Physics der Queensland University of Technology (QUT) unter der Leitung von Prof. Dr. Peter W. Roesky sowie Prof. Dr. Christopher Barner-Kowollik durchgeführt.
Die Arbeit wurde vom Fonds der Chemischen Industrie (FCI) in Form eines Kekulé-Stipendiums gefördert.
Hiermit erkläre ich, die vorliegende Arbeit selbstständig verfasst und keine anderen als die angegebenen Quellen und Hilfsmittel verwendet sowie Zitate kenntlich gemacht zu haben. Die Satzung des Karlsruher Instituts für Technologie (KIT) zur Sicherung guter wissenschaftlicher Praxis in der jeweils gültigen Fassung wurde beachtet. Des Weiteren erkläre ich, dass ich mich derzeit in keinem weiteren laufenden Promotionsverfahren befinde und auch keine vorausgegangenen Promotionsversuche unternommen habe.

Acknowledgements

First of all, I would like to express my gratitude to my supervisory team for their guidance and support throughout the work presented in this thesis. I would like to thank my principal supervisors, Prof. Dr. Peter W. Roesky and Prof. Dr. Christopher Barner-Kowollik, for the opportunity to work in their research groups and providing all infrastructure and support essential for the successful completion of all the interesting research challenges as well as taking the sheer infinite number of bureaucratic burdens associated with the binational doctorate. Further, I would like to thank my associate supervisors, A/Prof. Dr. Hendrik Frisch and Dr. Joshua O. Holloway, for always having open doors to discuss the millions of challenges of daily life lab work.

Special thanks outside the supervisory team go to Prof. Dr. Florian Weigend for taking over the Korreferat and the close collaboration in manifold projects alongside my research journey for more than four years. Thanks for teaching me all the secrets about the fascinating world of quantum chemistry, the art of praying for convergence, Badisch lessons and countless entertaining Webex sessions.

Dr. Laura Delafresnaye and Dr. Kai Mundsinger are acknowledged for their support with all kinds of organizational tasks and always taking immediate care of any of my thousands of exotic requests.

All collaboration partners are thanked for their contributions to the successful work presented in this thesis. Especially, Dr. Jochen Kammerer for his endurance and magic microscopy skills, Ada Quinn and Prof. Dr. Megan O'Mara for the dedicated work on molecular dynamics simulations and Dr. Florian Feist for sharing his immense synthetic expertise and all the insightful discussions.

Thanks also to all the people who willingly shared their expertise on all kinds of analytical techniques and research infrastructure, thereby providing critical support. Particularly, Dr. Aaron Micallef and Helga Berberich for NMR experiments, Dr. Joshua Carroll for anything related to lasers (pew pew!) and action plots, Dr. David Marshall and Petra Smie for mass spectrometry, Sibylle Schneider for single crystal X-ray diffraction experiments and Dr. Sebastian Spann for sharing his immense knowledge on DOSY.

All present and former members of the Roesky and Macroarc groups who I had the pleasure to get to know are gratefully acknowledged for the supportive and entertaining work environment. Especially, I would like to thank my lab mate Shubham (Shubham) for his unbridled enthusiasm and positive nature, always holding the mood in Lab 430 ("The Indian Base Camp") up high and never getting tired of telling me "this time it will work!". I am also thankful to all the open doors along the fourth floor corridor giving me asylum when chemistry made me escape the lab. In this regard, I would like to thank Gerlinde Greif, Dr. Noah Schwarz, Nicolas Günther-Schmidt, Dr. Da Jin, Dr. Vanitha Naina, Mohammad Iqbal, Dr. Xiaofei Sun, Dr. Frederic Krätschmer, Dr. Julia Feye and Stefanie Maier, the new inhabitants of floor four, David Frick, Elena Pross, Maxim Leskov and Louis Leyen as well as the extinct fifth floor members Dr. Adrian Hauser and Dr. Cedric Uhlmann.

A special thanks also goes to the members of the KIT-QUT Cotutelle gang who I had the once in a lifetime opportunity to share time in Australia and Germany with. Special thanks go to Dr. Patrick Maag for his inclusiveness and all the fruitful discussions, Dr. Rita Michenfelder for the entertaining coffee-less coffee breaks, Matthias Steurer for our unique Bay 2 alliance, Alicia Schmidt for great conversations and Brezel supply, Dr. Linh Duy Thai for the daily morning catchups in the lab and Jan Hobich for our German farewell party.

My all-time favorite Sri Lankan office neighbors, Anne Fernando Pulle and Dushani Kanchana (aka. Donkey Kong), are acknowledged for fruitful discussions and all the funny moments we shared. Will see you over at home in Sri Lanka!

Dr. Michael Gamer is thanked for general life advice, IT support, glassware supply and proofreading. Dr. Ralf Köppe is acknowledged for discussions on theoretical chemistry and scientific support with IR experiments.

The "SAP office" is thanked for always providing an enthusiastic work environment and having an open door to discuss any scientific or non-scientific needs. Thanks to Dr. Anna Stößer for chasing all the suppliers that did not deliver the chemicals fast enough for my demands and support with ChemA and research infrastructure. Thanks to Petra Smie for urgent mass spectrometry measurements and access to the secret cable box. Thanks to Sibylle Schneider for support with X-ray diffraction experiments, always finding the most challenging IT problem of the day for me and all the things revolving around lab equipment.

Our secretaries, Monika Kayas, Angie Pendl, Conny Weber and Sing Sun are thanked for help with all the paperwork associated with the PhD life.

All the hidden champions at the Institute of Inorganic Chemistry are thanked for their manifold support. I am thankful to Kalam Munshi for rescuing countless broken NMR tubes and all the other pieces of glassware that proved to be much less stable than I thought. Gabriele Leichle is thanked for always ensuring I had sufficient solvent for another column, finding all the chemicals than no one except for me was ever searching for in her chemical treasury and the always good mood down in the darkness of the basement. Thanks also to the team of the workshop for always helping out with tools and getting the best out of vacuum pumps sounding like they have been aircraft engines in their past lives.

The members of Team Théato, in particular Katharina Kuppinger, Nico Zuber and Dr. Sven Schneider, are thanked for helping out with dozens of polymer chemistry questions and GPC measurements over the years.

The Fond der Chemischen Industrie is thanked for providing financial support in form of a Kekulé fellowship (No. 110160).

QUT's Central Analytical Research Facility (CARF) supported by QUT's Research Portfolio, the School of Chemistry and Physics as well as the Faculty of Science are acknowledged for providing research infrastructure. Additionally, QUT is acknowledged for a QUT HDR Tuition Fee Sponsorship.

Last but not least, I would like to express my deepest gratitude to my family and friends for their continued unconditional support and encouragement over all the years. This thesis would not exist without you!

Chapter 1: Introduction

In his famous 1959 speech "There´s plenty of room at the bottom", Richard Feynman outlined the vision of "manipulating and controlling things on the small scale".[1] Before and after, the field of nanotechnology has fascinated scientists and over the years has evolved to a versatile playground for various fields of research. One area of particular interest is the synthesis and application of nanoparticles. In general, nanoparticles are substances with a spatial extent of less than 100 nm in at least one dimension.[2] Taking inspiration from naturally occurring proteins, which form nanosized particles with unique, outstanding properties from a linear strand of amino acids via intramolecular interactions, the field of single-chain nanoparticles (SCNPs) has emerged. SCNPs are constructed from individual synthetic macromolecular chains by intramolecular interactions of complementary functional groups (refer to **Figure 1.1**), resulting in more compact morphologies compared to the precursor macromolecules. Consequently, SCNPs expand on the opportunities offered by linear or intermolecularly crosslinked polymers as well as other types of nanoparticles.[3-4] Following the design principles of natural metalloproteins, our groups and others have focused on the metal functionalization of SCNPs, allowing to synergistically combine the tunable characteristics of polymeric materials with the diverse functionalities of metal complexes to rival nature's perfection.[5-24]

The current thesis aims at the synergistic combination of inorganic and polymer chemistry to critically push the state-of-the-art limits in the field of metal-functionalized SCNPs by addressing omnipresent challenges in synthesis and in-depth characterization. Further,

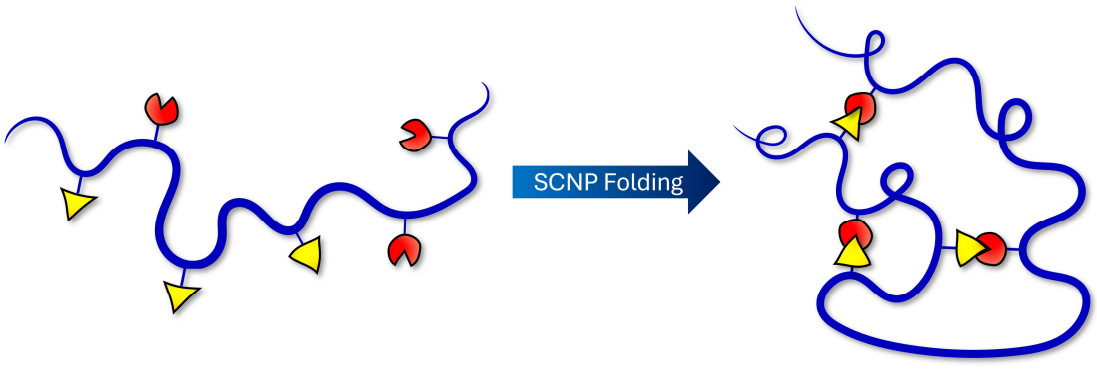

Figure 1.1 Schematic illustration of the folding of an individual macromolecular chain (left) to a single-chain nanoparticle (SCNP, right) via intramolecular interactions of complementary functional groups.

introducing advanced functionalities into SCNPs is targeted to broaden the scope of applications, with a particular focus on catalysis.

Chapter 2 outlines the theoretical foundations of the SCNP field, ranging from synthesis and characterization to metal functionalization and selected applications of SCNPs, highlighting their scope in materials science, with a special emphasis on catalysis. Chapter 3 summarizes the overarching aims of the current thesis, and the results are presented and discussed in detail in Chapter 4. A comprehensive overview of the results accompanied by directions for future research is provided in Chapter 5, and experimental details are given in Chapter 6.

Chapter 2: Theoretical Background

2.1 SYNTHESIS OF SINGLE-CHAIN NANOPARTICLES

The first examples of intramolecularly crosslinked individual macromolecular chains date back to the 1950s and early works focused on the physical properties of polymers upon intrachain collapse.[25-33] After that, however, the field was dormant for decades and revived at the beginning of the 21st century as a versatile approach to generate nanoparticles of very small sizes in a controlled manner.[13,34] Advancements in the synthesis of well-defined, highly functionalized polymers via controlled polymerization techniques, such as living anionic polymerizations,[35] radical polymerizations with living characteristics[36-39] or sequence-controlled synthesis,[40] and post-polymerization modification[41] enabled the rapid progress of the field over the last two decades.

From a fundamental perspective, the intramolecular collapse of individual macromolecular chains to form SCNPs from a non-crosslinked precursor can be achieved in three different ways (refer to **Figure 2.1**). First, the crosslinking can result from the homodimerization of identical functional groups distributed along the polymer main chain. Second, heterodimerization can occur between different functional groups. And third, SCNP folding can result from the reaction of functional groups on the macromolecule with an added external crosslinker.

The crosslinking units can either be randomly distributed along the polymer main chain, which

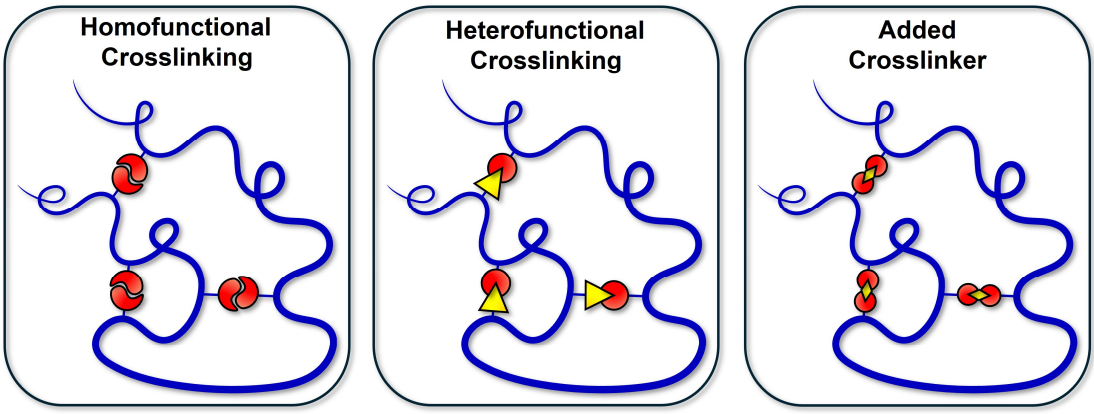

Figure 2.1 Schematic illustration of SCNP formation by intramolecular crosslinking resulting from the reaction of identical functional groups (left), different functional groups (center) and functional groups on the macromolecular chain with an added external crosslinker (right).

is commonly referred to as repeat unit folding, or be located at predefined positions, referred to as selective point folding. The latter allows for precise fine-tuning of the folding properties, however, it comes at the expense of a major synthetic challenge. Therefore, repeat unit folding is the most commonly employed approach in SCNP syntheses described in the literature, despite leading to a less-defined and chaotic collapse.[42]

In either case, the intramolecular collapse can be based on covalent or non-covalent interactions. Single-chain folding under the formation of covalent bonds is achieved by intramolecular covalent bond forming reactions of suitable functional groups triggered by an external stimulus after polymerization. Examples include Friedel-Crafts alkylations,[43] (photo-)cycloadditions,[44-53] alkene metatheses,[54] reactions of nucleophilic and electrophilic centers[7,55-58] or the formation of disulfide bridges.[59-60] Non-covalent crosslinking is often based on the formation of intramolecular hydrogen bonds[61-63] or solvophobic interactions.[64-68] Broadening the traditional classification to also include coordinative bonding, the coordination of structural units of the polymer to metal centers has also been employed as a SCNP folding reaction.[5-24] Furthermore, the post-compaction of SCNPs after the initial chain collapse by additional, orthogonal folding units has been described.[69]

Making use of this advanced synthetic toolbox, a plethora of different morphologies have been realized. Examples range from simple rings, over tadpole- or dumbbell-shaped structures to sparse or globular morphologies.[70] Depending on the chemical nature of the intramolecular linkages, the folding process can either be irreversible, resulting in a locked conformation of the macromolecular chain, or reversible, allowing for on-demand SCNP unfolding.[4]

Given the desire for exclusive intramolecular crosslinking, one major challenge throughout the synthesis of SCNPs is the prevention of intermolecular interactions of individual macromolecular chains as the latter may result in problems such as insolubility of the resulting materials, ill-defined morphologies or limited reproducibility. Traditionally, syntheses were carried out under highly dilute conditions, often significantly below 1 $mg \cdot mL^{-1}$, hence limiting the scalability and consequently the application scope of SCNPs in general.[4] Various methods have been developed to overcome this obstacle (refer to **Figure 2.2**).

A common approach is constituted by the slow addition of a concentrated polymer solution to a solution of a reactive crosslinker under rapid stirring, resulting in a very low local

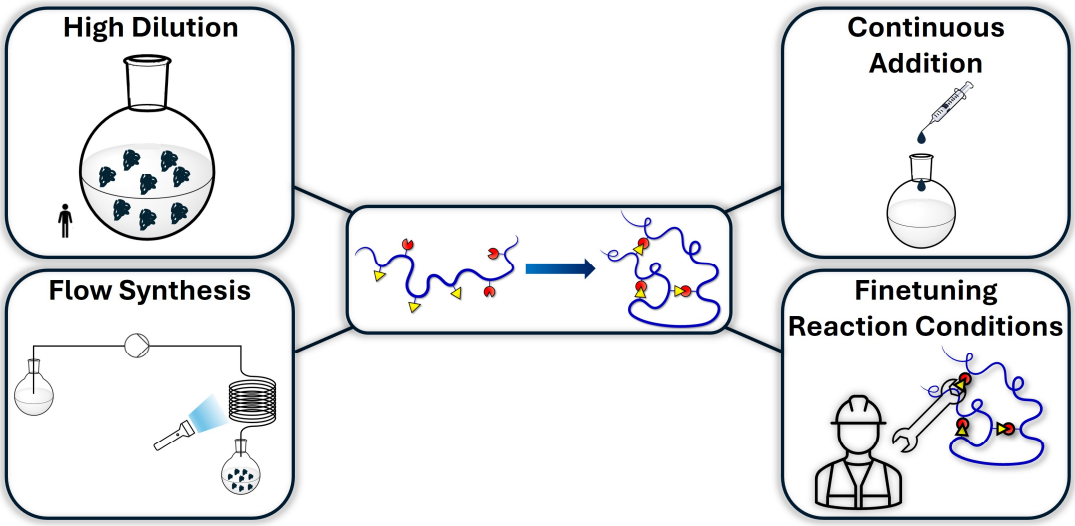

Figure 2.2 Commonly employed strategies to prevent intermolecular crosslinking throughout SCNP synthesis.

concentration of actually reacting polymer at a given time when unreacted polymer is only added after complete consumption of the previously added one.[71]

Recently, Galant *et al.* exploited the photodimerization abilities of anthracene units incorporated as pendent units into a methacrylate polymer to demonstrate for the first time how transferring a photochemical batch reaction to photoflow conditions can significantly enhance the efficiency of the SCNP formation process, thereby opening a route to access SCNPs on the gram scale.[72]

Apart from these generally applicable synthetic methodologies, a number of more specialized techniques have been developed for specific purposes, which aim at favoring intramolecular reactions over their intermolecular counterparts. For instance, Qiao and coworkers employed sterically demanding polyethylene glycol (PEG) side chains to shield the reactive groups in a linear precursor polymer to prevent interactions with other chains, thereby achieving SCNP folding without intermolecular crosslinking at an unprecedently high concentration of 100 mg·mL^{-1}.[73] The general observation that SCNPs can be prepared at comparably high concentrations from weak polyelectrolyte precursor polymers was investigated theoretically by Pomposo and coworkers, finding that the long-range electrostatic repulsion between intramolecularly formed blobs in weak polyelectrolyte polymers restrict the crosslinking process to the interior of each blob, thus preventing interchain aggregation. SCNPs can consequently be synthesized up to concentrations at which the electrostatic blobs of different macromolecular chains start touching. This concentration is commonly significantly higher than the critical overlap concentration between individual macromolecular chains of non-

polyelectrolyte polymers, resulting in intermolecular crosslinking of the latter at lower concentrations compared to weak electrolyte polymers.[74] In another example, Frisch and Menzel *et al.* reported a significantly increased quantum yield for the intramolecular [2+2] photocycloaddition of styrylpyrene compared to the competing intermolecular process. The authors attributed this to the higher local concentration of photoreactive units within a polymer chain relative to the global concentration in the reaction vessel.[53]

Going beyond mere single-chain folding, various advanced synthetic protocols were reported to complement SCNPs with manifold functionalities for a plethora of applications (refer to Chapters 2.3 and 2.4). The functionalities can either be provided by the crosslinking moieties themselves or be incorporated via further functionalization of the polymer backbone.

2.2 CHARACTERIZATION OF SINGLE-CHAIN NANOPARTICLES

SCNPs are formed by the introduction of intramolecular linkages into linear, non-crosslinked macromolecular chains. The commonly employed characterization techniques thus aim at evidencing the successful formation of intramolecular crosslinks. To achieve this, various analytical methods have been applied in the literature, collecting evidence for SCNP formation from spectroscopy, size-sensitive characterization, morphological analysis and computational methods (refer to **Figure 2.3**).[4]

Most commonly, the formation of intramolecular crosslinks upon SCNP synthesis is accompanied by changes in the chemical structure compared to the precursor polymer. Depending on the nature of these changes, different spectroscopic techniques can be applied to monitor the folding process.

Prominently, classical 1D nuclear magnetic resonance (NMR) spectroscopy, which detects changes in transitions between different nuclear spin states upon irradiation with electromagnetic waves in an external magnetic field depending on the local electron density surrounding a given nucleus, is employed to obtain detailed insights into the folding process by following the appearance, disappearance or shift of resonances associated with the reaction progress. Additionally, integration of the resonances in the spectra can provide valuable quantitative insights about the polymer composition and crosslinking density. As crosslinking a macromolecular chain is accompanied by a decrease in chain mobility, relaxation times are also influenced by the single-chain collapse, and measurements of the

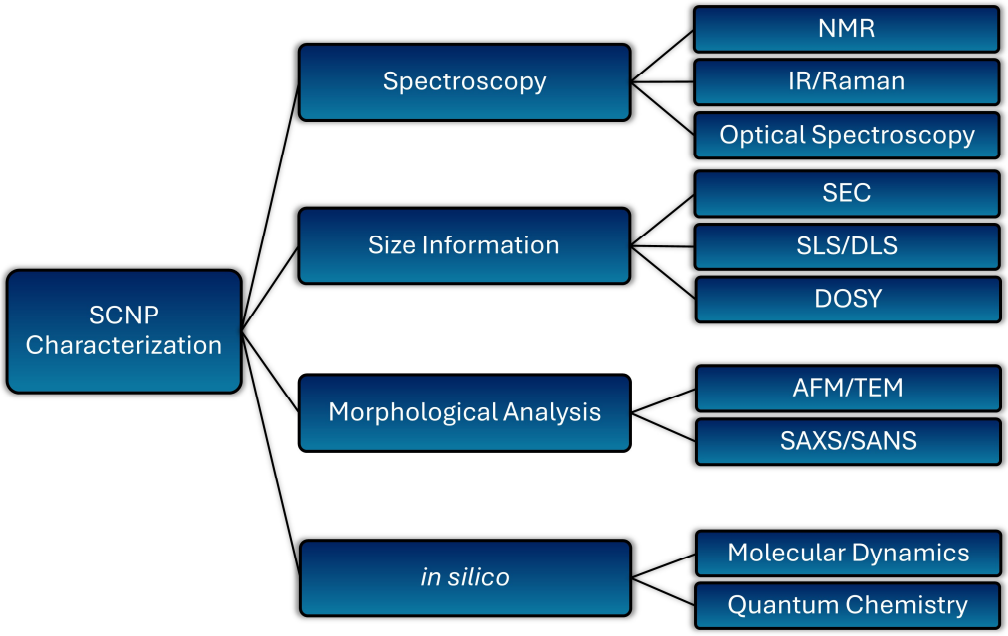

Figure 2.3 Examples of analytical techniques commonly employed for SCNP characterization.

transverse relaxation time (T_2) have been applied in the literature to evidence the folding reaction.[20,75] Further insights can be gained from higher dimensional NMR experiments, which correlate the interactions of different nuclei, with 2D NMR being the most widespread. For instance, Xiong *et al.* employed Nuclear Overhauser effect spectroscopy (NOESY), which provides information about the spatial proximity of different nuclei based on through-space interactions, to validate SCNP compaction by observing cross peaks between protons of different segments of their polymer which arise from intramolecular aggregation.[21] Conducting variable temperature (VT) NMR studies enables access to information regarding dynamic processes occurring on the NMR timescale, such as ligand exchange in metallopolymers or phase transitions.[3,76-77] While NMR spectroscopy is almost universally applicable in the SCNP field, further spectroscopic techniques find application, depending on the chemical nature of the specific SCNP folding reaction.

In cases where characteristic molecular vibrations are altered throughout the single-chain collapse, vibrational spectroscopy, for example infrared (IR) or Raman spectroscopy, can be applied.

When the folding process is accompanied by changes in the optical properties of the polymer sample, optical absorption and emission spectroscopy can proof valuable. Exemplarily, Berda and coworkers evidenced the photodimerization of polymer-bound anthracene, leading to SCNP compaction, by monitoring the absorbance decrease of the characteristic anthracene π-π^* absorption via ultraviolet-visible spectroscopy (UV/Vis).[78] Recently, Maag *et al.* introduced

a fluorescence read-out based on the Förster resonance energy transfer (FRET) between two organic dyes, which is exclusively observed in the folded state of their SCNP.[79]

When the elemental composition of the polymer changes throughout the folding process, techniques based on characteristic X-ray absorptions or emissions, such as energy-dispersive X-ray spectroscopy (EDX), X-ray absorption spectroscopy (XAS) or X-ray photoelectron spectroscopy (XPS), which provide information about the elements present in a given sample, can be employed. Similarly, when the single-chain collapse goes in hand with a change in molar mass, mass spectrometry can be employed to monitor SCNP formation.[80-81]

The presence of chiral structural elements in a SCNP allows for the application of circular dichroism (CD) spectroscopy, which detects the difference in absorption of circularly polarized light of different orientations. For example, the groups of Meijer and Palmans employed CD spectroscopy to evidence SCNP compaction by the formation of helical stacks of benzene-1,3,5-tricarboxamide units.[82]

As is evident from these examples, spectroscopic techniques enable in-depth insights into molecular structure and constitute an invaluable tool for deepening the understanding of SCNP formation. However, in most cases, the derived structural information is limited to bulk properties of the sample under investigation. When it comes to SCNPs, it becomes crucial to go beyond analyzing bulk properties to enable differentiation between the desired intramolecular crosslinking and undesirable intermolecular interactions. While the latter inevitably result in an increased size relative to the precursor macromolecule, the intramolecular processes characteristic of SCNPs often lead to a reduction in size. Thus, the application of size-sensitive analytical techniques is required.

The most prevalent example in the SCNP field is the use of size-exclusion chromatography (SEC), also referred to as gel permeation chromatography (GPC),[3-4] which separates molecules according to their solvodynamic volume by passing a solution of the sample over a column filled with a porous material with defined pore sizes. The smaller a molecule, the higher the accessible diffusion volume and consequently the longer the retention time on the stationary phase.[83] Upon SCNP compaction, the solvodynamic diameter of a macromolecule is often reduced compared to its precursor polymer, leading to a shift of the entire size distribution towards later retention times. Contrary, when intermolecular aggregation occurs, a shift of the entirety or parts of the size distribution towards earlier retention times can be observed. To correlate the elution time, which is dependent on experimental parameters, with

the molar mass or solvodynamic volume of a sample, the SEC setup can be calibrated with narrowly dispersed standards of known molar masses and sizes. This allows for approximate determinations of analyte molar masses and solvodynamic sizes based on the measured calibration curve. For polymers with chemical structures different from the employed standards, the so determined properties are inherently beset with uncertainties. Using this approach, the change in solvodynamic size resulting from the deviation of the SCNP conformation from a linear macromolecule leads to a difference in the apparent molar mass of a SCNP compared to its precursor, even in cases where the actual molar mass remains constant.[44] To correlate changes in elution time with actual molar masses, multi-detection SEC setups, which complement the commonly employed refractive index (RI) and ultraviolet (UV) absorption detectors by other means of detection, such as multi-angle light scattering (MALS) or viscometry, can be employed.[3-4] As the light scattering ability of a particle drastically increases with its size, MALS enables the determination of intermolecular aggregates at significantly lower concentrations than achievable with RI and UV detectors.[59] It is worth noting that in many cases a decrease in the SEC-derived dispersity index (*Đ*) is observed upon single-chain compaction, which has been investigated theoretically by Pomposo and coworkers.[84]

Under certain circumstances, interactions of the analyte with the stationary phase other than the purely size-based separation can occur, leading to erroneous size information derived from the measurement. This can be addressed by a change in the measurement conditions, for instance, by altering the solvent or stationary phase or by the addition of additives. For sensitive sample, effects of shear degradation may also be non-negligible.[83]

Visible light-based scattering techniques, such as static light scattering (SLS), based on the determination of the angle dependence of the intensity of scattered light, or dynamic light scattering (DLS), based on the measurement of the time dependence of the light intensity under a fixed angle, enable the non-destructive absolute molar mass and size analysis of macromolecules in solution based on first principles. Both methods have been applied extensively for SCNP characterization in the literature.[85] However, given the typical size range of SCNPs of less than 30 nm, the obtained data is to be considered with caution. The scattering intensity of the incident light is proportional to the sixth power of the particle diameter,[86] leading to a bias towards larger particles in the intensity-averaged size distributions, which becomes especially problematic when intermolecularly crosslinked particles are present.

When the shape and refractive index of the particles under consideration are known, the intensity distribution can be transformed into the number-averaged or volume-averaged size distribution, respectively, providing information about the fraction of particles of a given size.[87]

The change in solvodynamic volume of a particle directly affects its diffusion coefficient,[88-89] which can conveniently be measured by diffusion-ordered NMR spectroscopy (DOSY).[90-91] DOSY is based on the generation of magnetic field gradients along a NMR sample, leading to a dependence of the chemical shift evolution of the considered nucleus on its location within the sample. As diffusion influences a molecule's position within the sample, with the extent being dependent on time and the diffusion coefficient, the latter can be measured by recording the time-dependent NMR signal intensity at different gradient strengths and fitting the Stejskal-Tanner equation to the acquired data.[92] The resulting pseudo-2D spectrum correlates the diffusion coefficient with the related resonance in the 1D spectrum of the nucleus under consideration. Care must be taken when resonances of different molecules, for instance intramolecularly folded and intermolecularly crosslinked macromolecules, are isochronous, as this can yield average diffusion coefficients instead of the true diffusion coefficient of each species and requires sophisticated data treatment.[93] The Bruker pulse sequence employed for DOSY measurements throughout this thesis, *ledbpgp2s*, does not compensate for effects of convection. Thus, the determined diffusion coefficients are expected to be higher than the actual diffusion coefficients of the respective sample.[91]

The size analysis of a precursor polymer and the derived SCNP can provide valuable insights on the intramolecular nature of the crosslinking process and rule out the presence of undesired intermolecular aggregates. To gain further, more detailed insights on the internal structure of individual SCNPs, morphological investigations are necessary.

Direct visualization of nanosized objects is possible using high-resolution microscopy techniques, such as atomic force microscopy (AFM) or transmission electron microscopy (TEM). AFM makes use of the forces exerted by the sample on a cantilever, which is moved over a grid the sample is deposited on, to generate a topographic image. TEM generates an image from the detection of the transmission of a high energy electron beam through a specimen. Many studies make use of one or both techniques to corroborate their findings from other means of analysis. For example, the group of Paik employed AFM to generate 3D height profiles of three polystyrene SCNPs based on which size distributions were derived and

compared to the particle sizes determined by SEC and DLS.[94] In many cases, discrepancies between the microscopy images and solution based size data are observed, which are commonly traced back to modifications of the macromolecules throughout the sample preparation process or interactions with the cantilever tip in AFM or the electron beam in TEM, respectively.[3-4] Reported SCNP shapes vary from spherical particles[58] over ellipsoidal distortions[95] to oblong structures.[78] Most commonly, the investigations are conducted using dried samples, leading to inevitable morphological variations with respect to the solvated state.

Short wavelength scattering techniques, such as small-angle X-ray scattering (SAXS) and small-angle neutron scattering (SANS), which measure the intensity of scattered X-ray and neutron radiation, respectively, at small angles relative to the incident beam, enable the investigation of morphologies in solution in the size domain of individual macromolecular chains and below. Commonly, form factors and radii of gyration are determined. In a detailed systematic study, Lederer and colleagues employed SANS, along other techniques, to demonstrate the importance of chain length and crosslinking density on the extent of SCNP compaction.[96] Studies on the dynamics of SCNPs in solution showed that the intramolecular crosslinking increases internal friction and chain stiffness compared to the precursor polymers.[97]

In a body of work by Pomposo and colleagues, it was revealed that the good solvent conditions commonly employed throughout SCNP folding, under which polymers adopt self-avoiding conformations,[98] predominantly lead to local compactions of the linear precursor macromolecular chains, reminiscent of the sparse morphologies of intrinsically disordered proteins.[97,99] This results from the preference for reactions of functional groups separated by short contour distances under these conditions. Several strategies have been developed to further compact the folded structures to resemble the morphologies of globular proteins, including the use of orthogonal folding units,[100] very long crosslinkers,[101] or crosslinking under poor solvent conditions,[102] all leading to long-range loops between functional groups separated by long contour distances, favorable of global compaction.

Investigations of the structure and dynamics of SCNPs in the melt or solid state are impeded by the difficulty to access the large amounts of material necessary for the characterization.[3,103]

In recent years, computational methods have emerged to aid the interpretation of experimental data and deepen the understanding of SCNP behaviors. For small subunits of

SCNP systems, quantum chemical calculations can provide valuable rationalizations of experimental findings.[7,104] To model the entire polymeric system, coarse-grained or fully atomistic molecular dynamics simulations as well as Monte Carlo methods have been used, for instance, to propose novel synthetic pathways towards globular SCNPs,[105] to investigate the difference between homofunctional and heterofunctional collapse on SCNP morphology,[100] or to understand the structure and dynamics upon concentration variations.[106] The simulations enable an understanding of the processes occurring down to the level of single chains inaccessible in an experimental manner, providing insights into the different distributions of crosslinking sites in an ensemble of individual SCNPs, oftentimes evidencing topological polydispersity.

For all characterization methods, challenges are posed by the often pronounced dependence of SCNP sizes, shapes and properties on experimental parameters, such as solvent choice, temperature, or the presence of other species, and the fact that batch-to-batch reproducibility might not necessarily be granted. In many cases, the low concentrations necessary to prevent intermolecular aggregation lead to low signal-to-noise ratios, resulting in compromised data quality and hence unreliable interpretations. In a critical survey, Blasco and colleagues have reviewed SCNP size data reported in the literature. The authors found strong variations of sizes using different characterization techniques on the same polymer, and SCNP densities calculated using the reported data often either exceeded the density of bulk material or were significantly lower than densities documented for the open-chain precursor polymers.[85] Consequently, precursor polymers and SCNPs should always be characterized under identical conditions and the properties considered in relation to each other. Generally, different complementary characterization techniques should be employed to obtain a reliable picture of the true nature of SCNPs, and care must be taken when drawing quantitative conclusions.

2.3 METAL-FUNCTIONALIZED SINGLE-CHAIN NANOPARTICLES

Metal functionalization of polymeric materials fuses the tunable characteristics of polymers with the wide range of functionalities of metals. Further, the synergistic combination of both can provide access to hybrid materials with properties beyond the ones of the individual constituents.[107-108] Nature uses this synergy in metalloproteins to fulfill vital functions in highly complex processes, such as photosynthesis, respiration or nitrogen fixation.[109] Especially metalloenzymes, belonging to the most potent catalysts on earth, have

served as inspiration for various areas of research.[110-111] In the realm of single-chain technology, metals can endow SCNPs with additional functionalities or serve as structure forming elements in the form of crosslinking moieties (refer to **Figure 2.4**). Different strategies have been developed to incorporate metals into SCNPs. Predominantly, metal functionalization is achieved by the addition of a metal-containing monomer throughout the synthesis of the linear precursor polymer, coordination of donor moieties incorporated in the macromolecular chain upon reaction with suitable metal precursors or the use of multifunctional metal complexes as SCNP crosslinkers, respectively.

One of the earliest examples of organometallic SCNPs was reported by Lemcoff and coworkers who synthesized a linear poly(1,5-cyclooctadiene) polymer which, upon reaction with the chlorobis(ethylene)rhodium(I) dimer, collapsed intramolecularly. Variation of the rhodium content allowed for the precise control of the SCNP contraction, with higher metal loadings leading to a more pronounced decrease in the solvodynamic volume compared to the precursor polymer.[112] Another early example was reported by the groups of Barner-Kowollik and Roesky who employed a homotelechelic α,ω-bis(triphenylphosphine) polymeric macroligand, which cyclized upon addition of Pd(II) ions under dilute conditions, to form a single-ring nanoparticle.[19]

By now, metals from all regions of the periodic table have successfully been incorporated into SCNPs, with transition metals being the most prevalent. By far, the most examples have been

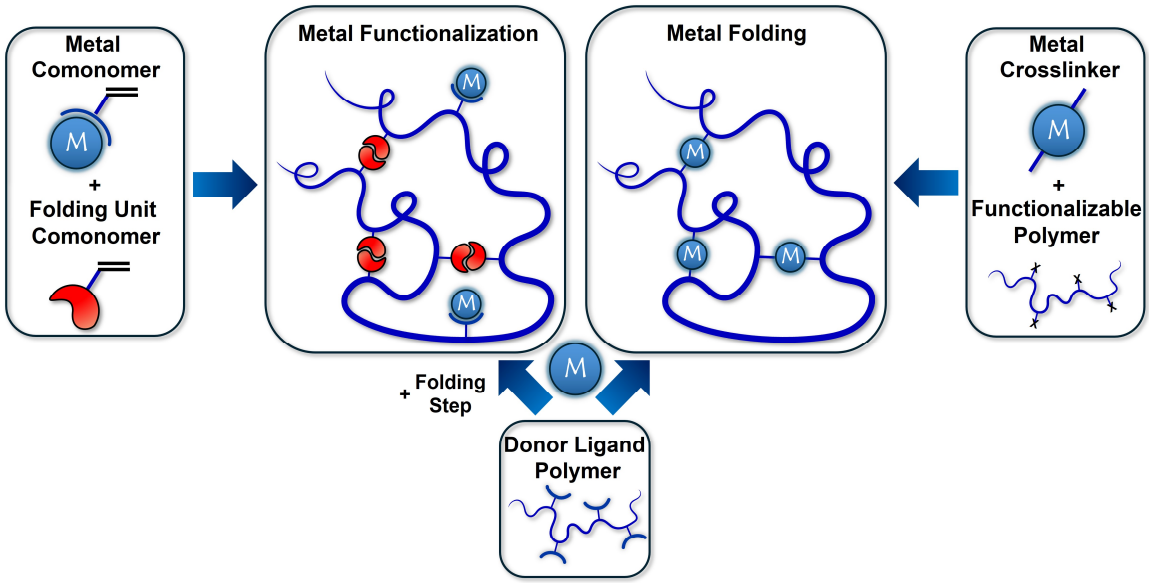

Figure 2.4 Schematic illustration of selected synthetic pathways towards metal-functionalized SCNPs using the metal as complementary functionality or structure forming crosslinker.

reported for the coinage metal copper.[5,9,14,21,24,94,102,113-130] In an early study, the Pomposo group reported on the synthesis of copper-functionalized SCNPs, exploiting the coordination of acetoacetoxy side chain units to Cu(II) ions to induce single-chain collapse in a methacrylate-based polymer. The resulting Cu(II) SCNPs showed catalytic activity in alkyne coupling reactions (refer to Chapter 2.4).[114] Following work by the same group aimed at the fine tuning of the metal distribution within individual SCNPs. Depending on the solvent the synthesis was conducted in, either a uniform distribution of Cu(II) ions all over the nanoparticle or clustering with high local Cu(II) concentrations at certain spatially confined regions of an individual SCNP was achieved.[102] The effect of the intrachain metal distribution on the catalytic performance was investigated in follow-up studies, finding a beneficial effect of the clustering in a copper-catalyzed azide-alkyne cycloaddition, highlighting the importance of understanding and tuning SCNP morphology for a desired function.[5] Reverting the previous approaches, copper has also been used to achieve SCNP unfolding. In norbornene polymers grafted with 2,2'-bipyridine-substituted benzene-1,3,5-tricarboxamide units, self-assembly of the latter induced intramolecular chain folding, which could efficiently be disrupted by the addition of Cu(II) ions, hence forming the metal-functionalized open-chain polymer.[113]

Apart from copper, SCNPs have been realized with the 3d metals titanium,[131] chromium,[132] iron,[7,16,126-127,133-140] cobalt,[126-127,141] nickel[16,127,142-143] and zinc.[23,144] Particularly worth noting in this regard is the first use of light as a trigger to induce the metal-mediated chain compaction, which was realized recently by exploiting the photoisomerization of spiropyran entities to their ring-opened form which forms stable metal complexes.[126] Also worth noting is an unconventional approach of Qian *et al.* who synthesized ZnS quantum dots with tunable sizes within a SCNP environment.[144]

Out of the 4d metals, yttrium,[6] molybdenum,[9] ruthenium,[82,145-148] rhodium,[22,104,112,149-152] palladium,[18-20,125,127,153-155] silver[156] and cadmium[144] have been employed for SCNP formation. For instance, building up on the previous work on single-ring nanoparticles mentioned above, Willenbacher *et al.* synthesized Pd(II) SCNPs folded via palladium coordination by polymer-bound triarylphosphine moieties following the repeat unit approach. The palladium coordination mode was investigated in detail by NMR spectroscopic studies combined with the synthesis of small molecule model complexes, establishing the hypothesis that a pair of two phosphorous atoms from the macromolecular chain binds to each palladium

ion in the SCNP in a *trans* arrangement.[20] An elegant demonstration of exploiting the reversibility of metal ligand bonds within SCNPs was reported by Diesendruck and coworkers. Addition of the chlorobis(ethylene)rhodium(I) dimer to a partially *gem*-dichlorocyclopropane-functionalized polybutadiene led to SCNP folding based on the ligand replacement of ethylene by polymer π bonds. Under sonication, these intramolecular crosslinks proved to be able to remove stress from the macromolecular backbone by scission of the metal ligand bonds, preventing main chain fragmentation that would occur without the weak intramolecular crosslinks. After termination of the mechanical stimulation, the Rh-π bonds showed the ability to reform spontaneously, providing a pathway for intramolecular autonomous repair.[150] Similar chemistry enabled the same group to transfer chemical information between two macromolecules, reminiscent of signal transductions in natural proteins. For that, a low molar mass polybutadiene was loaded with Rh(I) ions to form SCNPs. Upon addition of a higher molar mass polybutadiene, the Rh(I) ions were released from the smaller polymer and transferred to the larger one, resulting in distinct conformational changes in both macromolecular chains. The authors attributed this non-commutative chemical communication process to the higher effective denticity of the larger polymer.[152]

Concerning the 5d elements, SCNPs containing iridium,[149,157] platinum[10-11,14,158] and gold[6,8,12,75,159-160] have been reported in the literature. Remarkable is the combination of metals with further functionalities, as for instance recently demonstrated by Maag *et al.*, who combined Au(I) with a luminescent crosslinker within a SCNP, enabling the visualization and tracing of the catalytically active polymer.

Regarding the main group metals, only magnesium,[127] gallium[161] and the metalloid tellurium[162] have made their way into SCNP chemistry thus far. However, in the latter two cases the metal does not serve as structure forming element but imparts additional functionality to the nanoparticles.

For the lanthanides, SCNP functionalization has to date only been realized with europium[10] and gadolinium.[49] For the latter, an alkyne-functionalized diethylenetriaminepentaacetic acid derivative, which could be loaded with Gd(III), was used to induce intrachain crosslinking by azide-alkyne cycloaddition with pendant azide moieties in a methacrylate polymer. The authors studied the relaxivity compared to a small molecule analogue and a commercial magnetic resonance imaging (MRI) agent, identifying the Gd SCNPs as promising candidates for future MRI applications.[49]

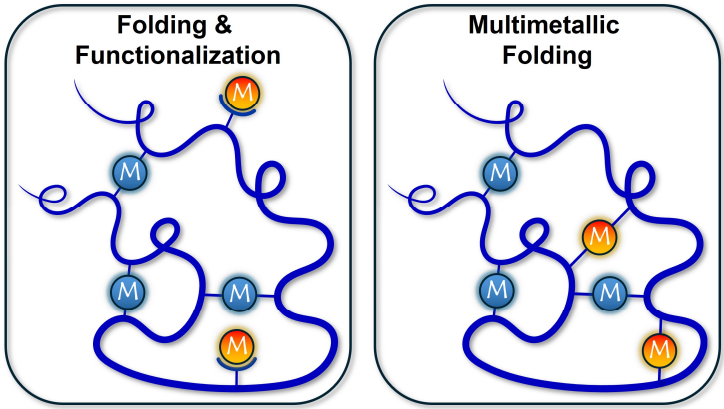

Figure 2.5 Illustrative depiction of different types of multimetallic SCNPs employing one metal as folding unit and another one as additional functionality (left) and employing different metals for multimetallic folding (right).

Transcending the domain of purely monometallic SCNPs, further functionalities can be introduced. Especially intriguing from a fundamental and application perspective, is the combination of different metals within a single SCNP. Such heteromultimetallic SCNPs can consist of several metals serving as folding units or one metal used to induce single-chain collapse, while another one is coordinated by pendant groups on the macromolecular main chain, without contributing to further chain compaction (refer to **Figure 2.5**).

Pioneering seminal work in the realm of heteromultimetallic SCNPs was conducted by Lemcoff and coworkers. Building on their previous work on Rh(I)-folded poly(1,5-cyclooctadiene),[112] the authors generalized their approach and prepared bimetallic Rh(I)-Ir(I) SCNPs by reacting the chlorobis(ethylene)rhodium(I) dimer and the chlorobis(cyclooctene)iridium(I) dimer with poly(1,5-cyclooctadiene) in dilute solution. It was demonstrated that the addition of the second metal subsequent to the first one resulted in a more pronounced compaction, with the extent being dependent on the total amount of incorporated metal and independent of the order of addition of the metal precursors. Metal incorporation proved to be possible in any desired ratio of the two metals.[149] The synthetic approach towards multimetallic SCNPs was extended by Knöfel *et al.* who introduced the use of orthogonal ligand systems to selectively bind metal ions. To achieve this, triarylphosphine as well as triarylphosphine oxide pendant groups were introduced into a styrene-based polymer. The former strongly bind to Pt(II) ions, while the latter possess a significantly reduced affinity for Pt(II) complexation. Contrary, the phosphine oxide moieties show a more pronounced tendency to coordinate to Eu(III) than the phosphine groups. A phosphine to platinum ratio of 2:1 and a phosphine oxide to europium ratio of 1:1 were suggested, leading to heterobimetallic SCNPs folded by the Pt(II)

ions and further functionalized by Eu(III) ions. The orthogonal nature of the binding events enables the efficient one-pot synthesis of the Eu(III)-Pt(II) SCNPs in the simultaneous presence of both metal precursors. Furthermore, additional experiments demonstrated that subsequent addition of the different metals resulted in the same final SCNPs, independent of the order of the metal addition.[10] A similar approach was followed by Bohlen and Kulendran *et al.* for the synthesis of heterobimetallic Y(III)-Au(I) SCNPs based on the selective coordination of carboxylate and phosphine ligands to Y(III) and Au(I), respectively, in a styrene polymer.[6] Most recently, the Pomposo group reported on the synthesis of bimetallic Cu(II)-Pt(II) SCNPs by light-triggered carbene formation for the complexation of Pt(II), followed by the addition of a Cu(II) salt, leading to further single-chain compaction upon complexation by pendant acetoacetoxy moieties on the methacrylate-based main chain. The resulting SCNPs proved to be capable of catalyzing a consecutive one-pot alkyne semihydrogenation-alkene dioxygenation reaction sequence, impressively demonstrating the synergistic effect the combination of two metals within a SCNP can provide (refer to Chapter 2.4).[14] Related to the synthesis of multimetallic SCNPs is also the recent work by Zebari *et al.*, reporting on Co SCNPs composited with ZnO nanoparticles to fine-tune the thermal and optical properties as well as the conductivity of the material.[141]

In general, challenges in the field of metal-functionalized SCNPs are the oftentimes demanding synthetic procedures and the analytical characterization of the resulting polymers. In terms of synthesis, one of the most crucial considerations is to ensure and validate that unreacted metal precursors are effectively removed from the metal SCNPs to avoid negative interferences with the subsequent applications and misinterpretations of experimental observations. The purification and analytical characterization of metal-functionalized SCNPs is often complicated by the thermodynamic instability or lability of the polymeric ligand metal bonds under the conditions employed for purification or analysis, respectively, potentially leading to uncontrolled metal leaching and consequently limited reproducibility. Another challenge is posed by the precise quantification of the metal content within a SCNP, which is a key factor in many applications, especially when comparisons to small molecule analogues or other metal-functionalized polymers are made. Depending on the chemical structure of the SCNPs, methods such as NMR, inductively coupled plasma mass spectrometry (ICP-MS) and optical emission spectroscopy (ICP-OES) or electron paramagnetic resonance spectroscopy (EPR) can be employed for this purpose. A further crucial consideration is the coordination

environment of a metal in a SCNP for which insights can oftentimes be gained by NMR spectroscopic analysis or the synthesis of small molecule model complexes.

2.4 APPLICATIONS OF SINGLE-CHAIN NANOPARTICLES

The advancements made regarding the synthesis of SCNPs enable the design and access to tailored macromolecular architectures with a precise control over chemical structure and morphology based on reversible or irreversible structural alterations. This allows for the fine-tuning of polymer structures, solubility properties, the targeted formation of hydrophilic or hydrophobic compartments and the responsiveness to external stimuli, opening up avenues for a plethora of potential academic and industrial applications. The main application fields of SCNPs explored in the literature are nanomedicine, sensing, the improvement of advanced polymeric materials and catalysis (refer to **Figure 2.6**).[3-4]

Their similarity in size to proteins and viruses makes SCNPs promising candidates for medical applications. The size tunability provided by varying molar mass and crosslinking density enables the engineering of nanoparticles in a size range preventing rapid clearance and allowing for the retention in different types of tissue. In the nanomedicine field, SCNPs mainly find application as delivery vehicles for therapeutically relevant cargo molecules and as next-generation imaging agents.[3] Exemplarily, Cheng *et al.* demonstrated the potential of SCNPs to target tumor cells, while concomitantly reducing the risk of premature drug release under physiological conditions in *in vitro* studies. For that, the hydrophilic anticancer drug

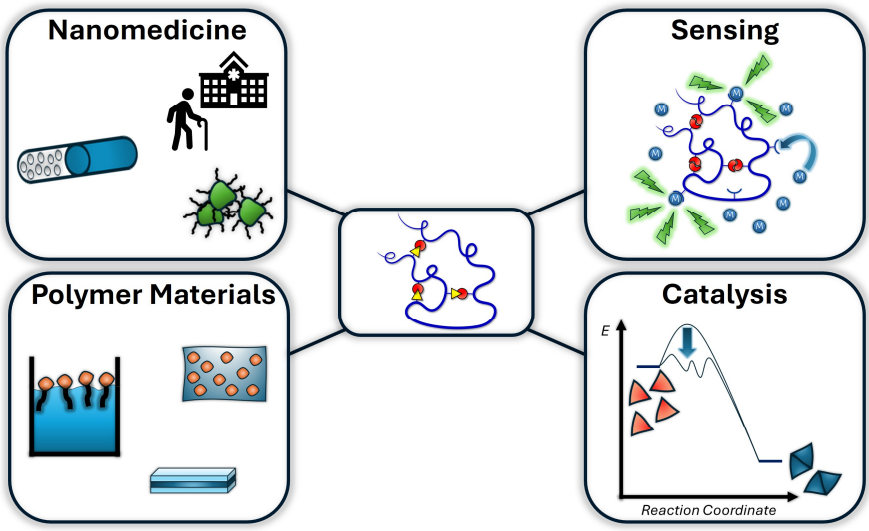

Figure 2.6 Graphical overview of the main application fields of SCNPs currently explored in the literature.

5-fluorouracil was loaded into a methacrylate-based polymer containing PEG side chains for water solubility and uracil-diamidopyridine moieties for SCNP folding by the formation of self-complementary sextuple hydrogen-bonded arrays. Investigations of the pH and temperature response of the nanocarrier indicated high stability under physiological conditions, whereas at lower pH values and slightly increased temperatures, as commonly found in tumor microenvironments, the drug was released with high efficiency.[163] In another example, Loinaz and coworkers aimed at advancing *in vivo* minimally invasive imaging of pancreatic adenocarcinoma. For that, biocompatible SCNPs based on a poly(methacrylic acid) polymer were prepared and functionalized with a peptide targeting receptors overexpressed in pancreatic cancer cells. Loading the SCNPs with the gamma emitter ^{67}Ga enabled *in vivo* investigations of the pharmacokinetic properties of the nanoparticles by single photon emission computerized tomography.[161]

The tunable reactions of SCNPs to external stimuli also hold potential for sensing applications. Seminal work in this realm was conducted by the groups of Voets and Palmans, making use of the disruption of the aggregation-induced emission of 2,2'-bipyridine-substituted benzene-1,3,5-tricarboxamide units within SCNPs upon addition of metal ions (refer to Chapter 2.3).[113] Further, Pomposo and Latorre-Sanchez reported on the colorimetric detection of the prolamin protein zein by exploiting the subtle balance of zein-pyridine-gold interactions in the presence of pyridine-functionalized SCNPs. In the absence of zein, the reduction of Au(III) with hydrazine in a solution of their SCNPs led to the formation of small gold nanoparticles, stabilized by pyridine coordination, resulting in a red-colored solution. Contrary, in the presence of zein, the high affinity of pyridine for zein binding prevented pyridine coordination to the growing gold nanoparticles, diminishing the stabilizing effect, consequently leading to the formation of larger gold nanoparticles, resulting in a blue-colored solution. The solution color varied linearly in a wide zein concentration range, enabling its sensitive and quantitatively precise colorimetric detection.[159]

Apart from nanomedicine and sensing, SCNPs have found miscellaneous applications as additive or functional component in a variety of polymeric materials. For instance, Zhang and Zhao exploited the surfactant properties of amphiphilic SCNPs for the generation of functional colloidal particles. Employing the SCNPs as surfactant in the suspension polymerization of styrene resulted in colloidal polystyrene particles with SCNPs on the surface. The latter could subsequently be cleaved off and the residual functionalities on the particle surface enabled

dye functionalization, resulting in fluorescence-labeled polymer nanoparticles.[164] In another example, the use of SCNPs as part of all-polymer nanocomposites has been demonstrated, wherein intramolecularly crosslinked polystyrene dispersed in a matrix of linear polystyrene critically influenced the blend viscosity.[165]

Inspired by nature's most efficient catalysts, naturally occurring enzymes, formed by the precise intramolecular folding of linear strands of amino acids, the urge for novel catalytic applications has been a major driving force within the SCNP field. Enzymes perform catalytic transformations with remarkable efficacy under mild conditions by creating well-defined pockets, providing beneficial stabilizing effects for key steps in catalytic processes, within their interior. However, their function is critically dependent on the reaction conditions, with many enzymes exclusively functioning in physiological surroundings. Furthermore, the reactivity scope is often limited to a small range of selected substrates. SCNPs offer a viable pathway towards the rational design of enzyme-inspired catalysts with improved resistivity towards different reaction conditions and featuring a broad substrate scope.[3-4,13,15]

For instance, Zeng *et al.* reported on CO_2-folded SCNPs as improved carboxylase mimics. A frustrated Lewis pair linear precursor polymer was collapsed intramolecularly by CO_2 addition, thereby efficiently activating the CO_2, enabling the carboxylation of various substrates at room temperature. Contrary to natural carboxylases, their SCNPs not only showed activity towards C(sp^3)-H bonds but also towards substrates featuring C(sp^2)-H and C(sp)-H bonds.[166] Various further examples of metal-free organocatalytic SCNPs are reported in the literature.[167-174]

Pioneering work on the catalytic application of metal-functionalized SCNPs has been conducted by the groups of Palmans and Meijer. Ruthenium functionalization of triarylphosphine moieties in a methacrylate polymer, folded via the helical self-assembly of pendant benzene-1,3,5-tricarboxamide units, resulted in a water soluble transfer hydrogenation catalyst, efficient even for substrates with poor water solubility.[82] Following work by the same authors, however, demonstrated that the helical self-assembly was not crucial for the catalytic performance of the system.[145] Studies conducted by the Pomposo group explored the unique opportunities the polymeric environment of a metal can provide for catalysis. For Cu(II)-folded SCNPs, the selective transformation to one oxidatively homo-coupled product from a mixture of terminal alkynes was observed, whereas analogous small molecule catalysts caused mixed homocoupling and heterocoupling of the substrates.[114] A similar observation has been made by Lemcoff and coworkers who employed Rh(I) catalysts

for the reaction of 4-nitrobenzaldehyde and phenylboronic acid. While for a small molecule Rh(I) catalyst the expected cross-coupling was observed, applying the Rh(I) SCNPs resulted in the almost exclusive formation of biphenyl, even under conditions favorable for cross-coupling. In the same work, the authors prepared Ir(I) SCNPs as active catalyst for the allylation of acetophenone. Evaporation of the solvent after completion of the reaction and washing of the residue enabled the recovery of the SCNP catalyst and its subsequent reuse in further catalytic cycles.[149]

The recyclability of SCNP catalysts, elegantly fusing the high activity of homogeneous catalysis with the simple catalyst reuse characteristic of heterogeneous catalysis, is a key benefit of polymer-supported catalysts over their small molecule equivalents. Further elegant demonstrations of recyclable SCNP catalysts were, for instance, reported by the groups of Barner-Kowollik and Roesky. For example, Pt(II)-folded SCNPs were employed for the amination of allyl alcohol and the catalyst recovered by precipitation or dialysis after completion of the catalytic reaction.[11] Similarly, in another study, heterobimetallic Y(III)-Au(I) SCNPs catalyzed the intramolecular hydroamination of aminoalkynes and were subsequently recovered by dialysis.[6] Furthermore, the recovery of Eu(III)-Pt(II) SCNPs after catalysis proved to be possible by column chromatography. Additionally, the luminescent properties of the Eu(III) ions allowed for visual catalyst tracing.[10]

Metal-functionalized SCNPs have also been explored for applications in asymmetric catalysis.[129,131-132] For instance, Zhang *et al.* prepared SCNPs containing chiral Ti(IV) oxazoline complexes as folding units for asymmetric sulfoxidations in water.[131]

A recent report by Pomposo and coworkers demonstrated, for the first time, the synergistic combination of two metals within a SCNP environment for a consecutive catalytic reaction sequence. The authors synthesized SCNPs folded by both, Cu(II) and Pt(II) ions, fusing the hydrogenation catalyst activity of Pt(II) ions with the ability of Cu(II) to catalyze alkene dioxygenations to realize a consecutive one-pot alkyne semihydrogenation-alkene dioxygenation for the synthesis of pharmaceutically and agriculturally relevant β-keto-*N*-alkoxyphthalimides from differently substituted phenylacetylenes and *N*-hydroxyphthal-imide.[14]

Broadening the application scope even further, SCNP catalysts have also been studied in biological media and cellular environments.[22,120,123,130,148,175] Exemplarily, Sathyan *et al.* encapsulated a dirhodium carboxylate catalyst in an amphiphilic polymer comprising dodecyl

and Jeffamine side chains and incubated HeLa cells with the resulting SCNPs. This enabled catalytic carbene insertion reactions between 2,3-diaminonapthalene and α-keto diazocarbenes followed by intramolecular cyclization to produce luminescent and biologically active benzoquinoxalines in a bioorthogonal fashion.[22]

These examples highlight the unique opportunities provided by SCNPs for a plethora of applications and pave the way for future explorations of academic and industrial uses going beyond the possibilities provided by small molecules, linear macromolecules or polymer networks. These promising perspectives necessitate the exploration of methods to upscale SCNP synthesis, foster advanced characterization techniques to gather more detailed insights into the structure and properties on the level of individual macromolecular chains and develop new multifunctional SCNP systems.

Chapter 3: Motivation and Thesis Outline

Single-chain nanoparticles (SCNPs) have been the subject of intense research and explored as a new class of polymeric materials in recent years. The tailored intramolecular crosslinking of synthetic macromolecular chains takes inspiration from the precise folding of linear strands of amino acids to highly functional proteins, vital for life on earth. The bioinspired approach opens avenues for advanced functional materials with properties going beyond what nature has to offer. Combining the tunable characteristics of synthetic macromolecules with the diverse range of functionalities provided by metals and their complexes is at the heart of the field of metal-functionalized SCNPs and defines the scope of this work.

This thesis aims at critically pushing the current boundaries of the field of metal-functionalized SCNPs by addressing omnipresent challenges concerning synthesis, characterization and catalytic applications by the synergistic combination of inorganic and polymer chemistry (refer to **Figure 3.1**).

Specifically, the first part of the thesis addresses the synthesis of SCNPs featuring barium ions as single-chain crosslinkers, thereby contributing to the currently underexplored field of main

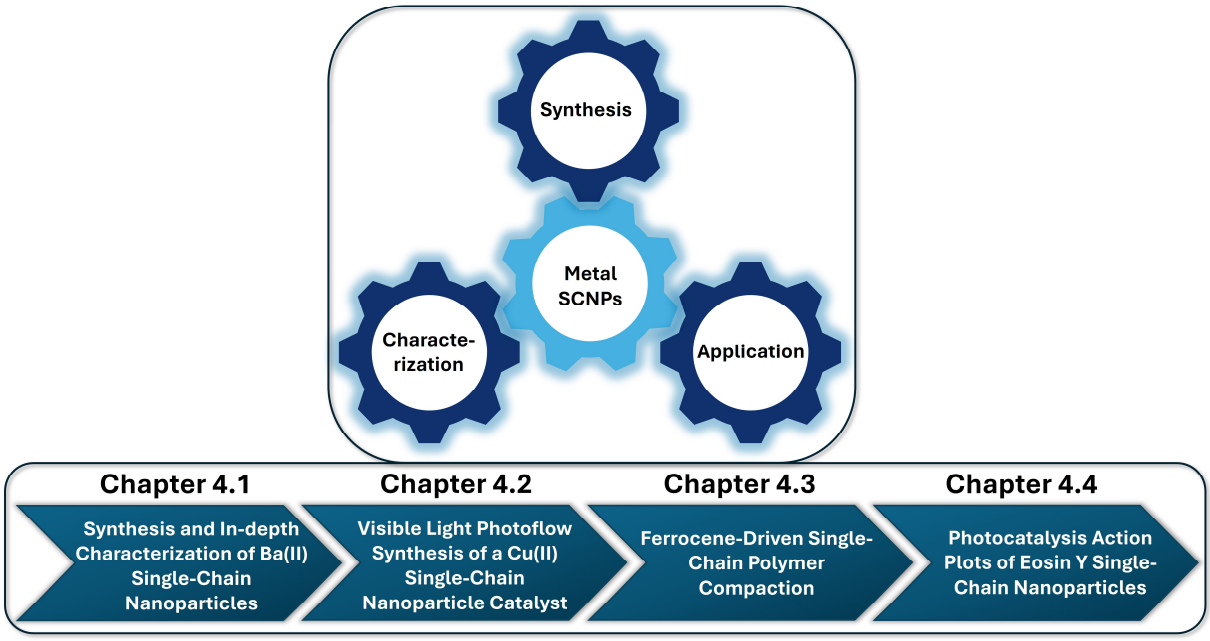

Figure 3.1 Outline of the work on the synthesis, characterization and catalytic application of metal-functionalized single-chain nanoparticles (SCNPs) presented in this thesis.

group metal SCNPs. The high contrast provided by the heavy barium atoms in transmission electron microscopy experiments is exploited for the imaging of the internal SCNP structure with atomic resolution, providing unprecedented experimental insights into the distribution of metal ions within metal-folded SCNPs inaccessible by any other analytical technique.

The second part of the thesis aims at exploring the synthesis of copper-functionalized SCNPs under continuous flow conditions to address the pervasive scalability challenge limiting SCNP synthesis. The resulting copper SCNPs are applied for catalytic transformations and their synthesis process is compared to a traditional batch synthesis protocol.

The third part of the thesis is devoted to advancing the field of multimetallic SCNPs by presenting heterobimetallic iron-palladium SCNPs and demonstrating their catalytic abilities.

The last part of the thesis is dedicated to demonstrating how metal ions can beneficially alter the properties of purely organic macromolecules. For that, the synthesis of polymers functionalized with the organic dye Eosin Y is described and the influence of zinc functionalization on the wavelength-resolved photocatalytic activity explored.

Chapter 4: Results and Discussion

4.1 SYNTHESIS AND IN-DEPTH CHARACTERIZATION OF BA(II) SINGLE-CHAIN NANOPARTICLES

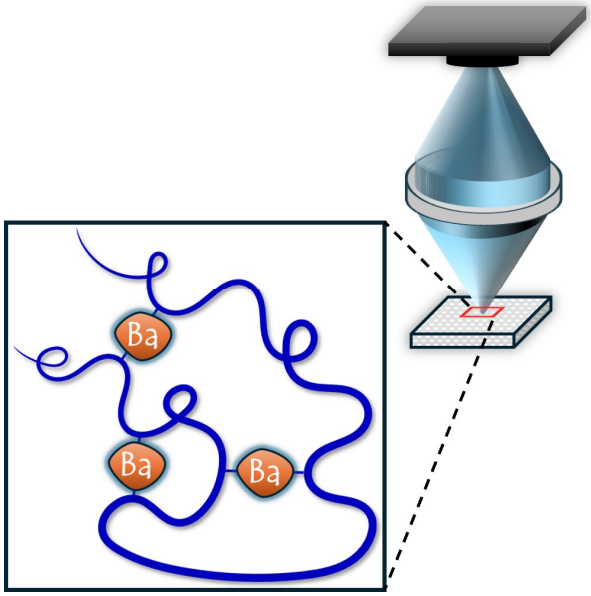

Figure 4.1 Graphical abstract of the chapter "Synthesis and In-depth Characterization of Ba(II) Single-Chain Nanoparticles".

Abstract

Ba(II) single-chain nanoparticles (SCNPs) were prepared based on two different polymeric backbones, specifically poly(styrene-*co*-4-vinylbenzoic acid) and poly(poly(ethylene glycol) methyl ether methacrylate-*co*-2-carboxyethyl acrylate). For both polymers, Ba(II)-induced single-chain folding was evidenced by ^{1}H nuclear magnetic resonance spectroscopy, size-exclusion chromatography, dynamic light scattering, diffusion-ordered spectroscopy and infrared spectroscopy, respectively. Further, the Ba(II) SCNPs derived from poly(poly(ethylene glycol) methyl ether methacrylate-*co*-2-carboxyethyl acrylate) were investigated by sophisticated molecular dynamics simulations and atomic resolution scanning transmission electron microscopy imaging, providing valuable insights into the dynamic behavior of the metal ions within the individual macromolecules. The dynamic interactions of the barium ions with the macromolecules enabled the on-demand unfolding of the SCNPs and the recovery of the pristine precursor polymer by exploiting the low solubility of barium sulfate in aqueous solution.

Table 4.1 Statement of contributions of coauthors of the publication "Control over Ba(II)-mediated Single-Chain Polymer Nanoparticle Compaction by Dynamic Metal Complexation" (*manuscript in preparation*).

Contributor	**Statement of contribution**
Sebastian Gillhuber	Conceptualization, Methodology, Formal analysis, Investigation, Writing – Original Draft, Review & Editing, Visualization, Project administration
Jochen A. Kammerer	Conceptualization, Methodology, Formal analysis, Investigation (Microscopy), Writing – Original Draft, Review & Editing, Visualization, Project administration
Ada Quinn	Conceptualization, Methodology, Formal analysis, Investigation (Simulations), Writing – Original Draft, Review & Editing, Visualization
Joshua O. Holloway	Writing – Review & Editing, Supervision
Kai Mundsinger	Resources
Evelina Liarou	Resources
Dmitri Golberg	Resources
Hendrik Frisch	Conceptualization, Writing – Review & Editing, Supervision, Project administration
Megan O'Mara	Conceptualization, Writing – Review & Editing, Supervision
Christopher Barner-Kowollik	Conceptualization, Writing – Review & Editing, Supervision, Project administration, Funding acquisition
Peter W. Roesky	Conceptualization, Writing – Review & Editing, Supervision, Project administration, Funding acquisition

4.1.1 Introduction

Main group metal-functionalized SCNPs are a scarcity in the literature. So far, only magnesium,[127] gallium[161] and the metalloid tellurium[162] have made their way into SCNP chemistry, and only in the first case the metal acts as single-chain crosslinker, whereas in the other cases it solely imparts an additional functionality to the respective SCNPs (refer to Chapter 2.3).

Owing to the high electropositivity of the s block elements, the bonding situation within their compounds is predominantly ionic in nature. Given the tendency of the alkaline earth metals to form divalent cations, their ionic bonds are commonly stronger than the ones formed by alkali metals of the same period as the latter favor the formation of monocations with a lower charge density. Additionally, taking into consideration that successful metal-induced SCNP formation requires the coordination of at least two polymer-bound ligands to a metal, makes the alkaline earth metals more promising candidates as they typically require two monoanionic ligands for charge compensation. Further, to achieve the highest degree of compaction, it seems desirable to use an alkaline earth metal with a large ionic radius to enable coordination of as many structural units of the macromolecular chain as possible to the metal ion, stabilizing the SCNP and leading to the formation of compact nanoparticles. These considerations make the largest, non-radioactive alkaline earth metal, barium, the most intriguing candidate for s block metal induced single-chain folding. Thus, the current chapter targets the synthesis of Ba(II)-folded SCNPs.

Various ligand systems have been explored for Ba(II) coordination in classical coordination chemistry, including but not limited to neutral or anionic carbon, nitrogen, oxygen, sulfur or mixed multidentate donor ligands. However, the high charge density and simple synthetic access to anionic oxygen donor ligands make them the most promising candidates for the formation of strong ionic bonds with Ba(II) ions. Outstanding in this realm are carboxylate-based ligand systems, due to their simple preparation from readily accessible carboxylic acid precursors and their ability for strong chelating coordination.[176-177]

Therefore, the current chapters aims at incorporating carboxylic acid functionalities in different polymer backbones to enable the formation of Ba(II)-folded SCNPs via the coordination of carboxylate ligands. Specifically, polymeric backbones based on styrene and poly(ethylene glycol) methyl ether methacrylate, respectively, providing access to Ba(II) SCNPs soluble in a wide variety of solvents, are to be explored and their properties examined.

4.1.2 Styrene-based Ba(II) Single-Chain Nanoparticles

To achieve the synthesis of Ba(II) SCNPs soluble in low polarity organic solvents, a styrene-based polymeric backbone was initially investigated. Due to the commercial availability of a variety of differently substituted styrene derivatives, a wide range of functionalized polystyrenes with varying degrees of functionalization can conveniently be accessed by copolymerization of styrene with suitably functionalized comonomers. Reversible deactivation radical polymerization (RDRP) techniques enable the targeted polymerization of styrene monomers, providing access to polystyrenes with a high control over the functionalization degree, dispersity and average molar mass.

Specifically, a copolymer of styrene and 4-vinylbenzoic acid was synthesized by nitroxide-mediated polymerization (NMP) as depicted in **Scheme 4.1** (Polymer **P1**).[37] While styrene constituted the inert polymer backbone, the carboxylic acid groups of the 4-vinylbenzoic acid moieties enabled simple and efficient post-polymerization modification. Given the statistical nature of the copolymerization process, statistical copolymers with a random distribution of the 4-vinylbenzoic acid monomers along the macromolecular chain were obtained. Hence, all SCNP folding reactions based on this copolymer follow the repeat unit approach (refer to Chapter 2.1).[42] SEC measurements in tetrahydrofuran (THF) indicated a number-averaged molar mass (M_n) of M_n = 19800 g·mol^{-1} and a dispersity of $Đ$ = 1.15. The ^{1}H NMR spectrum of **P1** acquired in THF-d_8 is depicted in **Figure 4.2**. The resonances in the chemical shift (δ) region δ = 2.42-1.18 ppm correspond to the protons of the aliphatic polymer backbone, the resonances at δ = 7.90-6.20 ppm to the aromatic ring protons and the resonance at δ = 11.22-11.10 ppm to the carboxylic acid proton, respectively. The assignments of the resonances of the individual aromatic ring protons can be deduced from the literature and render the determination of the copolymer composition by relative integration of the spectral

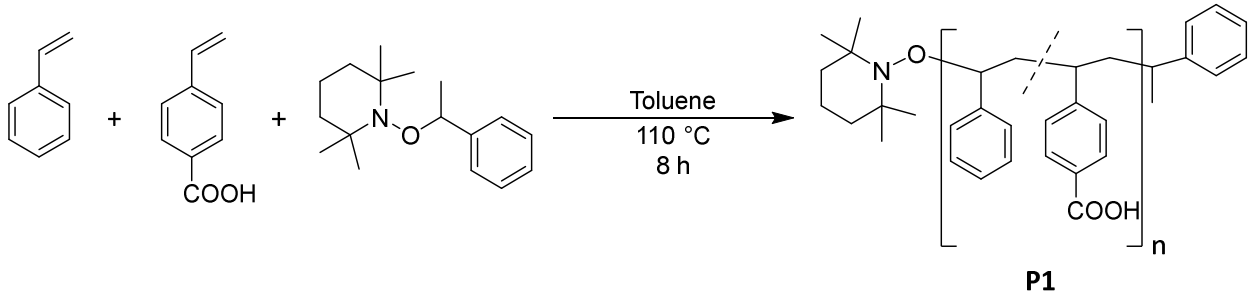

P1

Scheme 4.1 Synthesis of poly(styrene-*co*-4-vinylbenzoic acid) (Polymer **P1**) by nitroxide-mediated polymerization.

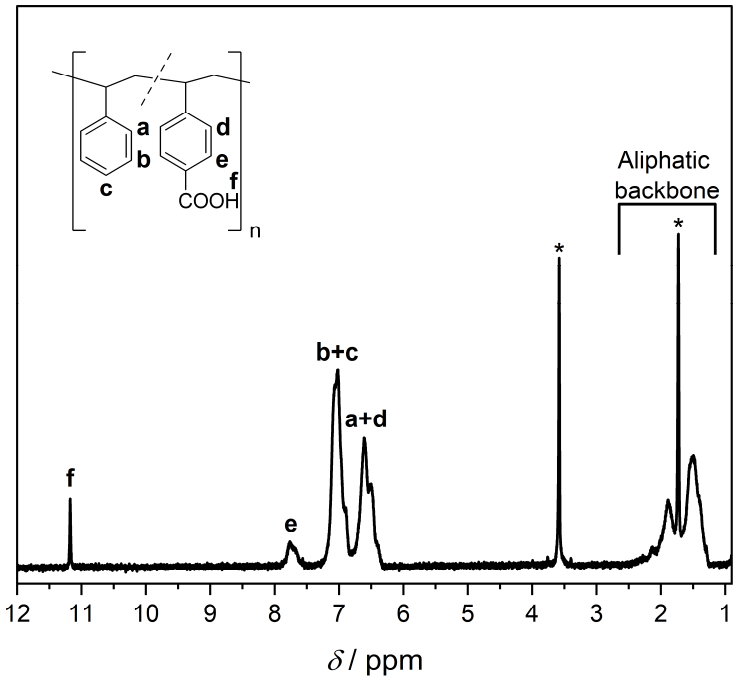

Figure 4.2 ^{1}H NMR spectrum (400 MHz, THF-d_8, 298 K) of polymer **P1**. Asterisks denote residual solvent resonances.

resonances possible.[178] The relative amount of 4-vinylbenzoic acid moieties incorporated into polymer **P1** can be estimated according to the following expression:

$$\frac{N_{\mathrm{4VBA}}}{N_{\mathrm{Styrene}} + N_{\mathrm{4VBA}}} = \frac{1}{\frac{3}{5} + \frac{2}{5}\frac{Int(\mathrm{a+b+c+d})}{Int(\mathrm{e})}}$$

Herein, N_{4VBA} and N_{Styrene} are the average number of 4-vinylbenzoic acid and styrene monomers, respectively, incorporated in a macromolecular chain of **P1**, *Int*(a+b+c+d) is the integral value obtained by the integration of the resonances at δ = 7.45-6.20 ppm relative to the value of the integral *Int*(e), obtained by the integration of the resonance at δ = 7.90-7.50 ppm. Integration of the corresponding resonances yielded a ratio of *Int*(a+b+c+d)/*Int*(e) of 16.7, equivalent to an incorporation ratio of 14 % functional monomers per macromolecular chain.

Starting from polymer **P1**, barium-mediated single-chain compaction could be achieved by the deprotonation of the carboxylic acid groups of **P1** with potassium *tert*-butoxide in dry THF under inert atmosphere and slow addition of the resulting solution of the potassium carboxylate salt to barium iodide dissolved in THF. A salt metathesis reaction resulted in the formation of the Ba(II)-folded **SCNP1-Ba**, which was obtained as a colorless solid after removal of the metathesis salt by filtration and solvent evaporation (refer to **Scheme 4.2**).

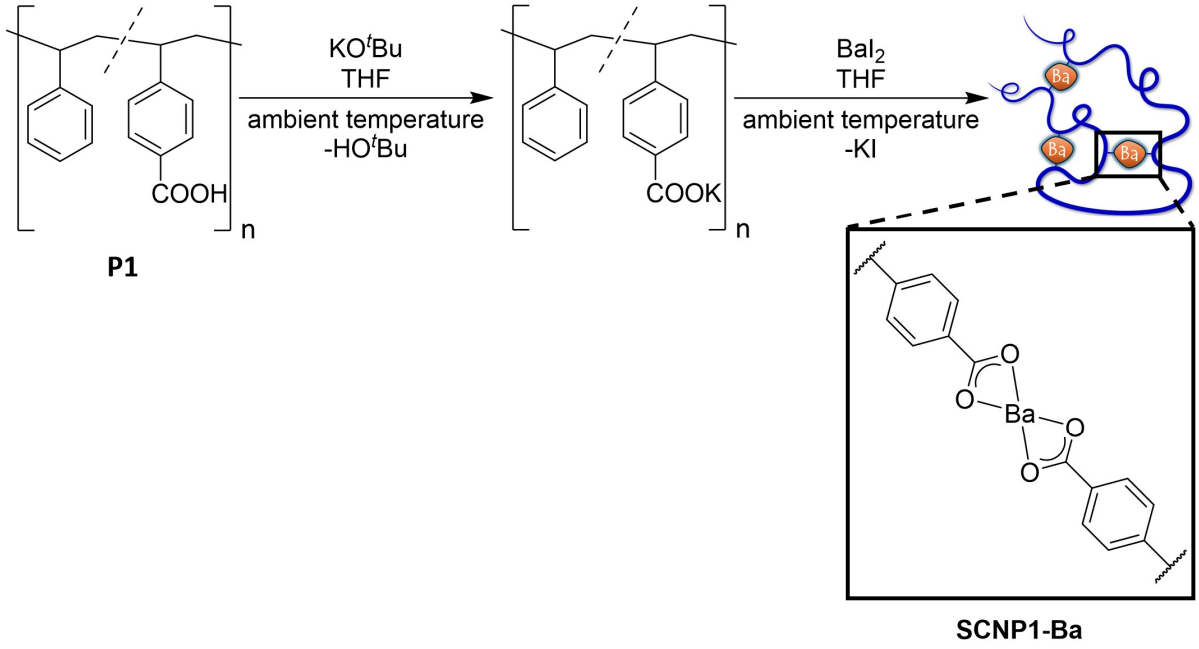

Scheme 4.2 Synthesis of **SCNP1-Ba** from **P1** by deprotonation and subsequent salt metathesis. The depiction of the folding unit is simplified (refer to the main text).

The stacked ^{1}H NMR spectra of polymer **P1** as well as **SCNP1-Ba** are shown in **Figure 4.3**. The complete disappearance of the carboxylic acid proton resonance at δ = 11.22-11.10 ppm evidenced the quantitative conversion of **P1**. All resonances of **SCNP1-Ba** are broadened

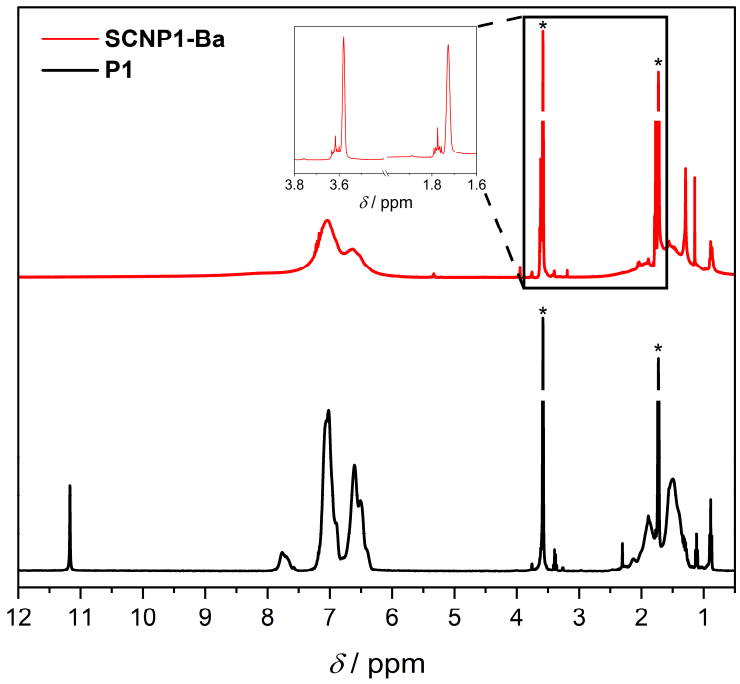

Figure 4.3 Stacked ^{1}H NMR spectra (400 MHz, THF-d_8, 298 K) of polymer **P1** (black) and **SCNP1-Ba** (red). Insert shows zoomed-in region of THF resonances. Asterisks denote residual solvent resonances.

relative to the corresponding ones of **P1**, indicative of a decrease in relaxation time caused by reduced chain-segment mobility upon single-chain compaction.[20,75] Newly arising resonances at δ = 3.62 ppm and δ = 1.77 ppm in the spectrum of **SCNP1-Ba** indicate the coordination of THF molecules to the barium ions within the polymer. However, coordination of THF to free barium ions in solution can also not be excluded to contribute to the observed resonances.

The successful conversion of the carboxylic acid moieties of **P1** to carboxylate groups in **SCNP1-Ba** could further be conveniently monitored by IR spectroscopy. The bands associated with the C=O stretching vibration of the carbonyl group in the monomeric ($\tilde{\nu}_{C=O}$ = 1731 cm^{-1}) and dimeric ($\tilde{\nu}_{C=O}$ = 1688 cm^{-1}) forms of the carboxylic acid moieties within **P1** have vanished in **SCNP1-Ba**. Concomitantly, two new bands have emerged at $\tilde{\nu}_{as,COO}$ = 1544 cm^{-1} and $\tilde{\nu}_{s,COO}$ = 1391 cm^{-1}, corresponding to the asymmetric and symmetric stretching vibrations of a carboxylate, respectively. The correlation between the wavenumber splitting of the symmetric and asymmetric carboxylate vibrations and the bonding situation and coordination geometry of metal carboxylates has been investigated in pioneering work by Deacon and Phillips.[179] The difference of 153 cm^{-1} observed in the present case is indicative of a multidentate binding of the carboxylate groups, potentially including chelating and bridging coordination. However, these interpretations are beset with uncertainties due to the various

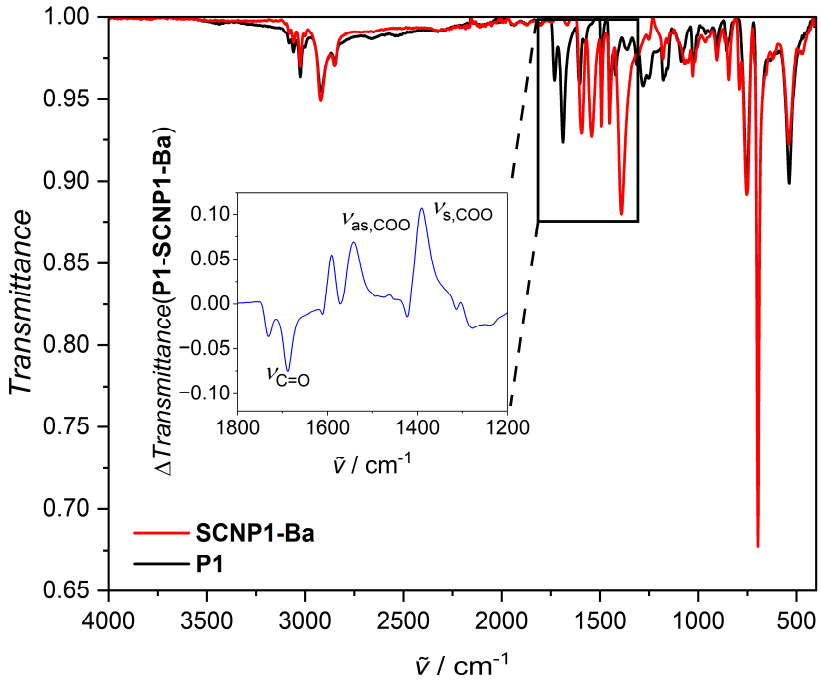

Figure 4.4 Superimposed FT-IR (ATR) spectra of polymer **P1** (black) and **SCNP1-Ba** (red). Insert shows the difference in transmittance (blue) between **P1** and **SCNP1-Ba** obtained by subtraction of the respective transmittance spectra in the selected region.

coordination modes potentially available to the carboxylate ligand and should consequently be treated with caution.

While NMR and IR spectroscopy provided an unequivocal proof of the successful conversion of the acid groups in **P1** to carboxylate groups in **SCNP1-Ba**, these techniques do not enable differentiation between the intramolecular crosslinking necessary for SCNP formation and undesirable intermolecular interactions. Thus, size-sensitive techniques were employed.

Figure 4.5a shows the SEC chromatograms of polymer **P1** as well as **SCNP1-Ba** obtained in THF. For **SCNP1-Ba**, a shift of the entire molar mass distribution towards lower apparent molar masses was observed relative to **P1**, characteristic of successful SCNP compaction. The number-averaged (M_n) and peak (M_p) molar masses decreased from M_n = 19800 g·mol^{-1} and M_p = 23400 g·mol^{-1} for **P1** to M_n = 14900 g·mol^{-1} and M_p = 20100 g·mol^{-1} for **SCNP1-Ba**. This was accompanied by a change in dispersity from $Đ$ = 1.15 (**P1**) to $Đ$ = 1.23 (**SCNP1-Ba**). To corroborate these findings, DLS measurements were conducted in THF, and the number-averaged size distributions of polymer **P1** as well as **SCNP1-Ba** are shown in **Figure 4.5b**. In line with the SEC results, a decrease in the solvodynamic diameter D_s was observed for **SCNP1-Ba** (D_s = 5.16 nm) compared to **P1** (D_h = 5.81 nm), also indicative of SCNP folding. Furthermore, an increase of the average diffusion coefficient (*D)* of **SCNP1-Ba** (D = 1.62·10^{-10} m^2·s^{-1}) relative to **P1** (D = 1.44·10^{-10} m^2·s^{-1}) was found via ^{1}H DOSY NMR in THF-d_8 (refer to **Figure 4.6**). According to the Stokes-Einstein equation, an increase in the diffusion coefficient goes in hand with a decrease in the solvodynamic diameter, again validating successful SCNP formation.

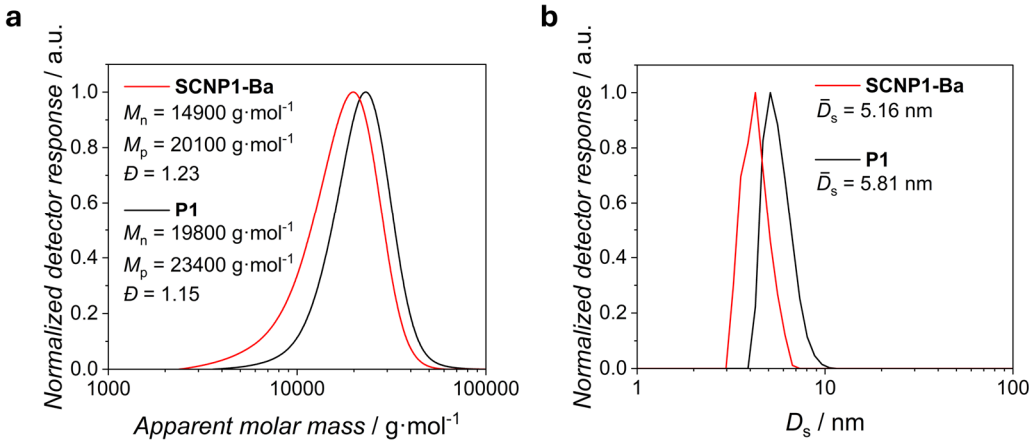

Figure 4.5 Superimposed **(a)** SEC chromatograms (THF, RI, PS cal.) and **(b)** number-weighted DLS size distributions (THF, mean diameter by number, average values derived from five measurements) of polymer **P1** (black) and **SCNP1-Ba** (red).

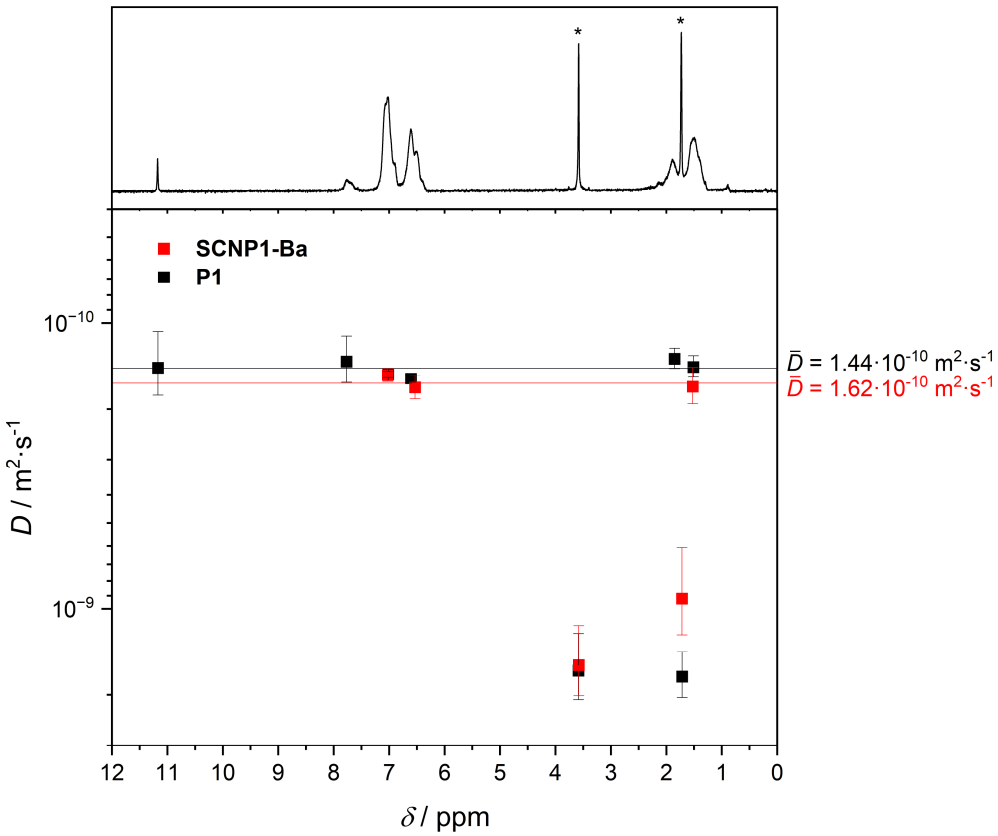

Figure 4.6 Superimposed ^{1}H DOSY NMR spectra (400 MHz, THF-d_8, 298 K) of polymer **P1** (black) and **SCNP1-Ba** (red). Spectral trace on top refers to **P1**. Error bars refer to data fitting error. Horizontal lines indicate average diffusion coefficients. Asterisks denote residual solvent resonances.

The observed single-chain compaction demands for the coordination of more than one carboxylate group to every Ba(II) ion in **SCNP1-Ba** on average, as is also required for charge compensation. However, as briefly discussed above, further insights into the chemical structure of the actual folding unit are not experimentally accessible. Potential barium coordination modes within Ba(II) SCNPs are discussed in more detail in Chapter 4.1.3.

4.1.3 Poly(ethylene glycol) methyl ether methacrylate-based Ba(II) Single-Chain Nanoparticles

To achieve the synthesis of Ba(II) SCNPs soluble in polar organic solvents and water, a methacrylate-based polymeric backbone with PEG side chains was investigated. Similar to styrene polymerization, RDRP techniques also enable the targeted polymerization of acrylate and methacrylate monomers, providing high control over the functionalization degree, dispersity and average molar mass of the resulting polymers.

Specifically, a copolymer of poly(ethylene glycol) methyl ether methacrylate (PEGMEMA, average M_n = 300 g·mol^{-1}) and 2-carboxyethyl acrylate was synthesized by reversible addition-

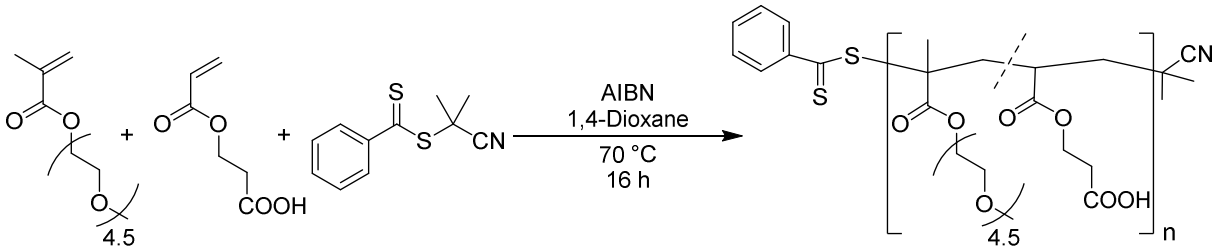

P2

Scheme 4.3 Synthesis of poly(PEGMEMA-*co*-2-carboxyethyl acrylate) (Polymer **P2**) by reversible addition-fragmentation chain transfer polymerization.

fragmentation chain transfer polymerization (RAFT) as depicted in **Scheme 4.3** (Polymer **P2**).[38-39] While PEGMEMA provided solubility in polar solvents, the carboxylic acid groups of the 2-carboxyethyl acrylate moieties enabled the post-polymerization modification. Again, all SCNP folding reactions reported in this chapter follow the repeat unit approach (refer to Chapter 2.1).[42] SEC measurements in THF gave an indication of the number-averaged molar mass of M_n = 48700 g·mol^{-1} and dispersity of $Đ$ = 1.54. **Figure 4.7** shows the ^{1}H NMR spectrum of **P2** measured in D_2O. The aliphatic backbone resonances are located in the region δ = 2.34-0.65 ppm. The resonances associated with the PEG side chains dominate the spectrum. They correspond to the terminal methyl group (δ = 3.48-3.30 ppm), the ethylene glycol subunits (δ = 3.92-3.52 ppm) and the methylene group attached to the ester functionality connecting

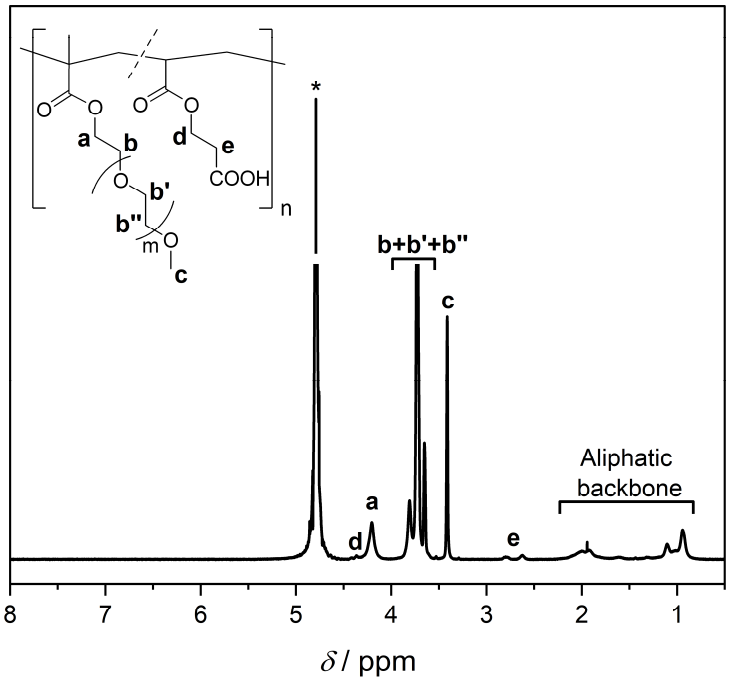

Figure 4.7 ^{1}H NMR spectrum (600 MHz, D_2O, 298 K) of polymer **P2**. Asterisk denotes residual solvent resonance.

the PEG side chain with the polymer backbone (δ = 4.30-4.04 ppm), respectively. The successful incorporation of the 2-carboxyethyl acrylate moieties is evident from the resonances at δ = 4.46-4.32 ppm and δ = 2.90-2.52 ppm, originating from the two distinct methylene groups of the ethylene bridge.

The relative amount of 2-carboxyethyl acrylate moieties incorporated into **P2** can be estimated according to:

$$\frac{N_{\mathrm{2CEA}}}{N_{\mathrm{PEGMEMA}} + N_{\mathrm{2CEA}}} = \frac{1}{1 + \frac{2}{3}\frac{Int(\mathrm{c})}{Int(\mathrm{e})}}$$

Herein, N_{2CEA} and $N_{PEGMEMA}$ are the average number of 2-carboxyethyl acrylate and PEGMEMA monomers, respectively, incorporated in a macromolecular chain of **P2**, *Int*(c) is obtained by integration of the resonance at δ = 3.48-3.30 ppm relative to the value of the integral *Int*(e), obtained by integration of the resonance at δ = 2.90-2.52 ppm. Integration of the corresponding resonances yielded a ratio of *Int*(c)/*Int*(e) of 9.1, equivalent to an incorporation ratio of 14 % functional monomers per macromolecular chain.

Having polymer **P2** at hand, the barium nanoparticles **SCNP2-Ba** were synthesized by slow addition of a solution of **P2** in water to an aqueous solution of barium hydroxide octahydrate (refer to **Scheme 4.4**). The basic nature of the barium hydroxide octahydrate ensured the quantitative deprotonation of the carboxylic acid functionalities in **P2**. However, considering the high dilution of the polymer solution, the carboxylic acid groups were expected to be deprotonated even in the absence of a strong base according to Ostwald's dilution law.

Figure 4.8 shows the stacked ^{1}H NMR spectra of polymer **P2** as well as **SCNP2-Ba** acquired in

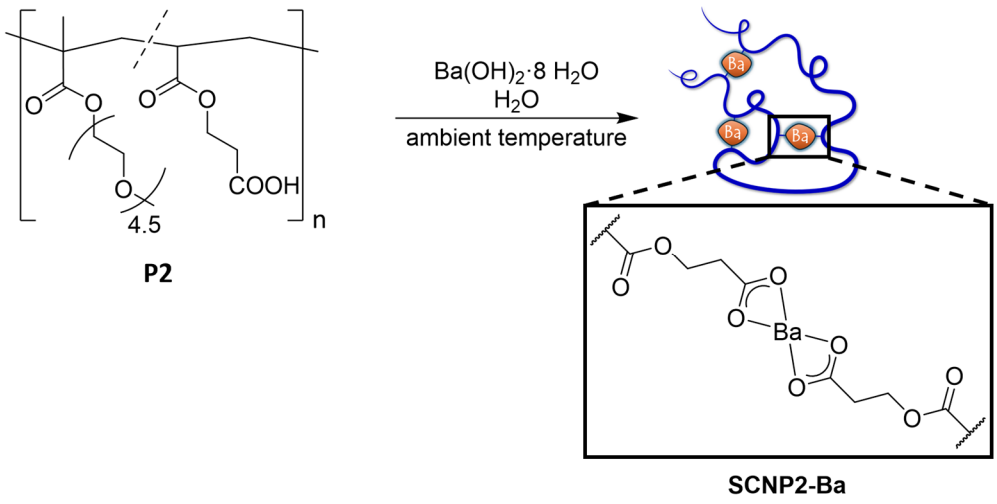

Scheme 4.4 Synthesis of **SCNP2-Ba** from **P2** by reaction with barium hydroxide octahydrate. The depiction of the folding unit is simplified (refer to the main text).

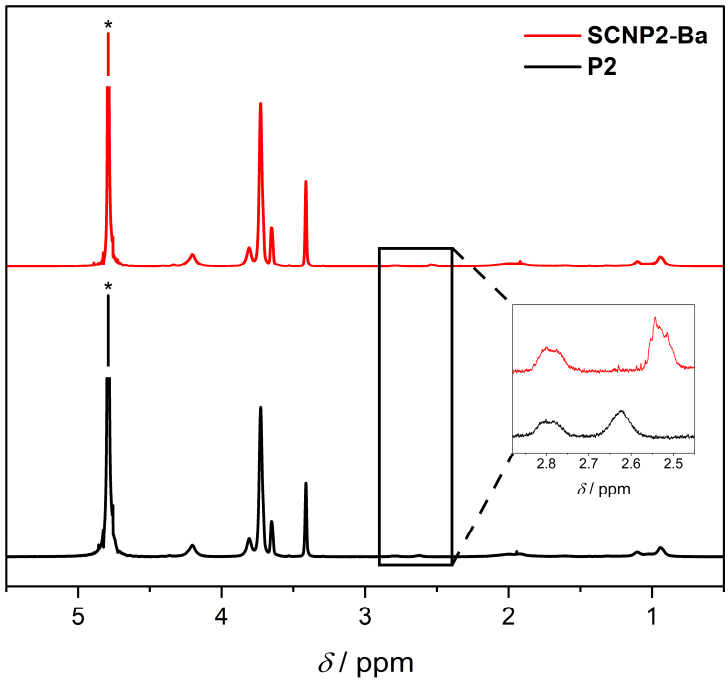

Figure 4.8 Stacked ^{1}H NMR spectra (600 MHz, D_2O, 298 K) of polymer **P2** (black) and **SCNP2-Ba** (red). Insert shows zoomed-in region of the resonances of the methylene group adjacent to the carboxyl group. Asterisks denote residual solvent resonances.

D_2O. The only remarkable difference between the spectra is a slight change in the resonances of the protons associated with the methylene group adjacent to the carboxyl functionality of

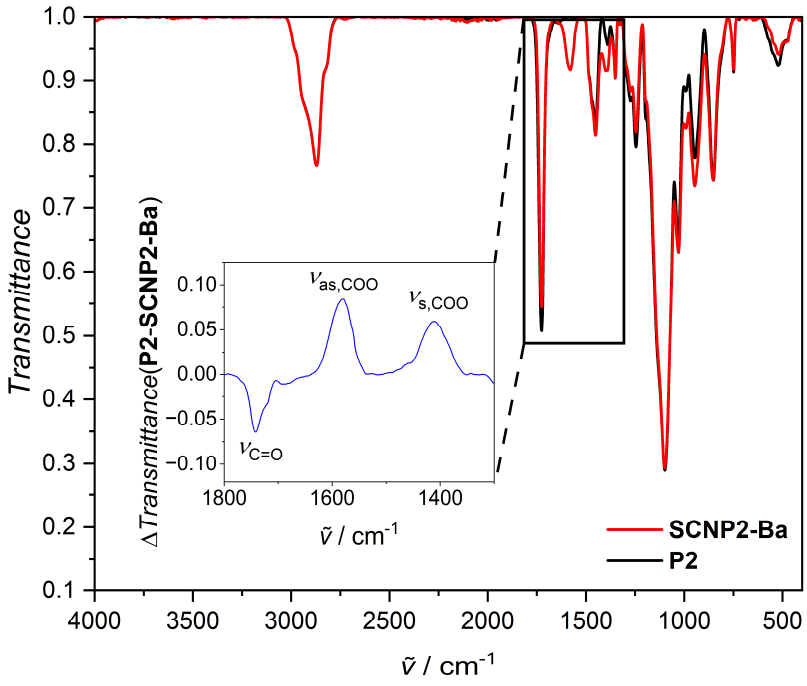

Figure 4.9 Superimposed FT-IR (ATR) spectra of polymer **P2** (black) and **SCNP2-Ba** (red). Insert shows the difference in transmittance (blue) between **P2** and **SCNP2-Ba** obtained by subtraction of the respective transmittance spectra in the selected region.

the 2-carboxyethyl acrylate moieties at δ = 2.90-2.44 ppm, indicating the complexation of the Ba(II) ions by the carboxylate groups. The carboxylic acid proton of the precursor polymer was not visible in the ^{1}H NMR spectrum of **P2**.

In analogy to Chapter 4.1.2, the conversion of the carboxylic acid moieties of **P2** to carboxylate groups in **SCNP2-Ba** could conveniently be followed via IR spectroscopy. A decrease in the intensity of the carbonyl band at $\tilde{\nu}_{C=O}$ = 1724 cm^{-1}, accompanied by the emergence of two new bands for the asymmetric carboxylate vibration at $\tilde{\nu}_{as,COO}$ = 1583 cm^{-1} and the symmetric carboxylate vibration at $\tilde{\nu}_{s,COO}$ = 1410 cm^{-1}, respectively, is evident (refer to **Figure 4.9**). Contrary to the situation in the styrene-based **SCNP1-Ba** (refer to **Figure 4.4**), the carbonyl band did not vanish completely as carbonyl groups are also part of the ester bonds in the side chains of **P2**, which are virtually uninfluenced by the SCNP folding process to **SCNP2-Ba**. The splitting between the symmetric and asymmetric carboxylate vibrations of 173 cm^{-1} again hints at a multidentate coordination of the carboxylate groups to the Ba(II) ions, potentially including chelating and bridging coordination.[179] Information regarding the coordination environment of the barium ions derived from molecular dynamics simulations is discussed in more detail below.

To validate successful SCNP formation, size-sensitive techniques were employed. The molar mass distribution of **SCNP2-Ba** obtained by SEC in THF was shifted towards lower apparent molar masses compared to the corresponding distribution of **P2** (refer to **Figure 4.10a**), evidencing single-chain compaction. The derived number-averaged and peak molar masses decreased from M_n = 48700 g·mol^{-1} and M_p = 56200 g·mol^{-1} for **P2** to M_n = 34600 g·mol^{-1} and

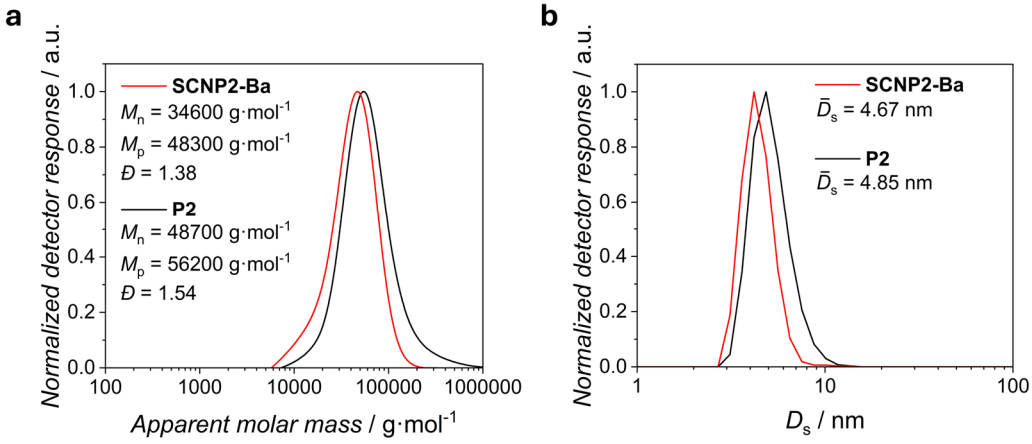

Figure 4.10 Superimposed **(a)** SEC chromatograms (THF, RI, PMMA cal.) and **(b)** number-weighted DLS size distributions (H_2O, mean diameter by number, average values derived from five measurements) of polymer **P2** (black) and **SCNP2-Ba** (red).

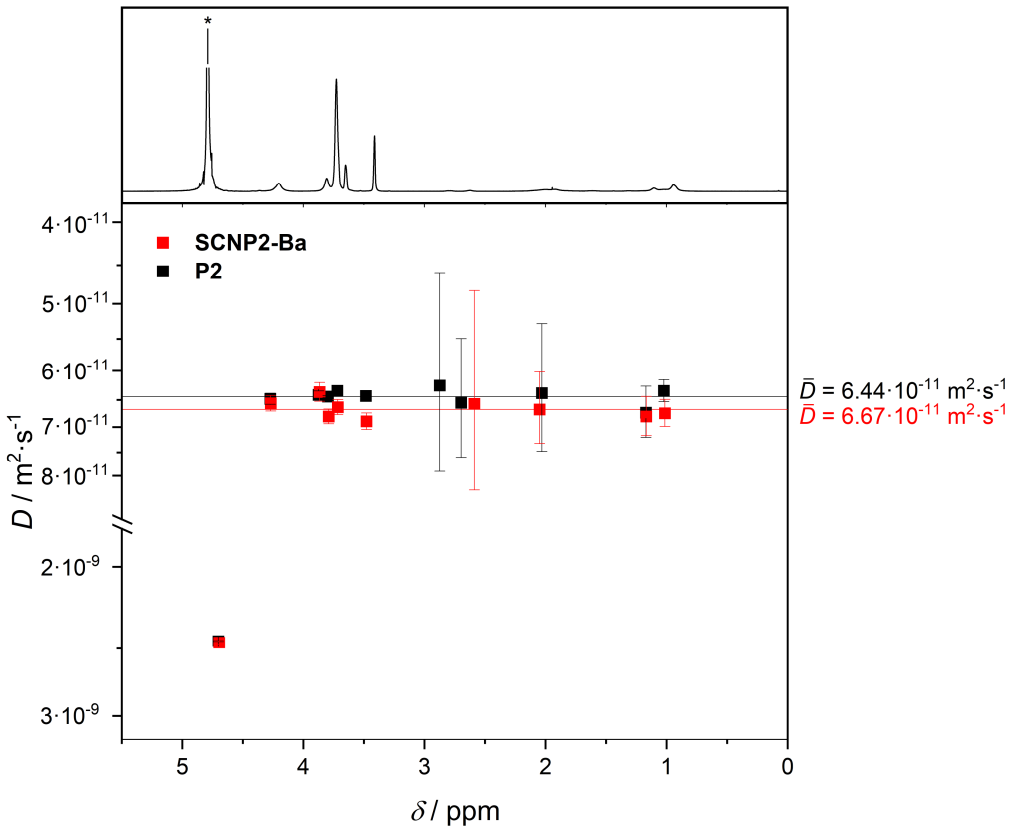

Figure 4.11 Superimposed ^{1}H DOSY NMR spectra (400 MHz, D_2O, 313 K) of polymer **P2** (black) and **SCNP2-Ba** (red). Spectral trace on top refers to **P2**. Error bars refer to data fitting error. Horizontal lines indicate average diffusion coefficients. Asterisk denotes residual solvent resonance.

M_p = 48300 g·mol^{-1} for **SCNP2-Ba**. Concomitantly, the dispersity decreased from $Đ$ = 1.54 (**P2**) to $Đ$ = 1.38 (**SCNP2-Ba**). The same trend was observed by DLS measurements in water. A decrease of the number-averaged solvodynamic diameter from D_s = 4.85 nm for **P2** to D_s = 4.67 nm for **SCNP2-Ba** was evident (refer to **Figure 4.10b**). Successful SCNP compaction was also evident from ^{1}H DOSY NMR in D_2O (refer to **Figure 4.11**), showing an increase of the average diffusion coefficient of **SCNP2-Ba** ($D = 6.67 \cdot 10^{-11}$ m^2·s^{-1}) with respect to **P2** ($D = 6.44 \cdot 10^{-11}$ m^2·s^{-1}).

Achieving on-demand control over polymer morphology is one of the driving forces of polymer chemistry in general and the SCNP field in particular. Especially intriguing in this regard is the targeted manipulation of the folding and unfolding process of individual macromolecular chains. Consequently, apart from SCNP folding (refer to Chapter 2.1), the reverse process of SCNP unfolding triggered by external stimuli has gained significant attention in recent years.[69] Various external triggers have been investigated, including mechanical force,[150,180] temperature[181] or pH[55,137] changes, disruption of self-assembly or host-guest interactions by chemical triggers[140,182-183] or electrochemically,[138] redox reactions,[184] or even light[185-187]

and further studied in computational work.[188-189] Out of the above listed examples, only two systems are based on the reversibility of metal polymer interactions.[137,150]

Gaining control over the folding state of SCNPs demands for the reversibility of the reaction responsible for the single-chain collapse. To deepen the understanding of the interactions of the Ba(II) ions with polymer **P2**, united atom molecular dynamics simulations were performed by Ada Quinn under the supervision of Prof. Megan O'Mara. Computational details are provided in Chapter 6.3.1.6. For simulation purposes, three atactic macromolecular chains, each consisting of one hundred seventy PEGMEMA and thirty 2-carboxyethyl acrylate monomers in random order, were initially constructed. The initially generated pseudo-linear conformations were condensed either through 250 ps NVT simulations to generate compact conformations or by 10 ns simulations inside a water solvent shell to generate extended conformations. Following this procedure, three condensed and three extended conformations were generated for each of the three constitutionally distinct macromolecular chains, resulting in a total of eighteen distinguishable macromolecular chains as starting points for the simulations in the presence of barium ions. The resulting input conformations were solvated using the SPC/E water model.[190] To investigate the interactions of **P2** with barium ions, solvent molecules were replaced by fifteen Ba(II) and thirty chloride ions for charge compensation, resulting in a stoichiometric ratio of one Ba(II) ion per two carboxylate functionalities. Consideration of the interactions of the eighteen distinguishable starting conformations with barium ions resulted in a total of thirty-six simulation systems. At first, each system was equilibrated through 10 ns unrestrained molecular dynamics simulations in the NPT ensemble. The final frame of each equilibration was used as the input for 300 ns triplicate NPT simulations. The interactions of the barium ions with the macromolecular chains were analyzed over the last 150 ns of each replicate simulation, and the derived values of all simulations combined in the final results, taking into consideration whether the starting conformation was compact or extended. The analyses were performed on frames spaced by 1 ns and all fifteen barium ions were investigated individually in every simulation frame.

The simulations revealed the dynamic nature of the metal polymer interactions with the barium ions constantly binding to and unbinding form the macromolecules across the simulation trajectories. On average, a given Ba(II) ion was in contact with at least one functional group of the macromolecule for about 66 % of the simulation time. **Figure 4.12** shows the distribution of the number of barium ions bound to a macromolecular chain over

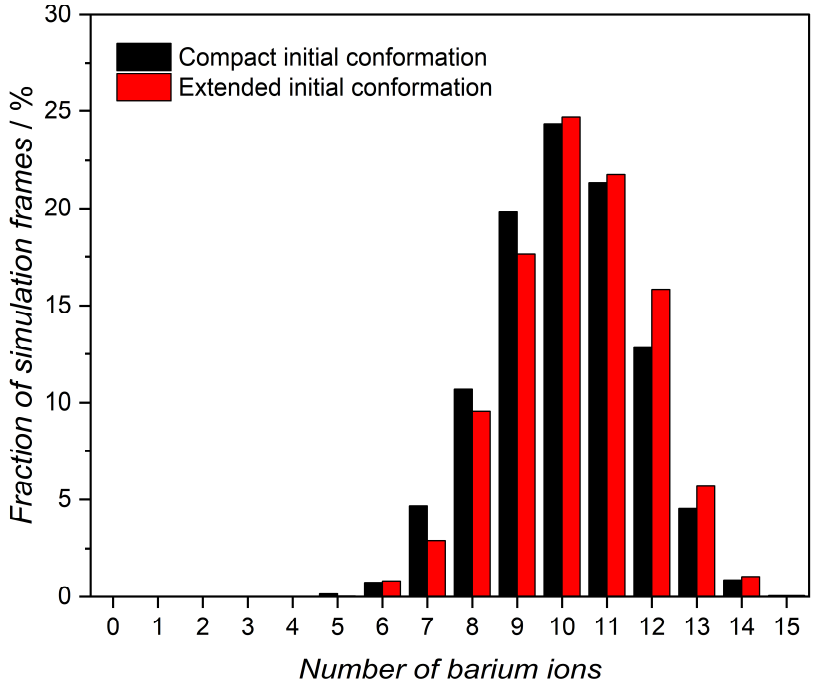

Figure 4.12 Distribution of the number of barium ions per macromolecular chain. Given is the fraction of the simulation frames in which the given number of barium ions are within 6 Å of any atom of the macromolecular chain with respect to the total number of evaluated simulation frames.

the simulation frames, indicating that the majority of SCNPs featured six to fourteen barium ions per nanoparticle under the employed conditions (refer to **Table 6.1**).

The barium ions were found to be surrounded by two defined coordination spheres (refer to **Figure 6.1**). Coordination of functional groups of the polymer to the innermost coordination sphere was rare and short lived, accounting for less than 1.5 % of the total simulation time (refer to **Table 6.2**). Instead, the majority of metal polymer interactions took place in the second coordination sphere, whereas the first coordination sphere was dominantly populated by solvent molecules. While interactions of ether and ester oxygen atoms of the polymer backbone with the Ba(II) ions occurred (refer to **Table 6.5** to **Table 6.7**), metal binding was predominantly achieved via the carboxylate groups (refer to **Table 6.3**). Carboxylate oxygen atoms were found within the second coordination sphere of the barium ions in more than 80 % of all metal polymer interactions (refer to **Figure 4.13a** and **Table 6.3**). In more than 25 % of the cases, more than one carboxylate group was coordinated to a given barium ion (refer to **Figure 4.13b-d** and **Table 6.4**). Noteworthy, these bridging interactions occurred more frequently in systems with an extended starting conformation (12 % of all metal polymer interactions) than in systems with a compact starting conformation (8 % of all metal polymer interactions), whereas the frequency of all metal polymer interactions proved to be

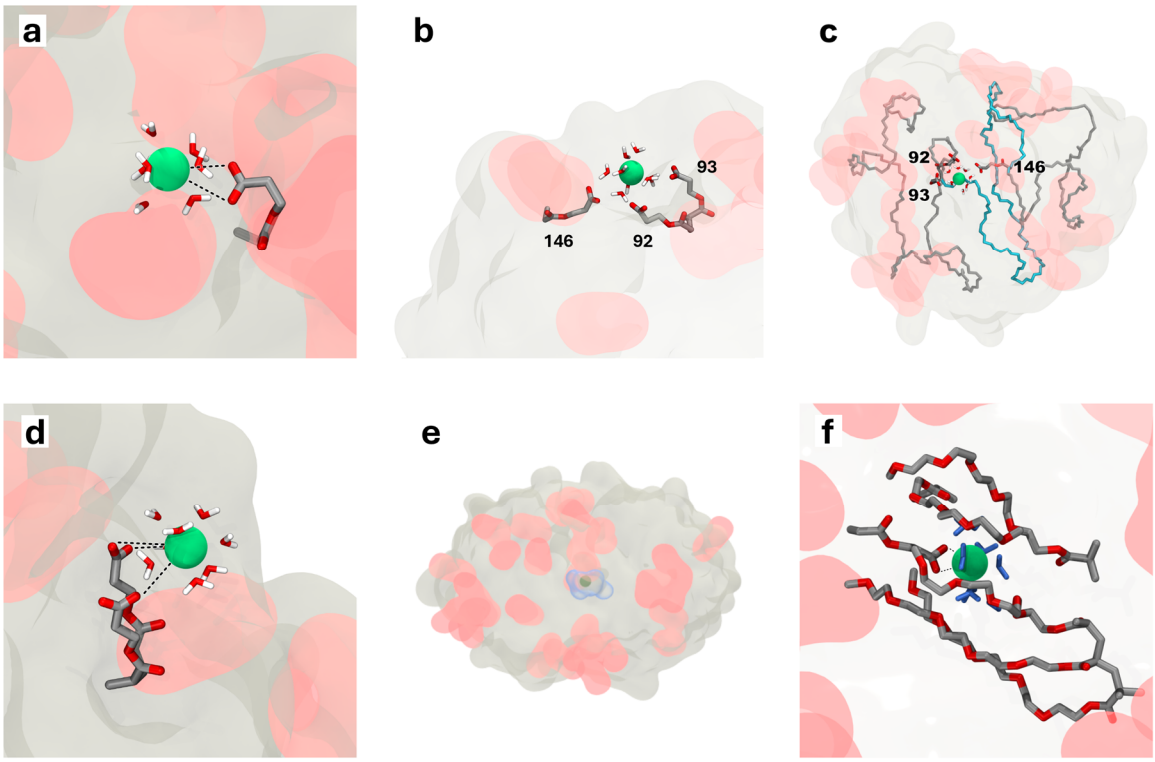

Figure 4.13 Graphical illustration of the interactions of Ba(II) ions with poly(PEGMEMA-*co*-2-carboxyethyl acrylate) investigated by united atom molecular dynamics simulations (modified GROMOS 54a7). **(a)** Illustration of one carboxylate group in the second barium coordination sphere. **(b)** Coordination of multiple carboxylates to the same barium ion, bridging distant regions of the macromolecular chain. **(c)** Zoomed-out contour between the distant carboxylates highlighted in cyan. Labels refer to position along the chain. **(d)** Interactions of carboxylate monomers adjacent in the macromolecular chain with the same barium ion. **(e)** Encapsulation of a hydrated barium ion within the macromolecular chain. **(f)** Zoom-in to the encapsulated solvated barium ion. Color code: PEGMEMA grey contours, 2-carboxyethyl acrylate red contours, water blue contours, hydrogen white, carbon grey, oxygen red, barium green.

independent of the initial chain conformation. In extremely rare cases, accounting for about 0.2 % of all metal polymer interactions, the presence of ten or more ether oxygen atoms of the PEG side chains in the second coordination sphere of the barium ions was identified (refer to **Table 6.5**). Detailed investigation of these rare events revealed that a barium ion, together with its associated solvation shell, could be encapsulated, leading to the dynamic movement of the metal ion through the macromolecule before returning to the solvent (refer to **Figure 4.13e** and **f**).

To determine the influence of metal coordination on the size of the macromolecules, radii of gyration were determined in the absence and presence of barium ions, respectively (refer to **Table 6.8**). In simulations with compact starting conformations, the macromolecules

remained tightly compact throughout the entire simulation. In simulations with extended starting conformations, the macromolecules collapsed to compact conformations within 100 ns and remained compact for the remainder of the simulation. It is noted in passing that for the extended starting conformations the radii of gyration continued to slightly decrease throughout the simulations, suggesting equilibrium has not been fully reached within the simulation time. Regardless of the initial conformation, the presence of Ba(II) ions did not influence the radius of gyration to a relevant extent. However, the presence of barium ions increased the rate of collapse of the macromolecules with extended initial conformations (refer to **Figure 6.2**). It is thus hypothesized that the barium ions influence the potential energy surface of the macromolecules in such a way that the occurrence of flexible extended conformations is reduced through electrostatic interactions bridging carboxylate sidechains from different regions of the SCNP, manifesting as an apparent reduction in average size when an ensemble of macromolecules is considered as is the case in size-sensitive experimental measurements such as SEC, DLS or DOSY.

The dynamic nature of the interactions of the barium ions with the macromolecules can be exploited to achieve targeted control over the folding state of the SCNPs. Specifically, control over the folding of **P2** and unfolding of **SCNP2-Ba** was reached by exploiting the well-known chemistry of barium in aqueous solution. As demonstrated in detail above, the coordination of polymer-bound carboxylate moieties to Ba(II) ions induced single-chain compaction. The latter could be reversed by the addition of a sulfate source to an aqueous solution of **SCNP2-Ba**, leading to the precipitation of barium sulfate owing to its very small solubility product in water.[191] To regenerate the precursor polymer **P2**, it is additionally necessary to add a proton source to reprotonate the carboxylate moieties, making sulfuric acid the ideal candidate to

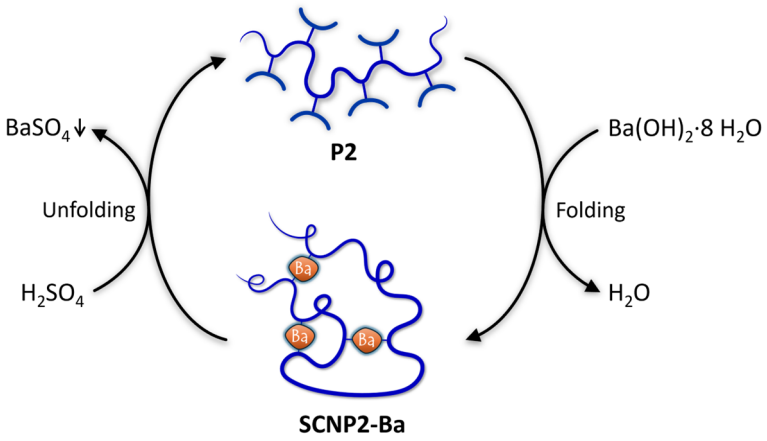

Figure 4.14 Graphical illustration of the reversible folding of **P2** and unfolding of **SCNP2-Ba**.

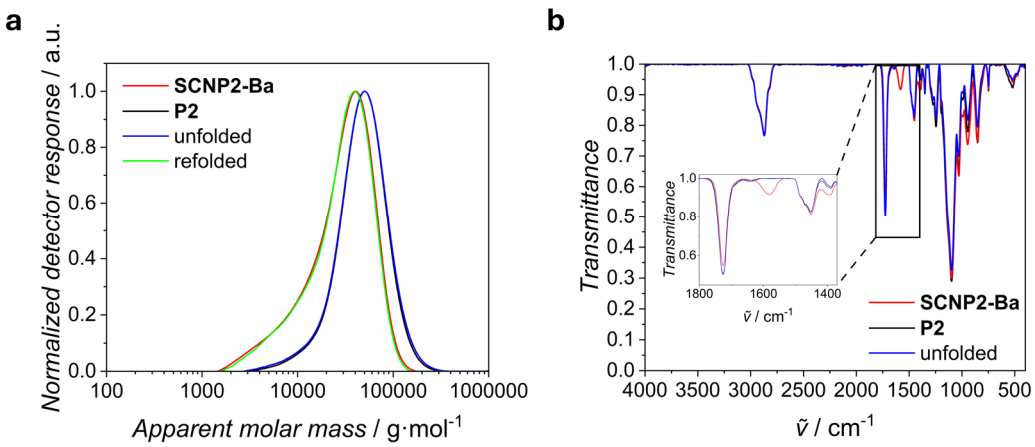

Figure 4.15 Superimposed **(a)** SEC chromatograms (THF, RI, PMMA cal.) and **(b)** FT-IR (ATR) spectra of polymer **P2** (black), **SCNP2-Ba** (red) and the products obtained after unfolding of **SCNP2-Ba** (blue) and refolding of the regenerated polymer (green).

achieve this in an elegant one-step procedure. The regenerated polymer can subsequently be employed in another folding reaction (refer to **Figure 4.14**).

The superimposed SEC chromatograms in **Figure 4.15a**, showing virtually no deviations between **P2** and the product regenerated after unfolding and **SCNP2-Ba** and the product obtained in a second folding step, respectively, demonstrate the excellent reversibility of the process on a macromolecular level. The reversibility on the molecular level is evident from the superimposed IR spectra of **P2**, **SCNP2-Ba** and the product obtained after unfolding of the latter (refer to **Figure 4.15b**). Upon unfolding, the intensity of the carbonyl vibrational band at $\tilde{\nu}_{C=O}$ = 1724 cm^{-1} is recovered to the original value of **P2**, whereas it was reduced for **SCNP2-Ba**. Further, unfolding led to the disappearance of the bands associated with the asymmetric ($\tilde{\nu}_{as,COO}$ = 1583 cm^{-1}) and symmetric ($\tilde{\nu}_{s,COO}$ = 1410 cm^{-1}) carboxylate stretching vibrations.

Reproducible synthesis is a key factor determining the understanding and applications of single-chain technology. However, given the oftentimes synthetic unfeasibility of selective positioning of functionalities along a macromolecular chain, insights about the internal structure and distribution of functional moieties in SCNPs based on the repeat unit approach are highly desirable, yet challenging to obtain. For crystalline inorganic materials, atomic resolution scanning transmission electron microscopy (STEM) imaging has become a routine investigation method.[192] One of the major STEM imaging modes is annular dark field or *Z*-contrast imaging, detecting electrons scattered to large angles due to Coulomb interactions with the sample atoms. In this imaging mode, the scattering signal intensity scales with the square of the atomic number of the sample element under investigation, enabling the

detection of individual heavy atoms.[193] The contrast provided by the heavy barium atoms present in **SCNP2-Ba** was thus exploited to image the internal structure of a metal-functionalized SCNP with atomic resolution for the first time. Due to their small atomic numbers, the other elements constituting the polymer chain, specifically, hydrogen, carbon, nitrogen, oxygen and sulfur, respectively, were not visible in the microscopy images. STEM experiments were carried out and analyzed by Dr. Jochen Kammerer.

Initially, samples of **SCNP2-Ba** were prepared by dilution of the reaction mixture by a factor of one thousand and drop casting of the resulting solution on standard ultra-thin carbon film TEM grids followed by blotting of the excess solvent and drying. At low magnifications, barium-rich clusters were visible as bright areas (refer to **Figure 4.16a**), and at higher magnifications individual barium atoms could be identified as well-separated bright spots (refer to **Figure 4.16b**).

From the atomic resolution STEM images, the number of barium ions per individual SCNP could in principle be obtained by direct counting of the visible atoms. The automated counting of individual well-separated atoms is a routine task,[194] however, the situation becomes drastically more complex when images are populated with overlapping atoms, rendering the identification of individual atoms challenging. To circumvent this challenge in the present case, the number of barium ions per nanoparticle was determined by integration of the signal intensity of identified individual barium clusters, which is justified by the direct proportionality of the measured dark field *Z*-contrast signal intensity to the number of atoms.[195] In detail, individual barium atoms were initially identified in high magnification images and their integrated signal intensity determined as the sum of the measured signal intensities within the marked area corrected by the average signal of the surrounding area to account for the background. Subsequently, the measured signal intensity within the area of a barium cluster identified in the high magnification image was integrated and the background corrected in the same way. This enabled the quantification of the number of barium atoms within the identified cluster based on the previously determined intensity per barium atom. This information could then be used to calculate the average integrated signal intensity per barium atom for the identified cluster at lower magnification. Based on this data, the number of barium atoms within other clusters visible in the low magnification image could be determined, enabling the analysis of a large number of clusters at low magnification.

Evaluation of 472 clusters identified in low magnification images resulted in a mean and median barium content of 32 and 26 atoms, respectively.

However, the determined number of barium atoms is expected to not be representative of the situation of **SCNP2-Ba** in solution directly after the synthesis. The sample preparation required a significant dilution of the reaction mixture to be capable of imaging individual clusters. Given the dynamic nature of the barium polymer interactions discussed in detail above, dilution is expected to shift the relevant equilibria, leading to a different number of barium ions per SCNP in the prepared microscopy samples compared to the situation at higher concentrations during synthesis. Further complications arose from the diffusion of barium atoms observed throughout the microscopy image acquisition caused by energy transfer from the high energy electron beam to the sample (refer to **Figure 6.3a**). This is expected to result in an overestimation of the determined number of atoms per SCNP due to potential multiple imaging of the same atom. This could be circumvented by imaging at cryogenic temperatures, limiting diffusion, however, the formation of an ice layer on the sample upon cooling impeded atomic resolution imaging under cryogenic conditions with the employed experimental setup. An overestimation of the number of barium ions per SCNP may further be caused by agglomeration of individual SCNPs upon drying throughout the sample preparation procedure, meaning the imaged barium clusters would actually correspond to an unknown

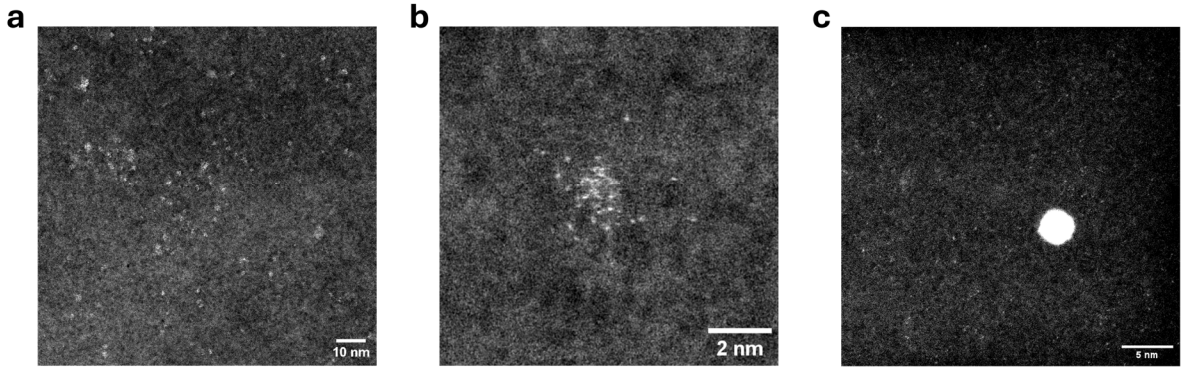

Figure 4.16 STEM images of samples of **SCNP2-Ba** prepared at a polymer concentration of 0.001 mg·mL^{-1} on carbon film. **(a)** Low magnification overview image showing bright individual clusters with high local barium concentrations. **(b)** High magnification image of an individual cluster with atomic resolution. The sample was prepared by manual blotting and drying after deposition of an aqueous solution of **SCNP2-Ba**. **(c)** STEM image of a sample prepared employing a Gatan Cryoplunge 3 setup for blotting and drying after deposition of an aqueous solution of **SCNP2-Ba**. The large bright spot is a gold nanoparticle used as focus aid. The bright background is a result of hydrocarbon contamination.

number of agglomerated individual SCNPs. To reduce the latter effect and establish a more reproducible sample preparation method, the application of a cryoplunge setup for blotting and subsequent drying was explored. The samples prepared using the cryoplunge setup showed a drastically reduced density of bright areas on the substrate, mainly corresponding to individual barium atoms, suggesting that every imaged SCNP only contained one to two barium atoms, indicating that agglomeration upon drying might have indeed been a critical issue in the previously discussed images (refer to **Figure 4.16c**).

Despite the discussed limitations concerning the precise quantification of the barium loading of individual SCNPs, atomic resolution STEM imaging holds key potential for the exploration of the internal structure of metal-functionalized SCNPs not achievable by any other analytical technique.

4.1.4 Summary

The synthesis of two Ba(II)-folded single-chain nanoparticles (SCNPs) with different polarity is described. Specifically, barium-mediated single-chain compaction was achieved by the reaction of suitable Ba(II) precursors with carboxylic acid functionalities in copolymers of styrene and 4-vinylbenzoic acid (Polymer **P1**) as well as poly(ethylene glycol) methyl ether methacrylate and 2-carboxyethyl acrylate (Polymer **P2**), respectively. The resulting nanoparticles **SCNP1-Ba** and **SCNP2-Ba** were characterized by nuclear magnetic resonance (NMR) and infrared (IR) spectroscopy, and the successful intramolecular folding verified by size-exclusion chromatography (SEC), dynamic light scattering (DLS) and diffusion-ordered spectroscopy (DOSY). Sophisticated molecular dynamics simulations revealed the reversible nature of the barium polymer interactions in solutions of **SCNP2-Ba** which provided a pathway towards targeted control over the polymer morphology by exploiting the low solubility of barium sulfate to reverse the SCNP folding reaction. The high contrast provided by the heavy metal ions enabled the scanning transmission electron microscopy (STEM) imaging of individual barium atoms within **SCNP2-Ba**, providing unprecedented in-depth insights into the number and distribution of metal ions on the level of individual macromolecules inaccessible by any other analytical technique.

This chapter focused on the exploration of new synthetic methods and unprecedented in-depth characterization techniques. Going beyond the classical batch synthesis protocols employed here, the following chapter aims at addressing the scalability challenge prevalent to SCNP synthesis by exploring the continuous flow synthesis of metal-functionalized SCNPs.

4.2 VISIBLE LIGHT PHOTOFLOW SYNTHESIS OF A CU(II) SINGLE-CHAIN NANOPARTICLE CATALYST

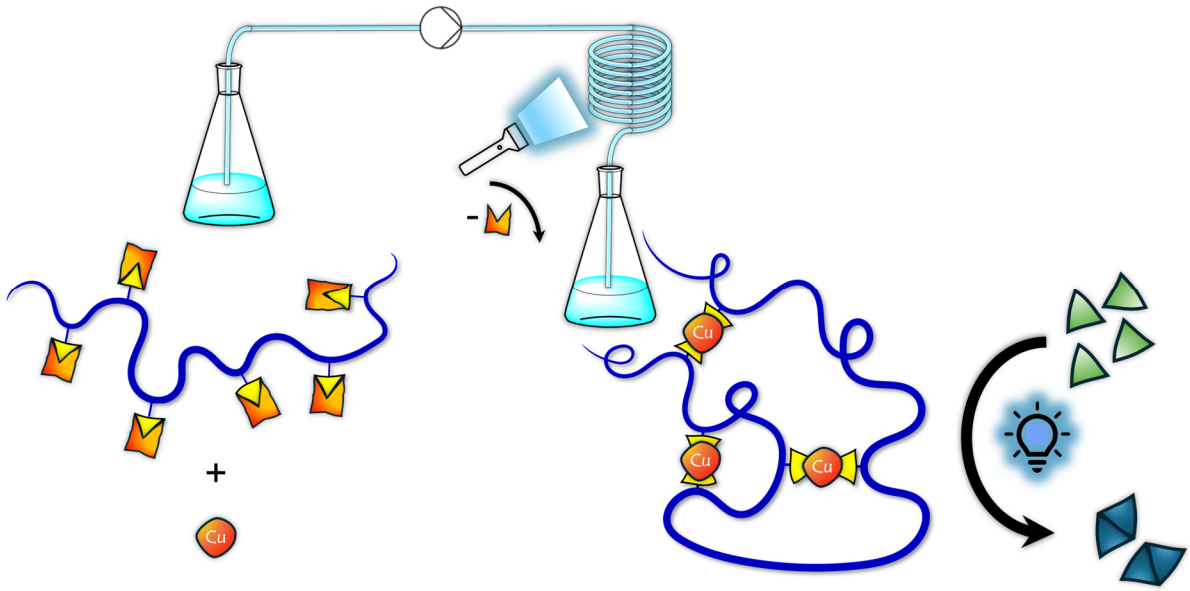

Figure 4.17 Graphical abstract of the chapter "Visible Light Photoflow Synthesis of a Cu(II) Single-Chain Nanoparticle Catalyst".

Abstract

Catalytically active Cu(II) single-chain nanoparticles (SCNPs) were prepared by visible light (λ_{max} = 410 nm) driven flow synthesis using a commercially available photoflow reactor. The design approach is based on a copolymer of poly(ethylene glycol) methyl ether methacrylate and a photocleavable 2-((((2-nitrobenzyl)oxy)carbonyl)amino)ethyl methacrylate monomer, which can liberate amine groups upon visible light irradiation, allowing for single-chain collapse by the complexation of Cu(II) ions. The successful applicability of this design approach for the batch photochemical synthesis of Cu(II) SCNPs and the transfer of the concept to photoflow conditions, enabling the continuous production of metal-functionalized SCNPs, is demonstrated. Critically, the ability of the prepared Cu(II) SCNPs to function as a photocatalyst for the cleavage of carbon-carbon single and double bonds is examined on the examples of xanthene-9-carboxylic acid and oleic acid, demonstrating the advantageous effect SCNPs can provide over analogous small molecule catalysts.

Table 4.2 Statement of contributions of coauthors of the publication "Visible Light Photoflow Synthesis of a Cu(II) Single-Chain Polymer Nanoparticle Catalyst" (*Chem. Sci.* **2024**, *15*, 15280-15290).

Contributor	**Statement of contribution**
Sebastian Gillhuber	Conceptualization, Methodology, Formal analysis, Investigation, Writing – Original Draft, Review & Editing, Visualization, Project administration
Joshua O. Holloway	Conceptualization, Writing – Review & Editing, Supervision, Project administration
Kai Mundsinger	Writing – Review & Editing, Resources
Jochen A. Kammerer	Investigation (EDX), Writing – Review & Editing
Jeffrey R. Harmer	Investigation (EPR), Writing – Review & Editing
Hendrik Frisch	Conceptualization, Writing – Review & Editing, Supervision, Project administration
Christopher Barner-Kowollik	Conceptualization, Writing – Review & Editing, Supervision, Project administration, Funding acquisition
Peter W. Roesky	Conceptualization, Writing – Review & Editing, Supervision, Project administration, Funding acquisition

Parts of this chapter have been reproduced from the published literature.[24]

4.2.1 Introduction

To obtain well-defined nanoparticles, the synthesis of SCNPs commonly requires highly dilute conditions to ensure exclusive intramolecular crosslinking and prevent any intermolecular aggregations. However, working under high dilution limits the scalability and consequently the application scope of SCNPs in general. Several strategies have been explored in the literature to circumvent this issue and achieve single-chain folding at higher concentrations or with increased efficiency (refer to Chapter 2.1). One approach to address the scalability challenge is given by transferring established batch processes to flow procedures, enabling the continuous production of SCNPs. Generally, flow chemistry has found a variety of applications in organic and polymer synthesis and offers significant advantages in terms of facile scalability and pathways towards commercial production.[72,196-202] In the realm of SCNPs, the groups of Barner-Kowollik and Diesendruck have recently demonstrated for the first time how transferring a photochemical batch reaction to photoflow conditions can significantly enhance the efficiency of the process, thereby opening a route to access SCNPs on the gram scale. For that, the authors exploited the photodimerization of pendant anthracene units in a methacrylate polymer triggered by λ_{max} = 366 nm light emitting diode (LED) irradiation, and the flow process proved to reach the same crosslinking density at least four times faster than the previously reported batch process.[72,78] Subsequent life cycle assessments evaluated the environmental impact of the batch and flow approaches, finding the flow process combined with atmospheric pressure distillation solvent recovery to be the most environmentally benign.[202] However, despite the conceivable advantages offered by flow approaches, no efforts towards continuous flow production of SCNPs for an application seem to have been undertaken yet.

An ideal system for the flow synthesis of SCNPs allows the mixing of the linear precursor polymer and crosslinker without any immediate initial reaction occurring, thus enabling the simple preparation of one single reaction mixture to be subjected to flow synthesis. During flow synthesis, a suitable trigger must activate either the precursor polymer or the crosslinker, thereby inducing the single-chain collapse. While different triggers are conceivable, including but not limited to thermal, electrochemical or photochemical stimuli, our groups are particularly interested in using light to access highly functional tailor-made macromolecular architectures as light efficiently enables high spatiotemporal control over chemical reactions.[184-185,187,203]

The single-chain collapse approach commonly used for the synthesis of metal-functionalized SCNPs is based on the coordination of Lewis basic functional groups incorporated in the polymer chain to metals (refer to Chapter 2.3). One way of transferring this approach to flow photochemistry is to equip the Lewis basic groups within the linear precursor polymer with photolabile protecting groups, thereby enabling mixing with a metal precursor without any immediate reaction occurring. Thus, a copolymer featuring at least one photobasic comonomer constitutes an ideal system for the photoflow synthesis of metal-functionalized SCNPs.

The concept of using photolabile protection groups has emerged more than 50 years ago[204-208] and has since found manifold applications in organic and polymer synthesis as well as in biological contexts.[209] Especially, the use of photolabile *ortho*-nitrobenzyl groups has attracted significant attention in polymer chemistry due to the simple tunability of the cleavage wavelength, the versatility in terms of accessible functional groups after photocleavage as well as the experimentally and theoretically well-studied cleavage mechanism.[210]

Based on these considerations, this chapter targets a critical gap in the literature by introducing the first synthesis of catalytically active SCNPs under photoflow conditions. The design approach is based on a poly(ethylene glycol) methyl ether methacrylate (PEGMEMA) polymer backbone, copolymerized with a photocleavable 2-((((2-nitrobenzyl)oxy)carbonyl)-amino)ethyl methacrylate (*o*NBMA) monomer, which can liberate amine groups upon visible light irradiation, allowing single-chain collapse by complexation of Cu(II) ions via the liberated amines. Initially, the photochemical response of the photolabile monomer is investigated following the well-established photochemical action plot methodology.[211-212] Based on the insights gained from the photochemical action plot, the successful applicability of the concept in batch SCNP synthesis is demonstrated and subsequently transferred to flow conditions using a commercially available photoflow reactor. Critically, the catalytic performance of the resulting Cu(II) SCNPs for the visible light photocatalyzed cleavage of carbon-carbon single and double bonds on the examples of xanthene-9-carboxylic acid and oleic acid is explored, demonstrating the advantageous effect the SCNP environment can provide compared to similar small molecule catalysts.

4.2.2 Photochemical Action Plot of 2-((((2-Nitrobenzyl)oxy)carbonyl)amino)-ethyl methacrylate

Understanding the response of a chemical system to light irradiation is key for any photochemical process. Most commonly, the optical absorption spectrum of a compound is recorded to obtain insights into the excitation processes upon light irradiation. However, while the absorption spectrum provides detailed information regarding the initially populated excited states, conclusions about the time evolution of the excited state dynamics after the initial excitation cannot be drawn directly. Yet, this information is crucial to understanding and predicting chemical reactivity following initial electronic excitation. It is evident from the literature that the optical absorption spectrum of a molecule is often strongly disparate from the reactivity profile when probed with the same number of photons at different wavelengths. The latter can be achieved following the photochemical action plot methodology developed by the Barner-Kowollik group. A photochemical action plot of a given reaction can be obtained by irradiating a sample with the same defined number of photons at different wavelengths and tracking the consumption of the starting material or the conversion to the desired product in dependence on the irradiation wavelength.[211-212]

To shine light on the irradiation response of the photocleavable functionalities employed for the light-driven formation of Cu(II) SCNPs in this chapter, a photochemical action plot of the

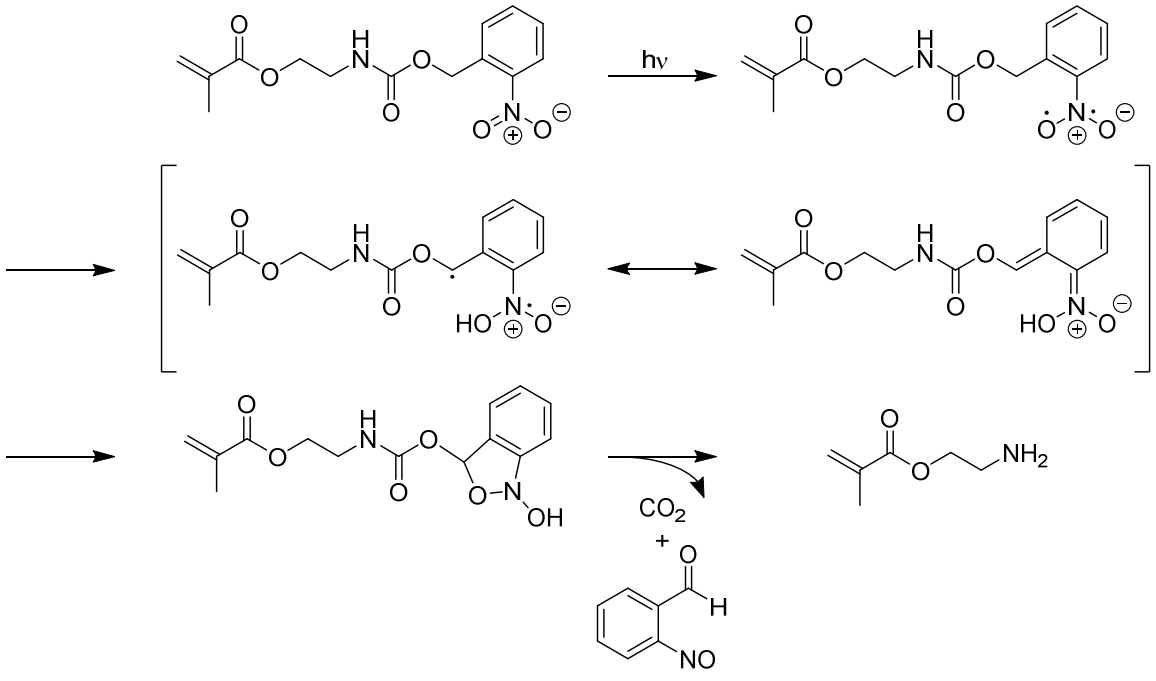

Scheme 4.5 Proposed mechanism of the cleavage of 2-((((2-nitrobenzyl)oxy)carbonyl)amino)ethyl methacrylate (*o*NBMA) to 2-aminoethyl methacrylate upon light irradiation.

*o*NBMA monomer, used in the polymer syntheses relevant to this chapter, was recorded. The light-induced cleavage of the latter to 2-aminoethyl methacrylate, carbon dioxide and *ortho*-nitrosobenzaldehyde is likely to follow the cleavage mechanism shown in **Scheme 4.5**.[210] The initial excitation of the nitro group enables the excited state intramolecular transfer of a benzylic hydrogen to an oxygen atom of the nitro group, followed by intramolecular cyclization and subsequent formation of the cleavage products.

The photochemical action plot shown in **Figure 4.18** was recorded by irradiating an acetonitrile solution of *o*NBMA at an initial concentration of 1.62 mmol·L^{-1} with 1.99·10^{18} photons in the wavelength range from 230 nm to 440 nm in 10 nm increments and determining the consumption of the starting material using liquid chromatography.

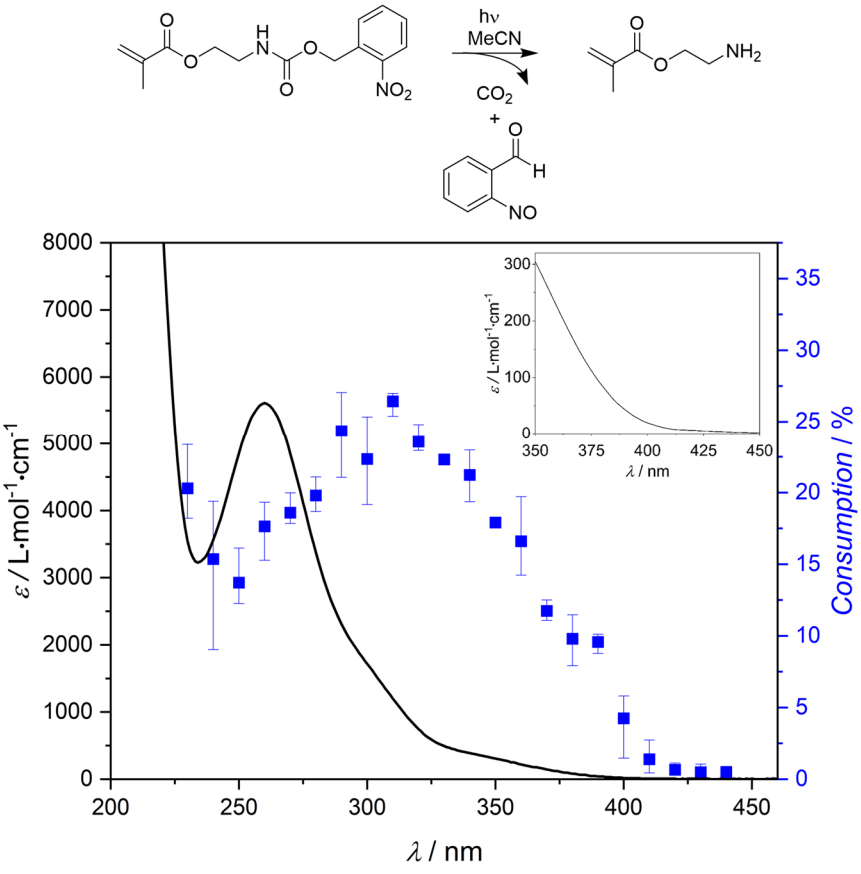

Figure 4.18 Photochemical action plot of the photocleavage of 2-((((2-nitrobenzyl)oxy)carbonyl)-amino)ethyl methacrylate (*o*NBMA) to 2-aminoethyl methacrylate in acetonitrile at an initial concentration of 1.62 mmol·L^{-1}, showing the consumption of the starting material upon irradiation with the same number of photons (1.99·10^{18} photons) at different wavelengths superimposed with the UV/Vis spectrum of the starting material. Error bars indicate the lowest and highest determined conversion at each wavelength, respectively. The insert shows the extinction spectrum at high wavelengths.

Each data point was recorded in triplicate and the error bars refer to the lowest and highest determined conversion at each wavelength, respectively. Details on the experimental procedures are provided in Chapter 6.3.2.1.

From the photochemical action plot, it is evident that the maximum of the wavelength-dependent reactivity pattern is red-shifted by about 50 nm compared to the extinction maximum of *o*NBMA, an observation previously made for *ortho*-nitrobenzyl photocleavage reactions.[213] Detailed theoretical work on *ortho*-nitrobenzyl acetates indicates that the lowest energy excited singlet and triplet states, respectively, are of particular relevance for the initial excited state intramolecular hydrogen transfer in the cleavage mechanism of *ortho*-nitrobenzyl compounds. However, these states are predominantly populated via internal conversion and intersystem crossing pathways after initial excitation to energetically higher lying excited states with larger oscillator strengths.[214] Direct excitation of the states relevant to the reaction progress upon irradiation at higher wavelengths instead of taking the alternate path of initial excitation to an unreactive state followed by energy redistribution may be considered a rationalization of the discrepancy between extinction spectrum and reactivity profile observed here.

Most commonly, photochemical action plots are employed to determine the wavelength of maximum photoreaction efficiency. However, in the current case, the observed reactivity above 400 nm, where the extinction coefficient is significantly below 100 $L \cdot mol^{-1} \cdot cm^{-1}$ (refer to insert in **Figure 4.18**), was of particular interest as this suggested that visible light could be employed for the cleavage of the photolabile protecting group. A similar finding has previously been reported in the literature.[215] While the photochemical behaviour of monomeric systems is not necessarily representative of their polymeric counterparts,[213] this observation indicated that visible light may be employed for the SCNP syntheses reported in this chapter.

4.2.3 Light-Driven Batch Synthesis of Cu(II) Single-Chain Nanoparticles

To incorporate the photolabile monomer into a polymer and enable single-chain folding by metal complexation upon light-induced deprotection of the amine moieties, *o*NBMA was copolymerized with PEGMEMA (average M_n = 300 $g \cdot mol^{-1}$) by RAFT polymerization as depicted in **Scheme 4.6**, resulting in polymer **P3**. Given the statistical nature of this copolymerization process, all SCNP folding reactions based on this polymer follow the repeat unit approach (refer to Chapter 2.1).[42]

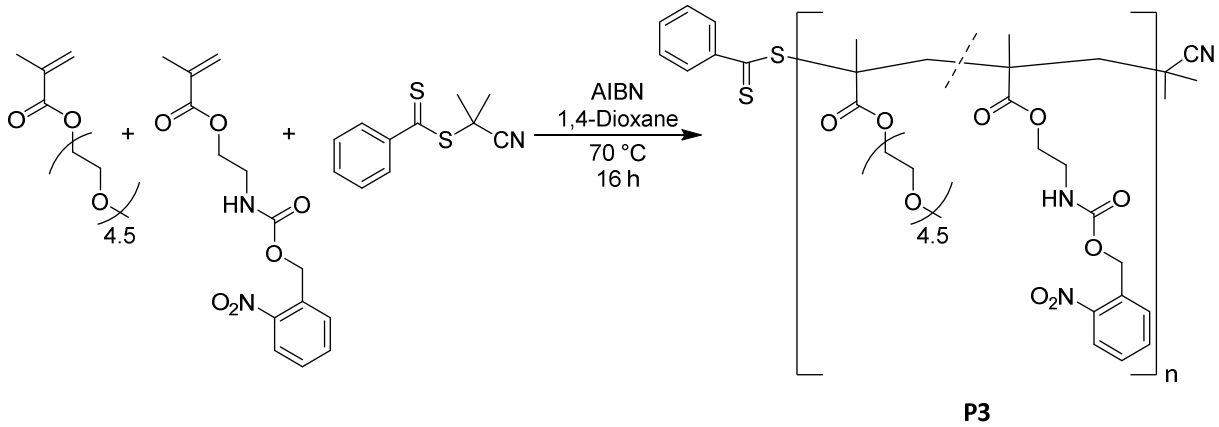

P3

Scheme 4.6 Synthesis of poly(PEGMEMA-*co*-*o*NBMA) (Polymer **P3**) by reversible addition-fragmentation chain transfer polymerization.

SEC measurements in THF indicated a number-averaged molar mass of M_n = 28200 g·mol^{-1} and dispersity of $Đ$ = 1.23. The ^{1}H NMR spectrum of **P3** measured in CD_3CN is depicted in **Figure 4.19**. The aliphatic backbone resonances can be found at δ = 2.05-0.70 ppm. The resonances of the PEG side chains of the PEGMEMA moieties dominate the spectrum and arise from the terminal methyl group (δ = 3.34-3.24 ppm), the ethylene glycol subunits (δ = 3.75-3.35 ppm) and the methylene group attached to the ester functionality connecting the PEG side chain with the polymer backbone (δ = 4.20-3.90 ppm), respectively. The resonances associated with the photolabile *o*NBMA moieties correspond to the methylene groups of the ethylene bridge

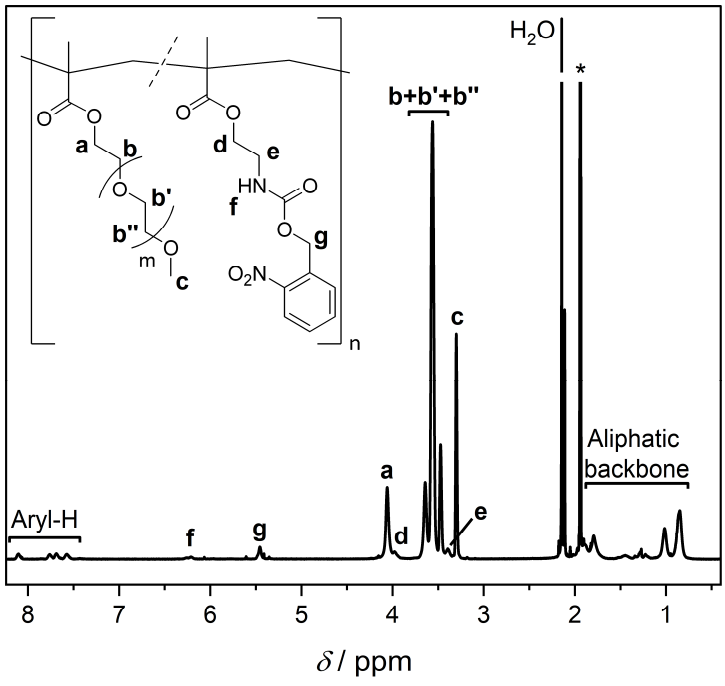

Figure 4.19 ^{1}H NMR spectrum (600 MHz, CD_3CN, 298 K) of polymer **P3**. Asterisk denotes residual solvent resonance.

connecting polymer backbone and carbamate functionality (δ = 3.44-3.34 ppm and δ = 4.00-3.86 ppm), the benzylic protons (δ = 5.52-5.38 ppm), the amide proton (δ = 6.35-6.15 ppm) and the aromatic protons (δ = 8.20-7.45 ppm), respectively.

The relative amount of photolabile moieties incorporated into **P3** can be estimated according to:

$$\frac{N_{o\mathrm{NBMA}}}{N_{\mathrm{PEGMEMA}} + N_{o\mathrm{NBMA}}} = \frac{1}{1 + \frac{2}{3}\frac{Int(\mathrm{c})}{Int(\mathrm{g})}}$$

Herein, $N_{o\mathrm{NBMA}}$ and N_{PEGMEMA} are the average number of *o*NBMA and PEGMEMA monomers, respectively, incorporated in a macromolecular chain of **P3**, *Int*(c) is obtained by integration of the resonance at δ = 3.34-3.24 ppm relative to the value of the integral *Int*(g), obtained by integration of the resonance at δ = 5.52-5.38 ppm. Integration of the corresponding resonances yielded a ratio of *Int*(c)/*Int*(g) of 9.2, equivalent to an incorporation ratio of 14 % functional monomers per macromolecular chain.

The incorporation of the photolabile *o*NBMA monomer into **P3** enables the liberation of pendant amine moieties upon light irradiation (refer to Chapter 4.2.2) which can be employed for the coordination of metals, thereby inducing single-chain folding under appropriate conditions. Specifically, **P3** was mixed with copper(II) chloride dihydrate in acetonitrile and irradiated with a 400 nm LED in a classical batch photochemical process, yielding the intramolecularly folded **SCNP3-Cu-Batch** (refer to **Scheme 4.7**).

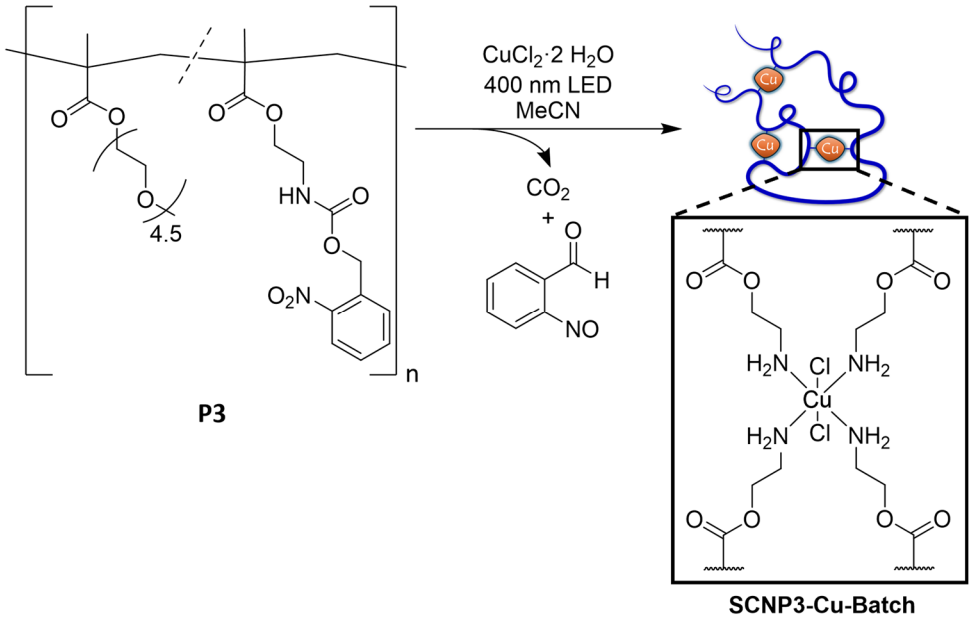

Scheme 4.7 Synthesis of **SCNP3-Cu-Batch** by LED irradiation of **P3** in the presence of $CuCl_2 \cdot 2\ H_2O$. The depiction of the folding unit is based on a model complex (refer to **Figure 4.24**).

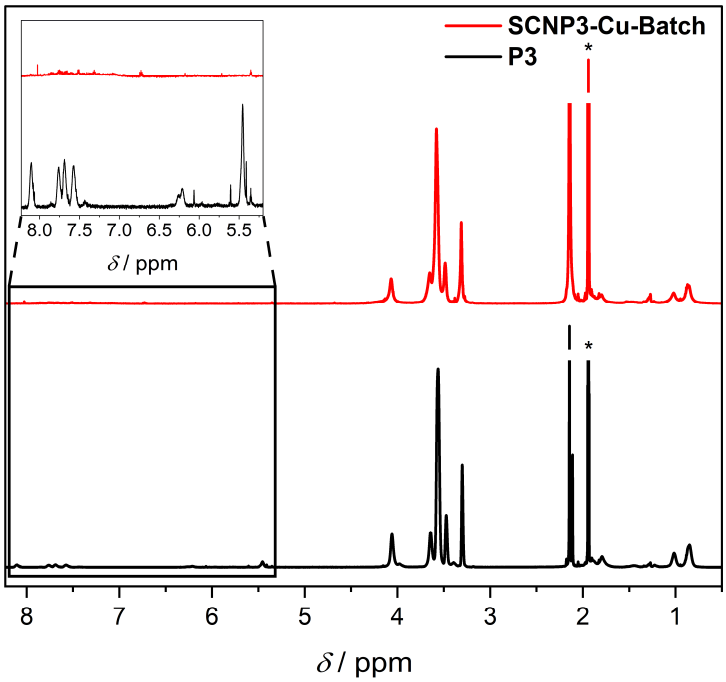

Figure 4.20 Stacked ^{1}H NMR spectra (600 MHz, CD_3CN, 298 K) of polymer **P3** (black) and **SCNP3-Cu-Batch** (red). Insert shows zoomed-in region of the resonances associated with the photolabile protecting group. Asterisks denote residual solvent resonances.

^{1}H NMR spectroscopy indicated the quantitative deprotection of the linear precursor polymer throughout the reaction by disappearance of the resonances associated with the photolabile *ortho*-nitrobenzyl group at δ = 8.20-7.45 ppm, 6.35-6.15 ppm and 5.52-5.38 ppm (refer to **Figure 4.20**). Monitoring the intensity of the aforementioned resonances over time indicated the quantitative deprotection of the amine moieties within 50 minutes (refer to **Figure 4.21a**).

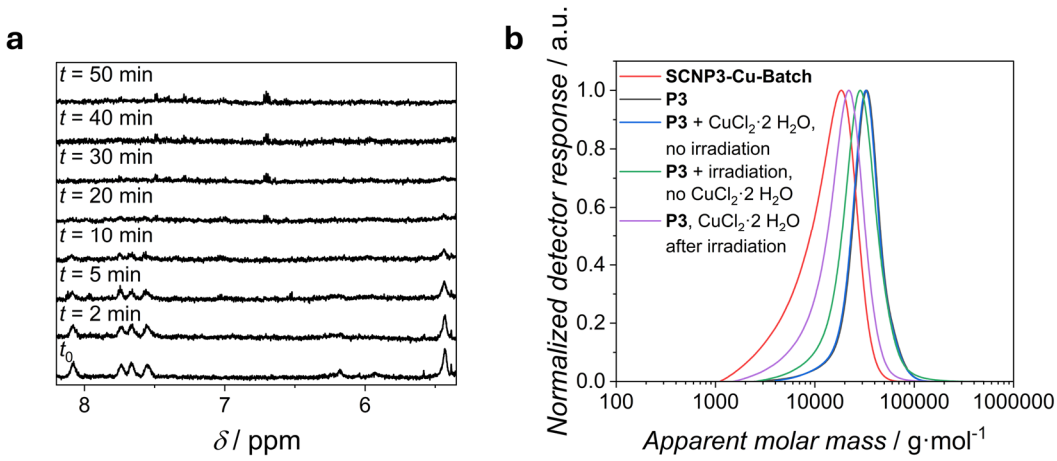

Figure 4.21 (a) Stacked ^{1}H NMR spectra (600 MHz, CD_3CN, 298 K) showing the resonances associated with the photolabile protecting group of **P3** after different times of irradiation with a 400 nm LED in the presence of $CuCl_2 \cdot 2\ H_2O$ in acetonitrile and **(b)** SEC chromatograms (THF, RI, PMMA cal.) of different control reactions (refer to the main text and Chapter 6.3.2.3 for details).

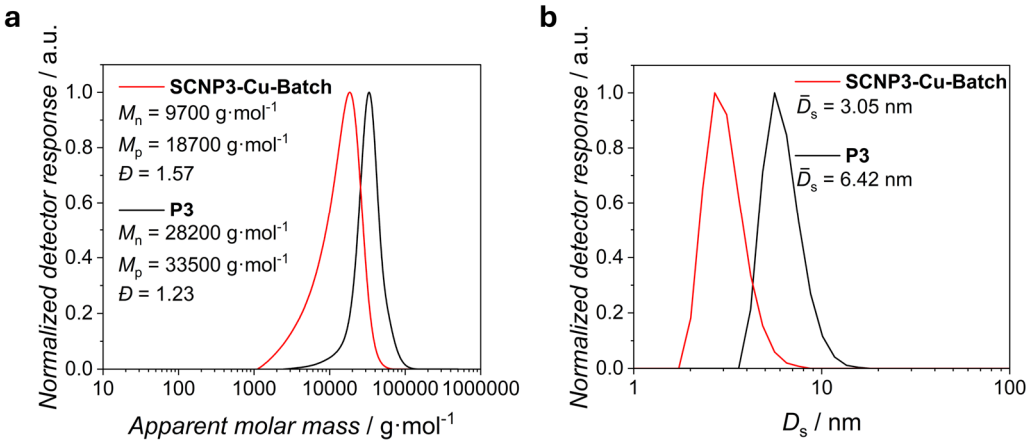

Figure 4.22 Superimposed **(a)** SEC chromatograms (THF, RI, PMMA cal.) and **(b)** number-weighted DLS size distributions (CH_3CN, mean diameter by number, average values derived from five measurements) of polymer **P3** (black) and **SCNP3-Cu-Batch** (red).

Successful single-chain compaction was evident from size-sensitive analytical data. According to SEC in THF, the molar mass distribution of **SCNP3-Cu-Batch** was shifted towards lower apparent molar masses relative to that of **P3** (refer to **Figure 4.22a**). Specifically, the number-averaged and peak molar masses derived from SEC decreased from M_n = 28200 g·mol^{-1} and M_p = 33500 g·mol^{-1} for **P3** to M_n = 9700 g·mol^{-1} and M_p = 18700 g·mol^{-1} for **SCNP3-Cu-Batch**, accompanied by an increase in dispersity from $Đ$ = 1.23 for **P3** to $Đ$ = 1.57 for **SCNP3-Cu-Batch**. Further evidence of successful single-chain folding came from DLS measurements in acetonitrile, showing a decrease in the number-averaged solvodynamic diameter from D_s = 6.42 nm for **P3** to D_s = 3.05 nm for **SCNP3-Cu-Batch** (refer to **Figure 4.22b**). Similarly, ^{1}H DOSY NMR in CD_3CN indicated an increase of the average diffusion coefficient from $D = 1.43 \cdot 10^{-10}$ m^2·s^{-1} for **P3** to $D = 1.71 \cdot 10^{-10}$ m^2·s^{-1} for **SCNP3-Cu-Batch** (refer to **Figure 4.23**). It is worth noting that a decrease in the solvodynamic volume of **P3** is also expected upon irradiation in the absence of copper ions as the cleavage of the photolabile protecting groups decreases the molar mass of the polymer. Furthermore, reactions of the liberated amines with ester groups in the polymer backbone, potentially contributing to single-chain compaction even in the absence of metal ions, have been reported for similar polymers in the literature.[216-217] However, the associated changes in size were less pronounced than the compaction observed in the presence of the metal salt (refer to red and green curves in **Figure 4.21b**). Preventing uncontrollable reactions of the liberated amines with the polymer backbone made it critical to conduct the synthesis of **SCNP3-Cu-Batch** by irradiation of **P3** in

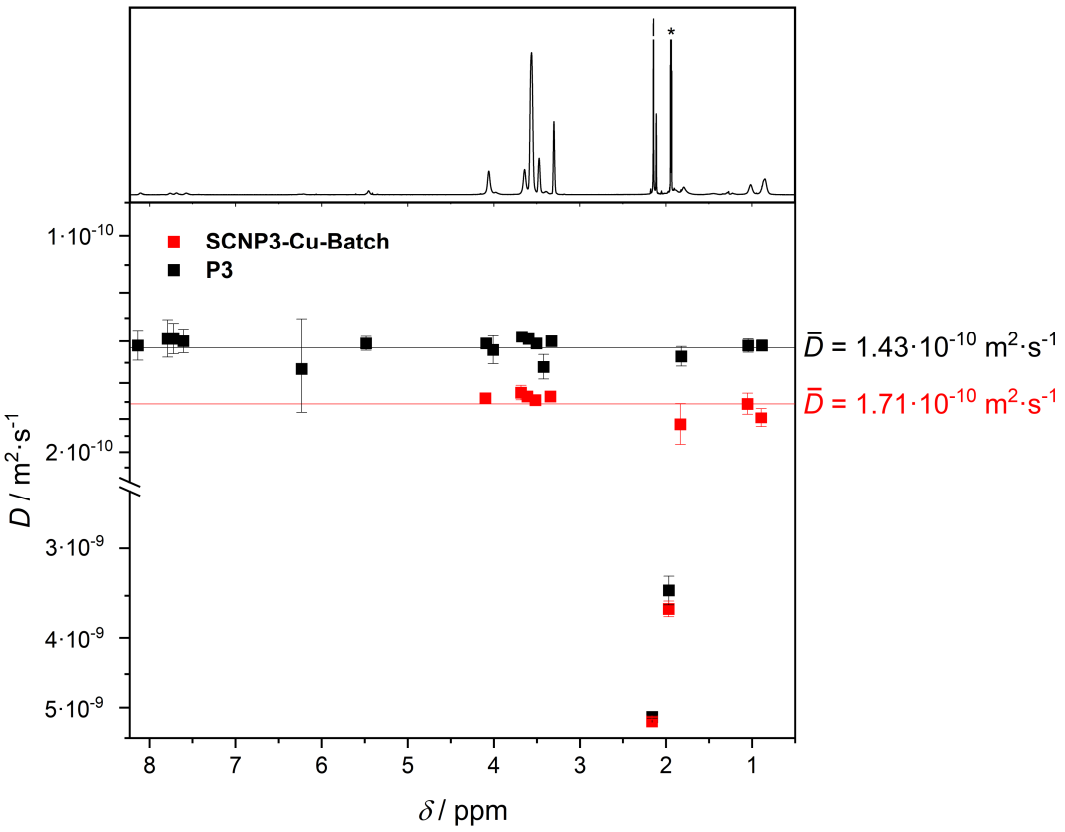

Figure 4.23 Superimposed ^{1}H DOSY NMR spectra (400 MHz, CD_3CN, 301 K) of polymer **P3** (black) and **SCNP3-Cu-Batch** (red). Spectral trace on top refers to **P3**. Error bars refer to data fitting error. Horizontal lines indicate average diffusion coefficients. Asterisk denotes residual solvent resonance.

the concomitant presence of the metal source. Adding the metal salt subsequent to irradiation led to a less pronounced SCNP compaction, presumably as a consequence of less amine functionalities being available for the given reason (refer to purple and red curves

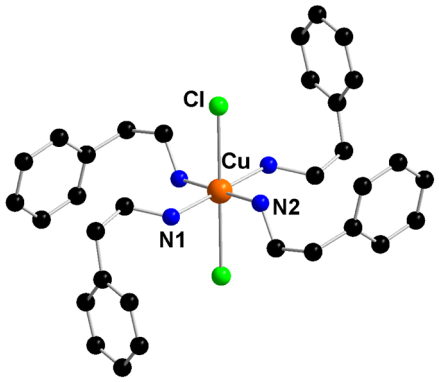

Figure 4.24 Molecular structure in the solid state of the model complex [(2-phenylethylamine)$_4$CuCl$_2$]. Selected bond distances [Å] and angles [°]: Cu-N1 2.033(2), Cu-N2 2.044(2), Cu-Cl 2.8080(7), N1-Cu-N2 87.01(9), N1-Cu-Cl 98.04(7), N2-Cu-Cl 83.46(7). Color code: Carbon black, nitrogen blue, chlorine green, copper bronze. Hydrogen atoms and non-coordinating solvent molecules are omitted for clarity.

in **Figure 4.21b**). Without irradiation, no signs of single-chain folding were evident from SEC analysis (refer to black and blue curves in **Figure 4.21b**).

To gather a more detailed understanding of the structure of the actual SCNP folding unit of **SCNP3-Cu-Batch**, a small molecule model complex was synthesized. For that, 2-phenylethylamine was chosen as a small molecule mimic of the ethylamine moieties liberated after cleavage of the *ortho*-nitrobenzyl protecting groups upon irradiation of **P3**. The mixing of 2-phenylethylamine with copper(II) chloride dihydrate in acetonitrile resulted in the hexa-coordinated complex [(2-phenylethylamine)$_4$CuCl$_2$], the molecular structure in the solid state of which is depicted in **Figure 4.24**. The complex crystallizes in the monoclinic space group $P2_1/n$ with half the complex and a non-coordinating acetonitrile molecule in the asymmetric unit. The central copper ion is coordinated by four 2-phenylethylamine ligands in a square planar fashion with Cu-N distances of 2.033(2)-2.044(2) Å and a N1-Cu-N2 angle of 87.01(9)°. The additional coordination of two chloride ions with a Cu-Cl distance of 2.8080(7) Å leads to a Jahn-Teller distorted octahedron, as expected for the d^9 ion Cu(II).[218] A similar coordination by four amine moieties and two chloride ions is anticipated for the copper ions within **SCNP3-Cu-Batch**. However, the coordination environment within the SCNP may differ from that observed in the model complex due to flexibility constraints within the polymer framework and the presence of additional oxygen atoms. Nonetheless, the model complex unambiguously evidences the binding capabilities of ethylamine based ligand systems to Cu(II) ions under the conditions employed throughout the SCNP syntheses described in this chapter.

4.2.4 Light-Driven Flow Synthesis of Cu(II) Single-Chain Nanoparticles

The successful synthesis of **SCNP3-Cu-Batch** unequivocally evidences that the developed methodology of equipping a polymer with photobasic functional groups combines access to metal-functionalized SCNPs with spatiotemporal control over the folding process. To explore SCNP synthesis in flow, a new batch of the precursor polymer (Polymer **P3'**) was prepared analogously to **P3**. SEC measurements of **P3'** in THF indicated a number-averaged molar mass of M_n = 30900 g·mol^{-1} and dispersity of $Đ$ = 1.18. Using ^{1}H NMR spectroscopy, the amount of photolabile functional groups within the copolymer was estimated to be approximately 15 %. As outlined in Chapter 4.2.1, the methodology described for the proof-of-concept preparation of **SCNP3-Cu-Batch** constitutes an ideal approach towards SCNP flow synthesis as it allows the mixing of the linear precursor polymer and crosslinker without any immediate initial reaction occurring, thus enabling the simple preparation of one single reaction mixture to be subjected

to flow synthesis. Irradiation of a solution of **P3'** in the presence of copper(II) chloride dihydrate in acetonitrile with a 410 nm LED, employing the commercially available Vapourtec E-series photoflow reactor (refer to Chapter 6.2.9 for details), triggered the deprotection of the polymer-bound amine moieties upon cleavage of the photolabile *ortho*-nitrobenzyl protecting groups, providing access to **SCNP3-Cu-Flow** in continuous flow.

To identify suitable conditions for the synthesis of **SCNP3-Cu-Flow**, varying flow rates and concentrations were initially screened and the corresponding ^{1}H NMR spectra and SEC chromatograms of the reaction mixtures analyzed (refer to **Figure 4.25**). At first, the synthesis was conducted in analogy to that of **SCNP3-Cu-Batch** at a polymer concentration of 2 mg·mL^{-1} and the flow rate varied between 0.2 mL·min^{-1} and 1 mL·min^{-1}. The analysis of the resonances associated with the photolabile protecting group indicated that quantitative

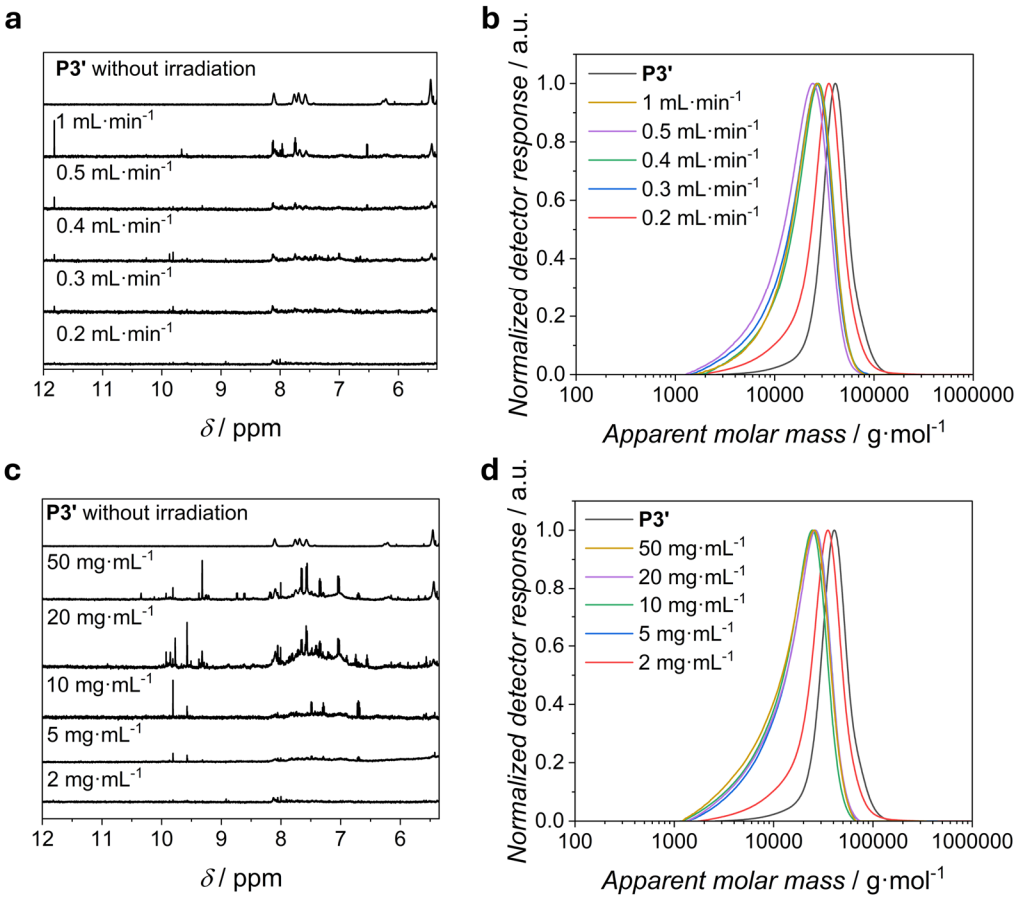

Figure 4.25 Stacked ^{1}H NMR spectra (600 MHz, CD_3CN, 298 K) showing the resonances associated with the photolabile protecting group and SEC chromatograms (THF, RI, PMMA cal.) recorded after irradiation of **P3'** in the presence of $CuCl_2 \cdot 2\ H_2O$ in acetonitrile with a 410 nm LED in a Vapourtec E-series photoflow reactor at **(a-b)** different flow rates at a constant polymer concentration of 2 mg·mL^{-1} and **(c-d)** different polymer concentrations at a constant flow rate of 0.2 mL·min^{-1}.

deprotection of the polymer-bound amine functionalities requires a flow rate of 0.2 mL·min^{-1} (refer to **Figure 4.25a**). The tubing volume exposed to light in the photoflow process is 10 mL, resulting in a total irradiation time of 50 minutes, which is similar to the time necessary for the complete deprotection of **P3** under batch conditions (refer to **Figure 4.21a**). Varying the polymer concentration at a flow rate of 0.2 mL·min^{-1} indicated that at polymer concentrations above 2 mg·mL^{-1} side reactions started occurring as was evident from several unassignable resonances in the aromatic region of the ^{1}H NMR spectra of the reaction mixtures at polymer concentrations between 5 mg·mL^{-1} and 50 mg·mL^{-1} (refer to **Figure 4.25c**). Interestingly, the SEC chromatograms of the corresponding reaction mixtures indicated a more pronounced apparent SCNP compaction and no signs of intermolecular interactions at flow rates higher than 0.2 mL·min^{-1} and polymer concentrations above 2 mg·mL^{-1} (refer to **Figure 4.25b** and **d**). At high flow rates, the observed increased compaction may result from the formation of long-range loops via the copper complexation by amine moieties separated by longer contour distances than is the case in a polymer in which all amine moieties are deprotected. A more pronounced compaction at high polymer concentrations may result from uncontrolled radical side reactions. The fact that no signs of intermolecular crosslinking were present, even at a polymer concentration of 50 mg·mL^{-1}, is in line with literature precedents of similar polymeric systems.[73-74]

The flow process is consequently not superior to the previously described batch protocol in terms of irradiation time and polymer concentration. However, the flow approach enables the simple and continuous production of any desired quantity of **SCNP3-Cu-Flow**. Contrary, upscaling the batch process would be limited by the difficulty to ensure a homogeneous light distribution through large sample volumes, and the conceivable alternative of running several batch reactions in a row would constitute a time-consuming and inefficient effort.

The analytical data of **SCNP3-Cu-Flow** is summarized in **Figure 4.26**. In analogy to the synthesis of **SCNP3-Cu-Batch**, ^{1}H NMR spectroscopy indicated the quantitative deprotection of the linear precursor polymer throughout the flow process by disappearance of the resonances associated with the photolabile *ortho*-nitrobenzyl group (refer to insert in **Figure 4.26a**). Successful SCNP folding was evidenced by size-sensitive analytical techniques. ^{1}H DOSY NMR in CD_3CN indicated an increase of the average diffusion coefficient from $D = 1.47 \cdot 10^{-10}$ m^2·s^{-1} for **P3'** to $D = 1.56 \cdot 10^{-10}$ m^2·s^{-1} for **SCNP3-Cu-Flow** (refer to **Figure 4.26b**). SEC in THF showed a shift of the entire molar mass distribution of **SCNP3-Cu-Flow** towards lower apparent molar

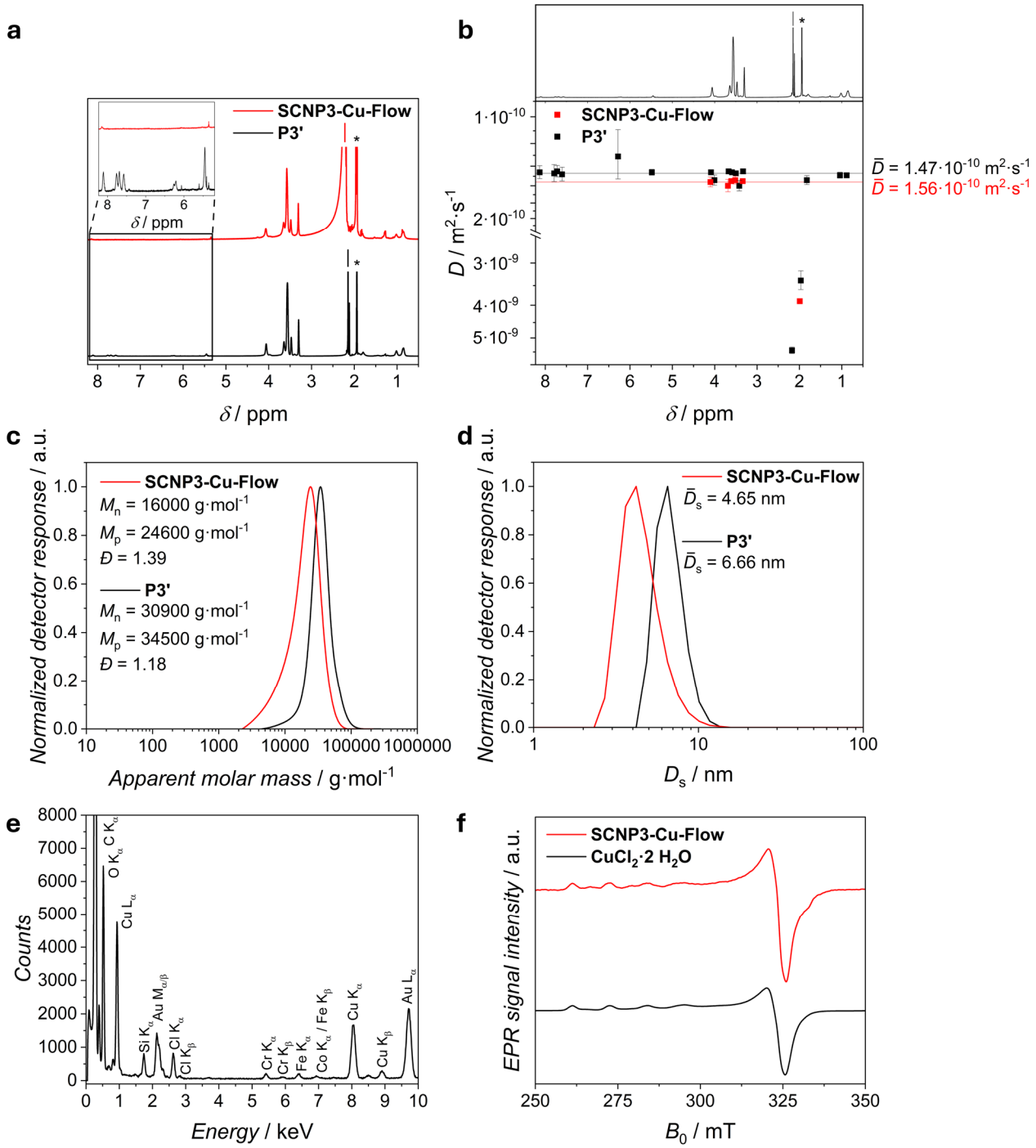

Figure 4.26 Analytical data of **SCNP3-Cu-Flow** and comparison to **P3'** and $CuCl_2 \cdot 2\ H_2O$. **(a)** ^1H NMR spectra (600 MHz, CD_3CN, 298 K). Insert shows zoomed-in region of the resonances associated with the photolabile protecting group**. (b)** ^1H DOSY NMR spectra (400 MHz, CD_3CN, 301 K). Spectral trace on top refers to **P3'**. Error bars refer to data fitting error. Horizontal lines indicate average diffusion coefficients. Asterisks denote residual solvent resonances. **(c)** SEC chromatograms (THF, RI, PMMA cal.). **(d)** Number-weighted DLS size distributions (CH_3CN, mean diameter by number, average values derived from five measurements). **(e)** EDX spectrum. Peaks are labeled with the symbols of the elements and the transitions they are characteristic of. Additional peaks not corresponding to the polymer sample result from Si (detector), Cr, Fe, Co (TEM background) and Au (TEM grid). **(f)** X-band CW EPR spectra (CH_3CN, 115 K).

masses relative to that of **P3'** (refer to **Figure 4.26c**). In detail, the number-averaged and peak molar masses derived from SEC analysis decreased from M_n = 30900 g·mol^{-1} and M_p = 34500 g·mol^{-1} for **P3'** to M_n = 16000 g·mol^{-1} and M_p = 24600 g·mol^{-1} for **SCNP3-Cu-Flow**, accompanied by an increase in dispersity from $Đ$ = 1.18 for **P3'** to $Đ$ = 1.39 for **SCNP3-Cu-Flow**. According to DLS measurements in acetonitrile, the number-averaged solvodynamic diameter decreased from D_s = 6.66 nm for **P3'** to D_s = 4.65 nm for **SCNP3-Cu-Flow** (refer to **Figure 4.26d**).

To remove any unreacted copper(II) chloride from the reaction mixture, the solution obtained after the photoflow process was subjected to purification by preparative SEC. To confirm that the polymer-bound copper was not accidently removed throughout this purification process, an EDX spectrum of **SCNP3-Cu-Flow** was acquired (refer to **Figure 4.26e**) and confirmed that copper is still present in the purified sample.

The paramagnetic nature of the Cu(II) ions present in **SCNP3-Cu-Flow** enabled the characterization by EPR spectroscopy (refer to **Figure 4.26f**). The obtained EPR spectrum in acetonitrile is qualitatively reminiscent of that of copper(II) chloride dihydrate and characteristic of an axially elongated Cu(II) complex as expected based on the model complex depicted in **Figure 4.24**. Moreover, EPR spectroscopy enabled the quantification of the metal loading of **SCNP3-Cu-Flow**. For that, a calibration curve based on defined concentrations of copper(II) chloride dihydrate in acetonitrile was recorded. The employed concentrations and resulting double integrals of the EPR signal intensity are listed in **Table 4.3**. To obtain a reliable quantification of the average metal loading, three batches of **SCNP3-Cu-Flow** were

Table 4.3 Summary of EPR results and derived data of the $CuCl_2 \cdot 2\ H_2O$ calibration samples as well as three batches of **SCNP3-Cu-Flow**. The given Cu(II) concentrations of samples of **SCNP3-Cu-Flow** were derived from a linear fit curve to the calibration data based on the measured double integrals of the EPR signal intensity.

		Double integral of EPR signal intensity / a.u	**Cu(II) concentration / mmol·L^{-1}**
$CuCl_2 \cdot 2\ H_2O$	Calibration 1	231.74	0.0587
	Calibration 2	629.86	0.117
	Calibration 3	2636.55	0.293
	Calibration 4	4951.72	0.587
SCNP3-Cu-Flow	Batch 1	101.98	0.0431
	Batch 2	236.94	0.0579
	Batch 3	197.97	0.0537

prepared and their EPR spectra recorded under conditions and instrument settings identical to the calibration samples. The determined double integrals of the EPR signal intensities as well as the derived Cu(II) concentrations are collated in **Table 4.3**. Based on this data, an average Cu(II) concentration in solutions of **SCNP3-Cu-Flow** of about 0.05 mmol·L^{-1} was determined.

4.2.5 Comparison of the Single-Chain Compaction of SCNP3-Cu-Batch and SCNP3-Cu-Flow

To compare the SCNP compaction achieved by the batch and flow process, respectively, the syntheses of **SCNP3-Cu-Batch** and **SCNP3-Cu-Flow** were conducted again starting from the same batch of the precursor polymer (**P3'**). To ensure comparability, both crude reaction mixtures were purified under the same conditions by preparative SEC in acetonitrile. The results of the size analysis by SEC, DLS and DOSY are depicted in **Figure 4.27** and summarized in **Table 4.4**.

According to SEC in *N,N*-dimethylacetamide (DMAc), the apparent peak molar mass decreased from M_p = 36200 g·mol^{-1} for **P3'** to M_p = 29000 g·mol^{-1} for **SCNP3-Cu-Batch** and M_p = 31900 g·mol^{-1} for **SCNP3-Cu-Flow**. DLS in acetonitrile showed a decrease in the number-averaged solvodynamic diameter from D_s = 6.66 nm for **P3'** to D_s = 2.40 nm for **SCNP3-Cu-Batch** and D_s = 4.65 nm for **SCNP3-Cu-Flow**, respectively. DOSY measurements in (deuterated) acetonitrile indicated an increase of the average diffusion coefficient from $D = 1.47 \cdot 10^{-10}$ m^2·s^{-1} for **P3'** to $D = 1.78 \cdot 10^{-10}$ m^2·s^{-1} for **SCNP3-Cu-Batch** and $1.56 \cdot 10^{-10}$ m^2·s^{-1} for **SCNP3-Cu-Flow**.

Overall, the data unambiguously evidences a decrease in size compared to the precursor polymer throughout the SCNP folding reactions conducted in batch and flow. It is suggested by the data that the observed compaction is more pronounced for **SCNP3-Cu-Batch** than for **SCNP3-Cu-Flow**. Possibly, this results from uncontrolled side reactions taking place in the batch process which do not seem to occur in the flow process under the optimized conditions employed for the synthesis of **SCNP3-Cu-Flow**. This hypothesis is supported by the screening of increased polymer concentrations for the flow synthesis (refer to Chapter 4.2.4) in which increasing the polymer concentration at a constant flow rate led to more pronounced side reactions, accompanied by a larger apparent compaction (refer to **Figure 4.25**).

However, a detailed understanding of the size differences between **SCNP3-Cu-Batch** and **SCNP3-Cu-Flow** would require in-depth knowledge of the processes occurring within the

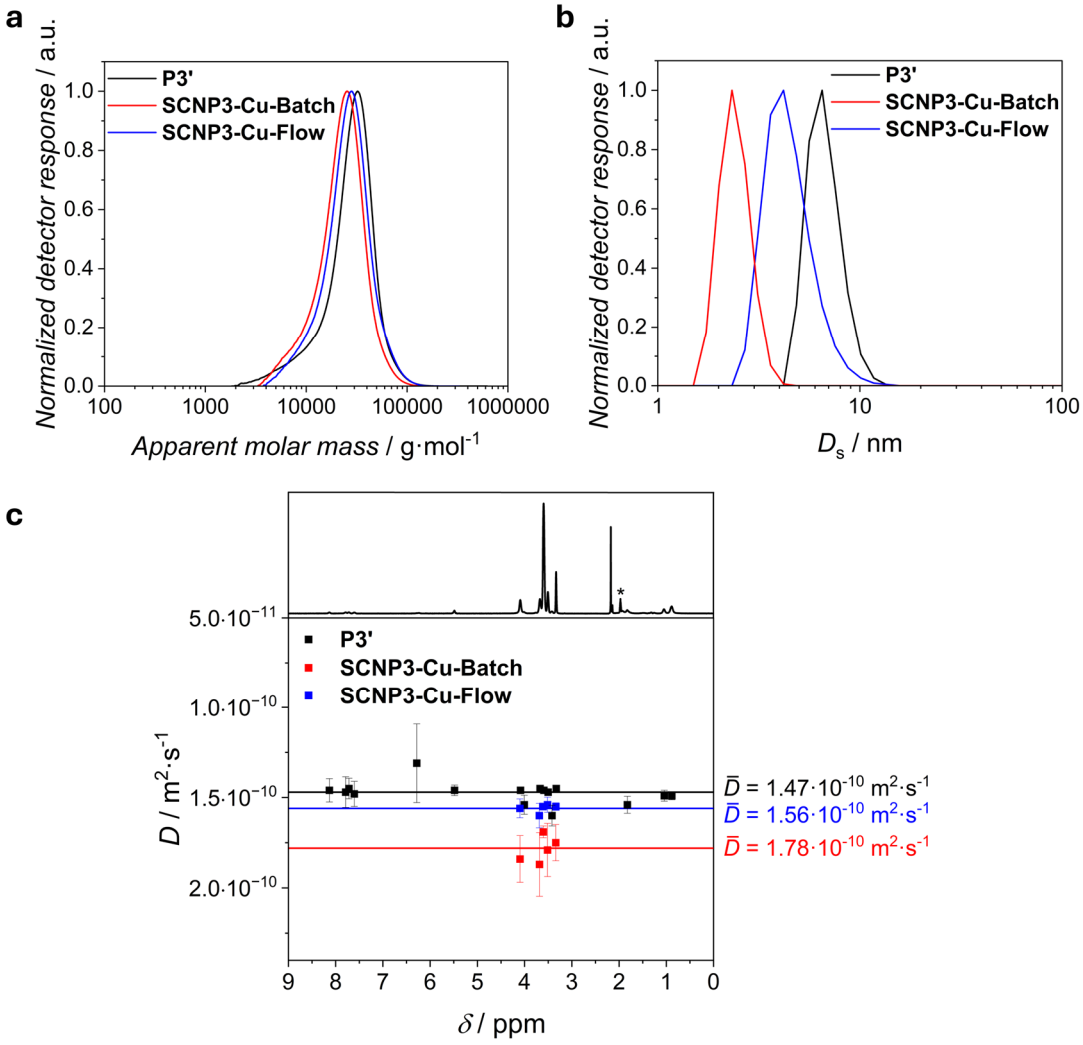

Figure 4.27 Comparison of the relative SCNP compaction of **P3'** (black), **SCNP3-Cu-Batch** (red) and **SCNP3-Cu-Flow** (blue). **(a)** SEC chromatograms (DMAc, RI, PMMA cal.). **(b)** Number-weighted DLS size distributions (CH_3CN). **(c)** ^1H DOSY NMR spectra (400 MHz, CD_3CN, 301 K). Spectral trace on top refers to **P3'**. Error bars refer to data fitting error. Horizontal lines indicate average diffusion coefficients. Asterisk denotes residual solvent resonance.

macromolecules on an atomistic level which, at the present stage, is not achievable using state-of-the-art analytical methods.

Additionally, it is refrained from undertaking detailed quantitative discussions of the data for the following reasons: (*i*) The THF SEC columns have been replaced after the data discussed in Chapters 4.2.3 and 4.2.4 have been recorded. The SCNP samples showed pronounced enthalpic interactions with the new THF SEC columns and the same cannot be excluded for the old columns used throughout earlier data acquisitions. Further, the integrity of the copper coordination under the harsh conditions of the DMAc SEC setup, running at 60 °C and with added lithium bromide, is highly questionable. (*ii*) The size range of the SCNPs is at the lower

Table 4.4 Summary of size analysis of **SCNP3-Cu-Batch** and **SCNP3-Cu-Flow**, both prepared from the same precursor polymer **P3'**.

	P3'	**SCNP3-Cu-Batch**	**SCNP3-Cu-Flow**
M_p / g·mol^{-1} (SEC, DMAc, RI, PMMA cal.)[1]	36200	29000	31900
D_s / nm (DLS, CH_3CN)[2]	6.66	2.40	4.65
D / m^2·s^{-1} (DOSY, CH_3CN/CD_3CN)[3]	$1.47 \cdot 10^{-10}$	$1.78 \cdot 10^{-10}$	$1.56 \cdot 10^{-10}$

[1] The column set of the THF SEC setup was replaced after the THF SEC data discussed in Chapters 4.2.3 and 4.2.4 was acquired. The new column set showed pronounced enthalpic interactions with the SCNP samples. Therefore, SEC data provided here was acquired in DMAc.
[2] Mean diameter by number. Average of five measurements.
[3] **SCNP3-Cu-Batch** and **SCNP3-Cu-Flow** were obtained as solutions in acetonitrile after synthesis. Deuterated acetonitrile was added for DOSY analysis.

detection limit of DLS, due to the weak scattering abilities of small particles, and should thus inherently be treated with caution. (*iii*) The pulse sequence used for the DOSY experiments (*ledbpgp2s*) does not compensate for effects of convection which are expected to be non-negligible under the measurement conditions. Thus, the size information derived from DOSY measurements is also to be considered with caution.

In summary, the data comparing the relative sizes of folded and unfolded polymers to follow the SCNP compaction process are to be considered qualitative in nature. Critically, making quantitative comparisons between the batch and flow SCNPs would not be scientifically sound when taking into account that the errors in the measured sizes upon repeated synthesis and measurements are of a similar magnitude as the differences in size between **SCNP3-Cu-Batch** and **SCNP3-Cu-Flow**.

4.2.6 Catalytic Applications of Cu(II) Single-Chain Nanoparticles

To evaluate the catalytic abilities of the Cu(II)-functionalized **SCNP3-Cu-Flow**, their application in the copper-catalyzed photocatalytic cleavage of carbon-carbon bonds, taking inspiration from the recent work by the groups of Lee and Jiang,[219] was evaluated. Specifically, the decarboxylation-oxygenation of xanthene-9-carboxylic acid and the oxidative double bond cleavage of oleic acid were investigated as these reactions were found to occur without the formation of side products, thus enabling the convenient tracking of the reaction progress by NMR spectroscopy (refer to **Figure 4.28**).

In detail, the catalysis substrates, either xanthene-9-carboxylic acid or oleic acid, respectively, were irradiated with a 400 nm LED in the presence of catalytic amounts of **SCNP3-Cu-Flow** under oxygen atmosphere (refer to Entry 1 in **Table 4.5**). Based on the determination of the average Cu(II) concentration within freshly prepared solutions of **SCNP3-Cu-Flow** by EPR

spectroscopy (refer to Chapter 4.2.4), the amount of added substrate was adjusted to achieve an effective Cu(II) catalyst loading of about 0.5 mol% with respect to the catalysis substrate. For xanthene-9-carboxylic acid, the quantitative decarboxylation and oxygenation to 9-xanthenone within 90 minutes was observed by ^{1}H NMR spectroscopy. For the oxidative double bond cleavage of oleic acid to nonanal and 9-oxononanoic acid, ^{1}H NMR spectroscopic analysis indicated a conversion close to 40 % to occur within 24 hours. Increased irradiation times of up to three days led to a maximum conversion of approximately 50 % (refer to **Figure 6.16**). Noteworthy, the same results were obtained when **SCNP3-Cu-Batch** was employed as the catalyst (refer to Entry 2 in **Table 4.5**), indicating that there are no remarkable differences between the SCNPs prepared by the batch and flow process, respectively, in terms of catalytic performance.

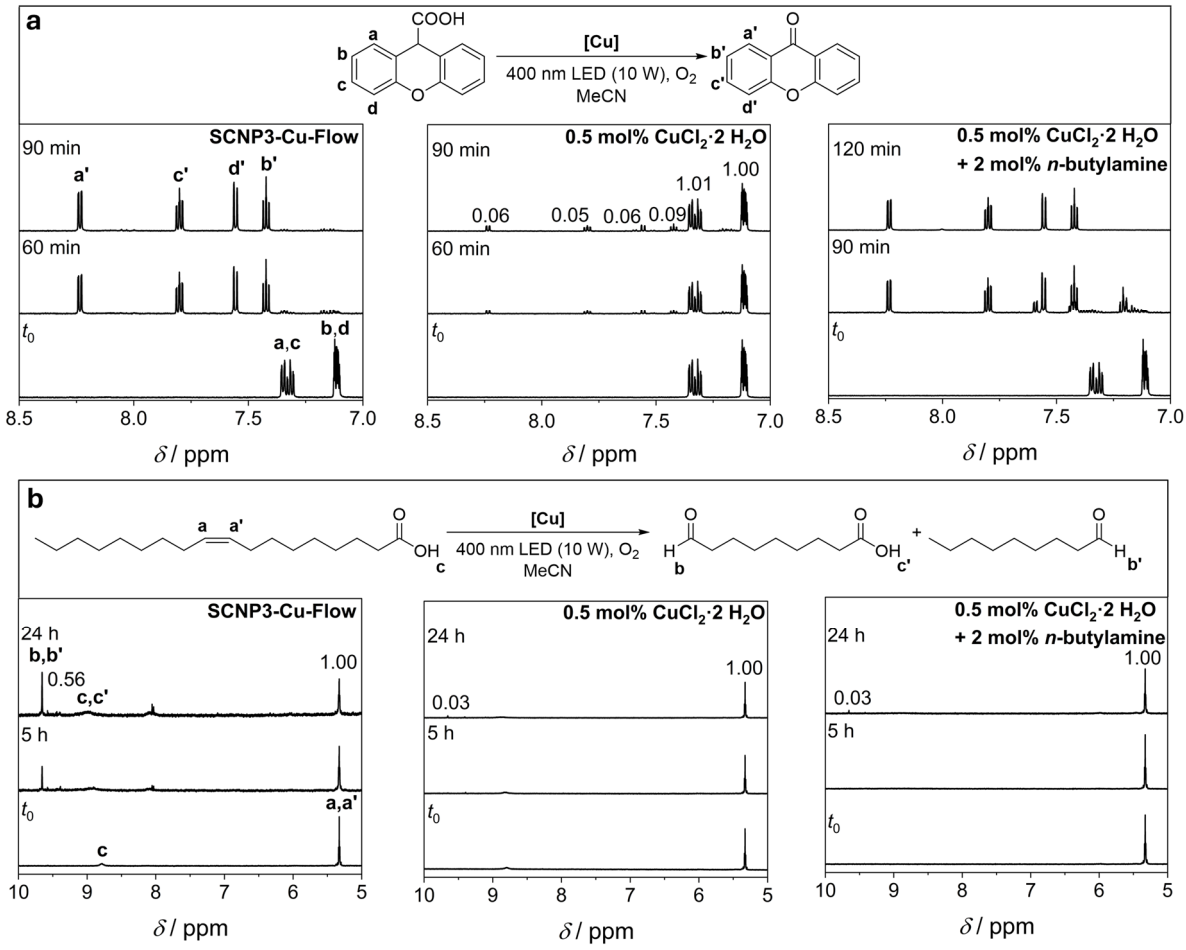

Figure 4.28 Reaction schemes and ^{1}H NMR spectra (600 MHz, CD_3CN, 298 K) of **(a)** the photocatalytic decarboxylation-oxygenation of xanthene-9-carboxylic acid and **(b)** the oxidative double bond cleavage of oleic acid employing **SCNP3-Cu-Flow** (left), $CuCl_2{\cdot}2\ H_2O$ (center) or $CuCl_2{\cdot}2\ H_2O$ in the presence of *n*-butylamine (right) as the catalyst. Resonance labels refer to the respective schemes above the spectra. Numbers on resonances denote integral values.

It is well established in the literature that the specific environment of the active catalyst within SCNPs can offer advantages over analogue small molecule catalysts.[13,15,114,149,171,220] In the present case, conducting the catalytic reactions in the presence of 0.5 mol% copper(II) chloride dihydrate, instead of **SCNP3-Cu-Flow**, resulted in a drastic decrease in the rate of the catalytic transformations (refer to Entry 3 in **Table 4.5**). For xanthene-9-carboxylic acid, only a conversion to the desired product of about 10 % was observed within 90 minutes, contrary to quantitative conversion with the SCNP catalyst. Similarly, the oxidative double bond cleavage of oleic acid proceeded with a conversion of less than 5 % within 24 hours, compared to about 40 % when **SCNP3-Cu-Flow** is employed. To reach reaction rates similar to those observed for **SCNP3-Cu-Flow**, the copper(II) chloride dihydrate load needed to be increased twenty-fold to 10 mol% (refer to Entry 4 in **Table 4.5**).

Additional experiments were carried out to rationalize the observed drastic discrepancies in catalytic performance between **SCNP3-Cu-Flow** and copper(II) chloride dihydrate. The characteristic differences between the SCNP and the small molecule catalyst are the presence of a polymeric environment around the catalytic center and the coordination of amine functionalities to the copper ions within **SCNP3-Cu-Flow**, which are both absent for copper(II) chloride dihydrate.

To investigate the significance of the presence of the polymeric backbone, a homopolymer of PEGMEMA (Poly(PEGMEMA)), mimicking the polymer backbone of **SCNP3-Cu-Flow**, was synthesized. Performing the catalytic reactions in the presence of this polymer at a catalyst loading of 0.5 mol% copper(II) chloride dihydrate did not affect the rates of the catalytic transformations (refer to Entry 5 in **Table 4.5**), indicating that the PEG environment is not substantial to the observed rate discrepancies. Further, running the catalytic reactions with **P3'** as the catalyst in the absence of any copper did also not result in any conversion (refer to Entry 7 in **Table 4.5**).

To mimic the coordination of the copper ions by primary amine moieties within **SCNP3-Cu-Flow**, the catalytic reactions were repeated with 0.5 mol% copper(II) chloride dihydrate in the presence of 2 mol% *n*-butylamine (refer to Entry 6 in **Table 4.5**). For xanthene-9-carboxylic acid, this resulted in a drastically increased catalytic rate compared to copper(II) chloride dihydrate in the absence of the primary amine, and the reaction to 9-xanthenone was completed within 120 minutes. As a corollary, the direct coordination environment of the

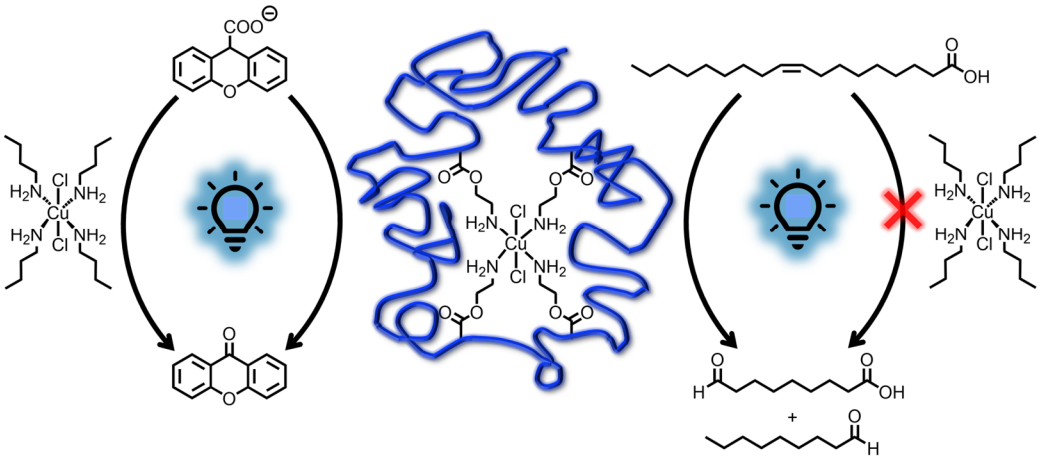

Figure 4.29 Graphical illustration of the stabilizing effect the polymeric environment of **SCNP3-Cu-Flow** provides for the catalytically active moiety. While the photocatalytic decarboxylation-oxygenation of xanthene-9-carboxylic acid (left) is catalyzed by **SCNP3-Cu-Flow** as well as tetra(*n*-butylamine)-copper(II) chloride, the latter is inactive in the oxidative cleavage of oleic acid (right).

copper ions plays a critical role, rationalizing the observed drastic differences in catalytic performance between **SCNP3-Cu-Flow** and copper(II) chloride dihydrate.

However, no such effect was observed for oleic acid, and conducting the catalytic reaction with copper(II) chloride dihydrate in the presence of *n*-butylamine did not increase the rate of the transformation. Instead, the presence of *n*-butylamine led to the disappearance of the carboxylic acid proton resonance at δ = 8.90-8.70 ppm in the ^{1}H NMR spectrum of this reaction mixture. This indicates an interaction of the amine moieties with the carboxylic acid proton, altering the nature of the primary amines, consequently hampering their ability for the coordination to the copper ions. Contrary, when **SCNP3-Cu-Flow** is employed as the catalyst, no changes of the carboxylic acid proton resonance were observed in the ^{1}H NMR spectrum of the corresponding reaction. It thus appears plausible that the amines remain bonded to the copper ions, exerting their advantageous effect on the catalytic rate, rationalizing the observed substantial increase in catalytic performance of **SCNP3-Cu-Flow** with respect to the small molecule copper(II) chloride dihydrate.

A rigorous rationalization of these findings would require precise knowledge of the pK_a values of all species present in the reaction solutions. Based on the literature,[221-224] the situation in acetonitrile is considerably different from that in aqueous solution and strongly depends on delicate equilibria. Further complications may arise from self-assembly or micelle formation upon deprotonation of oleic acid.[225] These considerations render an in-depth investigation of the observations challenging and beyond the scope of the current work.

Table 4.5 Summary of the results of the catalytic studies of the decarboxylation-oxygenation of xanthene-9-carboxylic acid to 9-xanthenone and the oxidative double bond cleavage of oleic acid to nonanal and 9-oxononanoic acid, respectively, derived from the NMR data provided in Chapter 6.3.2.7. Average values are given for experiments performed in triplicate.

Entry		Xanthene-9-carboxylic acid	Oleic acid
1	**SCNP3-Cu-Flow**	100 %	37 %
2	**SCNP3-Cu-Batch**	100 %	35 %
3	0.5 mol% $CuCl_2 \cdot 2\ H_2O$	12 %	3 %
4	10 mol% $CuCl_2 \cdot 2\ H_2O$	100 %	38 %
5	0.5 mol% $CuCl_2 \cdot 2\ H_2O$ + Poly(PEGMEMA)	Trace amounts	2 %
6	0.5 mol% $CuCl_2 \cdot 2\ H_2O$ + 2 mol% *n*-butylamine	100 %	3 %
7	**P3'**	Trace amounts	0 %
8	**P3'**+ $CuCl_2 \cdot 2\ H_2O$ + preparative SEC	Trace amounts	0 %
9	$CuCl_2 \cdot 2\ H_2O$ without LED irradiation	0 %	0 %
10	**SCNP3-Cu-Flow** without LED irradiation	0 %	0 %
11	LED irradiation without catalyst	Trace amounts	0 %

Nonetheless, the results demonstrate that shielding the catalytic entity within the SCNP environment has a critical and positive effect on catalysis, enabling reactivities unachievable with analogue small molecule catalysts (refer to **Figure 4.29**).

Control reactions ensured that the concomitant presence of the copper catalyst and LED irradiation is critical for the catalytic transformations to proceed (refer to Entries 9-11 in **Table 4.5**) and that the workup of **SCNP3-Cu-Flow** by preparative SEC effectively removed unreacted copper(II) chloride after the SCNP synthesis (refer to Entry 8 in **Table 4.5**).

4.2.7 Summary

This chapter describes the first visible light driven photoflow synthesis of catalytically active single-chain nanoparticles (SCNPs). The design approach is based on a poly(ethylene glycol) methyl ether methacrylate polymer backbone, copolymerized with a photocleavable 2-((((2-nitrobenzyl)oxy)carbonyl)amino)ethyl methacrylate monomer (Polymer **P3**), which can liberate amine groups upon visible light irradiation, allowing single-chain collapse by the complexation of Cu(II) ions via the liberated amines. At first, the response of the photobasic

2-((((2-nitrobenzyl)oxy)carbonyl)amino)ethyl methacrylate monomer was probed based on the photochemical action plot methodology, demonstrating that visible light can be employed for the cleavage of the photolabile protecting groups. Irradiation of **P3** in the presence of copper(II) chloride dihydrate with a light emitting diode (LED) centered at 400 nm in a classical batch photochemical process enabled access to **SCNP3-Cu-Batch**, the single-chain collapse of which was verified by size-exclusion chromatography (SEC), dynamic light scattering (DLS) and diffusion-ordered spectroscopy (DOSY). The structure of the folding unit was investigated in more detail by the synthesis of a small molecule Cu(II) model complex.

Building upon the successful proof-of-concept synthesis of **SCNP3-Cu-Batch**, a new batch of photolabile polymer (Polymer **P3'**) was prepared for exploration of SCNP synthesis in continuous flow. Irradiation of **P3'** with a LED centered at 410 nm in the presence of copper(II) chloride dihydrate using a commercially available photoflow reactor resulted in **SCNP3-Cu-Flow**, the single-chain folding of which was again evidenced by SEC, DLS and DOSY measurements. Electron paramagnetic resonance spectroscopy (EPR) enabled the quantification of the average Cu(II) content within solutions of **SCNP3-Cu-Flow**.

The catalytic activity of the prepared Cu(II)-functionalized SCNPs in the visible light photocatalyzed cleavage of carbon-carbon single and double bonds was explored on the examples of xanthene-9-carboxylic acid and oleic acid. The SCNP catalyst proved to be significantly more efficient than the small molecule copper(II) chloride dihydrate, which was traced back to the coordination of amine ligands to the copper ions within the SCNP environment. While the addition of *n*-butylamine to copper(II) chloride dihydrate improved the performance of the latter in the photocatalytic decarboxylation-oxygenation of xanthene-9-carboxylic acid, no such effect of amine addition was observed for the oxidative cleavage of the double bond of oleic acid due to interactions of the added amine with the catalysis substrate. The latter were efficiently suppressed for the SCNP catalyst, demonstrating the advantageous effect the SCNP environment can provide compared to similar small molecule catalysts.

The metal-functionalized SCNPs discussed in Chapters 4.1 and 4.2 featured only a single metallic element within the nanoparticle structures. Building on these results to further enhance the chemical space of metal-functionalized SCNPs, the following chapter aims at the synthesis of heteromultimetallic structures and their catalytic application.

4.3 FERROCENE-DRIVEN SINGLE-CHAIN POLYMER COMPACTION

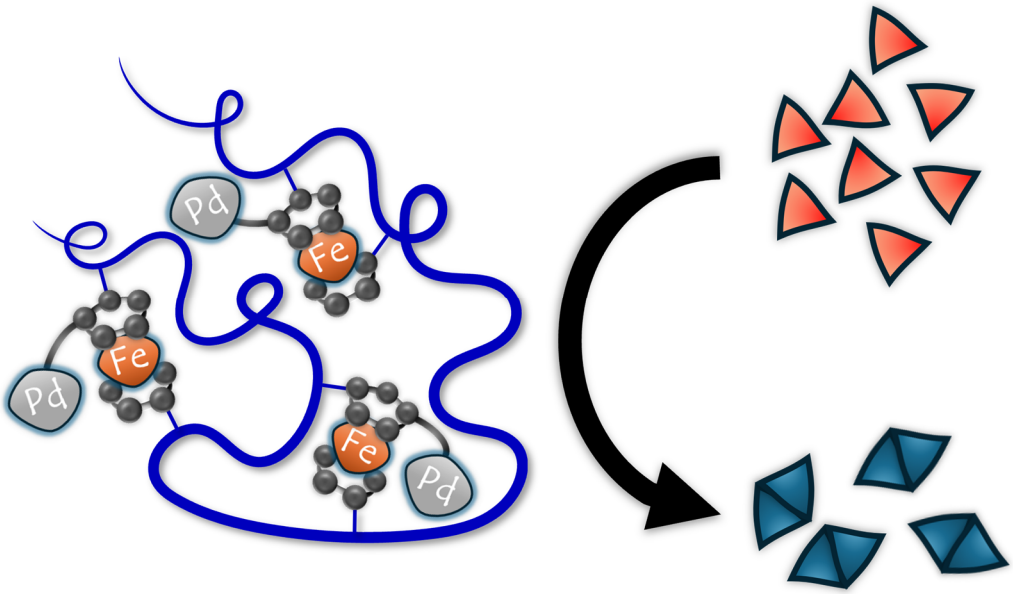

Figure 4.30 Graphical abstract of the chapter "Ferrocene-Driven Single-Chain Polymer Compaction".

Abstract

For the first time, ferrocene was introduced as a covalent crosslinker for single-chain nanoparticle synthesis. In detail, 1,1'-dilithioferrocene was employed to induce the single-chain collapse of a poly(styrene-*co*-4-chloromethyl styrene) copolymer and the successful intramolecular folding evidenced by ^{1}H nuclear magnetic resonance spectroscopy, size-exclusion chromatography, dynamic light scattering and diffusion-ordered spectroscopy. Supplementing the ferrocene crosslinker with the bidentate nitrogen donor ligand 1,10-phenanthroline by employing the ferrocene derivative 2-ferrocenyl-1,10-phenathroline as single-chain crosslinker enabled the installation of a Pd(II) catalytic site, resulting in the first heterobimetallic ferrocene-palladium single-chain nanoparticle. Critically, the latter was successfully employed for the catalytic intramolecular hydroamination of the aminoalkyne 2,2-diphenyl-4-heptyn-1-amine.

Table 4.6 Statement of contributions of coauthors of the publication "Ferrocene-driven single-chain polymer compaction" (*Chem. Commun.* **2023**, *59*, 4672-4675).

Contributor	**Statement of contribution**
Sebastian Gillhuber	Conceptualization, Methodology, Formal analysis, Investigation, Writing – Original Draft, Review & Editing, Visualization, Project administration
Joshua O. Holloway	Conceptualization, Writing – Review & Editing, Supervision, Project administration
Hendrik Frisch	Conceptualization, Writing – Review & Editing, Supervision, Project administration
Florian Feist	Investigation (Supporting), Writing – Review & Editing
Florian Weigend	Conceptualization, Writing – Review & Editing, Supervision (Quantum Chemistry)
Christopher Barner-Kowollik	Conceptualization, Writing – Review & Editing, Supervision, Project administration, Funding acquisition
Peter W. Roesky	Conceptualization, Writing – Review & Editing, Supervision, Project administration, Funding acquisition

Parts of this chapter have been reproduced from the Confirmation of Candidature document of the author as well as the published literature.[7]

4.3.1 Introduction

Since its discovery in 1951, the cyclopentadienyl compound ferrocene has attracted significant interest and constituted a milestone in the area of organometallic chemistry.[226] Its outstanding stability combined with solubility in many common organic solvents enables a plethora of functionalization reactions on the cyclopentadienyl (Cp) rings. Besides the modification of one Cp ring, symmetrical or unsymmetrical difunctionalization of both Cp rings is possible, and even higher functionalized ferrocenes are synthetically accessible, opening opportunities for a variety of subsequent reactions.[226-228]

In principle, two ways of incorporating ferrocene into polymers are conceivable, specifically, the polymerization of ferrocene-containing monomers or a post-polymerization modification approach introducing ferrocene moieties after polymer synthesis.[229] Early studies focused on the free radical homopolymerization and copolymerization of vinylferrocene.[229-232] However, only low molecular weight polymers with broad molecular weight distributions could be obtained due to pronounced termination and chain transfer reactions resulting from electron transfer from the ferrocene moieties to chain radicals.[233] To address this drawback, a large variety of ferrocene monomers featuring spacers between ferrocene and the polymerizable functionality have been synthesized over the last decades. Early examples include ferrocenylmethyl acrylate and ferrocenylmethyl methacrylate[234] or 2-ferrocenylethyl acrylate and 2-ferrocenylethyl methacrylate.[235] Besides free radical polymerizations, alternative polymerization techniques including living ionic polymerization,[236-239] ring-opening metathesis polymerization,[240] acyclic diene metathesis polymerization[241] or reversible deactivation radical polymerization[242-248] have been employed for the polymerization of ferrocene-based monomers. On the other hand, the large variety of existing ferrocene derivatives paves the way for anchoring ferrocene moieties to a polymer backbone subsequent to polymerization. For instance, Merchant and Meredith *et al.* incorporated ferrocene units into a polymer by reacting linear poly(ethyleneimine) with haloalkylferrocenes in a nucleophilic substitution reaction.[249] Complementary to this, Jäkle and coworkers achieved ferrocene incorporation by the reaction of electrophilic polymers with organometallic ferrocene derivatives.[250-251]

Once attached to a polymer backbone, the ferrocene units impart their reversible redox properties, attributed to the stability and ease of access of the oxidation states +II and +III of the central iron ion, onto the polymer, enabling applications in reversible redox reactions.

Oxidation and reduction can be achieved by chemical oxidizing and reducing agents, respectively, or even electrochemically. For poly(vinylferrocene) and some of its derivatives, cyclovoltammetric studies have indicated that the electrochemical behavior of polymer-bound ferrocenes is similar to that observed in their monomeric counterparts.[231] Further, Robinson and Lawrence have investigated the electrochemical stability of poly(vinylferrocene)-based copolymers and found a critical dependence on the copolymer composition.[232] In recent years, a vast variety of ferrocene-containing, redox-responsive polymers was studied, ranging from stimuli-responsive hydrogels[252-254] over surface-anchored polymers[243] to polymeric micelles and nanoparticles.[244,255-256] Recently, Schubert and coworkers also demonstrated the applicability of 2-ferrocenylethyl methacrylate-based polymers in redox flow batteries, thereby opening up a new application field of ferrocene-functionalized polymers.[257]

In the realm of SCNP chemistry, only three examples of ferrocene-containing nanoparticles were reported in the literature so far. In 2000, Rotello and coworkers used 6-ferrocenyluracil as an electroactive guest to induce hydrogen bond-based SCNP folding. In cyclovoltammetric studies, they demonstrated that encapsulation of the ferrocene derivative into a polymer prevents the aggregation and concomitant precipitation of oxidized ferrocenium species, thus making the redox process almost completely reversible.[139] The redox properties of ferrocene have also been successfully employed to realize reversible, voltage-responsive SCNP folding and unfolding. Specifically, the ability of β-cyclodextrin (β-CD) to form stable inclusion complexes with uncharged ferrocene, whereas charged ferrocenium is repelled from the β-CD core, was exploited to induce single-chain collapse with a 1,8-diamino-3,6-dioxaoctane-bridged bis(ferrocene) crosslinker, which can be reversed by an external voltage stimulus.[138] Furthermore, β-CD´s ability to form inclusion complexes with ferrocene was exploited by Wang *et al.* to reverse single-chain folding. For that, a copolymer of poly(ethylene glycol) methyl ether acrylate and 2-(ferrocenecarboxylate ethyl) methacrylate was synthesized. In dilute aqueous solution, hydrophobic interactions of the ferrocene-containing part of the polymer led to the formation of single-chain micelles. When β-CD was added, the ferrocene moieties were complexed which in turn unfolded the micelles.[140]

However, all the outlined examples of ferrocene-containing SCNPs are based on non-covalent folding approaches, limiting the stability of the resulting nanoparticles. This chapter addresses a critical gap in the literature by introducing ferrocene as a covalently bonded SCNP

crosslinker. Critically, employing a donor ligand-functionalized ferrocene derivative provided access to the first heterobimetallic ferrocene-palladium SCNP, the catalytic activity of which is examined.

4.3.2 Covalently Crosslinked Ferrocene Single-Chain Nanoparticles

As the direct polymerization of ferrocene-containing monomers is challenging, typically leading to polymers featuring low molar masses, high dispersity and often poor solubility properties (refer to Chapter 4.3.1), the ferrocene moieties were not envisaged as pendant groups of the polymer main chain but as SCNP folding units instead. Therefore, a post-polymerization modification approach was targeted for covalently anchoring ferrocene functionalities to SCNPs. In detail, a copolymer of styrene and 4-chloromethyl styrene (Polymer **P4**) was synthesized by NMP (refer to **Scheme 4.8**). Given the statistical nature of this copolymerization process, all SCNP folding reactions reported in this chapter follow the repeat unit approach (refer to Chapter 2.1).[42] While styrene constituted the inert polymer backbone, the chlorobenzyl groups of the 4-chloromethyl styrene moieties enabled simple and efficient post-polymerization modification by nucleophilic substitution. SEC measurements in DMAc gave an indication of the number-averaged molar mass of M_n = 16300 g·mol^{-1} and dispersity of $Đ$ = 1.15.

The ^{1}H NMR spectrum of **P4** acquired in THF-d_8 is depicted in **Figure 4.31**. The resonances at δ = 2.37-1.22 ppm correspond to the aliphatic polymer backbone, the resonance at δ = 4.68-4.38 ppm to the benzylic protons of the 4-chloromethyl styrene moieties and the resonances at δ = 7.40-6.26 ppm to the aromatic ring protons, respectively.

Relative integration of the resonances associated with the benzylic and aromatic protons allowed for the determination of the copolymer composition. The relative amount of

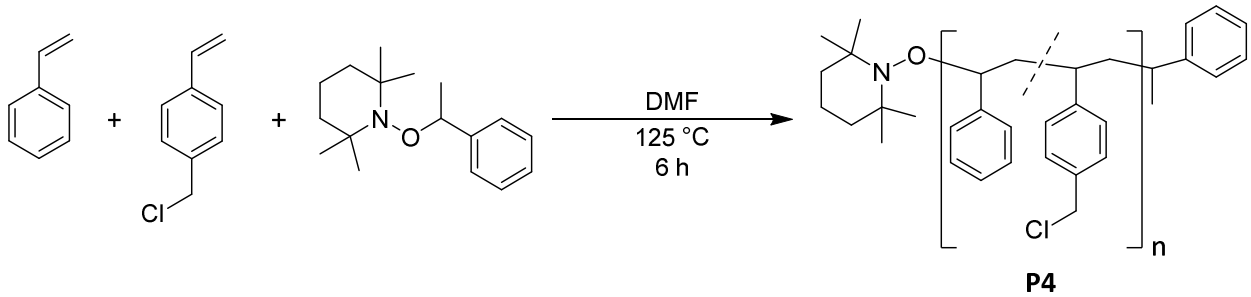

P4

Scheme 4.8 Synthesis of poly(styrene-*co*-4-chloromethyl styrene) (Polymer **P4**) by nitroxide-mediated polymerization.

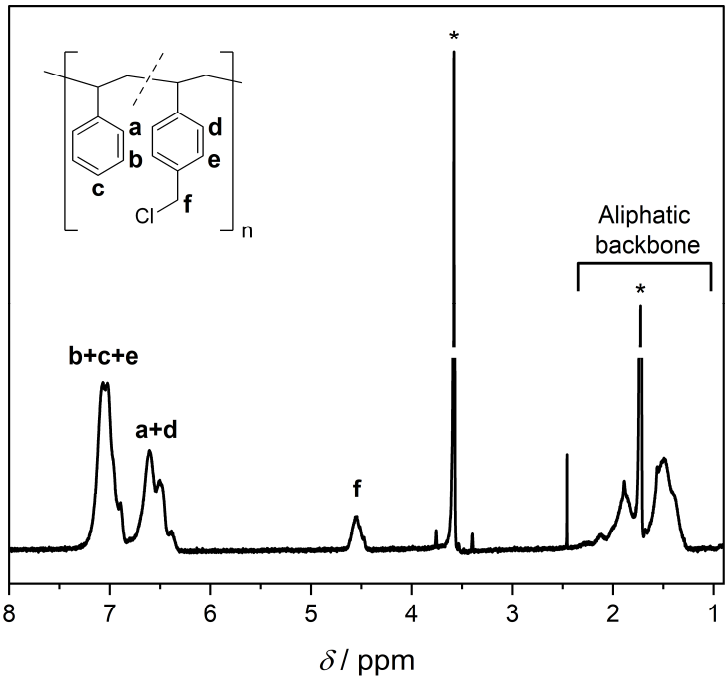

Figure 4.31 ^{1}H NMR spectrum (400 MHz, THF-d_8, 298 K) of polymer **P4**. Asterisks denote residual solvent resonances.

4-chloromethyl styrene moieties incorporated into polymer **P4** can be estimated according to the following expression:

$$\frac{N_{\mathrm{CMS}}}{N_{\mathrm{Styrene}} + N_{\mathrm{CMS}}} = \frac{5}{1 + 2\dfrac{Int(\mathrm{a+b+c+d+e})}{Int(\mathrm{f})}}$$

Herein, N_{CMS} and N_{Styrene} are the average number of 4-chloromethyl styrene and styrene monomers, respectively, incorporated in a macromolecular chain of **P4**, *Int*(a+b+c+d+e) is the integral value obtained by the integration of the resonances at δ = 7.40-6.26 ppm relative to the value of the integral *Int*(f), obtained by the integration of the resonance at δ = 4.68-4.38 ppm. Integration of the corresponding resonances yielded a ratio of *Int*(a+b+c+d+e)/*Int*(f) of 16.7, equivalent to an incorporation ratio of 14 % functional monomers per macromolecular chain.

To achieve single-chain folding of the open chain precursor polymer **P4** with covalently bound ferrocene as a crosslinker, a ferrocene derivative featuring at least two nucleophilic reactive sites was necessary. The most simple and well-established bifunctional, nucleophilic ferrocene derivative is 1,1'-dilithioferrocene, which was therefore prepared *in situ* and a solution of polymer **P4** slowly added to obtain the ferrocene-folded **SCNP4-Fc** (refer to **Scheme 4.9**). ^{1}H NMR spectroscopy indicated the quantitative consumption of the 4-chloromethyl styrene

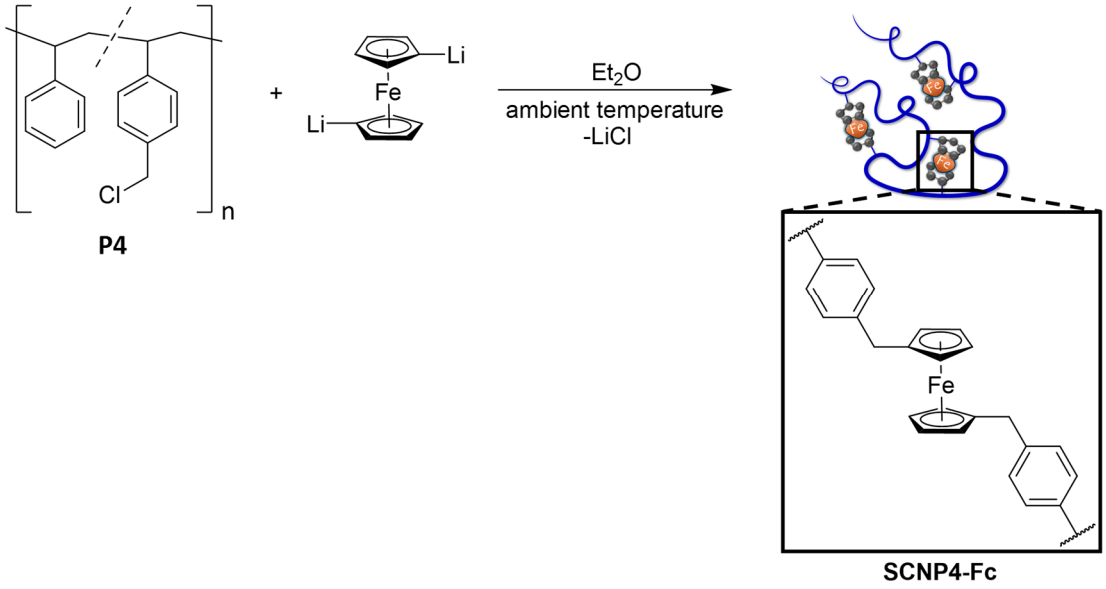

Scheme 4.9 Synthesis of the ferrocene-folded **SCNP4-Fc** by the reaction of **P4** with *in situ* prepared 1,1'-dilithioferrocene.

functionalities upon reaction with 1,1'-dilithioferrocene by the disappearance of the resonance associated with the benzylic protons of **P4** (refer to **Figure 4.32**). All resonances of **SCNP4-Fc** are broadened compared to the corresponding ones of **P4**, indicative of a decrease in relaxation time caused by reduced chain-segment mobility upon single-chain collapse.[20,75]

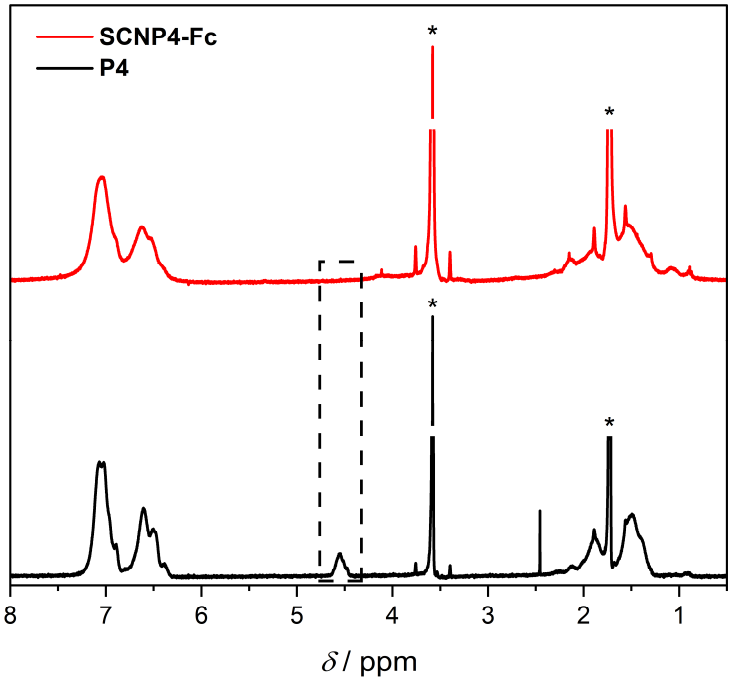

Figure 4.32 Stacked ^{1}H NMR spectra (400 MHz, THF-d_8, 298 K) of polymer **P4** (black) and **SCNP4-Fc** (red). The dashed box highlights the disappearance of the resonance associated with the benzylic protons of the 4-chloromethyl styrene moieties of **P4** upon the SCNP folding reaction. Asterisks denote residual solvent resonances.

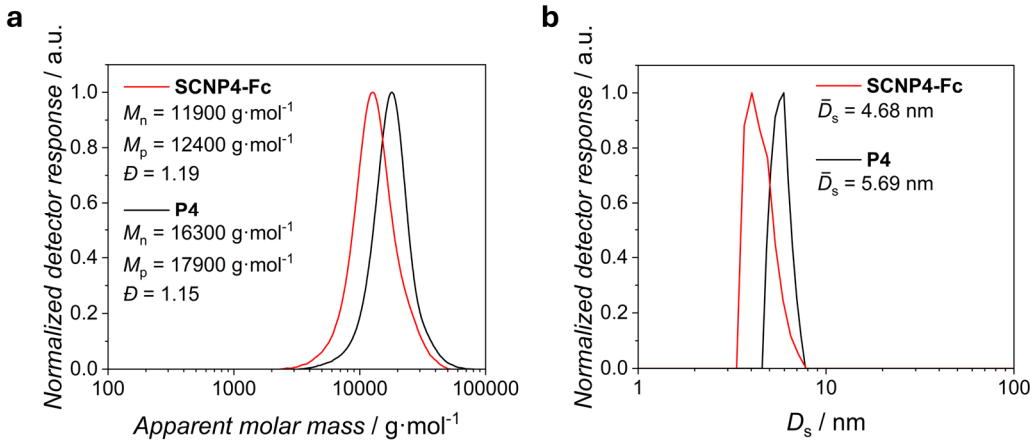

Figure 4.33 Superimposed **(a)** SEC chromatograms (DMAc, RI, PS cal.) and **(b)** number-weighted DLS size distributions (THF, mean diameter by number, average values derived from five measurements) of polymer **P4** (black) and **SCNP4-Fc** (red).

The intramolecular nature of the crosslinking was evident from size-sensitive analytical data. SEC in DMAc showed a shift of the entire molar mass distribution towards lower apparent molar masses upon reaction of **P4** with 1,1'-dilithioferrocene (refer to **Figure 4.33a**). The apparent number-averaged and peak molar masses decreased from M_n = 16300 g·mol^{-1} and

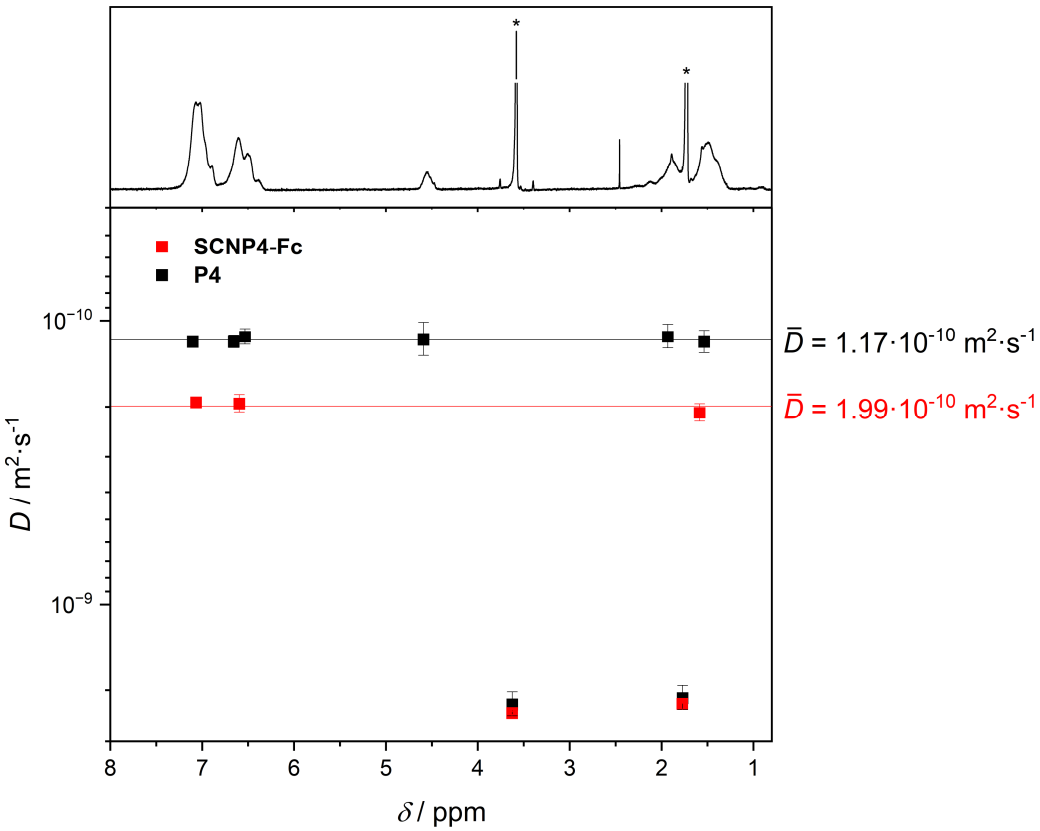

Figure 4.34 Superimposed ^{1}H DOSY NMR spectra (400 MHz, THF-d_8, 298 K) of polymer **P4** (black) and **SCNP4-Fc** (red). Spectral trace on top refers to **P4**. Error bars refer to data fitting error. Horizontal lines indicate average diffusion coefficients. Asterisks denote residual solvent resonances.

M_p = 17900 g·mol^{-1} for **P4** to M_n = 11900 g·mol^{-1} and M_p = 12400 g·mol^{-1} for **SCNP4-Fc**, accompanied by a slight increase of the dispersity from $Đ$ = 1.15 for **P4** to $Đ$ = 1.19 for **SCNP4-Fc**. Successful single-chain folding was corroborated by DLS in THF, showing a decrease of the solvodynamic diameter from D_s = 5.69 nm for **P4** to D_s = 4.68 nm for **SCNP4-Fc** (refer to **Figure 4.33b**). In line with these findings, ^{1}H DOSY NMR in THF-d_8 revealed an increase of the average diffusion coefficient from $D = 1.17 \cdot 10^{-10}$ m^2·s^{-1} for **P4** to $D = 1.99 \cdot 10^{-10}$ m^2·s^{-1} for **SCNP4-Fc** (refer to **Figure 4.34**).

It is noted in passing that after addition of the oxidizing agent 2,3-dichloro-5,6-dicyano-1,4-benzoquinone to a solution of **SCNP4-Fc** in diethyl ether the precipitation of a dark solid, presumably resulting from the reduced solubility of the cationic macromolecules in the low polarity solvent after oxidation of the incorporated ferrocene functionalities, was observed which could be redissolved upon addition of the reductant hydrazine. These observations suggest that ferrocene imparted its reversible redox properties to **SCNP4-Fc**, making the latter an interesting candidate for future applications of redox-switchable SCNPs.

4.3.3 Donor Ligand-Functionalized Ferrocene Single-Chain Nanoparticles

To complement the ferrocene-folded SCNPs with additional functionalities for future applications, for instance in redox-switchable catalysis, the incorporation of a second metal is highly desirable. In principle, two approaches seem conceivable to achieve this aim. On the one hand, the synthesis of a terpolymer containing one comonomer for folding and another one for metal complexation is possible. On the other hand, SCNP folding and the introduction of a functional group for metal complexation can be combined in an elegant all-in-one approach when a donor-functionalized ferrocene derivative is employed for intramolecular crosslinking. A promising candidate for the latter approach is 2-ferrocenyl-1,10-phenanthroline, fusing the stable ferrocene sandwich backbone with the bidentate nitrogen donor ligand 1,10-phenanthroline.

Thus, in analogy to the synthesis of **SCNP4-Fc**, 2-ferrocenyl-1,10-phenanthroline was lithiated *in situ* and reacted with **P4** to form **SCNP4-FcPhen** (refer to **Scheme 4.10**). However, the lithiation process of 2-ferrocenyl-1,10-phenanthroline is significantly more complex than that of ferrocene itself and discussed in detail below.

Again, ^{1}H NMR spectroscopy indicated the quantitative consumption of the 4-chloromethyl styrene moieties by disappearance of the resonance of the benzylic protons of **P4** at

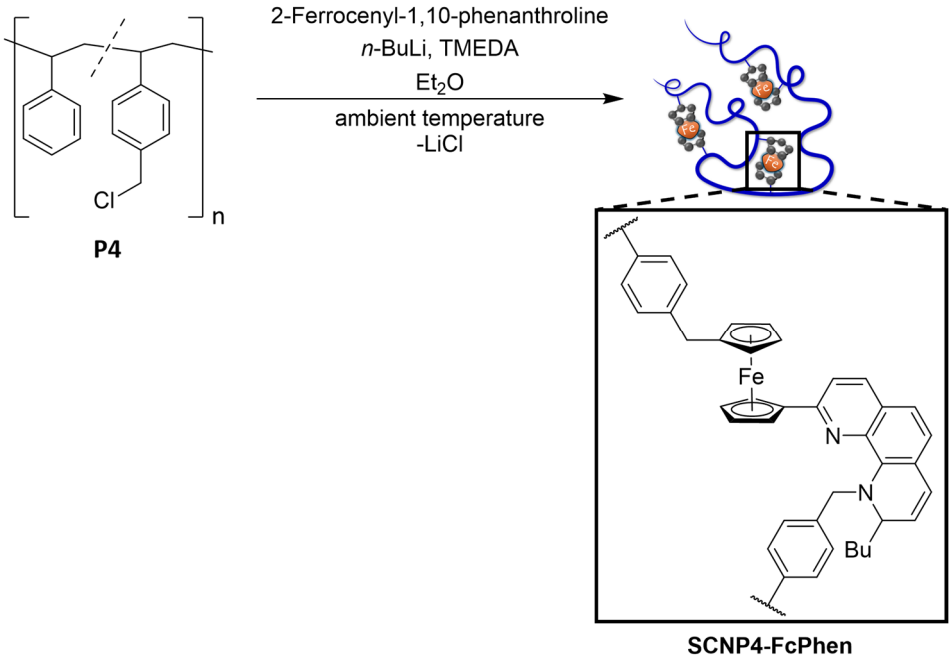

Scheme 4.10 Synthesis of **SCNP4-FcPhen** by the reaction of **P4** with *in situ* lithiated 2-ferrocenyl-1,10-phenanthroline. The depiction of the folding unit is based on density functional theory calculations (refer to the main text for details).

δ = 4.68-4.38 ppm. Additionally, the presence of low molecular weight impurities was evident from the ^{1}H NMR spectrum (refer to **Figure 4.35a**). The resonances belong to yet unidentified species, most probably resulting from the complex reaction of 2-ferrocenyl-1,10-phenanthroline with *n*-butyllithium and subsequent protonation during the workup of

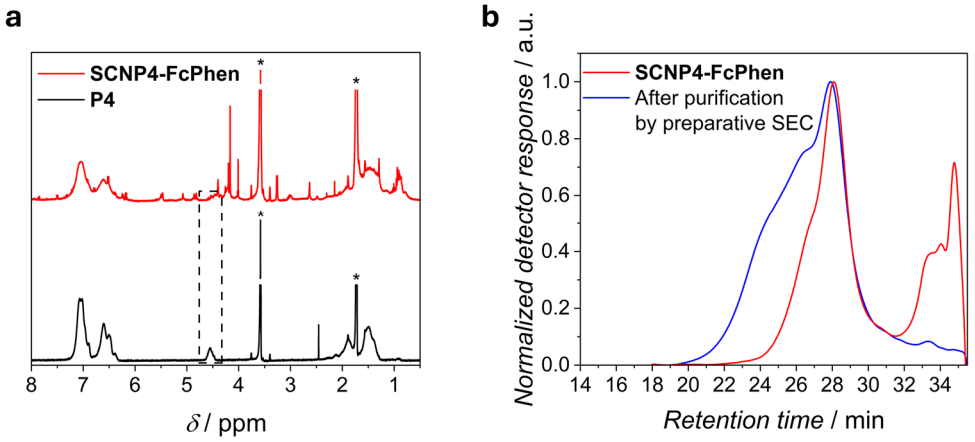

Figure 4.35 (a) Stacked ^{1}H NMR spectra (400 MHz, THF-d_8, 298 K) of polymer **P4** (black) and **SCNP4-FcPhen** (red). The dashed box highlights the disappearance of the resonance associated with the benzylic protons of the 4-chloromethyl styrene moieties of **P4** upon the SCNP folding reaction. Asterisks denote residual solvent resonances. **(b)** Superimposed SEC chromatograms (DMAc, RI) of **SCNP4-FcPhen** (red) and the product obtained after purification by preparative SEC (blue). Note that the blue curve is only representative of the soluble fraction of the sample obtained after purification.

SCNP4-FcPhen. The presence of these low molecular weight impurities was also evident from SEC analysis, revealing an intense peak at late elution times. However, these impurities proved to be critical to the stability of **SCNP4-FcPhen**. Purification by preparative SEC led to interchain crosslinking (refer to **Figure 4.35b**), accompanied by a drastically decreased solubility. Presumably, the observed interchain aggregation is the result of strong π-π interactions between the modified phenanthroline subunits of different macromolecular chains which seem to be suppressed by the presence of the 2-ferrocenyl-1,10-phenanthroline-derived low molecular weight impurities.

Despite the presence of these impurities, size-sensitive characterization of **SCNP4-FcPhen** by SEC, DLS and DOSY proved to be possible. SEC in DMAc indicated a shift of the peak of the molar mass distribution towards lower apparent molar masses, indicative of successful SCNP folding. Additionally, a shoulder in the SEC chromatogram towards high apparent molar masses is present. The latter could result from a small fraction of intermolecularly crosslinked macromolecular chains or from incomplete SCNP folding when the lithiated 2-ferrocenyl-1,10-phenanthroline only reacted on one of the reactive lithiated sites instead of at least two as would be required for chain compaction. In detail, the apparent number-averaged and peak molar masses decreased from M_n = 16300 g·mol^{-1} and M_p = 17900 g·mol^{-1} for **P4** to M_n = 14800 g·mol^{-1} and M_p = 14200 g·mol^{-1} for **SCNP4-FcPhen**, with a concomitant increase in dispersity from $Đ$ = 1.15 for **P4** to $Đ$ = 1.27 for **SCNP4-FcPhen** (refer to **Figure 4.36a**). DLS measurements in THF corroborated the SEC results, showing a decrease of the number-

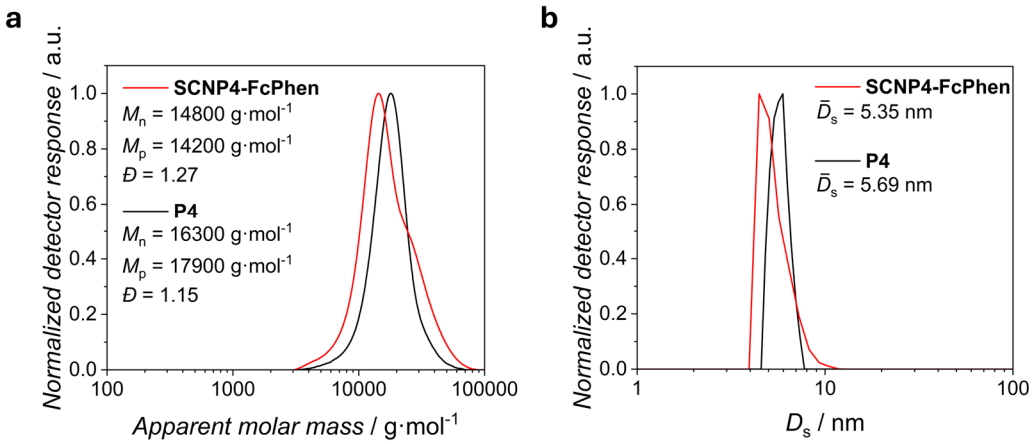

Figure 4.36 Superimposed **(a)** SEC chromatograms (DMAc, RI, PS cal.) and **(b)** number-weighted DLS size distributions (THF, mean diameter by number, average values derived from five measurements) of polymer **P4** (black) and **SCNP4-FcPhen** (red).

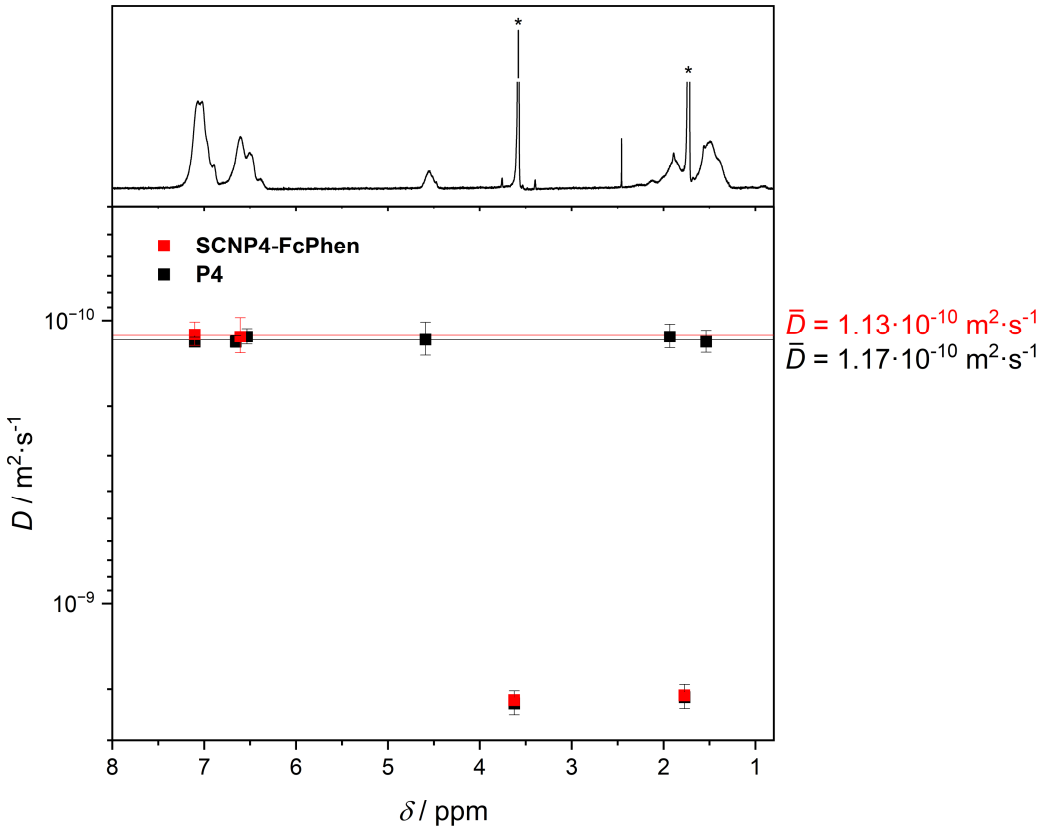

Figure 4.37 Superimposed ^{1}H DOSY NMR spectra (400 MHz, THF-d_8, 298 K) of polymer **P4** (black) and **SCNP4-FcPhen** (red). Spectral trace on top refers to **P4**. Error bars refer to data fitting error. Horizontal lines indicate average diffusion coefficients. Asterisks denote residual solvent resonances.

averaged solvodynamic diameter from D_s = 5.69 nm for **P4** to D_s = 5.35 nm for **SCNP4-FcPhen** (refer to **Figure 4.36b**). Owing to the low scattering abilities of small molecules, the low molecular weight impurities are expected to not negatively interfere with DLS measurements. ^{1}H DOSY NMR in THF-d_8 (refer to **Figure 4.37**) resulted in an average diffusion coefficient of D = 1.13·10^{-10} m^2·s^{-1} for **SCNP4-FcPhen**, similar to that of **P4** (D = 1.17·10^{-10} m^2·s^{-1}). The fact that no increase of the average diffusion coefficient associated with the polymeric resonances in the ^{1}H NMR spectrum of **SCNP4-FcPhen** was observed relative to **P4**, despite the indication of successful SCNP folding by SEC and DLS, can most probably be attributed to signal overlap of the SCNP resonances with the ones of higher molar mass species, the presence of which is indicated by the shoulder in the SEC chromatogram. Overlap of positive signals of two species with different diffusion coefficients is known to result in a compromise diffusion coefficient intermediate between the ones of the individual molecules when a monoexponential fitting procedure is employed.[258] The fact that the determined diffusion coefficient of **SCNP4-FcPhen** is almost identical to that of **P4** is consequently most probably a coincidence and not an indication of the absence of successful single-chain folding.

To obtain an in-depth understanding of the chemical structure of the crosslinking functionality within **SCNP4-FcPhen**, the initial lithiation process was investigated in more detail. The synthesis of **SCNP4-FcPhen** involves the *in situ* lithiation of 2-ferrocenyl-1,10-phenanthroline before the addition of polymer **P4** (refer to **Scheme 4.10**). When only the Cp rings of 2-ferrocenyl-1,10-phenanthroline are considered and stereochemistry is not taken into account, lithiation can occur on three chemically distinct positions when a free rotation of the Cp rings around the pseudo-C_5 axis and of the phenanthroline functionality around its bond to the ferrocene unit is assumed. Furthermore, it is known from the literature, that 1,10-phenanthroline can undergo nucleophilic attack by *n*-butyllithium in the 2-position, leading to accumulation of electron density on the neighboring nitrogen atom, imparting an increased nucleophilic character to the latter.[259-261] For instance, the reaction of 1,10-phenanthroline, *n*-butyllithium and benzyl bromide, resulting in 2-butyl-1,2-dihydro-1-(phenylmethyl)-1,10-phenanthroline, is reported in the literature.[261] Similarly, the reaction of 6-ferrocenyl-2,2'-bipyridine with *n*-butyllithium was reported to yield 6-ferrocenyl-6'-*n*-butyl-2,2'-bipyridine as well as an unidentified dibutylated derivative of 6-ferrocenyl-2,2'-bipyridine.[262]

It thus seems plausible, that analogous reactions take place when 2-ferrocenyl-1,10-

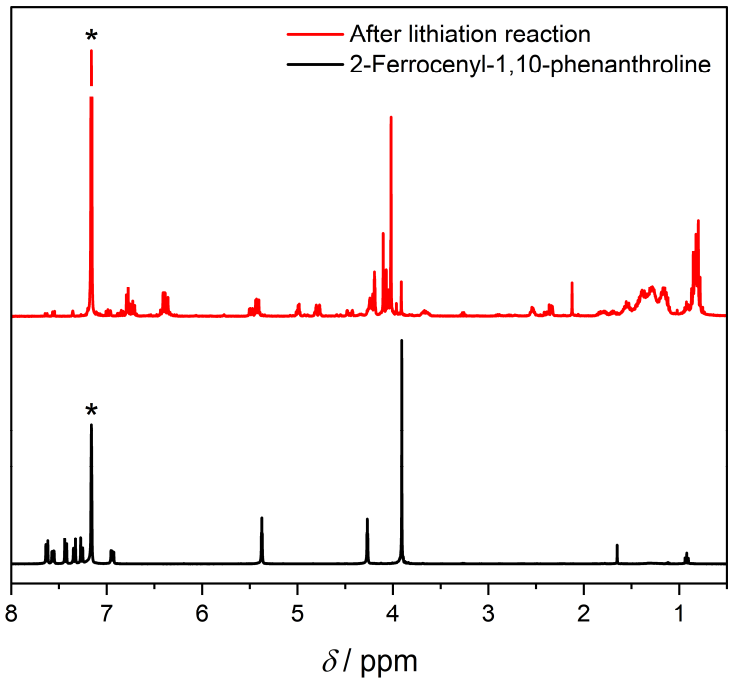

Figure 4.38 Stacked ^{1}H NMR spectra (400 MHz, C_6D_6, 298 K) of 2-ferrocenyl-1,10-phenanthroline (black) and the product mixture obtained after the reaction of 2-ferrocenyl-1,10-phenanthroline with *n*-butyllithium in the presence of *N,N,N',N'*-tetramethyl ethylenediamine in diethyl ether and quenching with D_2O (red). Asterisks denote residual solvent resonances.

phenanthroline is reacted with *n*-butyllithium. Based on the literature outlined above, it is expected that the lithium salt of 2-ferrocenyl-9,10-dihydro-9-*n*-butyl-1,10-phenanthroline is initially formed. Without further lithiation, the lithiated nitrogen atom of this species can act as a nucleophile and react with the chlorobenzyl functionalities of **P4** upon its addition. However, this does not result in single-chain compaction and is one potential reason for the shoulder towards high apparent molar masses present in the SEC chromatogram of **SCNP4-FcPhen** (refer to **Figure 4.36a**). To achieve single-chain folding, a second lithiation is necessary, which can take place either on the Cp rings of the ferrocene moiety or result from a second butylation step.

Experimentally, the potential functionalization of 2-ferrocenyl-1,10-phenanthroline with butyl groups was probed by reacting the latter with *n*-butyllithium in analogy to the synthetic procedure towards **SCNP4-FcPhen**. However, instead of adding **P4**, the reaction mixture was quenched with D_2O.

The ^1H NMR spectrum of the product obtained after evaporation of the solvent together with that of 2-ferrocenyl-1,10-phenanthroline is shown in **Figure 4.38**. The reaction mixture featured new resonances at δ = 1.88-0.60 ppm, going in line with the presence of butyl groups. Additionally, an upfield shift of the resonances associated with the former phenanthroline

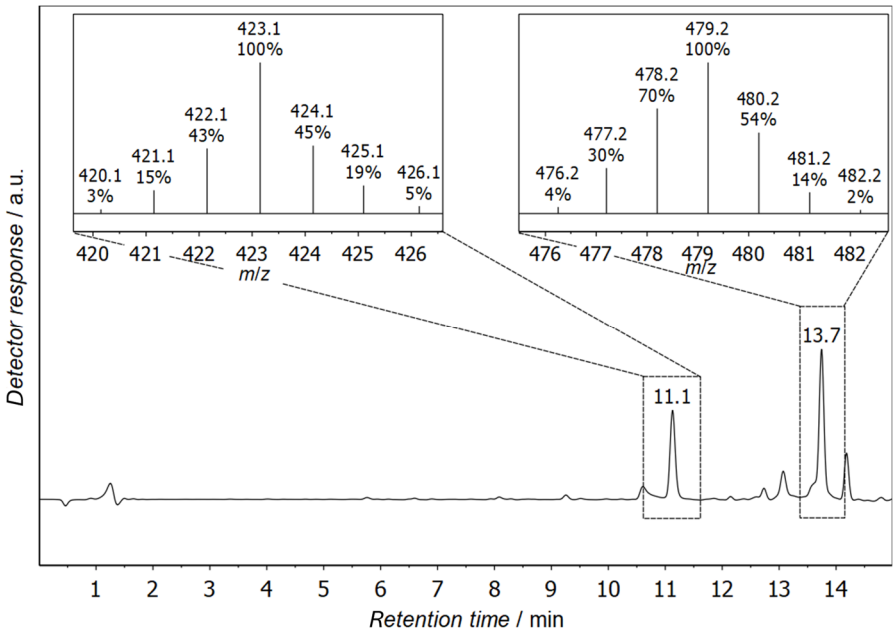

Figure 4.39 Liquid chromatography chromatogram (254 nm detector response) of the product mixture obtained after the reaction of 2-ferrocenyl-1,10-phenanthroline with *n*-butyllithium in the presence of *N,N,N',N'*-tetramethyl ethylenediamine in diethyl ether and quenching with D_2O. Inserts show the base peak region of the accumulated mass spectra (positive mode) of the corresponding peaks.

moiety is evident compared to the starting material, indicating a partial dearomatization of the phenanthroline rings. Resonances in the region δ = 4.34-3.82 ppm can be assigned to protons of ferrocene units. However, due to resonance overlap, a definite interpretation of the NMR spectrum was not feasible and additional ^{2}H NMR measurements provided no further insights.

The liquid chromatography chromatogram (refer to **Figure 4.39**) unambiguously evidenced the formation of different products throughout the reaction. The mass spectra corresponding to the most intense peaks, at 11.1 and 13.7 minutes elution time, are depicted as inserts in **Figure 4.39** and corroborate the NMR results. With base peak *m/z* values of 423.1 (11.1 minutes) and 479.2 (13.7 minutes), the formation of monobutylated and dibutylated derivatives of 2-ferrocenyl-1,10-phenanthroline is evident. The isotopic pattern is reminiscent of that of iron (natural abundance: ^{54}Fe 6 %, ^{56}Fe 92 %, ^{57}Fe 2 %, ^{58}Fe 0.3 %). However, due to peak overlap of different species, the natural abundance ratio is not completely resembled.

These experimental results indicate that the lithiation reaction of 2-ferrocenyl-1,10-phenanthroline yielded differently substituted derivatives of the starting material. However, the pronounced overlap of resonances in the NMR spectrum preclude an unambiguous determination of the location of the incorporated butyl groups as well as the positions of lithiation. Thus, density functional theory (DFT) calculations at the PBE0/dhf-TZVP/D4 level were performed to deduce further information regarding the structure of the folding unit of **SCNP4-FcPhen** (refer to Chapter 6.3.3.6 for computational details).

At first, the positions most prone to nucleophilic attack by *n*-butyllithium were determined. In general, the regioselectivity of nucleophilic attack is influenced by steric considerations, the nature of the frontier molecular orbitals and the charge distributions within the attacked and attacking molecule. The lowest uncopied molecular orbital (LUMO) of 2-ferrocenyl-1,10-phenanthroline is delocalized over the phenanthroline π system. However, the only sterically accessible atom combining a large contribution to the LUMO with a positive natural population analysis[263] (NPA) charge is C-9 within the 1,10-phenanthroline subunit (refer to **Figure 4.40a**). Thus, the initial nucleophilic attack by *n*-butyllithium is most likely to occur on this carbon atom, yielding the lithium salt of 2-ferrocenyl-9,10-dihydro-9-*n*-butyl-1,10-phenanthroline, in line with the literature discussed above.

Based on the same line of reasoning, a second nucleophilic attack of *n*-butyllithium is most likely to occur on C-4 of the 1,10-phenanthroline moiety of 2-ferrocenyl-9,10-dihydro-9-*n*-

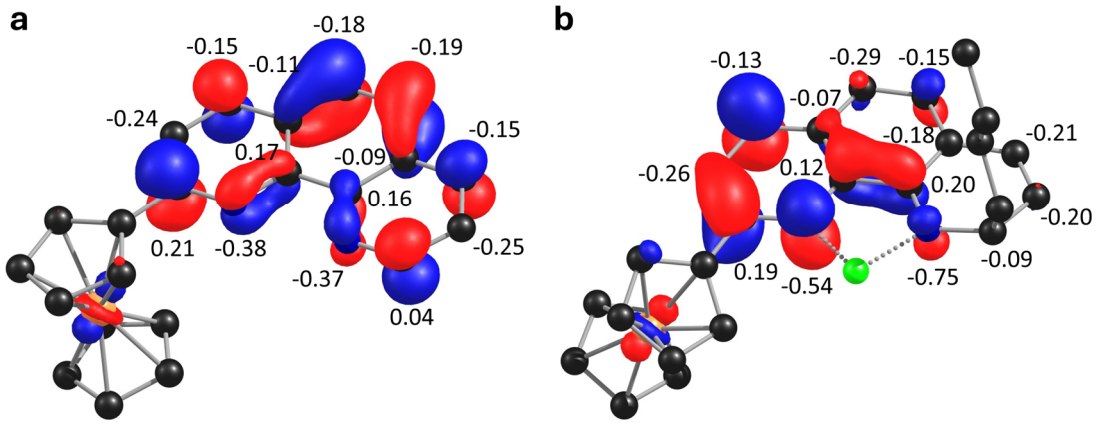

Figure 4.40 LUMOs of **(a)** 2-ferrocenyl-1,10-phenanthroline and **(b)** the lithium salt of 2-ferrocenyl-9,10-dihydro-9-*n*-butyl-1,10-phenanthroline (PBE0/dhf-TZVP/D4). Contours are drawn at 0.05 atomic units. Numbers denote NPA charges of the respective atoms of the phenanthroline subunit. Hydrogen atoms are omitted for clarity. Color code: Lithium green, carbon black, nitrogen blue, iron orange.

butyl-1,10-phenanthroline. Contributions of this carbon atom dominate the LUMO, and out of the sterically accessible carbon atoms, it is the one with the least negative NPA charge (refer to **Figure 4.40b**). Thus, onefold and twofold butylation of 2-ferrocenyl-1,10-phenanthroline is expected to lead to the lithium salts of 2-ferrocenyl-9,10-dihydro-9-*n*-butyl-1,10-phenanthroline and 2-ferrocenyl-1,4,9,10-tetrahydro-4,9-di(*n*-butyl)-1,10-phenanthroline, respectively. Reaction of the latter with the chlorobenzyl functionalities of **P4** would in principle allow for SCNP folding. However, additional quantum chemical calculations indicated that nucleophilic attack of both nitrogen atoms on the polymer would require a significant distortion of the phenanthroline moiety for steric reasons. Instead, it seems more realistic that only one of the nitrogen atoms of 2-ferrocenyl-1,4,9,10-tetrahydro-4,9-di(*n*-butyl)-1,10-phenanthroline reacts with the polymer and the second lithiated site is quenched throughout the workup procedure. This might contribute to the shoulder towards high apparent molar masses in the SEC chromatogram of **SCNP4-FcPhen** (refer to **Figure 4.36a**).

To achieve SCNP folding with the monobutylated derivative of 2-ferrocenyl-1,10-phenanthroline, a second lithiation on one of the Cp rings is required. To shed light on where this second lithiation is most likely to occur, the energies of the three possible chemically distinct dilithiated constitutional isomers were compared (refer to **Figure 4.41**). Taking the long reaction time of the lithiation step into account (refer to Chapter 6.3.3.3 for details), it is reasonable to assume that the reaction mixture reaches a state of thermodynamic equilibrium with the most stable isomer being the dominant species in the reaction solution. Comparing

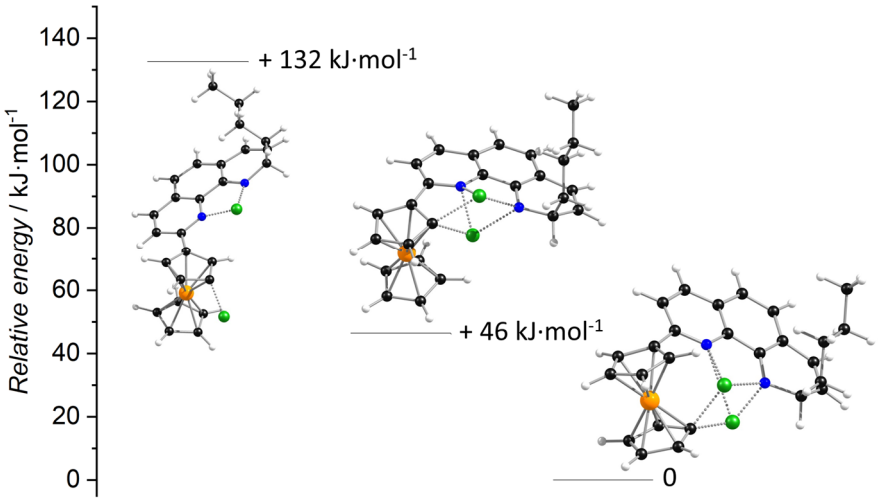

Figure 4.41 Relative energies (PBE0/dhf-TZVP/D4) of the three chemically distinct dilithiated constitutional isomers of 2-ferrocenyl-9,10-dihydro-9-*n*-butyl-1,10-phenanthroline. Color code: Hydrogen white, lithium green, carbon black, nitrogen blue, iron orange.

the relative energies of the different isomers revealed that it is energetically favorable for the second lithiation to occur in close spatial proximity to the nitrogen atoms due to additional coordination of the latter to the lithium ions. Additionally, it is evident that lithiation on the unsubstituted Cp ring is favored over lithiation on the substituted one by about 50 kJ·mol^{-1}.

Analysis of the NPA charges of the lowest energy isomer revealed that the negative charge is mainly centered on N-10, with a NPA charge of -0.83, and the lithiated carbon of the unsubstituted Cp ring, with a NPA charge of -0.67. Inspection of the atomic contributions to the highest occupied molecular orbital (HOMO) showed no relevant participation of the lithiated carbon atom but large contributions of the lithiated nitrogen. Hence, nucleophilic attack will preferably originate from N-10 when **P4** is added to the reaction mixture.

To investigate whether the additional aromatic group present after this initial nucleophilic substitution step could lead to a change of the position of the remaining lithiated site, model complexes with a 4-ethylbenzyl substituent on N-10 were constructed computationally and the relative energies of the two most stable constitutional isomers, with the lithium ion in close spatial proximity to the nitrogen atoms, compared (refer to **Figure 4.42**). Based on this, no changes of the position of lithiation are expected as the constitutional isomer lithiated on the unsubstituted Cp ring remained energetically favored by about 20 kJ·mol^{-1}. It is worth noting that the aromatic moiety contributes to the stabilization of the structures by coordination to the lithium ion. The reaction of the lithiated site remaining after the first

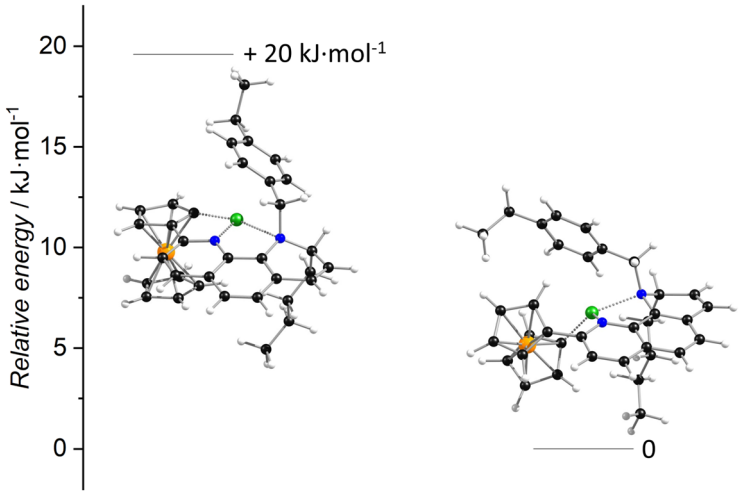

Figure 4.42 Relative energies (PBE0/dhf-TZVP/D4) of the two lowest energy constitutional isomers of lithiated 2-ferrocenyl-9,10-dihydro-9-*n*-butyl-10-(4-ethylbenzyl)-1,10-phenanthroline. Color code: Hydrogen white, lithium green, carbon black, nitrogen blue, iron orange.

reaction with the chloromethyl styrene moieties of **P4** is capable of inducing SCNP compaction.

In summary, these results highlight the complexity of the mixture obtained after the reaction of *n*-butyllithium with 2-ferrocenyl-1,10-phenanthroline as the initial step towards the synthesis of **SCNP4-FcPhen**. According to the experimental results, it is evident that monobutylated and dibutylated derivatives of 2-ferrocenyl-1,10-phenanthroline are the dominant species present in the reaction solution. Based on quantum chemical calculations, the most probable locations of the butyl groups after nucleophilic attack of *n*-butyllithium on 2-ferrocenyl-1,10-phenanthroline were determined to be the carbon atoms C-4 and C-9 of the 1,10-phenanthroline subunit. Steric considerations render SCNP folding due to a reaction of both nitrogen atoms of the lithium salt of the dibutylated 2-ferrocenyl-1,4,9,10-tetrahydro-4,9-di(*n*-butyl)-1,10-phenanthroline with the polymer highly unlikely. For the desired single-chain collapse to form **SCNP4-FcPhen**, it showed to be more plausible that a second lithiation occurs on the unsubstituted Cp ring of the ferrocene moiety after onefold butylation at C-9 of the 1,10-phenanthroline subunit. Single-chain folding is then predominantly achieved by the reaction of dilithiated 2-ferrocenyl-9,10-dihydro-9-*n*-butyl-1,10-phenanthroline on N-10 and one the five chemically equivalent carbon atoms of the unsubstituted Cp ring, leading to the folding unit depicted in **Scheme 4.10**.

4.3.4 Heterobimetallic Ferrocene-Palladium Single-Chain Nanoparticles

Employing the donor ligand-functionalized 2-ferrocenyl-1,10-phenanthroline as single-chain crosslinker enabled the functionalization of the resulting nanoparticles with an additional metal, providing access to unprecedented heterobimetallic ferrocene SCNPs. Focussing on catalytic applications of the ferrocene-folded nanoparticles, a suitable metal is characterized by catalytic activity and the absence of negative interferences with either the polymer backbone or the ferrocene functionalities. A suitable metal species fulfilling these prerequisites is Pd(II). Therefore, **SCNP4-FcPhen** was reacted with dichloro(1,5-cyclooctadiene)palladium(II) in dichloromethane (DCM) in a ligand substitution reaction as depicted in **Scheme 4.11**, resulting in the palladium-functionalized **SCNP4-FcPhen-Pd**.

Contrary to **SCNP4-FcPhen**, **SCNP4-FcPhen-Pd** could be obtained in analytically pure form and there was no evidence of the presence of low molecular weight impurities in the ^{1}H NMR spectrum of **SCNP4-FcPhen-Pd** (refer to **Figure 4.43a**). Palladium functionalization of **SCNP4-FcPhen** was expected to lead to a less compact structure and thus an increased solvodynamic volume, and indeed, SEC in DMAc revealed that the entire molar mass distribution of **SCNP4-FcPhen-Pd** was shifted towards higher apparent molar masses relative to that of

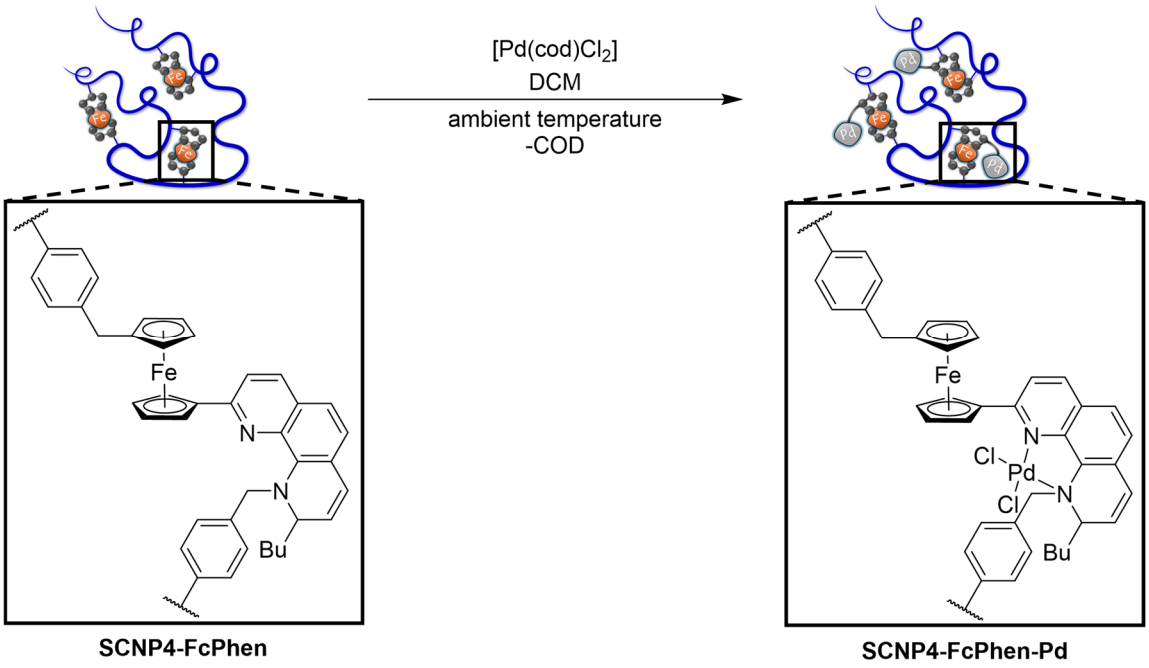

Scheme 4.11 Synthesis of **SCNP4-FcPhen-Pd** by the reaction of **SCNP4-FcPhen** with dichloro(1,5-cyclooctadiene)palladium(II). The depiction of the folding unit is based on density functional theory calculations (refer to Chapter 4.3.3 for details). COD/cod = uncoordinated/coordinated 1,5-cyclooctadiene.

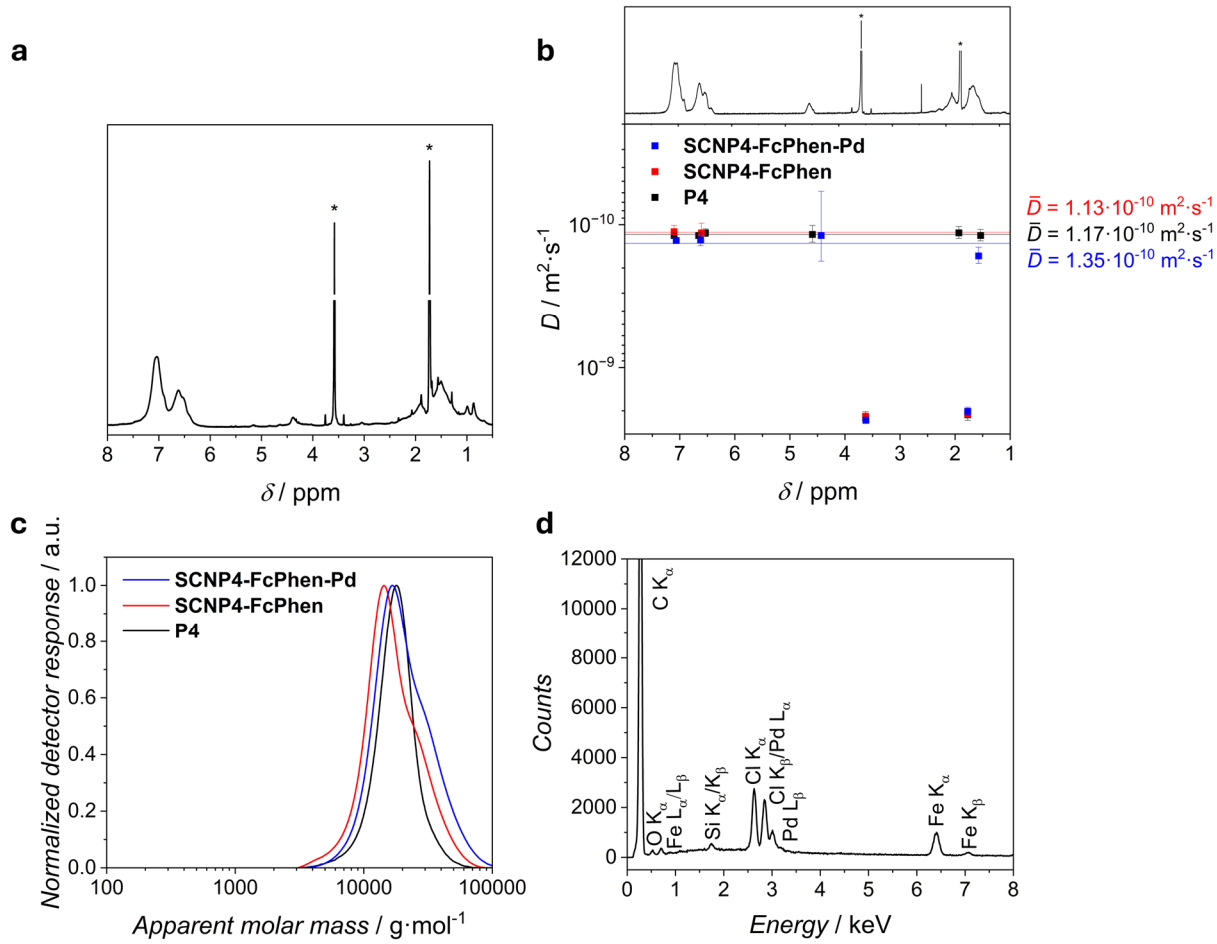

Figure 4.43 Analytical data of **SCNP4-FcPhen-Pd** and comparison to **P4** and **SCNP4-FcPhen**. **(a)** ^{1}H NMR spectrum (400 MHz, THF-d_8, 298 K). **(b)** ^{1}H DOSY NMR spectra (400 MHz, THF-d_8, 298 K). Spectral trace on top refers to **P4**. Error bars refer to data fitting error. Horizontal lines indicate average diffusion coefficients. Asterisks denote residual solvent resonances. **(c)** SEC chromatograms (DMAc, RI, PS cal.). **(d)** EDX spectrum. Peaks are labeled with the symbols of the elements and the transitions they are characteristic of. Additional peaks not corresponding to the polymer sample result from silicon (detector) and oxygen (TEM background).

SCNP4-FcPhen (refer to **Figure 4.43c**). The number-averaged and peak molar masses increased to M_n = 17700 g·mol^{-1} and M_p = 16600 g·mol^{-1}, compared to M_n = 14800 g·mol^{-1} and M_p = 14200 g·mol^{-1} for **SCNP4-FcPhen**, while the dispersity changed slightly from $Đ$ = 1.27 (**SCNP4-FcPhen**) to $Đ$ = 1.29 (**SCNP4-FcPhen-Pd**). The peak of the molar mass distribution was still shifted towards lower apparent molar masses compared to the unfolded precursor polymer **P4** (M_p = 17900 g·mol^{-1}). DLS measurements in THF were conducted, however, only inconclusive data, with deviations larger than the estimated particle size, were obtained. Presumably, this is a consequence of absorption of the red laser light used in the DLS setup by the sample. ^{1}H DOSY NMR measurements in THF-d_8 resulted in diffusion coefficients almost identical to the ones of **P4** and **SCNP4-FcPhen** (refer to **Figure 4.43b**). However, as discussed

in detail for **SCNP4-FcPhen** (refer to Chapter 4.3.3), the determined diffusion coefficients should be considered with caution due to overlap of the SCNP resonances with higher molar mass species, the presence of which is evident from the shoulder towards high apparent molar masses in the SEC chromatogram of **SCNP4-FcPhen-Pd**.

To validate that palladium was indeed present in the purified **SCNP4-FcPhen-Pd**, EDX measurements were conducted and the characteristic L_α and L_β emissions of palladium at 2.83 keV and 2.99 keV, respectively, as well as the chlorine K_α and K_β emissions at 2.62 keV and 2.81 keV, respectively, unambiguously confirmed the successful functionalization of **SCNP4-FcPhen-Pd** with the palladium(II) chloride moiety (refer to **Figure 4.43d**).

Successful palladium functionalization was further corroborated by UV/Vis spectroscopy (refer to **Figure 4.44a**). Similar to **P4** and **SCNP4-FcPhen**, the UV/Vis spectrum of **SCNP4-FcPhen-Pd** features strong absorptions around 250 nm, corresponding to the aromatic polymer backbone.[264] Both, the UV/Vis spectra of **SCNP4-FcPhen** as well as **SCNP4-FcPhen-Pd**, additionally show an absorption peak at λ_{max} = 384 nm with a tailing towards higher wavelengths which is also present in the UV/Vis spectrum of 2-ferrocenyl-1,10-phenanthroline (refer to **Figure 4.44b**) and thus indicative of the incorporation of the latter into the SCNPs. It is to be noted that in the case of **SCNP4-FcPhen** the small molecule

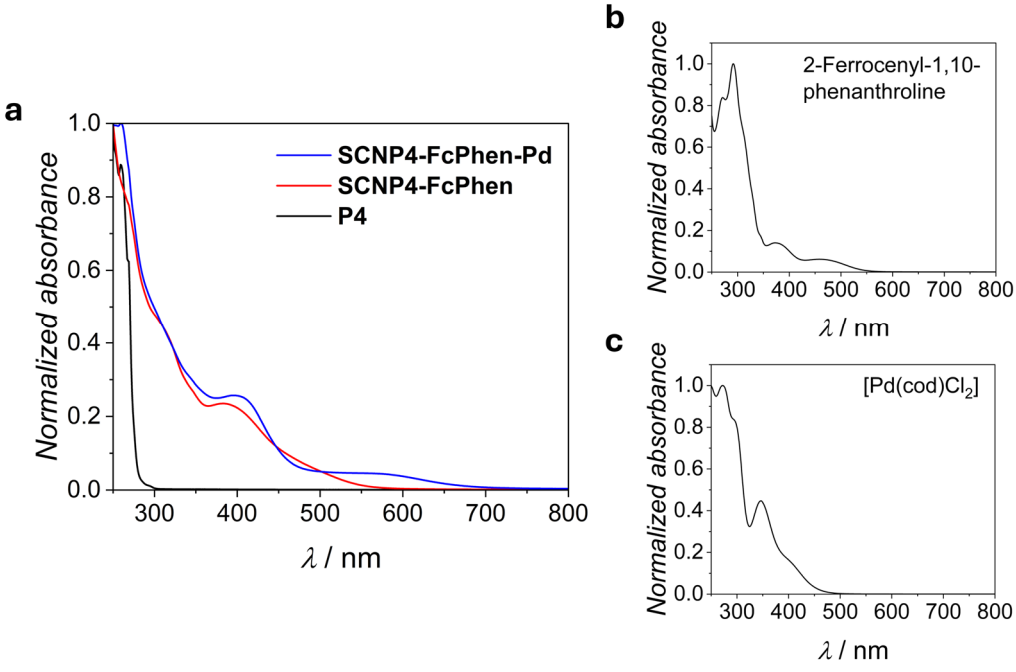

Figure 4.44 UV/Vis spectra (DCM, 298 K) of **(a)** polymer **P4** (black), **SCNP4-FcPhen** (red) and **SCNP4-FcPhen-Pd** (blue), **(b)** 2-ferrocenyl-1,10-phenanthroline and **(c)** dichloro(1,5-cyclooctadiene)palladium(II).

impurities are likely to also contribute to the observed absorption spectrum. Compared to **SCNP4-FcPhen**, a new band at λ_{max} = 568 nm arose in the UV/Vis spectrum of **SCNP4-FcPhen-Pd**, which is neither present in the spectrum of 2-ferrocenyl-1,10-phenanthroline (refer to **Figure 4.44b**) nor in that of dichloro(1,5-cyclooctadiene)palladium(II) (refer to **Figure 4.44c**), hence indicating the formation of a new species.

To gather more detailed insights into the nature of the observed transitions, time-dependent density functional theory (TDDFT) calculations (refer to Chapter 6.3.3.6 for computational details) were performed. Specifically, the excitation energies of the lowest energy singlet vertical excitations of the small molecule model systems depicted in **Figure 4.45a** were calculated at the PBE0/dhf-TZVP/D4 level of theory. For the model system **I**, representative of the 2-ferrocenyl-1,10-phenanthroline-based folding unit of **SCNP4-FcPhen**, the lowest energy singlet vertical excitation was calculated to 522 nm with a small oscillator strength of 0.001 (velocity representation), in good agreement with the absorption onset observed in the UV/Vis spectrum of **SCNP4-FcPhen**. Inspection of the non-relaxed difference density between

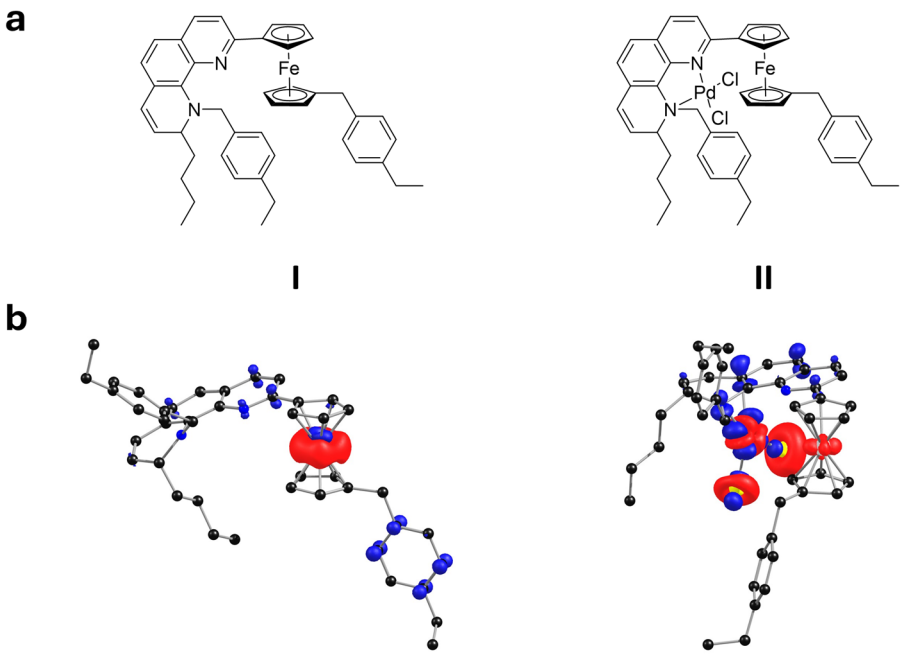

Figure 4.45 (a) Chemical structures of the small molecule model systems **I** and **II**. **(b)** Non-relaxed difference densities (PBE0/dhf-TZVP/D4) between the ground and lowest energy excited singlet state. Red color indicates a surplus of electron density for the ground state, blue for the excited state. Contours are drawn at 0.003 atomic units. Hydrogen atoms are omitted for clarity. Color code: Carbon black, nitrogen blue, chlorine yellow, iron orange, palladium red.

the ground state and the lowest energy excited singlet state (refer to **Figure 4.45b**) showed that this excitation is dominated by the transfer of electron density from the ferrocene iron center to the phenanthroline and phenyl π systems and d-d transitions on iron, respectively. For the model system **II**, representative of the functional unit within **SCNP4-FcPhen-Pd**, the lowest energy singlet vertical excitation was calculated to 654 nm with an oscillator strength of 0.002 (velocity representation), in line with the redshift of the absorption onset of **SCNP4-FcPhen-Pd** compared to **SCNP4-FcPhen** observed experimentally. Similar to **I**, the non-relaxed difference density between the ground state and the lowest energy excited singlet state (refer to **Figure 4.45b**) showed contributions of the ferrocene iron center as well as the phenanthroline π system. However, the dominating contributions are centered on the $PdCl_2$ subunit and feature d-d transitions on palladium and p-type contributions on the chlorine atoms. Hence, the redshift of the absorption onset observed experimentally for **SCNP4-FcPhen-Pd** compared to **SCNP4-FcPhen** is indicative of successful palladium functionalization. The palladium functionalization was expected to impart catalytic activity to **SCNP4-FcPhen-Pd**. A suitable catalytic reaction to test this hypothesis is ideally characterized by the absence of a redox step in the catalysis mechanism to avoid negative interferences with the ferrocene moieties. One reaction fulfilling this prerequisite is the catalytic intramolecular hydroamination of the aminoalkyne 2,2-diphenyl-4-heptyn-1-amine, which has been employed previously by our groups to benchmark the activity of SCNP catalysts,[6,8,12] as it is supposed to proceed via a mechanistic pathway in which palladium remains in the +II oxidation state.[265] Thus, the ability of **SCNP4-FcPhen-Pd** to function as a catalyst in the aforementioned reaction was tested. Dimethylanilinium tetrakis(pentafluorophenyl)borate was additionally added to the reaction mixture as it is known to be an efficient cocatalyst for hydroamination reactions.[266]

The reaction progress of the intramolecular hydroamination of 2,2-diphenyl-4-heptyn-1-amine to 3,3-diphenyl-5-propyl-3,4-dihydro-2*H*-pyrrole in C_6D_6 was monitored by ^{1}H NMR spectroscopy (refer to **Figure 4.46**). Virtually quantitative conversion of the substrate to the desired product was achieved within three hours at 60 °C, compared to zero conversion when only the cocatalyst was present (refer to **Figure 6.28**). It is noted in passing that the addition of iron(III) chloride to the reaction solution after complete consumption of the catalysis substrate led to the formation of a dark precipitate, presumably the oxidized form of **SCNP4-FcPhen-Pd**, indicating that the SCNP catalyst could be removed from the reaction mixture by

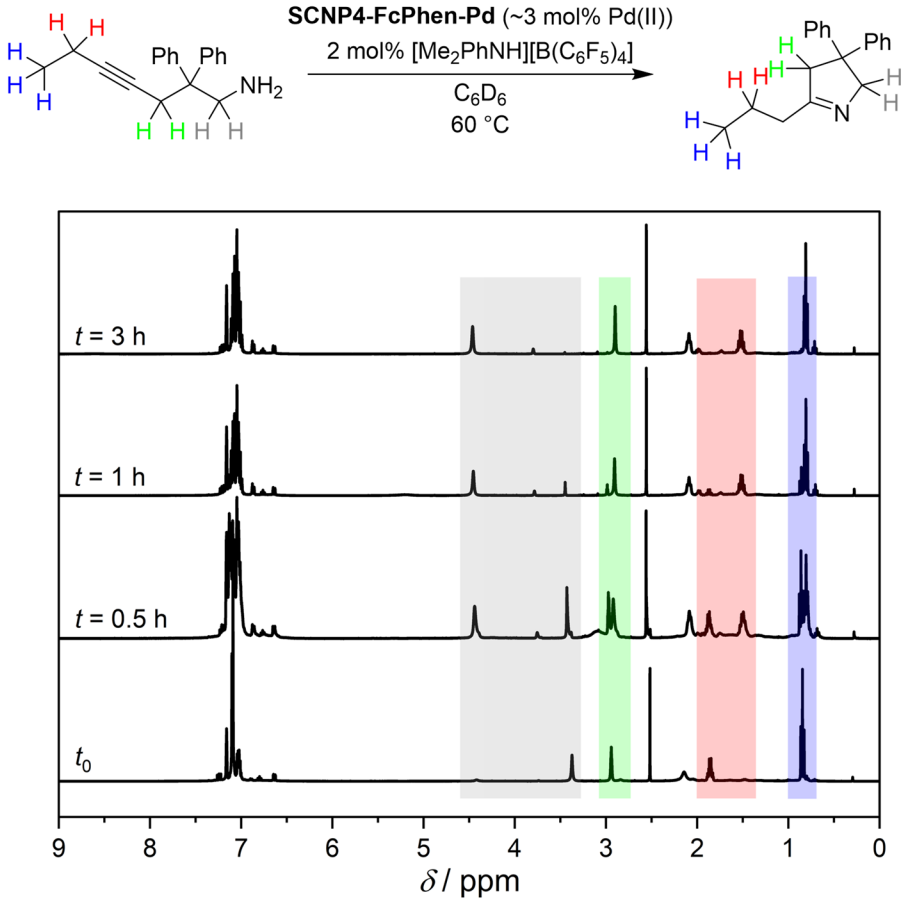

Figure 4.46 Reaction equation and stacked ^{1}H NMR spectra (400 MHz, C_6D_6, 333 K) illustrating the progress of the intramolecular hydroamination of 2,2-diphenyl-4-heptyn-1-amine to 3,3-diphenyl-5-propyl-3,4-dihydro-2*H*-pyrrole catalyzed by **SCNP4-FcPhen-Pd**. Colored boxes in the spectrum highlight the resonances associated with the protons of the corresponding color in the scheme on top.

precipitation. Iron(III) chloride has previously been employed in the literature to oxidize ferrocene-functionalized, redox-responsive polymers.[267] Attempts to redissolve and reuse the catalyst in a second catalytic cycle were unsuccessful. Nevertheless, this finding highlights that the synthesis of redox-responsive SCNP catalysts is possible and the simple separability of the catalyst from the reaction mixture after oxidation achievable, paving the way towards the exploration of ferrocene-based redox-recyclable SCNP catalysts.

4.3.5 Summary

The archetypical sandwich complex ferrocene was introduced as a covalently bonded single-chain nanoparticle (SCNP) crosslinker, inducing the intramolecular folding of a poly(styrene-*co*-4-chloromethyl styrene) copolymer (Polymer **P4**). In proof-of-concept work, **P4** was reacted with *in situ* prepared 1,1'-dilithioferrocene to form **SCNP4-Fc** and introduce ferrocene itself as SCNP folding unit. The successful intramolecular folding was evidenced by

nuclear magnetic resonance spectroscopy (NMR), size-exclusion chromatography (SEC), dynamic light scattering (DLS) and diffusion-ordered spectroscopy (DOSY).

Building upon this, the crosslinking ferrocene moiety was supplemented with the bidentate nitrogen donor ligand 1,10-phenanthroline and the ferrocene derivative 2-ferrocenyl-1,10-phenanthroline employed to induce the single-chain collapse, providing access to **SCNP4-FcPhen**. Characterization by NMR and SEC revealed that a small molecule impurity was critical to the stability of the nanoparticles. Size-sensitive characterization by SEC, DLS and DOSY verified the successful SCNP formation. The chemical structure of the crosslinking moiety was investigated in detail by experimental studies combined with density functional theory (DFT) calculations.

The donor ligand functionalization provided a pathway towards the coordination of additional metals, and the reaction of **SCNP4-FcPhen** with dichloro(1,5-cyclooctadiene)palladium(II) gave access to the first heterobimetallic ferrocene SCNP, **SCNP4-FcPhen-Pd**, which was investigated by NMR, SEC and DOSY. The successful palladium functionalization was further evidenced by energy-dispersive X-ray spectroscopy (EDX) and optical absorption spectroscopy combined with time-dependent density functional theory (TDDFT) calculations. The catalytic activity of **SCNP4-FcPhen-Pd** was demonstrated on the example of the catalytic intramolecular hydroamination of the aminoalkyne 2,2-diphenyl-4-heptyn-1-amine.

The exploration of further reactions of the multimetallic SCNPs described in this chapter could lead to the discovery of synergistic interactions of the metals, serving as blueprint for the investigation of interactions between different metal functionalities within other heteromultimetallic SCNPs. As a first step towards this direction, the following chapter explores the opportunities provided by the synergistic combination of metal ions with non-metal functionalities within the same SCNP.

4.4 PHOTOCATALYSIS ACTION PLOTS OF EOSIN Y SINGLE-CHAIN NANOPARTICLES

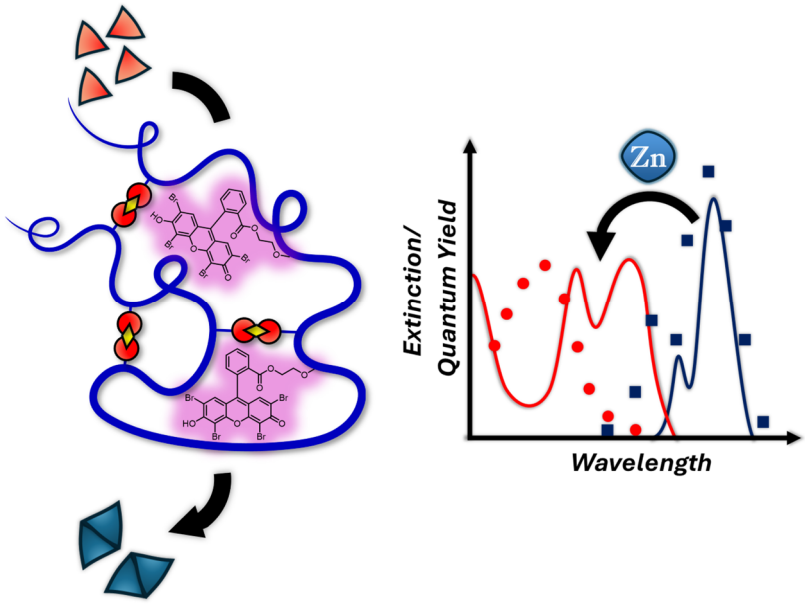

Figure 4.47 Graphical abstract of the chapter "Photocatalysis Action Plots of Eosin Y Single-Chain Nanoparticles".

Abstract

Single-chain nanoparticles (SCNPs) functionalized with the organic xanthene dye Eosin Y were prepared and employed as photocatalysts for the photosensitized oxidation of triphenylphosphine to triphenylphosphine oxide mediated by ambient oxygen. The wavelength-dependent catalyst activity was investigated by the photochemical action plot methodology which was, for the first time, applied to monitor the excitation wavelength dependence of a photocatalytic reaction. In detail, the synthesis of two different polymeric systems based on a poly(ethylene glycol) methyl ether methacrylate backbone is described. To probe the influence of the polymeric environment on the excitation wavelength response of the catalytic reaction, SCNPs with an organic dithiol crosslinker were initially prepared and the resulting photocatalysis action plot compared to a small molecule Eosin Y analogue. Further, a second polymer functionalized with pendant carboxylate moieties was prepared, the optical absorption spectrum of which could be drastically influenced by the addition of Zn(II) ions, accompanied by a distinct change of the irradiation wavelength response of the catalytic reaction. Base addition enabled the reversion of these changes, providing a pathway towards stimuli responsive alterations of the photocatalyst activity.

Table 4.7 Statement of contributions of coauthors of the publication "On-Off Switchable Photocatalysis by Zn(II)-driven Single-Chain Polymer Nanoparticle Compaction" (*Manuscript in preparation*).

Contributor	**Statement of contribution**
Sebastian Gillhuber	Conceptualization, Methodology, Formal analysis, Investigation, Writing – Original Draft, Review & Editing, Visualization, Project administration
Joshua O. Holloway	Writing – Review & Editing, Supervision
Hendrik Frisch	Conceptualization, Writing – Review & Editing, Supervision, Project administration
Florian Weigend	Conceptualization, Writing – Review & Editing, Supervision (Quantum Chemistry)
Christopher Barner-Kowollik	Conceptualization, Writing – Review & Editing, Supervision, Project administration, Funding acquisition
Peter W. Roesky	Conceptualization, Writing – Review & Editing, Supervision, Project administration, Funding acquisition

4.4.1 Introduction

In recent years, the combination of the unique environment provided by SCNPs with organic dyes gained significant attention in the literature due to the broad application scope, precise tunability and oftentimes low-cost commercial availability of a variety of dye molecules.[125,170-173,268-270] Pioneering work in the realm of photosensitization and photocatalysis with SCNPs was conducted by the groups of Palmans and Meijer. The authors equipped SCNPs, folded by the helical self-assembly of benzene-1,3,5-tricarboxamide units, with a porphyrin-based photosensitizer, enabling the production of singlet oxygen upon light exposure. The produced singlet oxygen proved to be capable of cleaving off a drug molecule additionally anchored to the SCNP, rendering the SCNP-based photosensitizer drug a promising candidate for applications in photodynamic therapy.[125] Accommodating the photosensitizer in the SCNP effectively prevented its aggregation, even in highly polar solvents such as water. The singlet oxygen generation abilities of SCNP-anchored porphyrins were also explored in follow-up studies in living cells, efficiently promoting light-induced localized toxicity, leading to cell death upon light irradiation.[268]

Elacqua and coworkers focussed on the triarylpyrylium functionalization of SCNPs to enhance the photocatalyst performance compared to small molecule analogues.[170,172,269] For instance, the confinement provided by the SCNP environment improved the efficiency of cocatalyzed [2+2] cycloadditions compared to non-confined small molecule catalysts, which the authors attributed to the improved efficiency of the single electron transfer between the triarylpyrylium catalyst and the polyarene cocatalyst within the compartmentalized nanoparticles.[172]

Increased performance of a SCNP-bound photosensitizer in comparison to its small molecule counterpart was also recently reported by Mundsinger *et al.* who found the oxidation of oleic acid to proceed with three times increased turnover number when catalyzed by Rose Bengal-functionalized SCNPs instead of the small molecule xanthene dye Rose Bengal. It was hypothesized that this is the result of the formation of hydrophobic compartments within the SCNP, driving the unpolar substrate into the active regions of the nanoparticles where singlet oxygen is produced, increasing the probability of singlet oxygen encounters of the substrate compared to the free small molecule photosensitizer in solution.[171]

Another well-established dye of the xanthene family is Eosin Y which has found manifold applications in photocatalysis in recent years.[271-273] Upon visible light irradiation, the initially

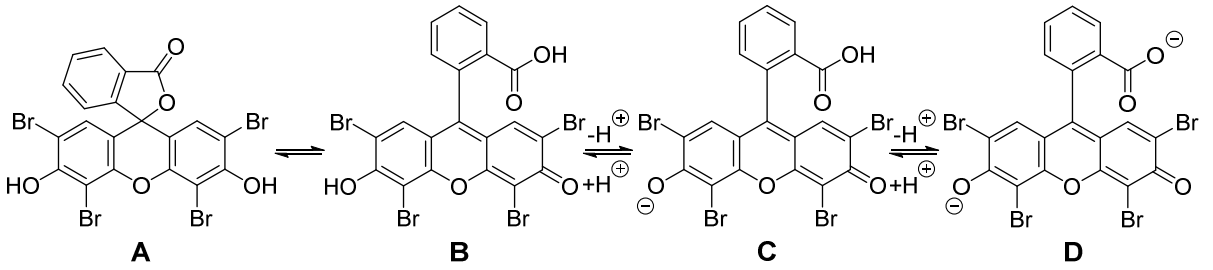

Scheme 4.12 Tautomerism and acid-base equilibria between the lactone (**A**), neutral (**B**), monanionic (**C**) and dianionic (**D**) forms of Eosin Y.

populated excited singlet state is rapidly converted to the lowest energy excited triplet state with a high intersystem crossing quantum yield.[274-275] The population of excited triplet states makes Eosin Y prone to triplet energy transfer, enabling, for instance, the efficient generation of singlet oxygen. Apart from that, Eosin Y can undergo excited state electron transfer processes, making it interesting for applications in photoredox reactions. However, the chemical and photophysical properties of Eosin Y are complicated by tautomerism and delicate acid-base equilibria as Eosin Y can exist in four different forms, specifically, the lactone form (**A**), the neutral form (**B**), the monoanionic form (**C**) and the dianionic form (**D**), respectively (refer to **Scheme 4.12**).[271-273]

This chapter aims at the functionalization of SCNPs with the xanthene dye Eosin Y for photocatalytic applications. Photochemical action plots (refer to Chapter 4.2.2) of the photosensitized oxidation of triphenylphosphine to triphenylphosphine oxide, catalyzed by polymer-bound Eosin Y as well as a small molecule Eosin Y analogue, are described to investigate the irradiation wavelength-dependent catalyst activity and probe the influence of the polymeric environment. In detail, two different Eosin Y polymers based on a poly(ethylene glycol) methyl ether methacrylate (PEGMEMA) backbone are outlined. At first, the photocatalysis action plots of the triphenylphosphine oxidation, catalyzed by Eosin Y SCNPs folded with an organic dithiol crosslinker and the small molecule Eosin Y derivative 2-(propionyloxy)ethyl 2-(2,4,5,7-tetrabromo-6-hydroxy-3-oxo-3*H*-xanthen-9-yl)benzoate (**EY**), respectively, are investigated. Subsequently, the opportunities provided by metal functionalization of a second Eosin Y polymer are explored. For that, a polymer functionalized with Eosin Y as well as pendant carboxylate functionalities is described, the optical absorption spectrum of which showed to be drastically influenced by the addition of Zn(II) ions and base. The influence of the metal functionalization on the irradiation wavelength response of the catalytic reaction is probed and compared to the small molecule Eosin Y analogue.

4.4.2 Effect of Single-Chain Confinement on Photocatalysis Action Plot

The discrepancy between the optical absorption spectrum of a compound and the efficiency of photoreactions a molecule is undergoing frequently observed in photochemical action plots (refer to Chapter 4.2.2) is the subject of active ongoing research. To date, no unified underlying theoretical framework providing a detailed understanding of the oftentimes observed disparities between absorptivity and reactivity exists.[211-212] To get closer to the ultimate goal of a comprehensive picture of the effects governing photochemical action plots, more action plot data of various photochemical systems is urgently required. Especially, photochemical action plot data on light-responsive SCNPs is scarce in the literature with only one example, exploring the folding process, reported to date.[276] Thus, this chapter aims at expanding the knowledge about the wavelength-dependent irradiation response of SCNP systems compared to small molecule counterparts by exploring the photochemical action plot of the light-driven oxidation of triphenylphosphine to triphenylphosphine oxide by ambient oxygen catalyzed by Eosin Y-functionalized SCNPs and small molecule analogues.

In principle, two approaches seem conceivable for the synthesis of Eosin Y-functionalized polymers, that is, the post-polymerization modification of an existing polymer with a suitable Eosin Y analogue or the direct polymerization of Eosin Y derivatives featuring polymerizable functional groups, respectively. For the synthesis of Eosin Y SCNPs described in this chapter, the latter approach was chosen. Specifically, the literature-known Eosin Y methacrylate monomer 2-(methacryloyloxy)ethyl 2-(2,4,5,7-tetrabromo-6-hydroxy-3-oxo-3*H*-xanthen-9-yl)benzoate (EYMA)[277] was copolymerized with poly(ethylene glycol) methyl ether methacrylate (PEGMEMA, average M_n = 300 g·mol^{-1}) and glycidyl methacrylate (GMA) by RAFT polymerization, resulting in polymer **P5** (refer to **Scheme 4.13**).

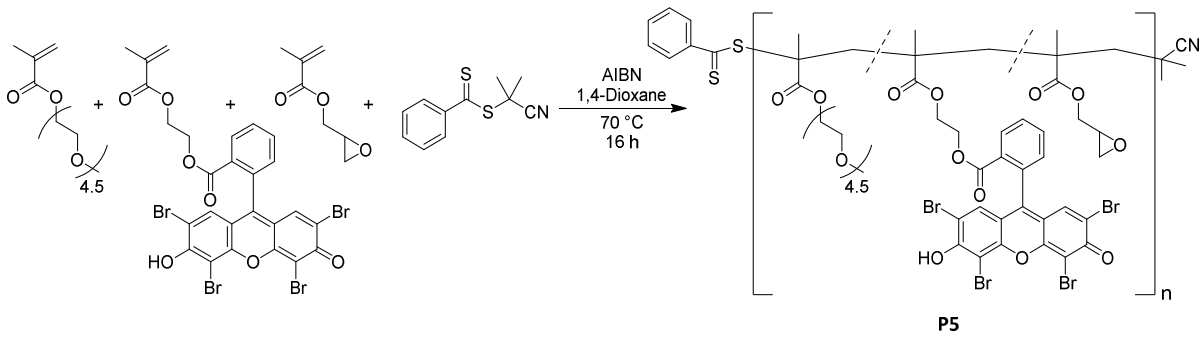

P5

Scheme 4.13 Synthesis of poly(PEGMEMA-*co*-EYMA-*co*-GMA) (Polymer **P5**) by reversible addition-fragmentation chain transfer polymerization.

The PEGMEMA backbone provided the polymer with solubility in a wide range of solvents, while the GMA moieties enabled efficient post-polymerization modification by ring opening reactions of the epoxide functionalities. Given the statistical nature of the described copolymerization process, all SCNP folding reactions reported in this chapter follow the repeat unit approach (refer to Chapter 2.1).[42]

SEC measurements in DMAc gave an indication of the number-averaged molar mass of M_n = 45300 g·mol^{-1} and dispersity of $Đ$ = 1.21. The ^{1}H NMR spectrum of **P5** acquired in CD_3CN is depicted in **Figure 4.48**. The resonances of the aliphatic backbone are located at δ = 2.07-0.65 ppm. The spectrum is dominated by the resonances associated with the PEG side chains, corresponding to the terminal methyl group (δ = 3.35-3.24 ppm), the ethylene glycol subunits (δ = 3.72-3.38 ppm) and the methylene group attached to the ester functionality connecting the PEG side chain with the polymer backbone (δ = 4.22-3.90 ppm), respectively. The successful incorporation of the GMA moieties into the copolymer is evident from the characteristic resonances of the epoxide functionality. Specifically, the resonances of the diastereotopic methylene ring protons at δ = 2.87-2.56 ppm, the methanetriyl group at δ = 3.24-3.14 ppm and the diastereotopic protons of the methylene group linking polymer backbone and epoxide ring at δ = 3.81-3.69 ppm and δ = 4.39-4.26 ppm, respectively. The

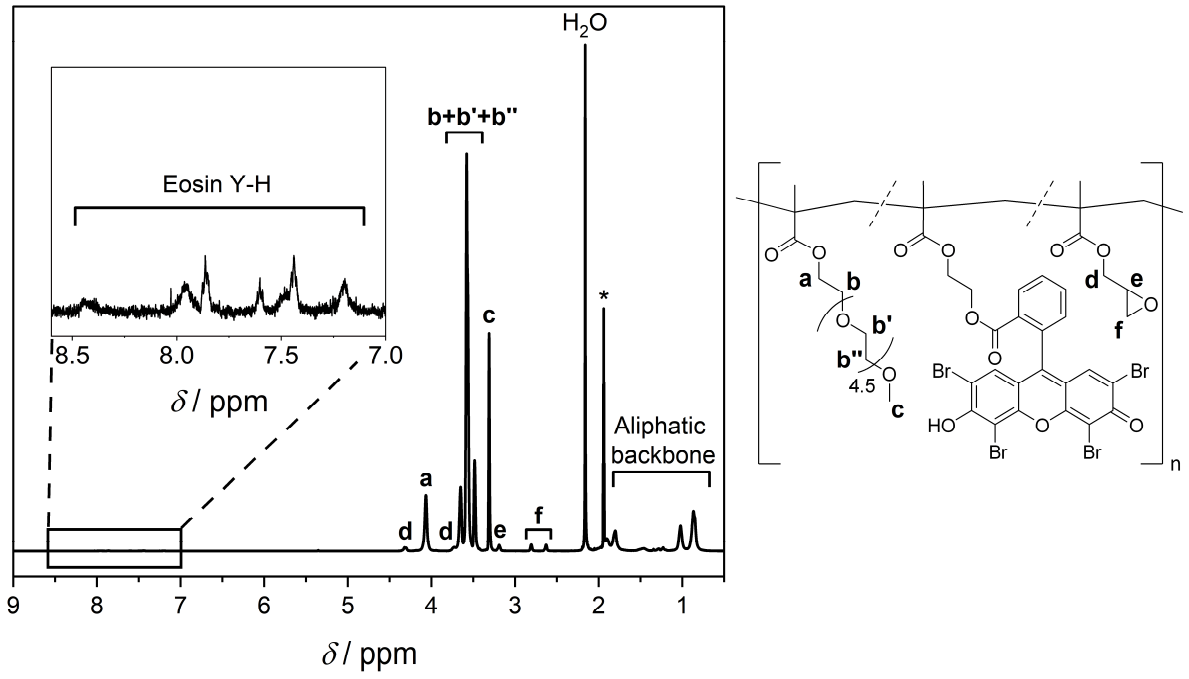

Figure 4.48 ^{1}H NMR spectrum (600 MHz, CD_3CN, 298 K) of polymer **P5**. Insert shows the zoomed-in region of the aromatic resonances associated with the EYMA moieties. Asterisk denotes residual solvent resonance.

resonances of the ethylene bridge connecting polymer backbone and Eosin Y functionality could not be resolved due to low signal intensity. However, the successful incorporation of the EYMA monomer is evidenced by the presence of the aromatic resonances at δ = 8.52-7.10 ppm (refer to insert in **Figure 4.48**).

The low signal intensity of the relevant resonances in the ^{1}H NMR spectrum precluded a meaningful quantification of the amount of EYMA incorporated into **P5**, however, based on the monomer feed ratio (refer to Chapter 6.3.4.1), it is expected that EYMA makes up about 1 % of the monomers per macromolecular chain. The amount of GMA relative to PEGMEMA moieties incorporated into **P5** can be estimated according to:

$$\frac{N_{\mathrm{GMA}}}{N_{\mathrm{PEGMEMA}} + N_{\mathrm{GMA}}} = \frac{1}{1 + \frac{2}{3}\frac{Int(\mathrm{c})}{Int(\mathrm{f})}}$$

Herein, N_{GMA} and N_{PEGMEMA} are the average number of GMA and PEGMEMA monomers, respectively, incorporated in a macromolecular chain of **P5**, *Int*(c) is obtained by integration of the resonance at δ = 3.35-3.24 ppm relative to the value of the integral *Int*(f), obtained by integration of the resonances at δ = 2.87-2.56 ppm. Integration of the corresponding resonances yielded a ratio of *Int*(c)/*Int*(f) of 8.3, equivalent to an incorporation ratio of 15 % functional monomers per macromolecular chain.

Starting from **P5**, single-chain folding was achieved by a thiol-epoxy click reaction[278-280] of the epoxide functionalities with 1,4-benzenedimethanethiol in methanol (**SCNP5-EY**, refer to **Scheme 4.14**). The successful epoxide ring opening could conveniently be followed by the

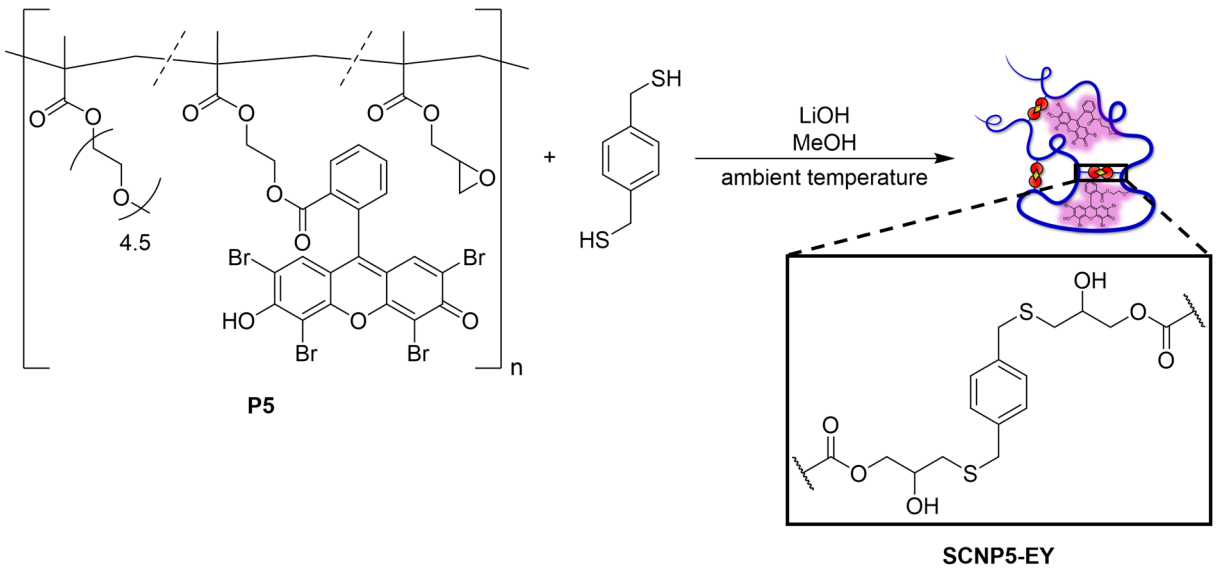

Scheme 4.14 Synthesis of **SCNP5-EY** by the reaction of **P5** with 1,4-benzenedimethanethiol via thiol-epoxy click chemistry.

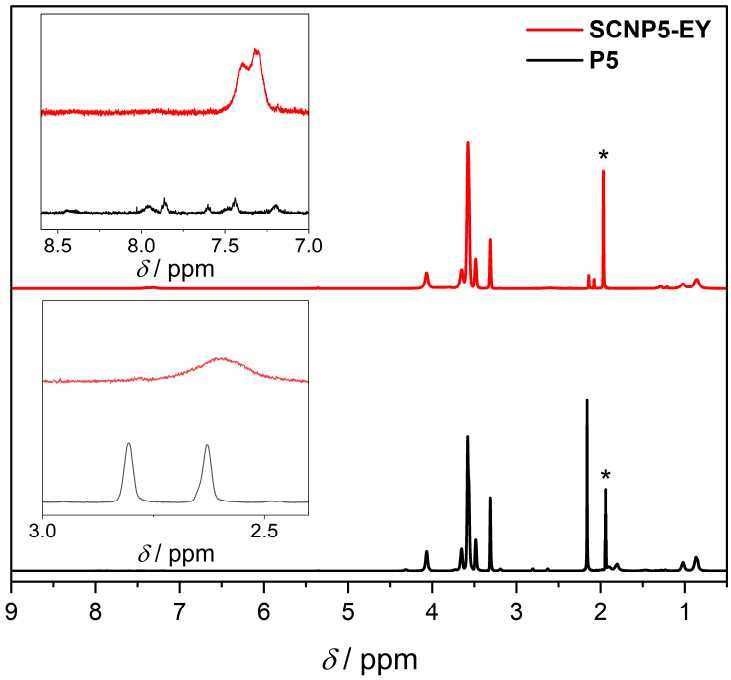

Figure 4.49 Stacked ^{1}H NMR spectra (600 MHz, CD_3CN, 298 K) of polymer **P5** (black) and **SCNP5-EY** (red). Inserts show the zoomed-in resonances relevant to the successful SCNP folding reaction (refer to the main text for details). Asterisks denote residual solvent resonances.

disappearance of the resonances associated with the methylene ring protons at δ = 2.87-2.56 ppm as well as the appearance of a new resonance at δ = 7.59-7.14 ppm, corresponding to the protons of the aromatic crosslinker, in the ^{1}H NMR spectrum of **SCNP5-EY** (refer to **Figure 4.49**).

Successful SCNP formation was validated by size-sensitive analytical techniques. The molar mass distribution of **SCNP5-EY** obtained by SEC in DMAc was shifted towards lower apparent molar masses compared to the corresponding distribution of **P5** (refer to **Figure 4.50a**). The

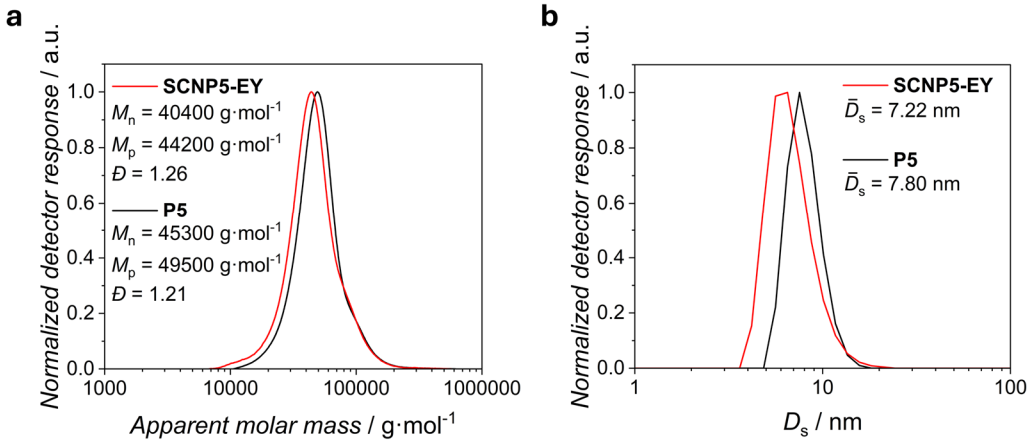

Figure 4.50 Superimposed **(a)** SEC chromatograms (DMAc, RI, PMMA cal.) and **(b)** number-weighted DLS size distributions (CH_3CN, mean diameter by number, average values derived from five measurements) of polymer **P5** (black) and **SCNP5-EY** (red).

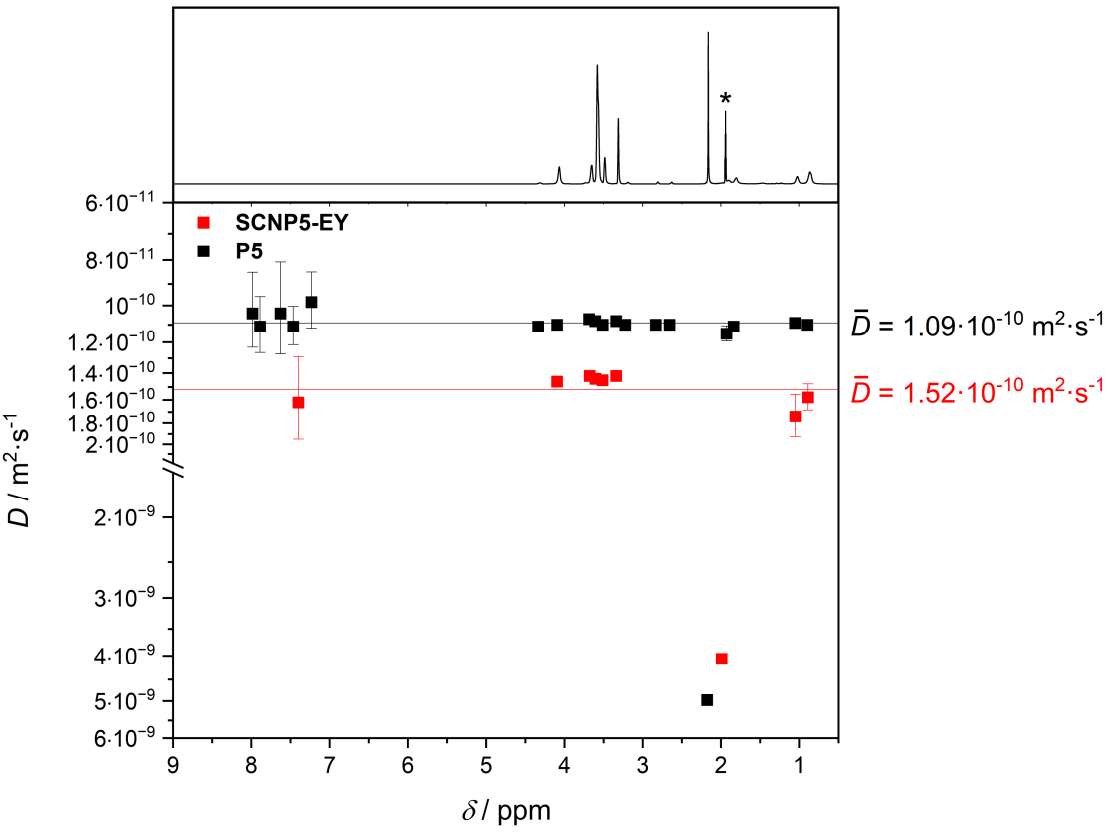

Figure 4.51 Superimposed ^{1}H DOSY NMR spectra (400 MHz, CD_3CN, 301 K) of polymer **P5** (black) and **SCNP5-EY** (red). Spectral trace on top refers to **P5**. Error bars refer to data fitting error. Horizontal lines indicate average diffusion coefficients. Asterisk denotes residual solvent resonance.

derived number-averaged and peak molar masses decreased from M_n = 45300 g·mol^{-1} and M_p = 49500 g·mol^{-1} for **P5** to M_n = 40400 g·mol^{-1} and M_p = 44200 g·mol^{-1} for **SCNP5-EY**. The dispersity changed slightly from $Đ$ = 1.21 (**P5**) to $Đ$ = 1.26 (**SCNP5-EY**). Similarly, DLS in acetonitrile evidenced a decrease in the number-averaged solvodynamic diameter from D_s = 7.80 nm for **P5** to D_s = 7.22 nm for **SCNP5-EY** (refer to **Figure 4.50b**). The same trend was observed by ^{1}H DOSY NMR measurements in CD_3CN, showing an increase in the average diffusion coefficient from D = 1.09·10^{-10} m^2·s^{-1} for **P5** to D = 1.52·10^{-10} m^2·s^{-1} for **SCNP5-EY** (refer to **Figure 4.51**).

One of the most prominent applications of Eosin Y is its use as a photosensitizer for the generation of singlet oxygen (refer to Chapter 4.4.1). The produced singlet oxygen can participate in subsequent reactions, for instance, the photocatalytic oxidation of organic and inorganic compounds.[271-272] To probe the catalytic abilities of **SCNP5-EY** for singlet oxygen production in dependence on the excitation wavelength by the photochemical action plot methodology, the photosensitized oxidation of triphenylphosphine to triphenylphosphine oxide by ambient oxygen, following the work by the groups of Gu and Guo on the Eosin Y-

catalyzed photooxidation of triarylphosphines,[281] was investigated. To explore the effect of the polymeric environment on the photocatalysis action plot, the small molecule model system 2-(propionyloxy)ethyl 2-(2,4,5,7-tetrabromo-6-hydroxy-3-oxo-3*H*-xanthen-9-yl)benzoate (**EY**), mimicking the Eosin Y moieties in **SCNP5-EY**, was additionally synthesized. It is worth noting that the complexity stemming from tautomerism and delicate acid-base equilibria, usually complicating the photochemistry of Eosin Y (refer to Chapter 4.4.1), is reduced in the systems considered in this chapter due to the esterification of the carboxylic acid functionality, preventing lactonization and proton transfer at this position. Thus, proton transfer equilibria are limited to the hydroxyl functionality, and it was experimentally ensured by UV/Vis spectroscopy that the deprotonated form is the predominating species in all cases considered here.

A calibration curve relating the peak absorbance at 540 nm to the **EY** concentration was recorded using the small molecule model system (refer to **Figure 6.30**). Based on this, solutions with an **EY** concentration of 13.4 µmol·L^{-1} in acetonitrile were prepared for the photochemical action plot experiments. Similarly, acetonitrile solutions of **SCNP5-EY** with the same 540 nm peak absorbance were prepared, ensuring comparability of the Eosin Y concentration in solutions of the small molecule model system and SCNP samples throughout the photochemical action plot experiments discussed in this chapter. A similar approach for the determination of the dye concentration in SCNP systems has been employed previously by our group.[171] It is noted in passing that this approach assumes identical transition dipole moments of the relevant electronic excitations in the small molecule and polymeric system, respectively, potentially limiting its reliability. However, given the good solvent conditions the experiments were conducted under, the differences in transition dipole moments of the electronic excitations of the chromophore are expected to be negligible as the dye is presumably primarily surrounded by solvent molecules in both cases.

Photochemical action plots of the photosensitized triphenylphosphine oxidation catalyzed by **EY** or **SCNP5-EY**, respectively, were recorded in acetonitrile in the wavelength range 360 nm to 580 nm in 20 nm increments. The dye concentration was adjusted to about 13.4 µmol·L^{-1} and the amount of triphenylphosphine adapted to result in a catalyst load of about 0.5 mol%. The samples were irradiated with $1.10 \cdot 10^{18}$ photons at each wavelength and the conversion of triphenylphosphine to triphenylphosphine oxide quantified by ^{1}H NMR spectroscopy. Each data point was recorded in triplicate and the error bars refer to the lowest and highest

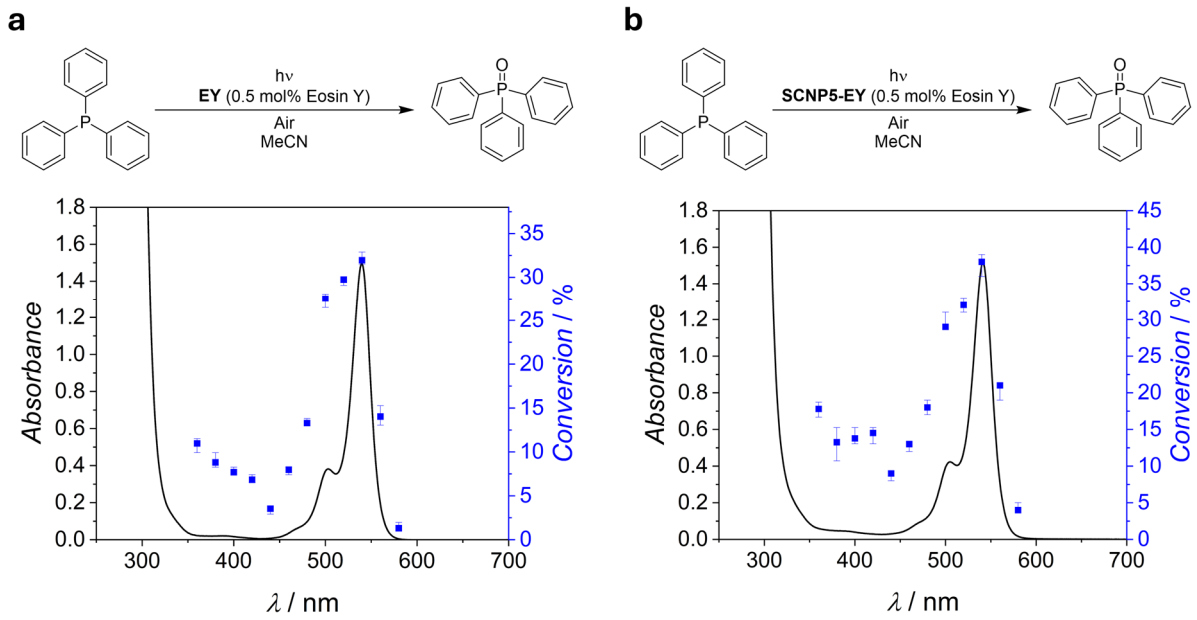

Figure 4.52 Photochemical action plots of the photosensitized oxidation of triphenylphosphine to triphenylphosphine oxide catalyzed by **(a)** small molecule **EY** and **(b) SCNP5-EY** at an Eosin Y concentration of about 13.4 µmol·L^{-1}, recorded in acetonitrile, showing the conversion of the starting material to the product upon irradiation with the same number of photons (1.10·10^{18} photons) at different wavelengths superimposed with the UV/Vis spectra of the corresponding reaction mixtures. Error bars indicate the lowest and highest determined conversion at each wavelength, respectively.

determined conversion at each wavelength, respectively. Details on the experimental procedures are provided in Chapter 6.3.4.4.

The obtained photochemical action plots are depicted in **Figure 4.52**. For **EY** as well as **SCNP5-EY** as the catalyst, it is evident that the highest conversion of the starting material to the catalysis product was achieved upon irradiation at 540 nm, coinciding with the maximum of the optical absorption spectrum. Further, in both cases, the wavelength-dependent reactivity pattern follows the absorption profile with a drastic decrease in absorptivity and reactivity around the respective peak. However, while the reactivity patterns of **EY** and **SCNP5-EY** are qualitatively similar, the achieved average conversions to the catalysis product were consistently about 5 % higher for **SCNP5-EY** than for **EY** over the entire wavelength interval probed, hinting at a beneficial effect of the polymeric environment on the rate of the catalytic transformation.

The discussed photochemical action plots constitute the first examples investigating a photocatalytic reaction, thus pioneering the area of photocatalysis action plots and serving as precedents for future research is this realm.

4.4.3 Tuning Photocatalysis Action Plots by Zn(II) Functionalization

The results outlined in Chapter 4.4.2 highlight the beneficial effect the polymeric environment can exert on the catalytic rate of the Eosin Y-photosensitized oxidation of triphenylphosphine. Apart from providing a local environment advantageous for catalytic transformations, polymers can conveniently be supplemented with further functionalities, enabling facile access to materials with tunable characteristics. To explore the opportunities provided by polymer modification on the photocatalysis action plot of the Eosin Y-sensitized catalytic oxidation of triphenylphosphine, a copolymer of poly(ethylene glycol) methyl ether methacrylate (PEGMEMA, average M_n = 300 g·mol^{-1}), 2-(methacryloyloxy)ethyl 2-(2,4,5,7-tetrabromo-6-hydroxy-3-oxo-3*H*-xanthen-9-yl)benzoate (EYMA)[277] and 2-carboxyethyl acrylate (2CEA) was prepared by RAFT polymerization (Polymer **P6**, refer to **Scheme 4.15**). The statistical nature of this copolymerization process makes all SCNP folding reactions based on this copolymer follow the repeat unit approach (refer to Chapter 2.1).[42] Compared to **P5**, the additional carboxylate functionalities, stemming from the 2CEA moieties, provided a pathway towards metal-crosslinked SCNPs, contrary to the purely organic **SCNP5-EY** folded by a dithiol crosslinker.

SEC measurements in DMAc indicated a number-averaged molar mass of M_n = 43900 g·mol^{-1} and dispersity of $Đ$ = 1.54. The ^{1}H NMR spectrum of **P6** acquired in CD_3CN is depicted in **Figure 4.53** and resembles the one of **P5** (refer to **Figure 4.48**). The resonances of the aliphatic polymer backbone can be found at δ = 2.47-0.56 ppm. The spectrum is dominated by the resonances associated with the PEG side chains, corresponding to the terminal methyl group (δ = 3.38-3.20 ppm), the ethylene glycol subunits (δ = 3.84-3.39 ppm) and the methylene group attached to the ester functionality connecting the PEG side chain to the polymer backbone (δ = 4.24-3.91 ppm), respectively. The successful incorporation of the 2CEA moieties is evident

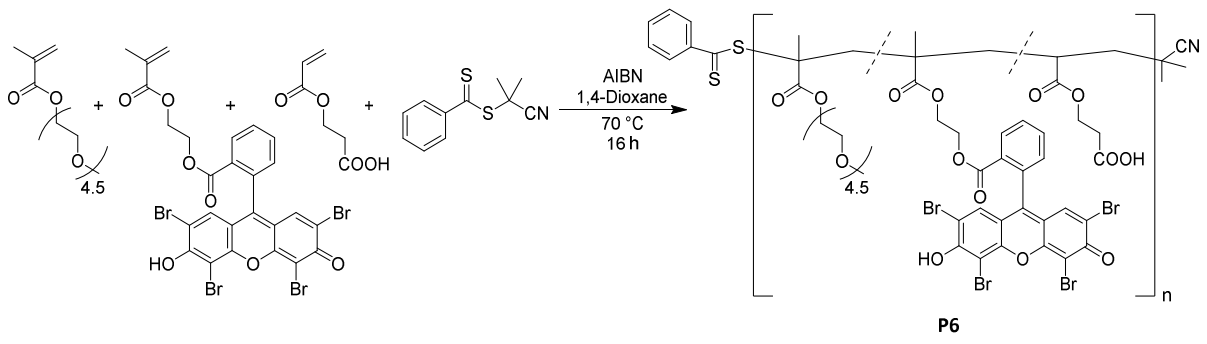

P6

Scheme 4.15 Synthesis of poly(PEGMEMA-*co*-EYMA-*co*-2CEA) (Polymer **P6**) by reversible addition-fragmentation chain transfer polymerization.

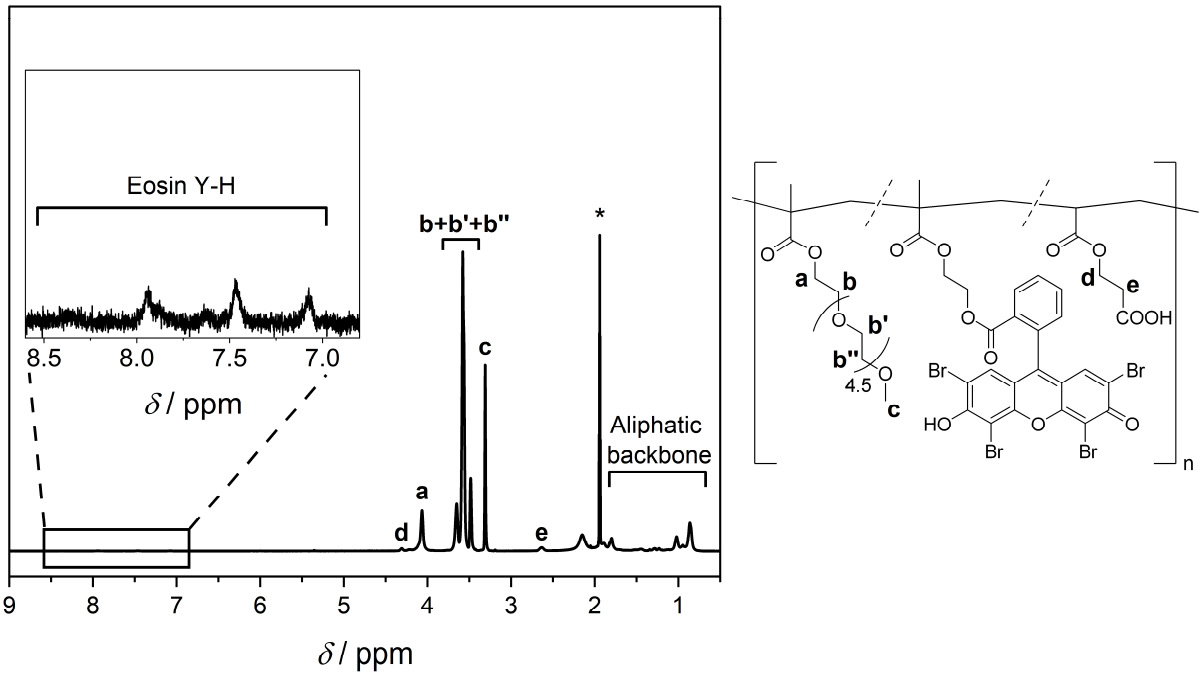

Figure 4.53 ^{1}H NMR spectrum (600 MHz, CD_3CN, 298 K) of polymer **P6**. Insert shows the zoomed-in region of the aromatic resonances associated with the EYMA moieties. Asterisk denotes residual solvent resonance.

from the resonances at δ = 4.38-4.26 ppm and δ = 2.72-2.52 ppm, originating from the two distinct methylene groups of the ethylene bridge. Similar to **P5**, the resonances of the ethylene linker connecting polymer backbone and Eosin Y functionality could not be resolved due to low signal intensity. Despite this, the successful incorporation of the EYMA monomer is evidenced by the presence of the aromatic resonances at δ = 8.64-6.94 ppm (refer to insert in **Figure 4.53**).

Again, the low signal intensity of the relevant resonances in the ^{1}H NMR spectrum precluded a meaningful quantification of the amount of EYMA incorporated into **P6**, however, based on the monomer feed ratio (refer to Chapter 6.3.4.3), EYMA is expected to make up about 1 % of the monomers per macromolecular chain. The amount of 2CEA relative to PEGMEMA moieties incorporated into **P6** can be estimated according to:

$$\frac{N_{\mathrm{2CEA}}}{N_{\mathrm{PEGMEMA}} + N_{\mathrm{2CEA}}} = \frac{1}{1 + \frac{2}{3}\frac{Int(\mathrm{c})}{Int(\mathrm{e})}}$$

Herein, N_{2CEA} and $N_{PEGMEMA}$ are the average number of 2CEA and PEGMEMA monomers, respectively, incorporated in a macromolecular chain of **P6**, *Int*(c) is obtained by integration of the resonance at δ = 3.38-3.20 ppm relative to the value of the integral *Int*(e), obtained by integration of the resonance at δ = 2.72-2.52 ppm. Integration of the corresponding

resonances yielded a ratio of *Int*(c)/*Int*(e) of 8.3, equivalent to an incorporation ratio of 15 % functional monomers per macromolecular chain.

In analogy to the work described in Chapter 4.4.2, the wavelength-resolved reactivity profile of the photosensitized oxidation of triphenylphosphine to triphenylphosphine oxide catalyzed by polymer **P6** was evaluated following the photochemical action plot methodology. Consistent with the previously described procedures, the action plot was recorded in acetonitrile in the wavelength range 360 nm to 580 nm in 20 nm increments. Again, the dye concentration was adjusted to about 13.4 µmol·L^{-1} based on the previously established calibration (refer to **Figure 6.30**) and the amount of triphenylphosphine adapted to result in a catalyst loading of about 0.5 mol%. The samples were irradiated with 1.10·10^{18} photons at each wavelength and the conversion of triphenylphosphine to triphenylphosphine oxide quantified by ^{1}H NMR spectroscopy. Each data point was recorded in triplicate and the error bars refer to the lowest and highest determined conversion at each wavelength, respectively. Details on the experimental procedures are provided in Chapter 6.3.4.4.

The obtained photochemical action plot is depicted in **Figure 4.54** together with the previously recorded one employing **EY** as the catalyst. Again, the highest conversion of the catalysis

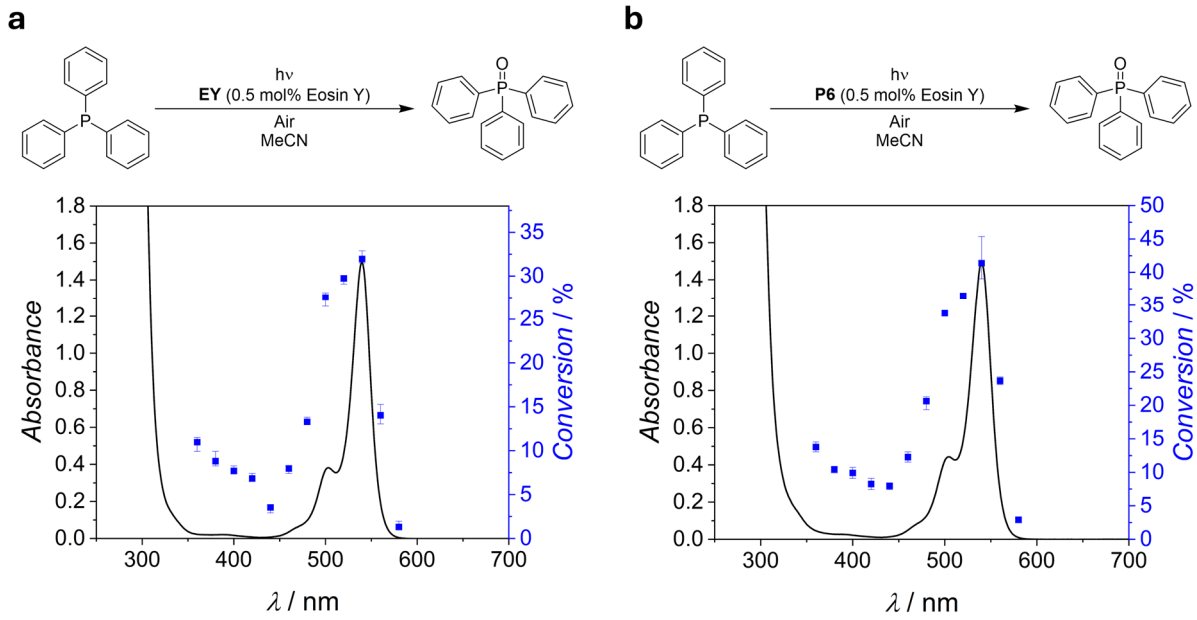

Figure 4.54 Photochemical action plots of the photosensitized oxidation of triphenylphosphine to triphenylphosphine oxide catalyzed by **(a)** small molecule **EY** and **(b) P6** at an Eosin Y concentration of about 13.4 µmol·L^{-1}, recorded in acetonitrile, showing the conversion of the starting material to the product upon irradiation with the same number of photons (1.10·10^{18} photons) at different wavelengths superimposed with the UV/Vis spectra of the corresponding reaction mixtures. Error bars indicate the lowest and highest determined conversion at each wavelength, respectively.

substrate to the desired product was achieved upon irradiation at 540 nm, the wavelength of the absorption maximum, and the wavelength-dependent reactivity pattern resembles the shape of the optical absorption profile. The beneficial effect of the polymeric environment on the catalytic rate is again indicated by consistently higher yields when **P6** instead of the small molecule **EY** is employed as the catalyst. In the current case, the effect is most pronounced between 480 nm to 560 nm, with up to 10 % higher conversions when the polymeric catalyst is utilized.

As outlined in Chapter 4.4.1, the photochemical properties of Eosin Y are strongly dependent on delicate equilibria involving the hydroxyl and carboxyl functionalities. While the carboxyl group is unavailable for further modifications in the present case due to its esterification, the hydroxyl functionality is accessible to chemical stimuli, for instance, interactions with metal cations.[282] The addition of zinc(II) triflate to acetonitrile solutions of **EY** or **P6**, respectively, was found to drastically alter the optical absorption spectrum. In detail, the absorbance peak centered at λ_{max} = 540 nm with a shoulder centered at λ = 504 nm (refer to **Figure 4.54**) disappeared, accompanied by the emergence of three new absorption bands centered at λ = 386 nm, 485 nm and 516 nm (refer to **Figure 4.56**), respectively.

To gather a more detailed understanding of the observed influence of metal addition on the electronic excitation spectra, time-dependent density functional theory (TDDFT) calculations at the BLYP/def2-TZVPP level of theory were performed (refer to Chapter 6.3.4.6 for computational details). For that, the model compounds **EY-Na**, representative of deprotonated **EY** as well as the Eosin Y moieties within **P6**, and **EY-Zn**, representative of Zn(II)-functionalized **EY** or **P6**, respectively, were considered (refer to **Figure 4.55a**).

In detail, singlet vertical excitation energies and oscillator strengths of the twenty lowest energy excitations were calculated (refer to **Table 6.25** and **Table 6.26**). Based on the determined values, electronic excitation spectra were simulated (refer to **Figure 4.55b**). The shape of the simulated absorption spectrum of **EY-Na** is in excellent agreement with the experimental UV/Vis spectra of the reaction solutions employed for recording the photochemical action plots depicted in **Figure 4.54**. According to the calculations, the highest intensity absorption peak is associated with two transitions ($\boldsymbol{i}_{\mathbf{EY\text{-}Na}}$ and $\boldsymbol{ii}_{\mathbf{EY\text{-}Na}}$) of similar excitation energies and oscillator strengths. The non-relaxed difference density plots (refer to **Figure 4.55c**) of the respective transitions are qualitatively identical and indicate a transfer of electron density from the xanthene unit to the attached substituted phenyl ring upon

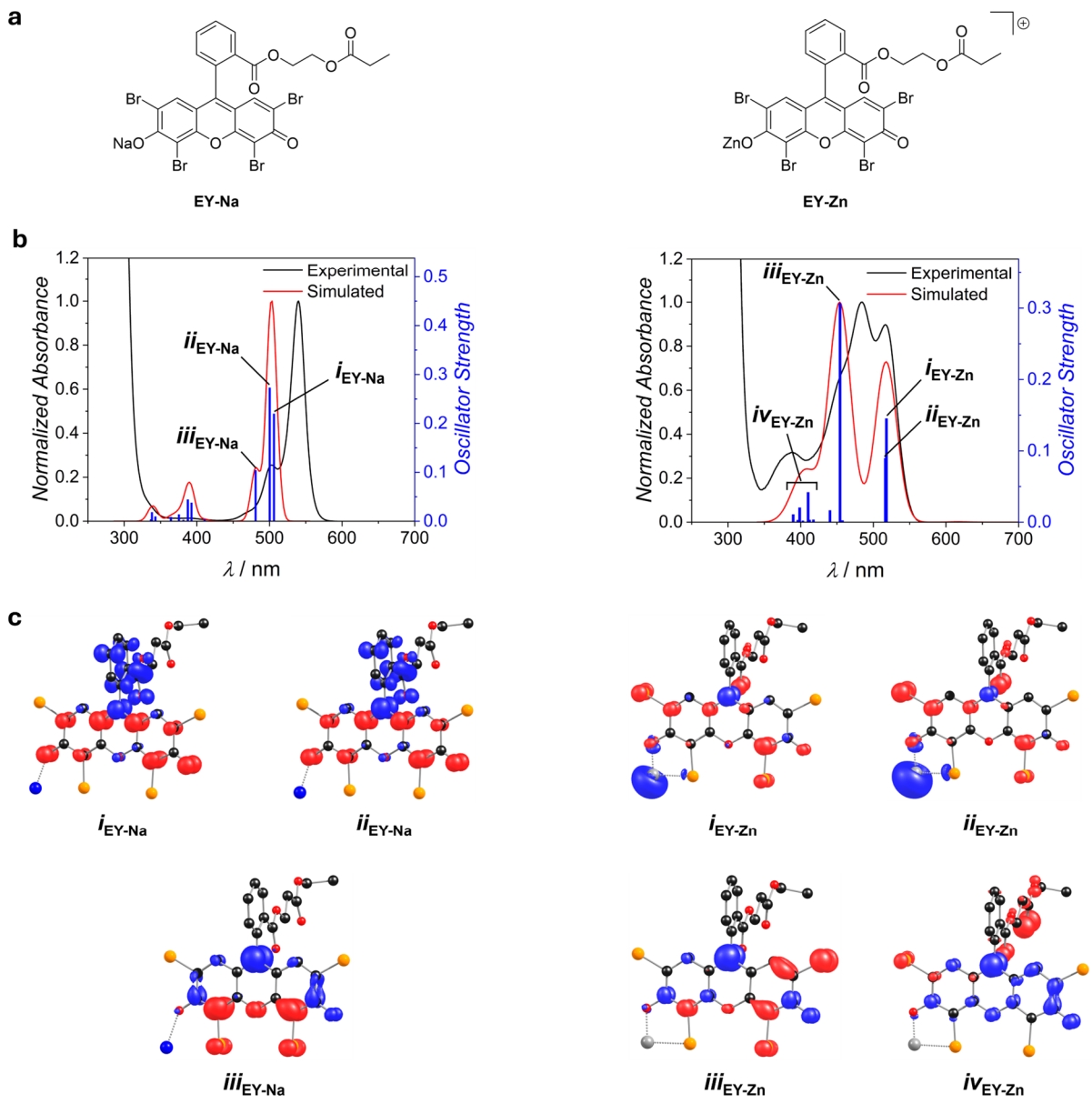

Figure 4.55 (a) Chemical structures of the model compounds **EY-Na** (left) and **EY-Zn** (right) considered in the quantum chemical calculations discussed in the main text. **(b)** Electronic excitation spectra of **EY-Na** (left) and **EY-Zn** (right) simulated based on the calculated singlet vertical excitation energies and oscillator strengths of the respective transitions superimposed with the experimental UV/Vis spectra (CH_3CN, 298 K) of the reaction solutions employed for the photochemical action plot experiments depicted in **Figure 4.54a** and **Figure 4.56a**. **(c)** Non-relaxed difference densities of the indicated excitations. Labels refer to the respective graphs on top. For the depiction of the non-relaxed difference density of $\boldsymbol{iv}_{\text{EY-Zn}}$, the included excitations were weighted by their oscillator strengths. Red color indicates a surplus of electron density for the ground state, blue for the excited state. Contours are drawn at 0.003 atomic units. Hydrogen atoms are omitted for clarity. Color code: Carbon black, oxygen red, sodium blue, zinc grey, bromine orange. Calculations were performed at the BLYP/def2-TZVPP level of theory (refer to Chapter 6.3.4.6 for details).

excitation. The shoulder towards higher excitation energies corresponds to a single excitation (***iii***$_{\mathbf{EY\text{-}Na}}$) centered on the xanthene core.

The pronounced influence of zinc functionalization on the optical absorption spectrum outlined above is also reflected in the calculations. Reminiscent of the experimental spectra of the reaction solutions employed for recording the photochemical action plots depicted in **Figure 4.56**, the simulated electronic excitation spectrum of **EY-Zn** features three distinct absorption bands (refer to **Figure 4.55b**). In analogy to **EY-Na**, the lowest energy excitation peak is constituted of two almost degenerate excitations (***i***$_{\mathbf{EY\text{-}Zn}}$ and ***ii***$_{\mathbf{EY\text{-}Zn}}$) with similar oscillator strengths. The non-relaxed difference density plots (refer to **Figure 4.55c**) indicate a large contribution of the zinc ion to the respective transitions, with electron density being transferred from the Eosin Y moiety to the metal upon excitation. The highest intensity peak in the simulated spectrum is dominated by a single excitation (***iii***$_{\mathbf{EY\text{-}Zn}}$) centered on the xanthene moiety. The highest energy absorption band features contributions of several energetically close lying transitions (***iv***$_{\mathbf{EY\text{-}Zn}}$) mainly corresponding to a transfer of electron density from the xanthene core to the phenyl ring substituent.

To investigate the effects associated with the discussed changes in the optical properties on the catalytic transformation, the photocatalysis action plots of the Eosin Y-sensitized triphenylphosphine oxidation employing the small molecule **EY** as well as polymer **P6,** each after the addition of zinc(II) triflate, as catalysts were studied (refer to **Figure 4.56**). Concentrations and irradiation conditions were kept consistent to the previously discussed action plots in this chapter (refer to Chapter 6.3.4.4 for experimental details).

The pronounced changes in the optical absorption spectra of the catalysts upon metal functionalization are also reflected in the wavelength-dependent reactivity patterns, which again resemble the absorption profiles. While in the absence of Zn(II) the highest conversion of triphenylphosphine to triphenylphosphine oxide was observed upon irradiation at 540 nm, the reactivity at this wavelength was drastically reduced after metal addition. Instead, the maximum catalyst efficiency was observed at 480 nm, with average conversions of 58 % (**EY** + $ZnOTf_2$) and 49 % (**P6** + $ZnOTf_2$), respectively. Overall, the achieved conversions were significantly higher in the wavelength range from 360 nm to 520 nm compared to the situation in the absence of the metal ions. Interestingly, the small molecule and polymeric catalysts performed similarly in terms of the achieved conversions upon irradiation at wavelengths between 360 nm to 460 nm and 560 nm to 580 nm, respectively. However, in the range

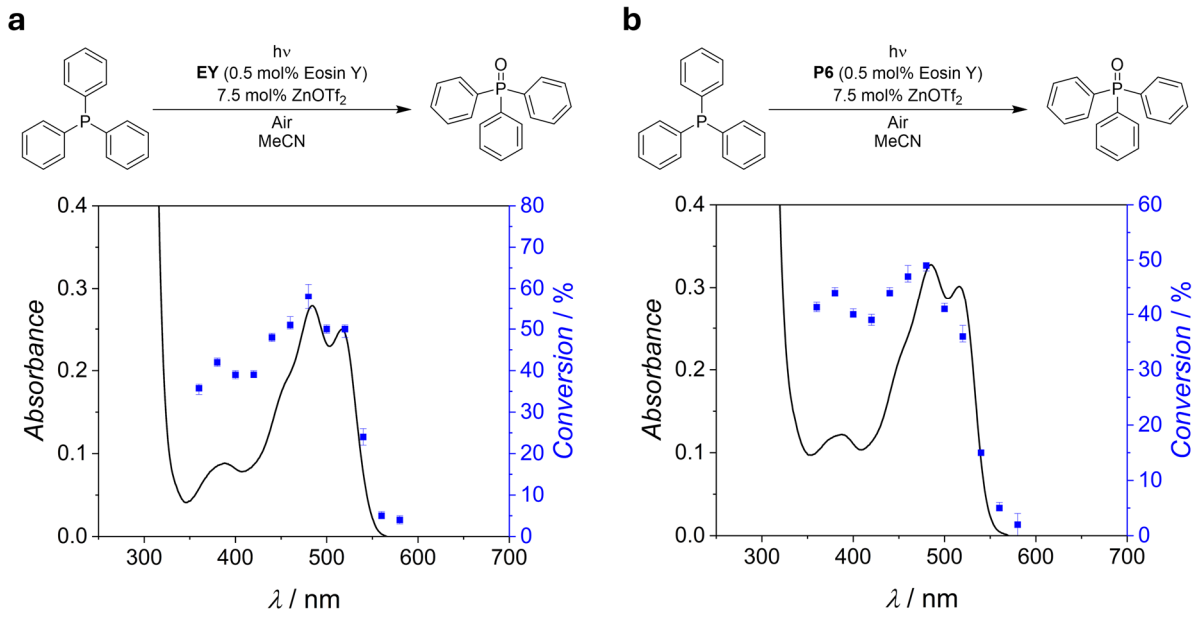

Figure 4.56 Photochemical action plots of the photosensitized oxidation of triphenylphosphine to triphenylphosphine oxide catalyzed by **(a)** small molecule **EY** and **(b) P6**, each after addition of zinc(II) triflate, at an Eosin Y concentration of about 13.4 µmol·L^{-1}, recorded in acetonitrile, showing the conversion of the starting material to the product upon irradiation with the same number of photons (1.10·10^{18} photons) at different wavelengths superimposed with the UV/Vis spectra of the corresponding reaction mixtures. Error bars indicate the lowest and highest determined conversion at each wavelength, respectively.

between 480 nm and 540 nm the small molecule catalyst showed a superior performance, with the difference to the polymeric catalyst being most pronounced at 520 nm, where the small molecule achieved a 14 % increased yield of the catalysis product compared to the polymer catalyst.

The distinct influence of Zn(II) addition on the optical properties and catalytic performance of the Eosin Y-based catalysts is expected to result from the direct interaction of the metal ions with the deprotonated Eosin Y hydroxy group. These interactions can be interrupted by the introduction of an additional ligand displacing the Eosin Y moieties from the inner Zn(II) coordination sphere. Upon deprotonation, the carboxylic acid functionalities present in **P6** can exert this effect, thus enabling access to a stimuli responsive polymeric Eosin Y photocatalyst. Addition of the base lithium hydroxide to an acetonitrile solution containing **P6** and zinc(II) triflate reverted the influence metal addition showed on the optical absorption spectrum of **P6**, except for slightly decreased absorbance values, indicating the successful recovery of the uncomplexed Eosin Y functionalities due to the complexation of the Zn(II) ions by the polymeric carboxylate groups. Contrary, the addition of lithium hydroxide to an acetonitrile

solution of **EY** and zinc(II) triflate did not result in the recovery of the pristine **EY** absorption spectrum, highlighting that the presence of the carboxylate functionalities is critical to the effect observed for **P6**. However, slight changes of the absorption profile with a partial recovery of the peak at λ = 540 nm were also observed for **EY**, indicating an interaction of the Zn(II)-**EY** complex with the added hydroxide ions, presumably partially releasing **EY** from the inner Zn(II) coordination sphere.

The discrepancies in the effects base addition showed on the optical absorption spectra of **EY** and **P6** in the presence of zinc(II) triflate are also reflected in the wavelength-resolved reactivity patterns of the photocatalytic triphenylphosphine oxidation as is evident from the photochemical action plots depicted in **Figure 4.57**. In the case of **P6**, within the methodological error boundaries, the same wavelength-dependent conversions of the catalysis substrate to the desired product were obtained as for the pristine polymer (refer to **Figure 4.54b**), demonstrating the effective reversion of the metal functionalization of the Eosin Y moieties upon base addition. In the case of **EY**, on the other hand, the wavelength-dependent reactivity pattern is not reminiscent of that of the pristine small molecule **EY** (refer

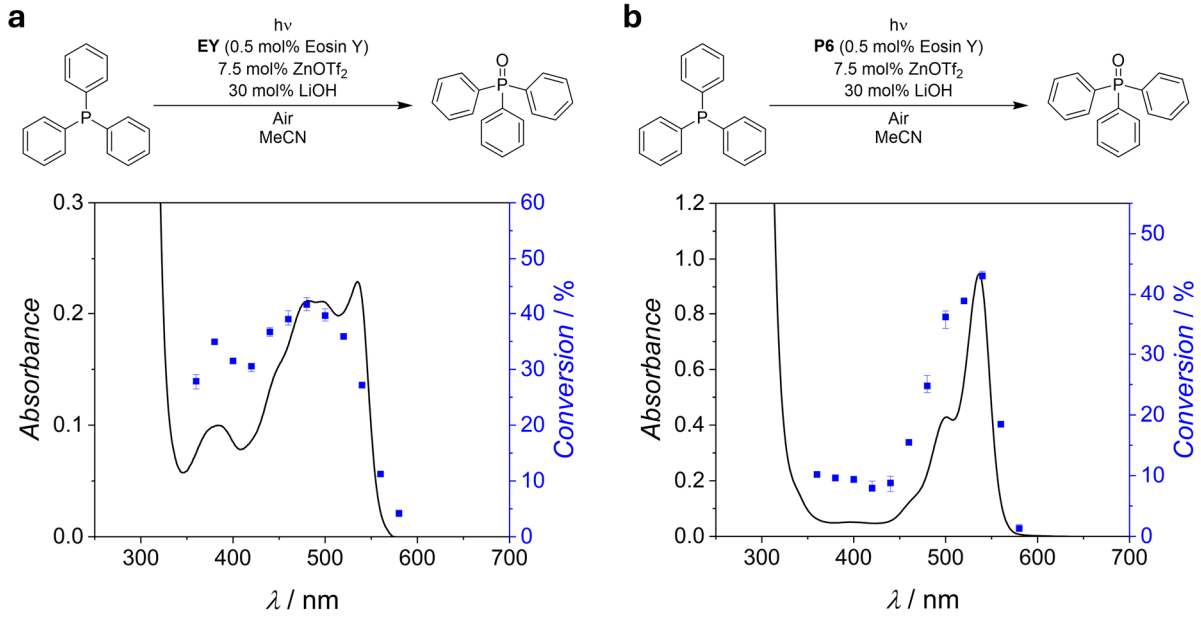

Figure 4.57 Photochemical action plots of the photosensitized oxidation of triphenylphosphine to triphenylphosphine oxide catalyzed by **(a)** small molecule **EY** and **(b) P6**, each after addition of lithium hydroxide and zinc(II) triflate, at an Eosin Y concentration of about 13.4 µmol·L^{-1}, recorded in acetonitrile, showing the conversion of the starting material to the product upon irradiation with the same number of photons (1.10·10^{18} photons) at different wavelengths superimposed with the UV/Vis spectra of the corresponding reaction mixtures. Error bars indicate the lowest and highest determined conversion at each wavelength, respectively.

to **Figure 4.54a**) and resembles the reactivity profile observed for **EY** in the presence of zinc(II) triflate instead (refer to **Figure 4.56a**), again highlighting that the presence of the carboxylate functionalities is critical to the effect observed for **P6**. It is worth noting that base addition consistently reduced the substrate conversions by about 10 % in the wavelength range from 360 nm to 520 nm compared to **EY** in the presence of zinc(II) triflate without added base, while the conversions remained almost uninfluenced in the region 540 nm to 580 nm.

To gather a more detailed understanding of the processes occurring upon metal functionalization of **EY** and **P6** as well as base addition, further experimental studies were undertaken. **Figure 4.58a** shows the aromatic region of the ^{1}H NMR spectra of **EY** acquired in CD_3CN in the absence and presence of zinc(II) triflate as well as in the concomitant presence of zinc(II) triflate and lithium hydroxide. It is evident that the addition of zinc(II) triflate to **EY** is accompanied by a downfield shift of the aromatic resonances, indicating removal of electron density from the xanthene core, in line with the expected interactions of the Lewis acidic metal ions with the dye molecules. This remained virtually unaltered upon lithium hydroxide addition. When zinc(II) triflate is added to an acetonitrile solution of **P6**, DLS measurements (refer to **Figure 4.58b**) revealed an increase in the solvodynamic diameter from D_s = 7.33 nm (**P6**) to D_s = 11.53 nm (**P6** + $ZnOTf_2$), showing that the metal ions are incorporated into the macromolecules, causing their swelling. Deprotonation of the polymer-bound carboxylic acid functionalities proved to compact the structures again, resulting in a solvodynamic diameter of D_s = 8.55 nm (**P6** + $ZnOTf_2$ + LiOH). This observation suggests the formation of SCNPs folded by the coordination of polymer carboxylate groups to the zinc ions.

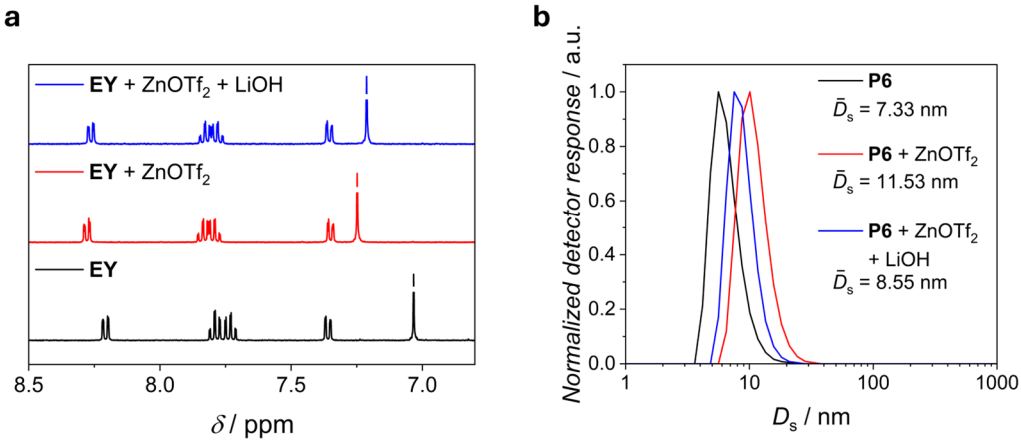

Figure 4.58 (a) Stacked ^{1}H NMR spectra (400 MHz, CD_3CN, 298 K) of **EY** (black) and **EY** after consecutive addition of zinc(II) triflate (red) and lithium hydroxide (blue). **(b)** Superimposed number-weighted DLS size distributions (CH_3CN, mean diameter by number, average values derived from five measurements) of **P6** (black) and **P6** after consecutive addition of zinc(II) triflate (red) and lithium hydroxide (blue).

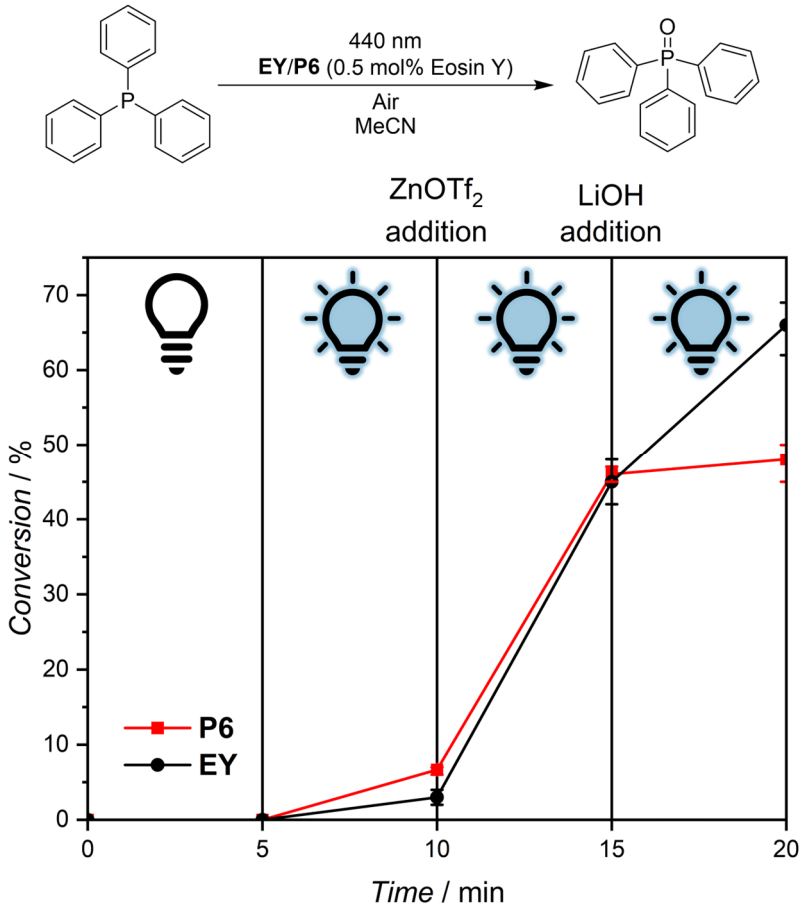

Figure 4.59 Conversion of triphenylphosphine to triphenylphosphine oxide in the photosensitized oxidation catalyzed by small molecule **EY** (black) and **P6** (red) at an Eosin Y concentration of about 13.4 µmol·L^{-1} in acetonitrile without irradiation (0-5 minutes), upon irradiation at 440 nm (5-10 minutes, 1.10·10^{18} photons) and continued irradiation at 440 nm after addition of zinc(II) triflate (10-15 minutes, 1.10·10^{18} photons) and lithium hydroxide (15-20 minutes, 1.10·10^{18} photons). Error bars indicate the lowest and highest determined conversion at each wavelength, respectively.

The response of **P6** to chemical stimuli, altering the optical absorption properties and concomitantly the rate of the photocatalytic transformation of triphenylphosphine to triphenylphosphine oxide, serves as a blueprint for chemically on-off switchable polymeric photocatalysts. To demonstrate the applicability of this concept, **P6** was again employed as a catalyst for the photosensitized triphenylphosphine oxidation in acetonitrile (refer to **Figure 4.59** and Chapter 6.3.4.5). Without irradiation, no conversion of the starting material was observed, demonstrating that light is critical for the catalytic reaction to take place. After five minutes in the dark, the sample was irradiated with 1.10·10^{18} photons within five minutes at 440 nm, a wavelength at which the photochemical action plot of **P6** showed a local minimum of the catalytic activity, thus marking an inactive state (refer to **Figure 4.54b**). As expected, only a negligible conversion of the substrate to the catalysis product of about 5 % was reached.

The catalyst could be switched on by the addition of zinc(II) triflate, leading to a substantial increase of the catalytic rate upon 440 nm light exposure (refer to **Figure 4.56b**). Irradiation at 440 nm with $1.10 \cdot 10^{18}$ photons over five minutes led to a substrate conversion of almost 50 %. The catalyst could be switched off again by the addition of lithium hydroxide, causing displacement of the dye moieties from the inner Zn(II) coordination sphere by the polymer-bound carboxylate functionalities, thus diminishing the effect of the metal ions on the catalytic rate (refer to **Figure 4.57b**). Indeed, continuing the irradiation at 440 nm with additional $1.10 \cdot 10^{18}$ photons over five minutes only led to a negligible increase of the catalysis product yield, demonstrating the successful on-off switching of the catalytic activity of the Eosin Y-functionalized polymeric photocatalyst **P6**. As indicated by the photochemical action plot data discussed in detail above, the same could not be achieved with the small molecule catalyst **EY** under otherwise identical conditions (refer to **Figure 4.59**). While addition of the metal salt successfully turned the catalytic activity on, it could not be switched off again by base addition as the hydroxide ions were insufficient to quantitatively replace **EY** from the inner coordination sphere of the zinc ions, highlighting the unique opportunities provided by multifunctional polymer catalysts.

4.4.4 Summary

The successful functionalization of macromolecules with the xanthene dye Eosin Y is described and the photosensitization capabilities, enabling the efficient oxygen-mediated photocatalytic oxidation of triphenylphosphine to triphenylphosphine oxide, were explored following the photochemical action plot methodology.

Initially, a copolymer of poly(ethylene glycol) methyl ether methacrylate, glycidyl methacrylate and the Eosin Y methacrylate monomer 2-(methacryloyloxy)ethyl 2-(2,4,5,7-tetrabromo-6-hydroxy-3-oxo-3*H*-xanthen-9-yl)benzoate (Polymer **P5**) was synthesized and collapsed intramolecularly by a thiol-epoxy click reaction of the polymeric epoxide functionalities with the organic dithiol crosslinker 1,4-benzenedimethanethiol, resulting in the first Eosin Y single-chain nanoparticles (SCNPs) **SCNP5-EY**. Successful single-chain folding was evidenced by nuclear magnetic resonance spectroscopy (NMR), size-exclusion chromatography (SEC), dynamic light scattering (DLS) and diffusion-ordered spectroscopy (DOSY).

The wavelength-dependent catalyst efficiency was explored following the photochemical action plot methodology and compared to the performance of the small molecule model

system 2-(propionyloxy)ethyl 2-(2,4,5,7-tetrabromo-6-hydroxy-3-oxo-3*H*-xanthen-9-yl)benzoate (**EY**), representative of the Eosin Y functionalities within the polymer. It was found that the polymeric catalyst **SCNP5-EY** consistently achieved a slightly higher yield of the catalysis product compared to **EY** under otherwise identical conditions, highlighting the beneficial effect provided by the SCNP environment. At the same time, the recorded action plots were the first examples investigating a photocatalytic reaction, thus pioneering a future research area revolving around photocatalysis action plots.

The unique opportunities provided by multifunctional polymers were explored in more detail for a second Eosin Y copolymer, constituted of poly(ethylene glycol) methyl ether methacrylate, 2-carboxyethyl acrylate and 2-(methacryloyloxy)ethyl 2-(2,4,5,7-tetrabromo-6-hydroxy-3-oxo-3*H*-xanthen-9-yl)benzoate (Polymer **P6**).

Employing **P6** as a catalyst for the photosensitized triphenylphosphine oxidation resulted in an action plot similar to the ones of **EY** and **SCNP5-EY**. The addition of zinc(II) triflate proved to exert a substantial influence on the optical absorption spectra of **EY** and **P6**, reflected in drastic changes of the wavelength-dependent reactivity profiles in the corresponding photocatalysis action plots, most likely resulting from interactions of the Eosin Y hydroxy group with the Zn(II) ions as indicated by time-dependent density functional theory (TDDFT) calculations. For **P6**, the influence of metal functionalization could be reversed by SCNP formation upon base addition, providing access to an on-off switchable polymeric photocatalyst.

Chapter 5: Summary and Outlook

5.1 SUMMARY AND OUTLOOK

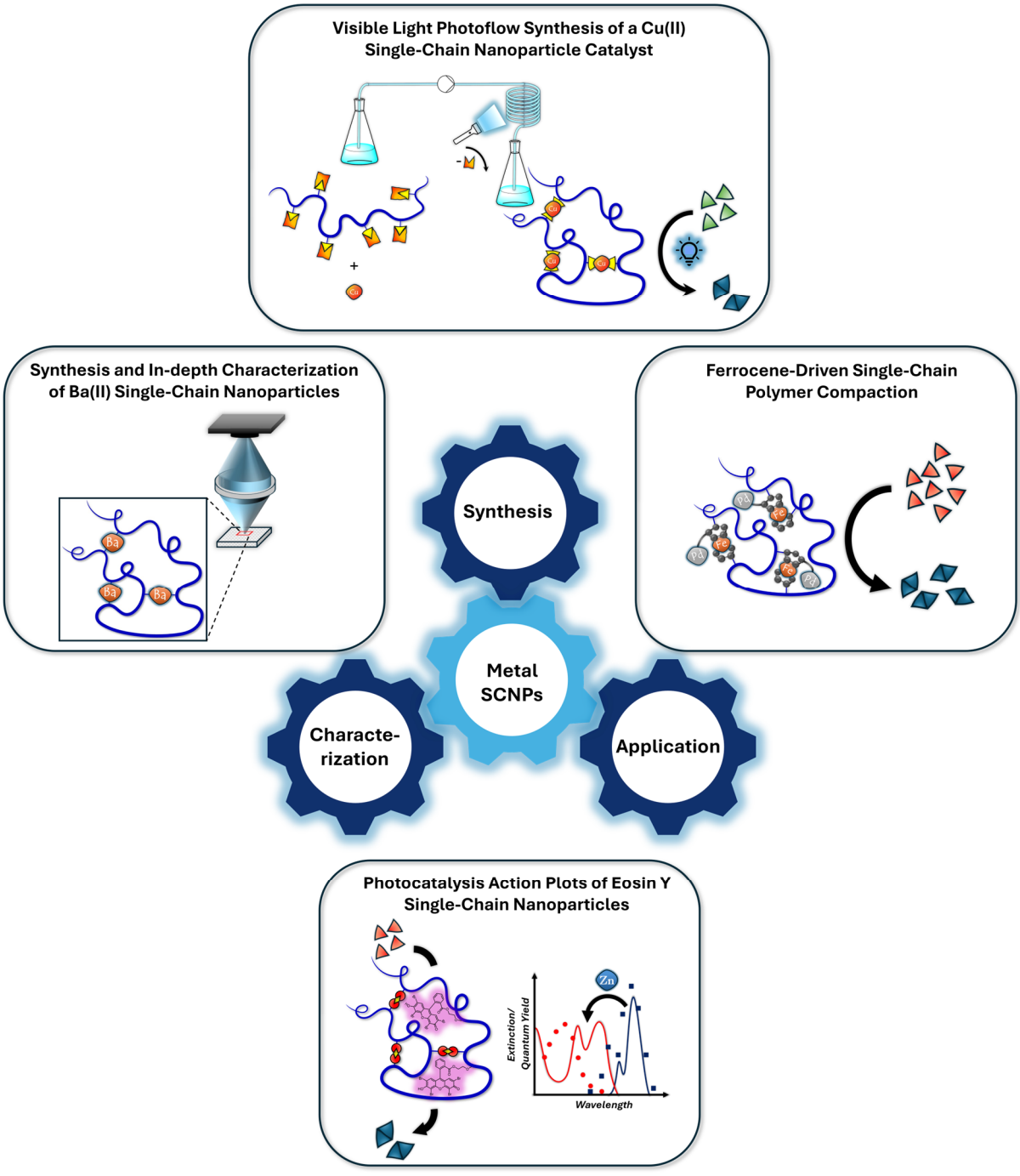

Figure 5.1 Overview of the work on the synthesis, characterization and catalytic application of metal-functionalized single-chain nanoparticles (SCNPs) presented in this thesis.

Single-chain nanoparticles (SCNPs), constructed by the intramolecular crosslinking of individual macromolecular chains, have been the subject of intense research and explored as a new class of polymeric materials in recent years. Combining the tunable characteristics of synthetic macromolecules with the diverse range of functionalities provided by metals and their complexes constitutes the field of metal-functionalized SCNPs.

The aim of the current thesis was to exploit the synergistic combination of inorganic and polymer chemistry to critically push the current boundaries of the field of metal-functionalized SCNPs by addressing the interconnected omnipresent challenges of synthesis and characterization as well as the utilization of the newly synthesized metal-functionalized SCNPs in advanced catalytic applications (refer to **Figure 5.1**).

Initially, the synthesis of barium-functionalized SCNPs was explored in Chapter 4.1, contributing to the currently underexplored field of main group metal SCNPs. The synthesis of two Ba(II)-folded SCNPs with different polarity is described. Specifically, barium-mediated single-chain compaction was achieved by the reaction of suitable Ba(II) precursors with carboxylic acid functionalities in copolymers of styrene and 4-vinylbenzoic acid (**SCNP1-Ba**) as well as poly(ethylene glycol) methyl ether methacrylate and 2-carboxyethyl acrylate (**SCNP2-Ba**), respectively. Sophisticated molecular dynamics simulations revealed the reversible nature of the barium polymer interactions in solutions of the acrylate-based SCNPs which enabled the targeted control over the polymer morphology by exploiting the low solubility of barium sulfate in aqueous solution to reverse the SCNP folding reaction. The high contrast provided by the heavy metal ions paved the way towards scanning transmission electron microscopy (STEM) imaging of individual barium atoms within SCNPs, providing unprecedented in-depth insights on the number and distribution of metal ions on the level of individual macromolecules inaccessible by any other analytical technique established to date. The described results are expected to inspire future work in the realm of main group element, especially s block metal-folded, SCNPs. For instance, the systematic synthesis of isostructural alkaline earth metal-folded SCNPs should give access to size-tunable metallopolymers by exploiting the differences in ionic radii of the elements when descending the periodic table, providing precise control over the size of functional pockets within the nanoparticles. This could be achieved by extending the synthetic strategy used for **SCNP1-Ba** and **SCNP2-Ba** to the lighter homologues of barium, starting from otherwise identical precursor compounds. Moreover, the developed methodology to image individual heavy atoms within SCNPs by

STEM is expected to lead to a critical enhancement of the understanding of the structure-property relationships of metal-functionalized SCNPs and other metallopolymers in general in future studies.

Chapter 4.2 aimed at addressing the prevalent scalability challenge in SCNP synthesis by describing the first visible light driven photoflow synthesis of catalytically active SCNPs. The design approach was based on a poly(ethylene glycol) methyl ether methacrylate polymer backbone, copolymerized with a photocleavable 2-((((2-nitrobenzyl)oxy)carbonyl)amino)ethyl methacrylate monomer, which can liberate amine groups upon visible light irradiation, leading to single-chain collapse by the complexation of Cu(II) ions via the liberated amines. Initial experiments were carried out following a classical batch synthesis protocol (**SCNP3-Cu-Batch**). After these successful proof-of-concept studies, the approach was transferred to continuous flow employing a commercially available photoflow reactor (**SCNP3-Cu-Flow**). The catalytic activity of the prepared Cu(II)-functionalized SCNPs for the visible light photocatalyzed cleavage of carbon-carbon single and double bonds was explored on the examples of xanthene-9-carboxylic acid and oleic acid. The SCNP catalyst proved to be significantly more efficient than the small molecule copper(II) chloride dihydrate, which was traced back to the coordination of amine ligands to the copper ions within the SCNP environment.

Upscaling the synthetically accessible amount of nanoparticles is crucial for future applications of single-chain technology. The described work serves as a blueprint for further explorations of the opportunities provided by continuous flow syntheses of functional SCNPs. To achieve efficient upscaling, future research efforts need to focus on increasing the polymer concentration and flowrate of the process described herein. This could be accomplished by employing a photolabile protecting group, the cleavage of which proceeds via a non-radical mechanistic pathway. Furthermore, the developed methodology of using photolabile protecting groups to achieve single-chain folding could be applied to the synthesis of multimetallic structures by the introduction of a second orthogonal ligand system into the polymer scaffold. If two photolabile protecting groups cleavable at different wavelengths were used, the formation of multimetallic SCNPs using different colors of light could be achieved.

The synthesis of heteromultimetallic SCNPs following non-photochemical pathways was explored in Chapter 4.3. The archetypical sandwich complex ferrocene was introduced as a covalently bonded SCNP crosslinker, inducing the intramolecular folding of a poly(styrene-*co*-

4-chloromethyl styrene) copolymer. In proof-of-concept work, the copolymer was reacted with *in situ* prepared 1,1'-dilithioferrocene to introduce ferrocene itself as SCNP folding unit (**SCNP4-Fc**). Building upon this, the crosslinking ferrocene moiety was supplemented with the bidentate nitrogen donor ligand 1,10-phenanthroline and the ferrocene derivative 2-ferrocenyl-1,10-phenanthroline employed to induce the single-chain collapse (**SCNP4-FcPhen**). The donor ligand functionalization provided a pathway towards the coordination of additional metals, and the reaction of **SCNP4-FcPhen** with dichloro(1,5-cyclooctadiene)-palladium(II) gave access to the first heterobimetallic ferrocene SCNP (**SCNP4-FcPhen-Pd**), the catalytic activity of which was demonstrated on the example of the intramolecular hydroamination of the aminoalkyne 2,2-diphenyl-4-heptyn-1-amine.

Additional experiments indicated the redox-responsive nature of the ferrocene functionalities within the SCNPs. Exploitation of the associated polarity change could provide access to redox-recyclable SCNP catalysts fusing the high catalytic activity of homogeneous catalysts with the simple catalyst separability and recyclability inherent to heterogeneous catalysts. In detail, the ferrocene moieties could be oxidized after completion of a catalytic reaction, leading to the precipitation of the SCNP catalyst in an unpolar solvent which could easily be separated from the catalysis product. The isolated catalyst could subsequently be reduced to restore solubility in unpolar solvents and be employed in further catalytic cycles. Apart from that, exploration of further reactions of the described multimetallic SCNPs could lead to the discovery of synergistic interactions of the metals, for instance, in catalytic cascade reactions.

Synergistic effects between metal ions and other functionalities within the same SCNP were explored in Chapter 4.4. Specifically, the successful functionalization of macromolecules with the xanthene dye Eosin Y is described and the photosensitization capabilities, enabling the efficient oxygen-mediated photocatalytic oxidation of triphenylphosphine to triphenyl-phosphine oxide, investigated following the photochemical action plot methodology. Initially, a copolymer of poly(ethylene glycol) methyl ether methacrylate, glycidyl methacrylate and the Eosin Y methacrylate monomer 2-(methacryloyloxy)ethyl 2-(2,4,5,7-tetrabromo-6-hydroxy-3-oxo-3*H*-xanthen-9-yl)benzoate was synthesized and collapsed intramolecularly by a thiol-epoxy click reaction of the polymeric epoxide functionalities with the organic dithiol crosslinker 1,4-benzenedimethanethiol, resulting in the first Eosin Y SCNPs (**SCNP5-EY**). The wavelength-dependent catalyst efficiency was explored following the photochemical action plot methodology and compared to the performance of the small molecule model system 2-

(propionyloxy)ethyl 2-(2,4,5,7-tetrabromo-6-hydroxy-3-oxo-3*H*-xanthen-9-yl)benzoate (**EY**), representative of the Eosin Y functionalities within the polymer. The polymeric catalyst consistently achieved a slightly higher yield of the catalysis product compared to the small molecule analogue under otherwise identical conditions, highlighting the beneficial effect of the SCNP environment.

The unique opportunities provided by multifunctional polymers were explored in more detail for a second Eosin Y copolymer, constituted of poly(ethylene glycol) methyl ether methacrylate, 2-carboxyethyl acrylate and 2-(methacryloyloxy)ethyl 2-(2,4,5,7-tetrabromo-6-hydroxy-3-oxo-3*H*-xanthen-9-yl)benzoate (Polymer **P6**). The addition of zinc(II) triflate proved to exert a substantial influence on the optical absorption spectrum of the copolymer, reflected in drastic changes of the wavelength-dependent reactivity profile in the corresponding photocatalysis action plot. The influence of metal functionalization could be reversed by SCNP formation upon base addition, providing access to an on-off switchable polymeric photocatalyst.

The described action plots are the first examples investigating a photocatalytic reaction, thus pioneering a future research area revolving around photocatalysis action plots. Continued research efforts in this direction are expected to enhance the efficiency of existing photocatalytic processes and facilitate their combination with other light-driven reactions. Further, the described polymeric systems could be explored with respect to the influence of different metals other than zinc on the photocatalysis action plots as well as other optical properties, such as luminescence lifetimes or emission quantum yields, in future work. Moreover, future studies could explore possible energy or electron transfer processes between the metal and dye functionalities within the polymers.

In summary, this thesis critically expanded the scope of metal-functionalized SCNPs with a particular focus on new synthetic methods, pioneering unprecedented characterization techniques and exploring advanced catalytic functions. The described work is expected to serve as inspiration for future research further pushing the boundaries of the SCNP field. Ideally, continued research efforts will lead to the scalable synthesis of SCNPs with metal functionalities positioned at defined locations within the nanoparticles to create active centers with tailor-made functionalities.

5.2 ZUSAMMENFASSUNG UND AUSBLICK

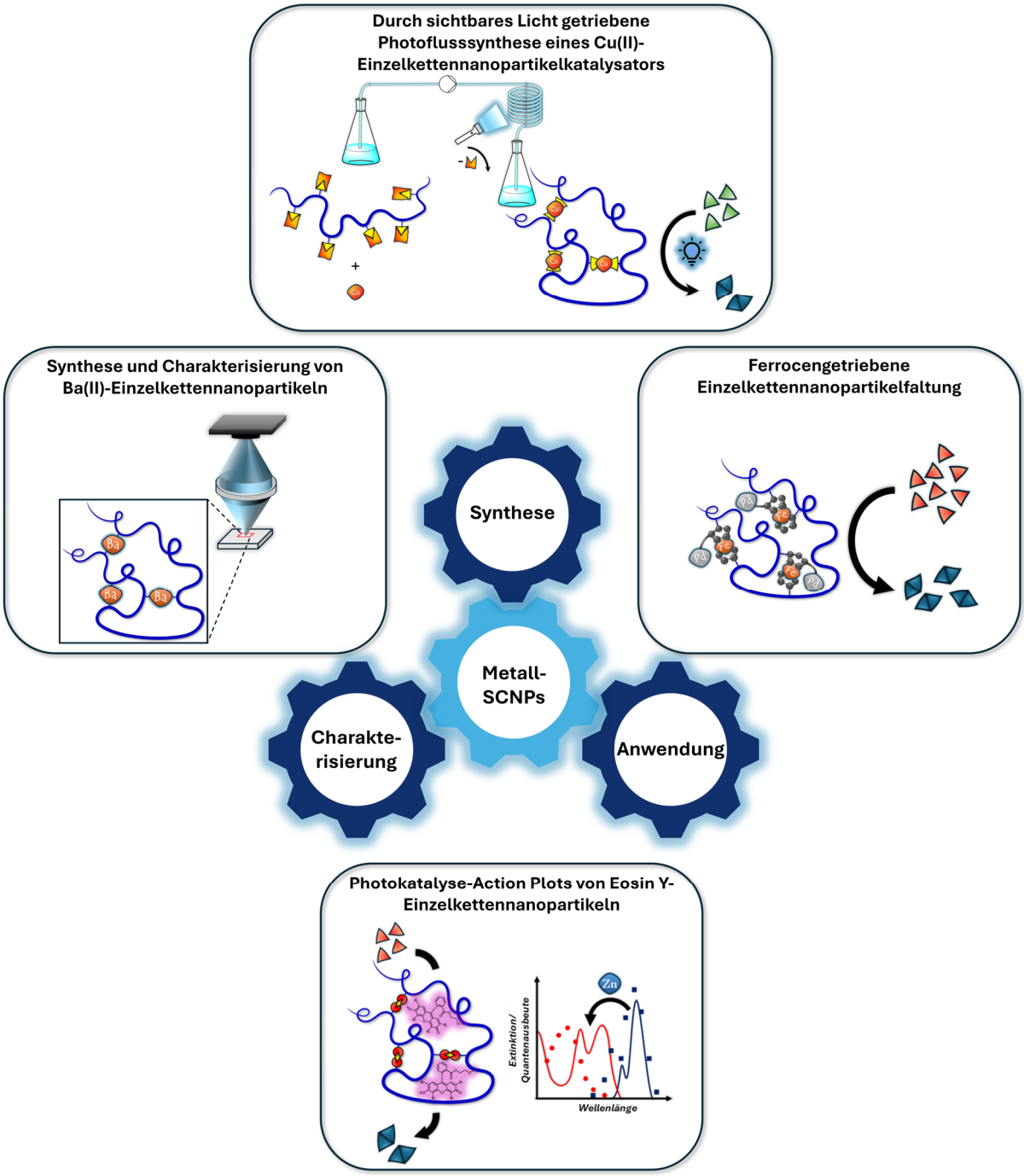

Abbildung 5.2 Überblick über die in der vorliegenden Dissertation dargelegten Arbeiten bezüglich der Synthese, Charakterisierung and katalytischen Anwendung metallfunktionalisierter Einzelkettennanopartikel (Single-chain nanoparticles, SCNPs).

Einzelkettennanopartikel (Single-chain nanoparticles, SCNPs) entstehen durch die intramolekulare Quervernetzung einzelner makromolekularer Ketten und waren in den vergangenen Jahren Gegenstand intensiver Forschung als eine neue Klasse polymerer Materialien. Die Kombination der abstimmbaren Eigenschaften synthetischer Makromoleküle mit den diversen Funktionalitäten von Metallen sowie deren Komplexen bildet das Gebiet der metallfunktionalisierten SCNPs.

Ziel der vorliegenden Arbeit war die synergistische Kombination von anorganischer Chemie und Polymerchemie, um die gegenwärtigen Grenzen des Gebiets der metallfunktionalisierten SCNPs zu verschieben. Dies sollte durch Adressierung allgegenwärtiger Herausforderungen in den Bereichen Synthese und Charakterisierung sowie die katalytische Anwendung der neu dargestellten metallfunktionalisierten SCNPs erreicht werden (siehe **Abbildung 5.2**).

Zu Beginn wurde in Kapitel 4.1 die Synthese bariumfunktionalisierter SCNPs dargelegt, um das weitgehend unerforschte Gebiet der Hauptgruppenmetall-SCNPs zu erweitern. Die Synthese zweier Ba(II)-gefalteter SCNPs mit verschiedenartiger Polarität ist beschrieben. Barium-vermittelte Einzelkettennanopartikelfaltung wurde durch die Reaktion geeigneter Ba(II)-Vorläuferverbindungen mit Carbonsäurefunktionalitäten in Copolymeren bestehend aus Styrol und 4-Vinylbenzoesäure (**SCNP1-Ba**) beziehungsweise Poly(ethylenglycol)methyl-ethermethacrylat und 2-Carboxyethylacrylat (**SCNP2-Ba**) erreicht. Molekulardynamiksimulationen offenbarten die reversible Natur der Barium-Polymer-Wechselwirkungen in Lösungen der acrylatbasierten SCNPs, was die gezielte Kontrolle der Polymermorphologie durch Ausnutzung der geringen Löslichkeit von Bariumsulfat in Wasser zur Umkehr der SCNP-Faltungsreaktion gestattete. Der durch die Schwermetallionen gegebene hohe Kontrast ermöglichte die Darstellung einzelner Bariumatome innerhalb der SCNPs durch Rastertransmissionselektronenmikroskopie, was beispiellose Einblicke in die Anzahl und Verteilung von Metallionen innerhalb isolierter Makromoleküle gestattete, welche derzeit durch keine andere etablierte analytische Methode zugänglich wären.

Es wird erwartet, dass die beschriebenen Ergebnisse als Inspiration für weitere Arbeiten auf dem Gebiet der Hauptgruppenelement-, insbesondere s-Block-Metall-gefalteter-, SCNPs dienen. Beispielsweise sollte die systematische Synthese isostruktureller Erdalkalimetall-SCNPs, durch Ausnutzung der Unterschiede in den Ionenradien der Elemente, Zugang zu größeneinstellbaren Metallopolymeren gewähren und somit präzise Kontrolle über die Größe funktioneller Taschen innerhalb der Nanopartikel ermöglichen. Erreicht werden könnte dies

durch die Übertragung des für **SCNP1-Ba** und **SCNP2-Ba** genutzten Syntheseansatzes auf die leichteren Homologen des Bariums, wobei von ansonsten identischen Ausgangsmaterialien ausgegangen werden kann. Des Weiteren wird erwartet, dass die neu entwickelte Methode der bildgebenden Darstellung einzelner Schwermetallatome innerhalb eines SCNPs durch Rastertransmissionselektronenmikroskopie in künftigen Studien zu signifikanten Fortschritten im Verständnis von Struktur-Eigenschafts-Beziehungen metallfunktionalisierter SCNPs, beziehungsweise Metallopolymeren im Allgemeinen, führt.

Kapitel 4.2 adressierte die omnipräsente Skalierbarkeitsproblematik von SCNP-Synthesen durch Beschreibung der ersten durch sichtbares Licht getriebenen Photoflusssynthese katalytisch aktiver SCNPs. Der Designansatz basierte auf einem Poly(ethylenglycol)methyl-ethermethacrylat-Polymerrückgrat copolymerisiert mit dem photospaltbaren Monomer 2-((((2-Nitrobenzyl)oxy)carbonyl)amino)ethylmethacrylat, das bei Bestrahlung mit sichtbarem Licht Aminogruppen freizusetzen vermag, deren Koordination an Cu(II)-Ionen zum Einzelkettenkollaps führte. Nach erfolgreichen Machbarkeitsstudien, einem klassischen Batchsynthesepotokoll folgend (**SCNP3-Cu-Batch**), wurde der Ansatz in kontinuierlichen Durchfluss unter Verwendung eines kommerziell erhältlichen Photoflussreaktors übertragen (**SCNP3-Cu-Flow**). Die katalytische Aktivität der dargestellten Cu(II)-funktionalisierten SCNPs wurde anhand der durch sichtbares Licht getriebenen katalytischen Spaltung von Kohlenstoff-Kohlenstoff Einfachbindungen und Doppelbindungen an den Beispielen Xanthen-9-carbonsäure und Ölsäure demonstriert. Der SCNP-Katalysator zeigte dabei eine gegenüber dem niedermolekularen Katalysator Kuper(II)-chlorid Dihydrat signifikant erhöhte Effizienz, was auf die Koordination von Aminliganden an die Kupferionen innerhalb der SCNP-Umgebung zurückgeführt werden konnte.

Die Aufskalierung der synthetisch zugänglichen Menge an Nanopartikeln ist von kritischer Relevanz für zukünftige Anwendungen der Einzelkettentechnologie. Die beschriebenen Arbeiten fungieren als Grundlage für die weitere Erforschung der durch kontinuierliche Flusssynthese für die Darstellung funktionaler SCNPs gebotenen Möglichkeiten. Um eine effiziente Skalierung zu erreichen, sollten künftige Forschungsarbeiten auf die Erhöhung der Polymerkonzentration und Flussrate des hierin beschriebenen Prozesses fokussiert werden. Dies könnte durch den Einsatz einer photolabilen Schutzgruppe, deren Spaltung über einen nicht-radikalischen mechanistischen Pfad verläuft, erreichbar sein. Darüber hinaus bietet die entwickelte Methodik der Verwendung photolabiler Schutzgruppen für die

Einzelkettenfaltung Potenzial zur Synthese multimetallischer Strukturen durch Einsatz eines zweiten, orthogonalen Ligandensystems innerhalb des Polymergerüsts. Durch Verwendung zweier photolabiler, durch sich differenzierende Lichtwellenlängen spaltbarer, Schutzgruppen könnte der Aufbau multimetallischer SCNPs durch verschiedene Lichtfarben erreicht werden. Die Synthese heteromultimetallischer SCNPs auf nicht-photochemischem Wege wurde in Kapitel 4.3 untersucht. Der archetypische Sandwichkomplex Ferrocen wurde als kovalent gebundener SCNP-Quervernetzer eingeführt, mit dem die intramolekulare Faltung eines Poly(styrol-*co*-4-chlormethylstyrol)-Copolymers erzielt werden konnte. In anfänglichen Studien wurde das Copolymer mit *in situ* präpariertem 1,1‘-Dilithioferrocen umgesetzt und somit Ferrocen selbst als Falteinheit eingeführt (**SCNP4-Fc**). Darauf aufbauend wurde die quervernetzende Einheit um den bidentaten Stickstoffdonorliganden 1,10-Phenanthrolin ergänzt, indem das Ferrocenderivat 2-Ferrocenyl-1,10-phenanthrolin für die Einzelketten-faltung verwendet wurde (**SCNP4-FcPhen**). Die Donorligandfunktionalisierung der Falteinheit gestattete den Aufbau des ersten heterobimetallischen Ferrocen-SCNPs (**SCNP4-FcPhen-Pd**) durch die Reaktion von **SCNP4-FcPhen** mit Dichlor(1,5-cyclooctadien)palladium(II). Die katalytische Aktivität desselben wurde am Beispiel der intramolekularen Hydroaminierung des Aminoalkins 2,2-Diphenyl-4-heptin-1-amin demonstriert.

Weitergehende Experimente indizierten die redox-responsive Natur der Ferroceneinheiten innerhalb der SCNPs. Die Ausnutzung der damit einhergehenden Polaritätsvariation könnte Zugang zu redox-rezyklierbaren SCNP-Katalysatoren gestatten und damit die Kombination der hohen katalytischen Aktivität von Homogenkatalysatoren mit der einfachen Abtrennbarkeit und Wiederverwendbarkeit von Heterogenkatalysatoren. Im Detail könnten die Ferrocen-einheiten nach Ablauf einer katalytischen Reaktion oxidiert werden, was in unpolaren Lösungsmitteln zur Ausfällung des Katalysators führen und diesen so vom Katalyseprodukt isolierbar machen sollte. Der isolierte Katalysator könnte schließlich reduzierenden Bedingungen unterworfen werden, was dessen Löslichkeit in unpolaren Lösungsmitteln wiederherstellen sollte, und im Anschluss für weitere Katalysezyklen verwendet werden. Davon abgesehen könnte die weitergehende Erforschung von Folgereaktionen der beschriebenen multimetallischen SCNPs zur Entdeckung synergistischer Interaktionen der Metalle führen, beispielsweise in katalytischen Kaskadereaktionen.

Synergistische Effekte zwischen Metallionen und weiteren Funktionalitäten innerhalb eines SCNPs wurden in Kapitel 4.4 betrachtet. Beschrieben ist die Funktionalisierung von

Makromolekülen mit dem Xanthenfarbstoff Eosin Y. Die Fähigkeit der resultierenden Polymere zur Photosensibilisierung von Sauerstoff zur Oxidation von Triphenylphosphan zu Triphenylphosphanoxid wurde mittels der photochemischen Action Plot-Methode untersucht. Zu Beginn erfolgte die Synthese eines Copolymers bestehend aus Poly(ethylenglycol)methylethermethacrylat, Glycidylmethacrylat sowie dem Eosin Y-Methacrylat-Monomer 2-(Methacryloyloxy)ethyl-2-(2,4,5,7-tetrabrom-6-hydroxy-3-oxo-3*H*-xanthen-9-yl)benzoat, welches durch eine Thiol-Epoxy Click-Reaktion der polymergebundenen Epoxid-Funktionalitäten mit dem organischen Dithiol 1,4-Benzoldimethanthiol intramolekular zum ersten Beispiel eines Eosin Y-SCNPs gefaltet wurde (**SCNP5-EY**). Die Wellenlängenabhängigkeit der Katalysatoreffizienz wurde mittels der photochemischen Action Plot-Methode untersucht und mit dem Modellsystem 2-(Propionyloxy)ethyl-2-(2,4,5,7-tetrabrom-6-hydroxy-3-oxo-3*H*-xanthen-9-yl)benzoat (**EY**) als niedermolekularem Repräsentanten der polymergebundenen Eosin Y-Funktionalitäten verglichen. Der polymere Katalysator erzielte dabei bei allen betrachteten Wellenlängen geringfügig höhere Ausbeuten des Katalyseprodukts verglichen mit dem niedermolekularen Modellsystem unter anderweitig identischen Reaktionsbedingungen, was den vorteilhaften Einfluss der SCNP-Umgebung unterstreicht.

Die durch multifunktionelle Polymere eröffneten einzigartigen Möglichkeiten wurden weitergehend anhand eines zweiten Eosin Y-Copolymers, bestehend aus Poly(ethylenglycol)-methylethermethacrylat, 2-Carboxyethylacrylat sowie dem Eosin Y-Methacrylat-Monomer 2-(Methacryloyloxy)ethyl-2-(2,4,5,7-tetrabrom-6-hydroxy-3-oxo-3*H*-xanthen-9-yl)benzoat, untersucht (Polymer **P6**). Durch Zugabe von Zink(II)-triflat konnte ein substantieller Effekt auf das optische Absorptionsspektrum des Copolymers ausgeübt werden, welcher sich in einer ausgeprägten Beeinflussung des wellenlängenabhängigen Reaktionsprofils im zugehörigen photochemischen Action Plot manifestierte. Der Einfluss der Metallfunktionalisierung konnte durch SCNP-Bildung bei Basenzugabe umgekehrt werden, wodurch ein selektives Einschalten und Ausschalten der photokatalytischen Aktivität bei einer gegebenen Wellenlänge erreicht werden konnte.

Die beschriebenen Action Plots stellen die ersten Beispiele derartiger Untersuchung an photokatalytischen Reaktionen dar und dienen somit als Inspiration für weitere Forschung im Gebiet der Photokatalyse-Action Plots. Es wird erwartet, dass dies zur Erhöhung der Effizienz existierender photokatalytischer Prozesse führt sowie deren Kombination mit anderen

lichtgetriebenen Reaktionen erleichtert. Daneben könnte in zukünftigen Arbeiten der Einfluss von Zink verschiedener Metallionen auf die Photokatalyse-Action Plots des dargestellten Polymersystems sowie weitere optische Eigenschaften, beispielsweise Lumineszenz-lebensdauern oder Emissionquantenausbeuten, weitergehend untersucht werden. Ferner könnten weitere Studien potenziell zwischen Metall und Farbstoff auftretende Energie- oder Elektronentransferprozesse erforschen.

Zusammenfassend stellt die vorliegende Dissertation eine signifikante Erweiterung der durch metallfunktionalisierte Einzelkettennanopartikel zugänglichen Möglichkeiten dar, wobei ein besonderer Fokus auf neue synthetische Methoden, beispiellose Charakterisierungstechniken sowie die Erforschung fortschrittlicher katalytischer Reaktionen gelegt wurde. Die Arbeit dient somit als Inspiration für künftige Forschung, um die Grenzen des SCNP-Gebiets weiter voranzutreiben. Im Idealfall führen weitergehende Forschungsarbeiten zur skalierbaren Synthese von SCNPs mit an definierten Positionen innerhalb der Nanopartikel lokalisierten Metallfunktionalitäten, um so aktive Zentren mit maßgeschneiderten Funktionen zu kreieren.

Chapter 6: Experimental Part

6.1 MATERIALS AND METHODS

Acetonitrile (HPLC grade, Fisher Chemical), acetonitrile-d_3 (99.8 % D, Sigma-Aldrich), barium hydroxide octahydrate (98 %, Sigma-Aldrich), barium iodide (97 %, anhydrous, abcr), 1,4-benzenedimethanethiol (98 %, Sigma-Aldrich), *n*-butylamine (99 %, Merck), copper(II) chloride dihydrate (99 %, ChemSupply), 2-cyano-2-propyl benzodithioate (97 %, Sigma-Aldrich), deuterium oxide (99.9 % D, Sigma-Aldrich), dichloro(1,5-cyclooctadiene)palladium(II) (36.7 % Pd, Alfa Aesar), diethyl ether (99.5 %, anhydrous, Thermo Fisher Scientific), dimethylanilinium tetrakis(pentafluorophenyl)borate (98 %, abcr), 1,4-dioxane (99.8 %, anhydrous, Sigma-Aldrich), ferrocene (98 %, Merck), lithium hydroxide (98 %, Sigma-Aldrich), methanol (99.8 %, VWR), *n*-butyllithium (1.6 mol·L^{-1} or 2.5 mol·L^{-1} in hexane, Thermo Fisher Scientific), *n*-hexane (95 %, Merck), *n*-pentane (98 %, anhydrous, Thermo Fisher Scientific), oleic acid (90 %, technical grade, Alfa Aesar), 2-phenylethylamine (99 %, Thermo Fisher Scientific), potassium *tert*-butoxide (98 %, Merck), pyrene (99 %, Sigma-Aldrich), triphenylphosphine (99 %, Sigma-Aldrich), 4-vinylbenzoic acid (97 %, Merck), xanthene-9-carboxylic acid (98 %, Combi-Blocks) and zinc(II) triflate (98 %, Sigma-Aldrich) were used as received. Azobisisobutyronitrile (obtained as 12 wt% solution in acetone, Sigma-Aldrich) was recrystallized from methanol prior to use. 2-Carboxyethyl acrylate (Sigma-Aldrich), 4-chloromethyl styrene (90 %, Thermo Fisher Scientific), glycidyl methacrylate (97 %, Sigma-Aldrich), poly(ethylene glycol) methyl ether methacrylate (average M_n = 300 g·mol^{-1}, Sigma-Aldrich) and styrene (99.5 %, Thermo Fisher Scientific) were passed over a column of basic alumina (VWR) prior to polymerization. Sephadex LH-20 (Cytiva) was swollen overnight in acetonitrile before use. Pre-wetted RC Spectra/Por dialysis tubing (10 kDa molecular weight cutoff) was used for dialysis.

2,2-Diphenyl-4-heptyn-1-amine,[6] 2-ferrocenyl-1,10-phenanthroline,[283] 2-(methacryloyl-oxy)ethyl 2-(2,4,5,7-tetrabromo-6-hydroxy-3-oxo-3*H*-xanthen-9-yl)benzoate,[277] 2-((((2-nitro-benzyl)oxy)carbonyl)amino)ethyl methacrylate,[284] 2-(propionyloxy)ethyl 2-(2,4,5,7-tetra-bromo-6-hydroxy-3-oxo-3*H*-xanthen-9-yl)benzoate[277,285] and 2,2,6,6-tetramethyl-1-(1-phe-nylethoxy)piperidine[11] were prepared according to literature procedures. 0.016 mol·L^{-1}

Sulfuric acid was prepared by dilution of concentrated sulfuric acid (95-98 %, Thermo Fisher Scientific).

Ultrapure Milli-Q water (18.2 MΩ·cm, TOC < 5 ppb) was used for experiments in water. In case dry solvents were required, dichloromethane, diethyl ether, toluene and tetrahydrofuran were dried using an MBraun SPS-800 solvent purification system. Dichloromethane was additionally refluxed over phosphorus pentoxide and subsequently distilled under nitrogen atmosphere. *N,N*-Dimethylformamide was pre-dried over potassium hydroxide, then refluxed over phosphorous pentoxide, distilled, degassed and stored over molecular sieves. Tetrahydrofuran was refluxed over potassium and subsequently distilled under nitrogen atmosphere. *N,N,N´,N´*-Tetramethyl ethylenediamine was pre-dried over potassium hydroxide, then refluxed over sodium hydride and subsequently distilled, degassed and stored over molecular sieves. Tetrahydrofuran-d_8 (99.5 % D, Eurisotop) and benzene-d_6 (99.5 % D, Eurisotop) were stored over Na/K alloy and distilled prior to use. Dry solvents were stored in Schlenk flasks or tubes with a J. Young valve under inert atmosphere.

All manipulations on air-sensitive compounds were performed under rigorous exclusion of oxygen and moisture under dry nitrogen or argon using standard Schlenk techniques on a dual manifold Schlenk line, interfaced to a high vacuum (< 10^{-3} mbar) pump, or in an argon-filled MBraun glovebox.

6.2 ANALYTICAL TECHNIQUES

6.2.1 Nuclear Magnetic Resonance Spectroscopy

Nuclear magnetic resonance spectra were recorded on Bruker spectrometers (Avance Neo 400 MHz, Avance III 400 MHz, Ultrashield 400 MHz, Ascend 600 LH) at 298 K, unless explicitly noted otherwise. The temperature was controlled using a Bruker Smart VT unit. All measurements were carried out in deuterated solvents. ^{1}H chemical shifts were referenced internally using the residual solvent resonances and are reported relative to tetramethylsilane. Assignments were determined based on chemical shifts. Resonances are labeled as singlet (s) or broad (br).

DOSY experiments were performed at 298 K using a Bruker Avance III 400 MHz spectrometer or at 301 K or 313 K using a Bruker UltraShield 400 MHz spectrometer. Averaged diffusion coefficients are given in the experimental section. The Bruker pulse sequence *ledbpgp2s* using bipolar gradients with longitudinal eddy current delay and two spoil gradients was used. 32 gradient points were recorded in a linear manner ranging from 2 % to 95 % or 98 % of the maximum applicable gradient strength. The gradient length (little delta) as well as the diffusion delay (big delta) were optimized prior to each DOSY measurement. The data was processed using TopSpin (Version 3.6.2 or 3.6.5) and Dynamics Center (Version 2.5.6 or 2.7.1). In some cases, the *assume constant offset* option of Dynamics Center was necessary to obtain fits of reasonable quality.

6.2.2 Infrared Spectroscopy

Infrared spectra were recorded in the region 4000-400 cm^{-1} with a resolution of 4 cm^{-1} on Bruker Alpha II or Alpha-P FTIR spectrometers equipped with a room temperature DLaTGS detector, and a diamond attenuated total reflection (ATR) unit. The signals were classified depending on the intensity relative to the most intense peak (vs = very strong (100-75 %), s = strong (75-50 %), m = medium (50-25 %), w = weak (25-0 %)).

6.2.3 Size-Exclusion Chromatography

Size-exclusion chromatography measurements in THF were conducted on PSS SECurity^{2} systems consisting of an Agilent 1200 or PSS SECurity Degasser, PSS SECurity TCC6000 Column Oven (35 °C), Agilent PLgel 5 µm Mixed columns (3 x Mixed-C + 1 x Mixed-E and a front column) or PSS SDV columns (8 x 150 mm 5 µm Precolumn, 8 x 300 mm 5 µm Analytical Columns (100000 Å, 1000 Å, and 100 Å)) and an Agilent 1200 BinPump or Agilent 1260 Infinity Isocratic

Pump, Agilent 1200 Infinity II Standard Autosampler or Agilent 1260 Infinity Standard Autosampler, Agilent 1200 Infinity II or Agilent 1260 Infinity Diode Array and Multiple Wavelength Detector, Agilent 1200 Infinity II or Agilent 1260 Infinity Refractive Index Detector (35 °C). HPLC grade THF, stabilized with BHT, was used as eluent at a flow rate of 1 mL·min^{-1}. Narrow disperse linear polystyrene (M_n: 370 g·mol^{-1} to 2.52·10^6 g·mol^{-1}) and poly(methyl methacrylate) (M_n: 202 g·mol^{-1} to 2.2·10^6 g·mol^{-1}) standards (PSS ReadyCal) were used as calibrants.

Size-exclusion chromatography measurements in DMAc were conducted on PSS SECurity^2 systems consisting of a PSS SECurity Degasser, PSS SECurity TCC6000 Column Oven (60 °C or 80 °C), PSS GRAM Column Set (8 x 50 mm 10 µm Guard Column, 3 × 8 x 300 mm 10 µm Analytical Columns (1000 Å, 1000 Å, and 30 Å) or 8 x 150 mm 10 µm Precolumn, 3 x 8 x 300 mm 10 µm Analytical Columns (1000 Å, 1000 Å, and 30 Å)) and an Agilent 1260 Infinity Isocratic Pump, Agilent 1260 Infinity Standard Autosampler, Agilent 1260 Infinity Diode Array and Multiple Wavelength Detector, Agilent 1260 Infinity Refractive Index Detector (35 °C). HPLC grade DMAc containing 0.1 wt% LiBr was used as eluent at a flow rate of 1 mL·min^{-1}. Narrow disperse linear polystyrene (M_n: 266 g·mol^{-1} to 2.52·10^6 g·mol^{-1}) and poly(methyl methacrylate) (M_n: 202 g·mol^{-1} to 2.2·10^6 g·mol^{-1}) standards (PSS ReadyCal) were used as calibrants.

All samples were passed through 0.22 µm PTFE membrane filters prior to the measurements. Molecular weight and dispersity analyses were performed with the PSS WinGPC UniChrom software (Version 8.33). Note that all given molar masses and dispersity values are beset with uncertainties due to deviations of the measured samples from the employed calibration standards.

6.2.4 Dynamic Light Scattering

Dynamic light scattering measurements were carried out on a Brookhaven Instruments NanoBrook Omni equipped with a 640 nm laser or on a Malvern Zetasizer NanoZS equipped with a 633 nm laser at 298 K. The polymer solutions were prepared by dissolving the samples at a concentration of approximately 5 mg·mL^{-1} and passing them through 0.22 µm PTFE or CME membrane filters into 10 mm path length quartz cuvettes. All measurements were conducted in backscattering mode with an angle of 173° relative to the incident beam. The Particle Solutions software (Version 3.6.0.7122) or Malvern Zetasizer software (Version 7.13) was used. Given solvodynamic diameters (D_s) were averaged over five consecutive

measurements. Note that all measured D_S values need to be treated with caution due to the weak visible light scattering abilities of the small particles considered in the current work.

6.2.5 Scanning Transmission Electron Microscopy

STEM imaging was performed with a JEOL JEM-ARM200F ("NeoARM") double corrected electron transmission microscope operating at 200 kV. To maximize the dark field signal and minimize the acquisition time and the time-dependent diffusion of barium atoms, a spot size of 4 with the largest condenser aperture was chosen. The dwell time was 1.3 µs. To reduce the influence of hydrocarbon contamination, the samples were heated to 40 ˚C during imaging. Details on the sample preparation are provided in Chapter 6.3.1.7.

6.2.6 UV/Vis Spectroscopy

UV/Vis spectra were recorded on a Shimadzu UV-2700 spectrophotometer equipped with a CPS-100 electronic temperature control cell positioner or on an Agilent Cary 5000 UV-VIS-NIR spectrophotometer at 298 K. Samples were dissolved in HPLC grade solvents and measured in Hellma Analytics quartz high precision cells with a path length of 10 mm.

6.2.7 Liquid Chromatography-Mass Spectrometry

LCMS measurements relevant to Chapter 4.2 were performed on an UltiMate 3000 UHPLC System (Dionex) consisting of a pump (LPG 3400SZ), autosampler (WPS 3000TRS), and a temperature-controlled column compartment (TCC 3000). Separation was performed on a C18 HPLC column (Phenomenex Luna 5 µm, 100 Å, 250 × 2.0 mm) operating at 40 °C. Water (containing 5 mmol·L^{-1} ammonium acetate) and acetonitrile were used as eluents. A gradient of acetonitrile/water at a combined flow rate of 0.40 mL·min^{-1} was applied, starting from 5:95 for 0.6 min and increased to 100:0 over 7 min, and subsequently held at 100:0 for 3 min before returning to 5:95 (v/v). The eluate was directed to a UV diode array (DAD 3000, Dionex) and subsequently into the heated electrospray ionization source of a Q Exactive Plus Biopharma high-resolution Orbitrap mass spectrometer (Thermo Fisher Scientific). A constant spray voltage of 3.0 kV, a dimensionless sheath gas, and a dimensionless auxiliary gas (N_2) flow rate of 30 and 10 were applied, respectively. The capillary temperature was set to 320 °C, the S-lens RF level was set to 60, and the auxiliary gas heater temperature was set to 150 °C. Spectra were acquired at a nominal mass resolving power of 70000 (defined at *m/z* 200).

LCMS measurements relevant to Chapter 4.3 were performed on an Agilent 1260 Infinity II system consisting of a quaternary pump (GB7111B), autosampler (G7129A), a temperature-

controlled column oven (G7114A) and a variable UV/Vis detector (G7114 A, VWD, flow cell G7114A 018). Separation was performed on a C18 HPLC-column (Agilent Poroshell 120 EC-C18 4.6 x 100 mm, 2.7 µm) operating at 40 °C. A gradient of acetonitrile/water (containing 10 mmol·L^{-1} ammonium acetate) 10:90 to 80:20 (v/v) at a flow rate of 1 mL·min^{-1} during 15 min was used as the eluting solvent. The flow was directed into an Agilent MSD (G6136BA, AP-ESI ion source). The instrument was calibrated in the *m/z* range 118-2121 in the positive mode and 113-2233 in the negative mode using a premixed calibration solution (Agilent). The following parameters were used: spray chamber flow: 12 L·min^{-1}, drying gas temperature: 350 K, capillary voltage: 3000 V, fragmentor voltage: 100 V.

6.2.8 Tunable Laser Setup for Photochemical Action Plot Experiments

Laser experiments were conducted using an Opotek HE Opolette 355 LD, producing 5 ns pulses with a flattop spatial profile with a 20 Hz repetition rate, tunable from 210 nm to 2400 nm. The output beam was initially passed through a beam expander (-50 mm and 100 mm lens combination) to ensure it is sufficiently large to uniformly irradiate the entire sample volume. The beam then passes through an electronic shutter and is directed upwards using a UV silica right angle prism. Finally, the beam enters the sample, suspended in an aluminium block, from below. The laser energy deposited into the sample was measured above the aluminium block before and after experiments using a Coherent EnergyMax thermopile sensor (J-25MB-LE) to account for any power fluctuations during irradiation. The photon number N_{Ph} reaching the sample in the laser vial at a given wavelength λ_1 can be derived from the set laser pulse energy using the following relation:

$$N_{\mathrm{Ph}} = \frac{T(\lambda_1)}{100}\frac{E_{\mathrm{Pulse}}(\lambda_1)\lambda_1 f_{\mathrm{rep}} t}{hc}$$

Herein, E_{Pulse} is the pulse energy recorded above the aluminium block (at the position of the vial), λ is the wavelength of the incident beam, f_{rep} is the laser repetition rate, t is the total irradiation time, h is Planck's constant, c is the speed of light and $T(\lambda)$ is the wavelength-dependent transmission of the laser vial in percent.

Once an initial measurement is completed and the desired photon number is known, the required energies to obtain the same number of photons in the laser vial at other wavelengths λ_2 in the same total irradiation time can be obtained:

$$E_{\mathrm{Pulse}}(\lambda_2) = E_{\mathrm{Pulse}}(\lambda_1)\frac{\lambda_1}{\lambda_2}\frac{T(\lambda_1)}{T(\lambda_2)}$$

6.2.9 Photoflow Reactor

Photoreactions under flow conditions were performed using a Vapourtec E-series platform with peristaltic pumps fitted with the UV-150 module and the VSD006 cooling module. The module consisted of a temperature-controlled irradiation chamber, a transparent fluorinated ethylene polymer (FEP) reactor coil (10 mL, Part number: 50-1581) and a LED assembly (390 to 420 nm, peak 410 nm, total power output of 12 W, Part number: 50-1444). The temperature was controlled to ambient temperature employing pre-cooled nitrogen (heat exchange in the cooling module).

6.2.10 Energy-Dispersive X-Ray Spectroscopy

Energy disperse X-ray spectroscopy measurements relevant to Chapter 4.2 were carried out in a JEOL JEM-ARM200F ("NeoARM") operating at 200 kV with a spot size of 4 and a 40 µm condenser aperture, resulting in a convergence angle of 24 to 29 mrad and a probe current of 7.48 nA. An EX-24360AHH type EDX detector was used with a total acquisition time of 20 min. 5 µL of a solution of **SCNP3-Cu-Flow,** directly after purification by preparative SEC, were deposited on an ultra-thin carbon film coated gold TEM grid (Electron Microscopy Sciences). Gold was chosen to exclude the TEM grid as the origin of the detected copper signal. After drying in air, the sample was outgassed at 60 °C under vacuum for several hours.

Energy disperse X-ray spectroscopy measurements relevant to Chapter 4.3 were carried out on an Ametec EDAX mounted on a Zeiss SEM Supra 35 VP scanning electron microscope. After drying under vacuum for several hours, the powdered sample of **SCNP4-Fc-Phen** was fixed on a conductive carbon pad on an aluminium sample holder.

6.2.11 Single Crystal X-Ray Diffractometry

A suitable crystal was covered in mineral oil (Aldrich) and mounted on a glass fibre. The crystal was transferred directly to the cold stream (100 K) of a STOE StadiVari diffractometer. The structure was solved by using the program SHELXS/T[286-287] and Olex2.[288] The remaining non-hydrogen atoms were located from successive difference Fourier map calculations. The refinements were carried out by using full-matrix least-squares techniques on F_0^2 by using the program SHELXL.[286-287] The hydrogen atoms were introduced into the geometrically calculated positions (SHELXL procedures) unless otherwise stated and refined riding on the corresponding parent atoms. The locations of the largest peaks in the final difference Fourier map calculations as well as the magnitude of the residual electron densities were of no

chemical significance. Summary of the crystal data, data collection and refinement are given in Table 6.13. Crystallographic data have been deposited with the Cambridge Crystallographic Data Centre as a supplementary publication no. CCDC 2314460. Copies of the data can be obtained free of charge on application to CCDC, 12 Union Road, Cambridge CB21EZ, UK (fax: +(44)1223-336-033; email: deposit@ccdc.cam.ac.uk).

6.2.12 Elemental Analysis

Elemental analyses were carried out with an Elementar Vario MICRO Cube.

6.2.13 Electron Paramagnetic Resonance Spectroscopy

Continuous-wave (CW) X-band (circa 9.424 GHz) electron paramagnetic resonance spectra were recorded on a Bruker Elexsys E540 spectrometer equipped with an Elexsys Super High Sensitivity probe head and liquid nitrogen cooling (ER4141 VTM Nitrogen VT Unit). The magnetic field was calibrated with 2,2-diphenyl-1-picrylhydrazyl (g = 2.0036) and measurements were carried out at 115 K using a modulation amplitude of 1.0 mT, a modulation frequency of 100 kHz and a microwave power of 20 mW (10 dB of 200 mW, non-saturating condition). To calculate the EPR intensities, spectra were baseline corrected with a 4^{th} order polynomial and the double integrals calculated numerically. All processing was carried out using MatLab (R2002b).

6.3 SYNTHETIC PROCEDURES AND ANALYTICAL DATA

In copolymers of known composition, the amount, n_i in mole, of a chosen functional monomer *i* was estimated according to the following relation:

$$n_i = \frac{x_i \cdot m_{\mathrm{Polymer}}}{\sum_j x_j \cdot M_{\mathrm{Monomer,j}}}$$

Herein, *x* is the average number fraction of the indexed monomer with respect to the total number of all monomers in a considered macromolecular chain, commonly estimated from ^{1}H NMR data or monomer feed ratios. m_{Polymer} is the weighed mass of polymer sample. M_{Monomer} refers to the molar mass of the respective indexed monomer. When the exact molar mass of a monomer was unknown, as was the case when monomers featured molar mass distributions themselves, the number-averaged molar mass was employed for the calculations. The contributions of end groups to the molar masses of the polymers were neglected in all calculations. Consequently, the given values are to be considered as estimates only and derived stoichiometric ratios are not quantitatively precise.

The depicted chemical structures of the SCNP folding units are to be considered illustrative only and are not necessarily fully representative of the actual chemical situations within the nanoparticles.

6.3.1 Synthesis and In-depth Characterization of Ba(II) Single-Chain Nanoparticles

6.3.1.1 Synthesis of P1

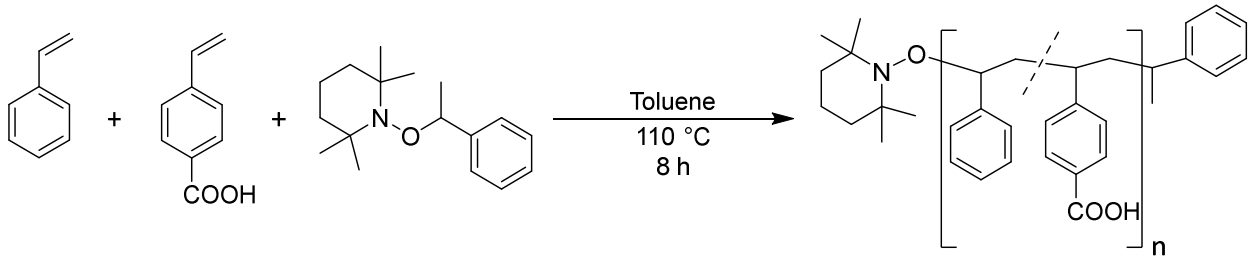

P1

46.6 mg of the NMP initiator 2,2,6,6-tetramethyl-1-(1-phenylethoxy)piperidine (0.178 mmol, 1.00 eq.) were dissolved in 2 mL of toluene and 4.20 mL of styrene (3.82 g, 36.7 mmol, 206 eq.) and 544 mg of 4-vinylbenzoic acid (3.67 mmol, 20.6 eq.) were added. The solution was degassed by three consecutive freeze-pump-thaw cycles and subsequently heated to 110 °C for 8 h. The reaction was stopped by cooling the flask with liquid nitrogen and opening it to air. The polymer was precipitated three times in cold methanol. The precipitate was isolated by centrifugation and dried under reduced pressure to give **P1** as a colorless solid (1.42 g).

^{1}H NMR (400 MHz, THF-d_8, 298 K): δ / ppm = 11.22-11.10 (s, COOH), 7.90-7.46 (br, aromatic), 7.38-6.20 (br, aromatic), 2.42-1.18 (br, aliphatic backbone).

SEC (THF, RI, PS cal.): M_n = 19800 g·mol^{-1}, M_w = 22900 g·mol^{-1}, M_p = 23400 g·mol^{-1}, $Đ$ = 1.15.

DLS (THF): D_s = 5.81 nm.

DOSY (400 MHz, THF-d_8, 298 K): D = 1.44·10^{-10} m^2·s^{-1}.

FT-IR (ATR): $\tilde{\nu}$ / cm^{-1} = 3081 (w), 3061 (w), 3024 (w), 2921 (w), 2852 (w), 1731 (w), 1688 (m), 1605 (w), 1576 (w), 1490 (w), 1450 (w), 1419 (w), 1364 (w), 1310 (w), 1281 (w), 1259 (w), 1173 (w), 1084 (w), 1018 (w), 904 (w), 852 (w), 755 (m), 695 (vs), 537 (m).

6.3.1.2 Synthesis of P2

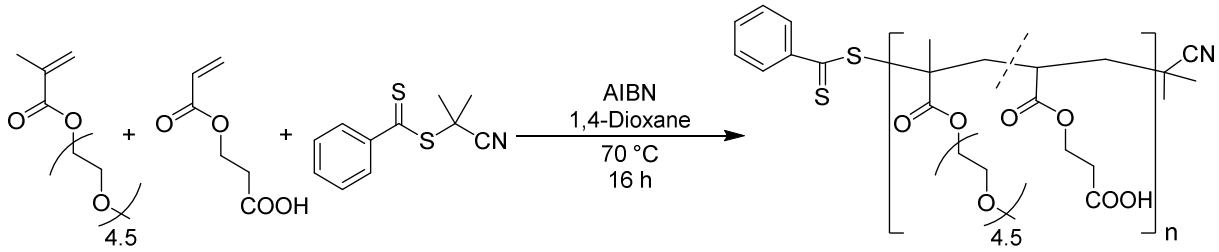

P2

10.0 mg of the RAFT agent 2-cyano-2-propyl benzodithioate (45.2 µmol, 1.00 eq.) and 1.48 mg of azobisisobutyronitrile (AIBN, 9.04 µmol, 0.200 eq.) were dissolved in 5.5 mL of 1,4-dioxane and 2.75 mL of poly(ethylene glycol) methyl ether methacrylate (PEGMEMA, M_n = 300 g·mol^{-1}, 2.89 g, 9.63 mmol, 214 eq.) and 0.161 mL of 2-carboxyethyl acrylate (2CEA, 196 mg, 1.36 mmol, 30.1 eq.) were added. The solution was degassed by three consecutive freeze-pump-thaw cycles and subsequently heated to 70 °C for 16 h. The reaction was stopped by cooling the flask to room temperature and opening it to air. The polymer was precipitated three times in a mixture of diethyl ether and *n*-pentane (1:1 v/v). The precipitate was isolated by centrifugation and dried under reduced pressure to give **P2** as an orange oil (2.43 g).

^{1}H NMR (600 MHz, D_2O, 298 K): δ / ppm = 4.46-4.32 (br, 2CEA-COOCH_2CH$_2$COOH), 4.30-4.04 (br, PEGMEMA-COOCH_2), 3.92-3.52 (br, PEGMEMA-OCH_2CH_2), 3.48-3.30 (br, PEGMEMA-OCH_3), 2.90-2.52 (br, 2CEA-COOCH$_2$CH_2COOH), 2.34-0.65 (br, aliphatic backbone).

SEC (THF, RI, PMMA cal.): M_n = 48700 g·mol^{-1}, M_w = 74800 g·mol^{-1}, M_p = 56200 g·mol^{-1}, $Đ$ = 1.54.

DLS (H_2O): D_s = 4.85 nm.

DOSY (400 MHz, D_2O, 313 K): D = 6.44·10^{-11} m^2·s^{-1}.

FT-IR (ATR): $\tilde{\nu}$ / cm^{-1} = 2944 (m), 2873 (m), 1724 (vs), 1640 (w), 1453 (m), 1391 (w), 1352 (w), 1275 (m), 1247 (m), 1100 (vs), 1030 (s), 993 (m), 948 (m), 855 (m), 750 (w), 521 (w).

6.3.1.3 Synthesis of SCNP1-Ba

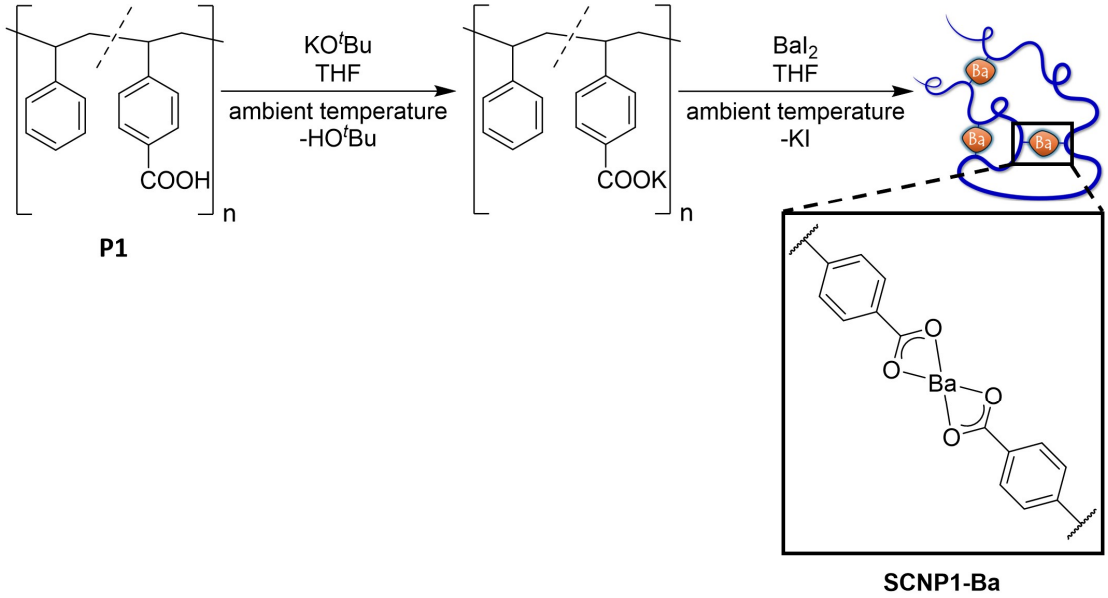

P1 **SCNP1-Ba**

50.0 mg of **P1** (63.5 µmol, 1.00 eq. carboxylic acid functionalities) were dissolved in 15 mL of THF and a solution of 7.12 mg of potassium *tert*-butoxide (63.5 µmol, 1.00 eq.) in 5 mL of THF was added. The obtained solution was diluted with 80 mL of THF and slowly added (5 mL·h^{-1}) to 12.4 mg of barium iodide (31.7 µmol, 0.500 eq.) in 20 mL of THF using a dropping funnel. After complete addition of the polymer solution, the reaction mixture was filtered to remove precipitated potassium iodide, and the solvent was evaporated under reduced pressure to give **SCNP1-Ba** as a colorless solid.

^{1}H NMR (400 MHz, THF-d_8, 298 K): δ / ppm = 8.64-6.00 (br, aromatic), 3.65-3.59 (br, THF-Ba), 1.80-1.75 (br, THF-Ba), 2.70-1.02 (br, aliphatic backbone).

SEC (THF, RI, PS cal.): M_n = 14900 g·mol^{-1}, M_w = 18400 g·mol^{-1}, M_p = 20100 g·mol^{-1}, $Đ$ = 1.23.

DLS (THF): D_s = 5.16 nm.

DOSY (400 MHz, THF-d_8, 298 K): D = 1.62·10^{-10} m^2·s^{-1}.

FT-IR (ATR): $\tilde{\nu}$ / cm^{-1} = 3082 (w), 3060 (w), 3026 (w), 2921 (w), 2845 (w), 1594 (m), 1544 (m), 1490 (m), 1448 (m), 1391 (m), 1179 (m), 1066 (w), 1024 (w), 905 (w), 843 (w), 790 (w), 750 (m), 696 (vs), 538 (m).

6.3.1.4 Synthesis of SCNP2-Ba

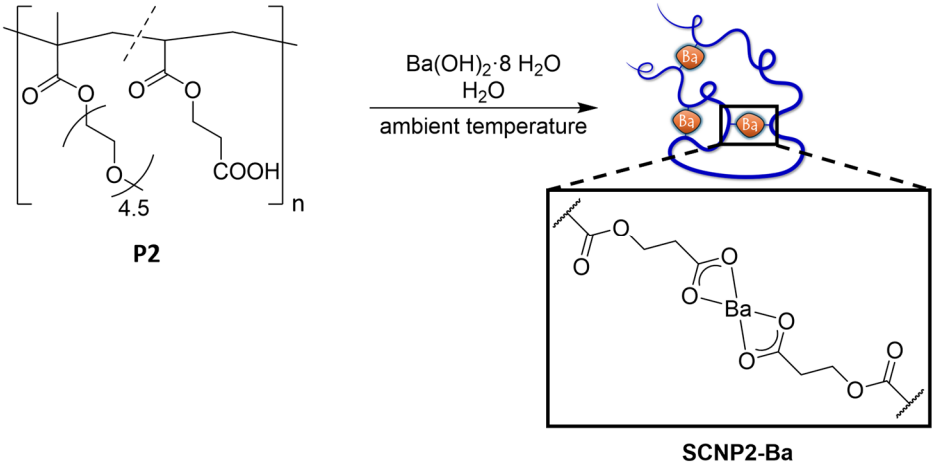

P2 **SCNP2-Ba**

0.794 mg of barium hydroxide octahydrate (2.51 µmol, 0.500 eq.) were dissolved in 5 mL of water and a solution of 10.0 mg of **P2** (5.03 µmol, 1.00 eq. carboxylic acid functionalities) in 5 mL of water was slowly added using a syringe pump (1 mL·h^{-1}). After complete addition of the polymer solution, the solvent was evaporated under reduced pressure to give **SCNP2-Ba** as a slightly orange oil.

^{1}H NMR (600 MHz, D_2O, 298 K): δ / ppm = 4.46-4.31 (br, 2CEA-COOCH_2CH$_2$COOBa), 4.30-4.04 (br, PEGMEMA-COOCH_2), 3.92-3.52 (br, PEGMEMA-OCH_2CH_2), 3.48-3.30 (br, PEGMEMA-OCH_3), 2.90-2.44 (br, 2CEA-COOCH$_2$CH_2COOBa), 2.34-0.65 (br, aliphatic backbone).

SEC (THF, RI, PMMA cal.): M_n = 34600 g·mol^{-1}, M_w = 47800 g·mol^{-1}, M_p = 48300 g·mol^{-1}, $Đ$ = 1.38.

DLS (H_2O): D_s = 4.67 nm.

DOSY (400 MHz, D_2O, 313 K): D = 6.67·10^{-11} m^2·s^{-1}.

FT-IR (ATR): $\tilde{\nu}$ / cm^{-1} = 2944 (w), 2873 (m), 1724 (s), 1583 (w), 1450 (m), 1400 (w), 1352 (w), 1272 (m), 1244 (m), 1100 (vs), 1027 (m), 948 (m), 855 (m), 747 (w), 524 (w).

6.3.1.5 Folding-Unfolding-Refolding Cycle of SCNP2-Ba

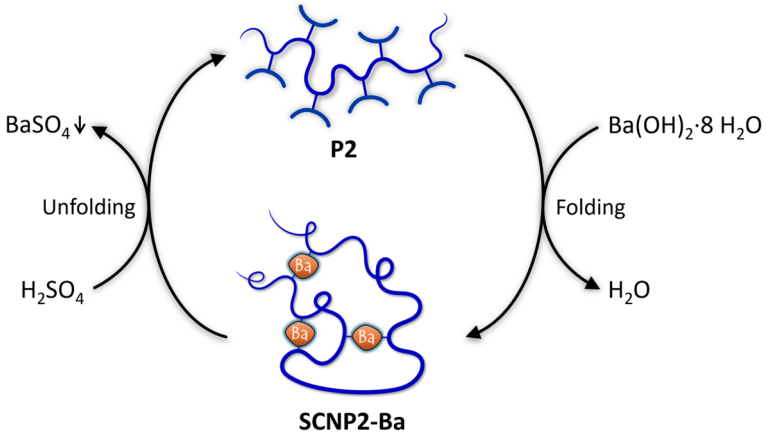

0.794 mg of barium hydroxide octahydrate (2.51 µmol, 0.500 eq.) were dissolved in 5 mL of water and a solution of 10.0 mg of **P2** (5.03 µmol, 1.00 eq. carboxylic acid functionalities) in 5 mL of water was slowly added using a syringe pump (1 mL·h^{-1}). After complete addition of the polymer solution, the solvent was evaporated under reduced pressure to give **SCNP2-Ba** as a slightly orange oil.

The obtained **SCNP2-Ba** was subsequently redissolved in 1 mL of water and 0.315 mL of 0.016 mol·L^{-1} sulfuric acid (5.03 µmol, 1.00 eq.) were added, leading to the precipitation of a colorless solid which was filtered off using a 0.22 µm CME membrane filter. Evaporation of the solvent under reduced pressure gave the regenerated unfolded polymer as an orange oil. The regenerated unfolded polymer was dissolved in 5 mL water and slowly added (1 mL·h^{-1}) to a solution of 2.00 mg of barium hydroxide octahydrate (6.34 µmol, 1.26 eq.) in 5 mL of water. After complete addition of the polymer solution, the solvent was evaporated under reduced pressure to give the refolded polymer as a slightly orange oil.

6.3.1.6 Computational Details

Molecular dynamics simulations were performed by Ada Quinn under the supervision of Prof. Megan O'Mara (University of Queensland). The work was supported by resources and services provided by the National Computational Infrastructure (NCI) and the Pawsey Supercomputing Research Center, which is supported by the Australian Government, and the University of Queensland's Research Computing Centre (RCC).

All simulations were performed using the GROMACS 2023.2 MD engine.[289-291] GROMOS 54a7 parameters and united atom geometries were generated for all conceivable forms of the monomers with the Automated Topology Builder v3.0.[292-294]

Individual monomer parameters were used to generate full polymer parameters using the GROMACS pdb2gmx tool, which combines parameters for biological monomers, such as amino acids, into parameters for biopolymers, such as proteins, based on coordinate data, such as a protein structure file in the PDB format. A virtual particle approximating a divalent barium ion was created by modification of the GROMOS 54a7 divalent calcium parameters. There are no published parameters for divalent barium ions which have been validated with relevant forcefields. Thus, a dummy particle named BAv was adapted using the charge and Lennard-Jones parameters from the existing GROMOS 54a7 Ca^{2+} parameters, but with a mass of 137.905 u. All parameters were compiled into a modified gromos54a7 forcefield in the gromacs format, which is available from Ada Quinn upon request. The sidechain carboxylate group was predicted to have a pK_a of 3.9,[295] thus these functional groups were modelled as deprotonated anionic carboxylates in all simulations. Parameters for protonated carboxylic acid monomers were generated, and are included in the forcefield, but were not used in the reported simulations.

For united atom simulations of macromolecules, it is necessary to explicitly model all characteristics of the constituting monomers, including stereochemistry and sidechain composition. A new software tool, *polyconf.py*, was developed by Ada Quinn to assemble arbitrary macromolecular chains *in silico*. In detail, three atactic macromolecular chains with random stereochemistry, each constituted of eighty-five PEGMEMA monomers featuring four ethylene glycol subunits in the side chain, eighty-five PEGMEMA monomers featuring five ethylene glycol subunits in the side chain and thirty 2-carboxyethyl acrylate monomers, all randomly distributed along the macromolecular chain, were generated. For the three constructed macromolecular chains, pseudo-linear conformations were generated by

randomizing the rotation of dihedrals. Subsequently, the pseudo-linear conformations were condensed through 250 ps NVT vacuum simulations to generate compact conformations, or by 10 ns simulations inside a water solvent shell to generate extended conformations. For each of the three distinct macromolecules, three condensed and three extended conformations were generated this way. The resulting eighteen macromolecules were solvated in water using the SPC/E model.[190] To investigate the interactions of **P2** with barium ions, solvent molecules were replaced by fifteen Ba^{2+} and thirty Cl^{-} ions for charge compensation, resulting in a stoichiometric ratio of one Ba^{2+} ion per two carboxylate functionalities. Consideration of the interactions of the eighteen distinguishable starting conformations with barium ions resulted in a total of thirty-six simulation systems. At first, each system was equilibrated through 10 ns unrestrained molecular dynamics simulations in the NPT ensemble. The final frame of each equilibration was used as the input for 300 ns triplicate NPT simulations. Initial velocities in each replicate simulation were assigned by a Boltzmann distribution. The temperature was maintained at 310 K using the Bussi-Donadio-Parrinello velocity rescale thermostat[296] and a coupling constant of 0.1 ps. The pressure was maintained at 1 bar using isotropic pressure coupling with the Parrinello-Rahman barostat[297] using a 5 ps coupling constant and an isothermal compressibility of $4.5 \cdot 10^{-5}$ bar^{-1}. SETTLE[298] was used to constrain the geometry of water molecules and LINCS[299] was used to constrain the covalent bond lengths of the solute. The electrostatic interactions were calculated using the Reaction Field scheme,[300] and non-covalent interactions were determined via the Verlet scheme[301] with a 1.0 nm cut-off.

Radial distribution functions of Ba^{2+} were calculated with MDAnalysis version 1.0.[302] Mean radial distribution functions were calculated over the last 150 ns of each replicate simulation. The barium polymer interactions were examined by quantifying the number of oxygen atoms from polymer functional groups, specifically carboxylates, backbone esters and PEG ethers, within the first and second solvation shells of each barium ion using custom code built on MDAnalysis. The first solvation shell was defined as particles located within 3.5 Å of the Ba^{2+} ion. The second solvation shell was defined as particles located between 3.5 Å and 6 Å from the Ba^{2+} ion. These values were chosen based on the Ba^{2+} radial distribution functions.

The interactions of the barium ions with the macromolecular chains were analyzed over the last 150 ns of each replicate simulation, and the derived values of all simulations combined in the final results, taking into consideration whether the starting conformation was compact or

extended. The analyses were performed on frames spaced by 1 ns and all fifteen barium ions were investigated individually in every simulation frame.

The frequency of contact between Ba^{2+} and specified polymer functional groups is reported as the proportion of all metal polymer interactions.

Radii of gyration were calculated using GROMACS tools. The mean radii of gyration were calculated over the last 150 ns of each replicate simulation.

Table 6.1 Fraction of the simulation frames in which the given number of barium ions are within 6 Å of any atom of the macromolecular chain with respect to the total number of evaluated simulation frames.

	Initial conformation	
	Compact	**Extended**
Number of barium ions within 6 Å of any atom of the macromolecular chain		
0	not detected	not detected
1	not detected	not detected
2	not detected	not detected
3	not detected	not detected
4	not detected	not detected
5	0.15 %	0.03 %
6	0.74 %	0.82 %
7	4.67 %	2.89 %
8	10.67 %	9.58 %
9	19.80 %	17.63 %
10	24.35 %	24.69 %
11	21.31 %	21.78 %
12	12.86 %	15.83 %
13	4.54 %	5.68 %
14	0.86 %	1.04 %
15	0.05 %	0.05 %

Table 6.2 Frequency of barium polymer interactions.

	Initial conformation	
	Compact	**Extended**
Fraction of simulation time in which any polymer oxygen atom is found in the first barium solvation shell	1.45 %	1.29 %
Fraction of simulation time in which any polymer oxygen atom is found in the second barium solvation shell	65.51 %	66.85 %

Table 6.3 Fraction of barium polymer interactions involving the given number of carboxylate groups in the second barium solvation shell with respect to the total number of barium polymer interactions.

	Initial conformation	
	Compact	**Extended**
Number of carboxylate groups in second barium solvation shell		
0	15.19 %	13.91 %
1	56.81 %	53.18 %
2	24.46 %	27.87 %
3	3.45 %	4.87 %
4	0.10 %	0.16 %
5	not detected	< 0.01 %

Table 6.4 Fraction of barium polymer interactions involving coordination of multiple carboxylates separated by at least nine other monomers along the chain contour to the same barium ion with respect to the total number of barium polymer interactions.

	Initial conformation	
	Compact	**Extended**
Interaction of distant carboxylates present	7.85 %	11.89 %

Table 6.5 Fraction of barium polymer interactions involving the given number of ether oxygen atoms of the PEG side chains in the second barium solvation shell with respect to the total number of barium polymer interactions.

	Initial conformation	
	Compact	**Extended**
Number of PEG ether oxygen atoms in second barium solvation shell		
0	50.63 %	47.79 %
1	28.03 %	28.8 %
2	13.38 %	14.13 %
3	4.62 %	4.83 %
4	1.59 %	1.97 %
5	0.63 %	0.98 %
6	0.40 %	0.58 %
7	0.27 %	0.38 %
8	0.13 %	0.21 %
9	0.11 %	0.12 %
10	0.10 %	0.11 %
11	0.05 %	0.06 %
12	0.02 %	0.03 %

Table 6.5 continued

13	0.03 %	0.01 %
14	0.01 %	not detected

Table 6.6 Fraction of barium polymer interactions involving the given number of esterified oxygen atoms of the polymeric ester groups in the second barium solvation shell with respect to the total number of barium polymer interactions.

	Initial conformation	
	Compact	**Extended**
Number of esterified oxygen atoms in second barium solvation shell		
0	80.03 %	78.50 %
1	16.34 %	17.33 %
2	3.42 %	3.91 %
3	0.2 %	0.26 %
4	0.01 %	< 0.01 %

Table 6.7 Fraction of barium polymer interactions involving the given number of carbonyl oxygen atoms of the polymeric ester groups in the second barium solvation shell with respect to the total number of barium polymer interactions.

	Initial conformation	
	Compact	**Extended**
Number of carbonyl oxygen atoms in second barium solvation shell		
0	63.03 %	62.58 %
1	23.78 %	23.83 %
2	10.83 %	11.37 %
3	2.04 %	1.69 %
4	0.30 %	0.43 %
5	0.02 %	0.09 %
6	< 0.01 %	0.01 %
7	not detected	< 0.01 %

Table 6.8 Polymer mean radii of gyration and standard deviations in the presence and absence of barium ions in nm.

	Initial conformation	
	Compact	**Extended**
No Ba^{2+}	2.20 +/- 0.04	2.33 +/- 0.17
In presence of Ba^{2+}	2.19 +/- 0.04	2.26 +/- 0.09

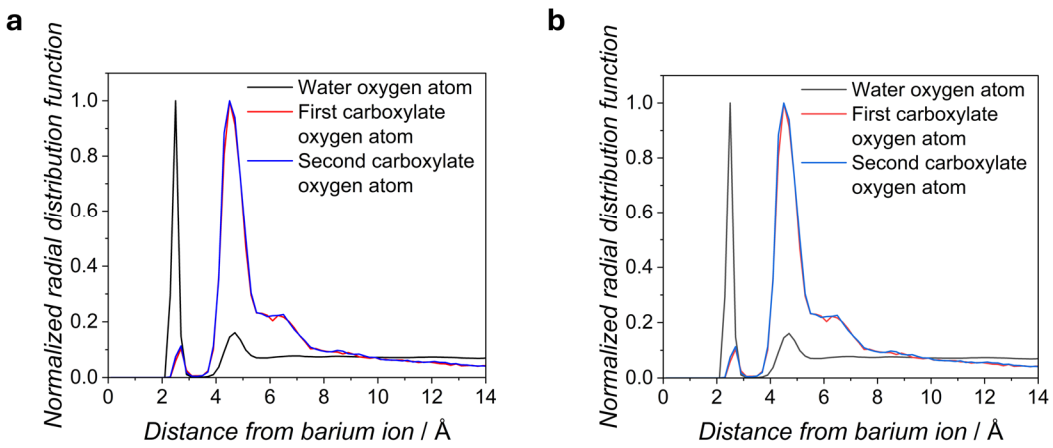

Figure 6.1 Radial distribution functions showing the presence of two distinct coordination spheres around a barium ion for **(a)** compact and **(b)** extended initial conformations of the simulated macromolecules. The depicted radial distribution functions represent only one of the simulated macromolecules in each case but are representative of all simulations.

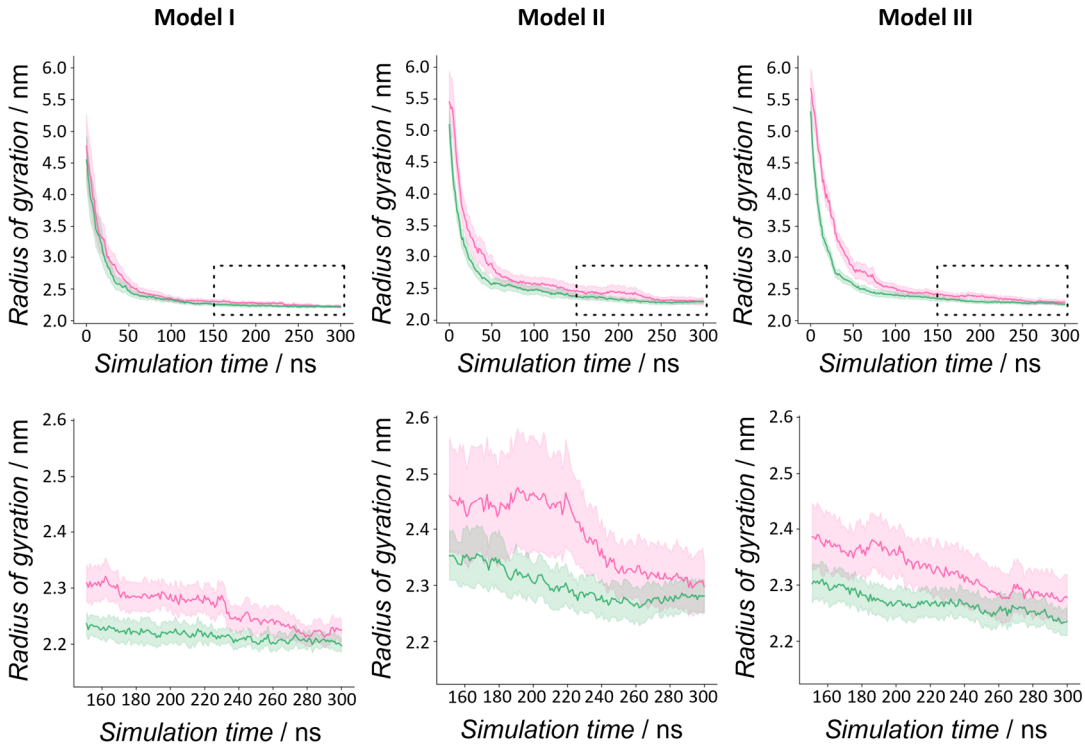

Figure 6.2 Radii of gyration over the simulation time of the three constitutionally distinct macromolecular chains (Models I-III) starting from the generated extended conformations in the absence (red) and presence (green) of barium ions. The radii of gyration are averaged over the replicate simulations of the three extended conformations generated for each constitutionally distinct macromolecular chain. Shading refers to plus/minus the standard deviation. During the last 150 ns, the extended conformations continued to condense. In simulations containing barium ions (green) the radius of gyration collapsed more quickly than in simulations without barium ions (red). The graphs on the bottom show the zoomed-in regions highlighted with the dashed boxes in the respective graphs on top.

6.3.1.7 Scanning Transmission Electron Microscopy Imaging of SCNP2-Ba

Scanning transmission electron microscopy experiments on **SCNP2-Ba** were conducted and analyzed by Dr. Jochen Kammerer (Queensland University of Technology).

Several sample preparation techniques for the generation of STEM samples from solubilized SCNPs have been explored to achieve the imaging of individual SCNPs with atomic resolution. Ultimately, the SCNPs must be deposited on an electron transparent sample substrate in a well-separated fashion to enable differentiation between individual SCNPs.

For experiments employing standard ultra-thin carbon film TEM grids (4-6 nm film thickness), aqueous solutions of **SCNP2-Ba** with an initial polymer concentration of 1 mg·mL^{-1} (refer to Chapter 6.3.1.4 for details) were diluted with water to a polymer concentration of 0.001 mg·mL^{-1} and subsequently deposited on a plasma cleaned TEM grid with pre-deposited gold nanoparticles, blotted with a filter paper after one minute, and left to dry.

To increase the reproducibility of the sample preparation procedure and reduce effects of agglomeration upon drying, aqueous solutions of **SCNP2-Ba** with a polymer concentration of 0.001 mg·mL^{-1} were deposited on plasma cleaned ultra-thin carbon film TEM grids (4-6 nm film thickness) and transferred to a Gatan Cryoplunge 3 setup for blotting with a blot time of 4 s at a relative humidity greater than 90 %. After preparation, the samples were heated to 80 ˚C under vacuum for at least 8 h to reduce hydrocarbon contamination.

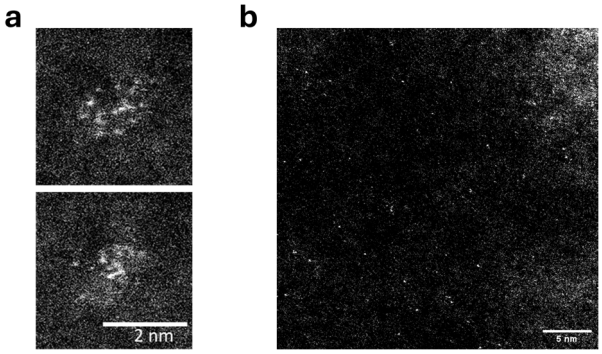

Figure 6.3 (a) Two stacked subsequent STEM images of the same barium cluster illustrating the movement of the barium atoms during image acquisition. The sample was prepared by manual blotting and drying after deposition of an aqueous solution of **SCNP2-Ba** with a polymer concentration of 0.001 mg·mL^{-1} on a standard ultra-thin carbon film TEM grid. **(b)** STEM image on an amorphous silicon membrane. This substrate offers strong contrast and reduced hydrocarbon contamination compared to a standard carbon substrate. The sample was prepared by manual blotting and drying after deposition of an aqueous solution of **SCNP2-Ba** with a polymer concentration of 0.01 mg·mL^{-1}.

Energy transfer from the high energy electron beam to the sample repeatedly led to the diffusion of barium atoms on the TEM grid during image acquisition (refer to **Figure 6.3a**). Intuitively, one would lower the beam current to reduce energy transfer to the barium atoms, however, this was found to be inefficient as longer dwell times were required to collect the necessary signal intensity. Imaging at cryogenic temperatures might be promising to reduce barium atom diffusion, but the formation of an ice layer upon cooling impeded atomic resolution imaging with the employed experimental setup. The effects of atom diffusion could be mitigated by lowering the magnification to reduce the electron energy transferred onto each atom while still providing sufficiently high resolution to identify individual atoms.

The employed standard ultra-thin carbon film TEM grids featured pronounced hydrocarbon contaminations, leading to a bright background, hence reducing the contrast between barium atoms and background. To address this, samples were also prepared on amorphous silicon membranes (5 nm thickness, Pure Silicon TEM Windows) following the manual blotting procedure outlined above but with a polymer concentration of 0.01 $mg \cdot mL^{-1}$ (refer to **Figure 6.3b**). The obtained results were consistent with the data derived from the samples prepared using the Gatan Cryoplunge 3 setup (refer to **Figure 4.16c**).

6.3.2 Visible Light Photoflow Synthesis of a Cu(II) Single-Chain Nanoparticle Catalyst

Figure 6.4 shows the emission spectra of the LEDs employed in the synthetic procedures described in Chapter 6.3.2.

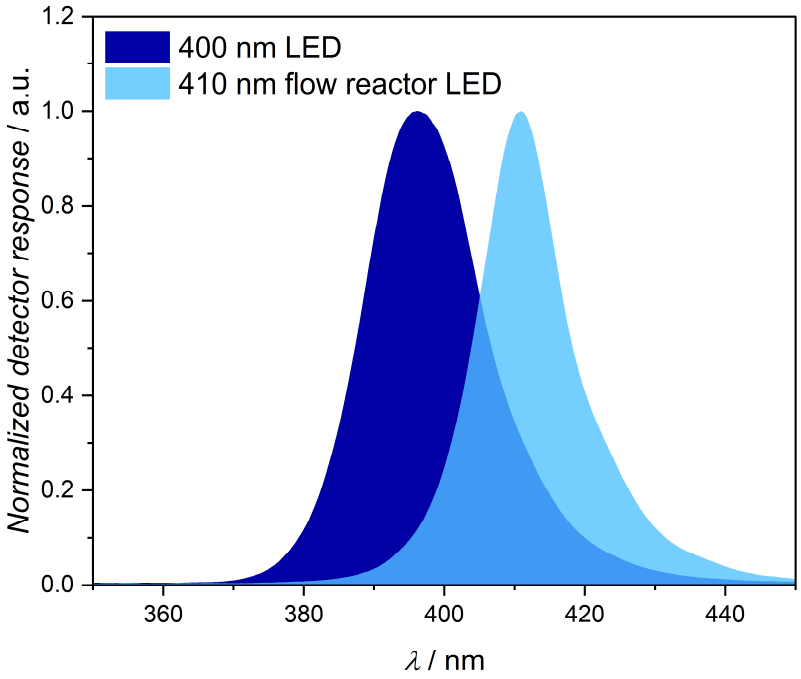

Figure 6.4 Emission spectra of the light emitting diodes (LEDs) employed in the synthetic procedures described in Chapter 6.3.2. The spectra were recorded on an Ocean Optics Miniature Spectrometer FLAME-T-UV-VIS.

6.3.2.1 Photochemical Action Plot of 2-((((2-Nitrobenzyl)oxy)carbonyl)amino)-ethyl methacrylate

A stock solution of 2-((((2-nitrobenzyl)oxy)carbonyl)amino)ethyl methacrylate with a concentration of 0.5 $mg \cdot mL^{-1}$ (1.62 $mmol \cdot L^{-1}$) in acetonitrile was prepared and sparged with argon. For each of the wavelengths given in **Table 6.9** (230-440 nm in 10 nm increments), 0.4 mL of this stock solution were transferred into a laser vial (0.8 mL, 7 mm x 40 mm, clear glass (for $\lambda \geq 310$ nm) or quartz (for $\lambda \leq 300$ nm)) under inert atmosphere and irradiated for eight minutes with a monochromatic nanosecond pulsed laser (refer to Chapter 6.2.8 for details). The energy per pulse was adjusted to keep the total number of photons at each wavelength the same with respect to the total irradiation time (refer to **Table 6.9** and Chapter 6.2.8 for details).

Following irradiation, 0.04 mg of pyrene (0.198 µmol) were added to each vial as an internal standard and the resulting solutions were analyzed by liquid chromatography (refer to Chapter 6.2.7 for details). Comparing the ratio of the areas (based on the integration of the 254 nm UV detector response) of the peaks belonging to the starting material (2-((((2-nitrobenzyl)oxy)carbonyl)amino)ethyl methacrylate) and pyrene with the same ratio for a similarly prepared sample which has not been irradiated enabled the determination of the amount of consumed starting material upon irradiation (refer to **Table 6.10** and **Table 6.11**). For each wavelength, the experiments were carried out in triplicate and the results are summarized in **Table 6.12**.

The experiments for different wavelengths were conducted on different days. Thus, the preparation of stock solutions and liquid chromatography runs were also conducted on different days. To ensure comparability of the recorded data over all wavelengths, the mean ratio of the peak areas of the starting material and pyrene without irradiation was used as the reference state for zero conversion (refer to **Table 6.11**). **Table 6.11** also contains information about the same samples being injected three times on the liquid chromatography column (included in the mean ratio mentioned previously), indicating that statistical errors rather result from sample preparation and pulse energy fluctuations during irradiation than from the liquid chromatography run and subsequent peak integration itself.

Table 6.9 Photon energies, laser vial transmittance values and energies per pulse for the wavelengths reported in the photochemical action plot in Chapter 4.2.2. Note that due to the low transmittance values of the clear glass laser vials below 300 nm, quartz laser vials were used instead.

Wavelength / nm	Photon energy / 10^{-19} J	Vial transmittance / %	Energy per pulse / µJ
230	8.64	81.4 (Quartz)	219.4
240	8.28	85.9 (Quartz)	199.4
250	7.95	82.6 (Quartz)	199.1
260	7.64	87.8 (Quartz)	180.0
270	7.36	88.9 (Quartz)	171.2
280	7.09	83.8 (Quartz)	175.2
290	6.85	90.0 (Quartz)	157.5
300	6.62	92.6 (Quartz)	147.9
310	6.41	66.3	200.0
320	6.21	72.7	176.6
330	6.02	77.0	161.7
340	5.84	79.8	151.4
350	5.68	81.7	143.7
360	5.52	83.0	137.6
370	5.37	83.8	132.5
380	5.23	84.4	128.2
390	5.09	84.7	124.3
400	4.97	85.0	120.9
410	4.84	85.1	117.7
420	4.73	85.2	114.8
430	4.62	85.3	112.0
440	4.51	85.4	109.4

Table 6.10 Relative peak areas of the UV detector responses (254 nm) obtained by integration of the corresponding peaks in the liquid chromatography chromatogram after irradiation of the starting material 2-((((2-nitrobenzyl)oxy)carbonyl)amino)ethyl methacrylate ($A_{rel,SM}$) and addition of the internal standard pyrene ($A_{rel,IS}$) and their ratio at the wavelengths reported in the photochemical action plot in Chapter 4.2.2. Each experiment was performed in triplicate.

Wavelength / nm	Relative peak area starting material ($A_{rel,SM}$) / %	Relative peak area internal standard ($A_{rel,IS}$) / %	Ratio $A_{rel,SM}/A_{rel,IS}$
230	53.52	46.48	1.15
	55.14	44.86	1.23
	54.81	45.19	1.21
240	54.78	45.22	1.21
	55.31	44.69	1.24
	57.75	42.25	1.37
250	56.87	43.13	1.32
	56.73	43.27	1.31
	55.76	44.24	1.26
260	54.80	45.20	1.21
	55.10	44.90	1.23
	56.01	43.99	1.27
270	54.60	45.40	1.20
	55.21	44.79	1.23
	55.25	44.75	1.23
280	54.25	45.75	1.19
	55.00	45.00	1.22
	54.71	45.29	1.21
290	54.26	45.74	1.19
	53.01	46.99	1.13
	52.30	47.70	1.10
300	54.85	45.15	1.21
	52.88	47.12	1.12
	53.79	46.21	1.16
310	52.32	47.68	1.10
	52.86	47.14	1.12
	52.34	47.66	1.10
320	53.06	46.94	1.13
	53.66	46.34	1.16
	53.65	46.35	1.16
330	53.83	46.17	1.17
	53.93	46.07	1.17
	53.83	46.17	1.17

Table 6.10 continued

340	54.17	45.83	1.18
	53.65	46.35	1.16
	54.79	45.21	1.21
350	55.28	44.72	1.24
	55.21	44.79	1.23
	55.20	44.80	1.23
360	54.66	45.34	1.21
	56.29	43.71	1.29
	55.82	44.18	1.26
370	56.80	43.20	1.31
	57.04	42.96	1.33
	57.20	42.80	1.34
380	57.09	42.91	1.33
	58.05	41.95	1.38
	57.49	42.51	1.35
390	57.46	42.54	1.35
	57.82	42.18	1.37
	57.54	42.46	1.36
400	58.69	41.31	1.42
	58.60	41.40	1.42
	59.69	40.31	1.48
410	59.38	40.62	1.46
	59.80	40.20	1.49
	59.94	40.06	1.50
420	59.80	40.28	1.48
	59.72	39.93	1.50
	59.92	40.08	1.50
430	59.79	40.21	1.49
	59.99	40.01	1.50
	60.00	40.00	1.50
440	59.95	40.05	1.50
	59.99	40.01	1.50
	59.83	40.17	1.49

Table 6.11 Relative peak areas of the UV detector responses (254 nm) obtained by integration of the corresponding peaks in the liquid chromatography chromatogram of an unirradiated mixture of the starting material 2-((((2-nitrobenzyl)oxy)carbonyl)amino)ethyl methacrylate ($A_{rel,SM}$) and internal standard pyrene ($A_{rel,IS}$) and their ratio. Six samples were prepared on different days (Samples 1-6). For three of them (Samples 4-6), liquid chromatography runs were performed three times (Inject 1-3).

Sample		**Relative peak area starting material ($A_{rel,SM}$) / %**	**Relative peak area internal standard ($A_{rel,IS}$) / %**	**Ratio $A_{rel,SM}/A_{rel,IS}$**
1		59.92	40.08	1.50
2		60.57	39.43	1.54
3		60.57	39.43	1.54
4	Inject 1	59.80	40.20	1.49
	Inject 2	59.83	40.17	1.49
	Inject 3	59.81	40.19	1.49
5	Inject 1	59.67	40.33	1.48
	Inject 2	59.67	40.33	1.48
	Inject 3	59.66	40.34	1.48
6	Inject 1	60.24	39.76	1.52
	Inject 2	60.27	39.73	1.52
	Inject 3	60.26	39.74	1.52
				Mean: 1.50

Table 6.12 Average, lowest and highest conversion determined for each wavelength reported in the photochemical action plot in Chapter 4.2.2 derived from the data given in **Table 6.10** and **Table 6.11**.

Wavelength / nm	Average conversion / %	Lowest conversion / %	Highest conversion / %
230	20.2	18.1	23.3
240	15.3	9.0	19.3
250	13.6	12.2	16.1
260	17.6	15.2	19.3
270	18.5	17.8	19.9
280	19.7	18.6	21.0
290	24.3	21.0	27.0
300	22.3	19.1	25.3
310	26.4	25.3	26.9
320	23.5	22.9	24.7
330	22.2	22.0	22.4
340	21.2	19.3	22.9
350	17.8	17.7	17.9
360	16.6	14.2	19.7
370	11.7	11.0	12.4
380	9.7	7.8	11.4
390	9.5	8.7	10.0
400	4.2	1.4	5.7
410	1.3	0.4	2.6
420	0.7	0.4	1.1
430	0.4	0.1	1.0
440	0.4	0.1	0.8

6.3.2.2 Synthesis of P3 and P3'

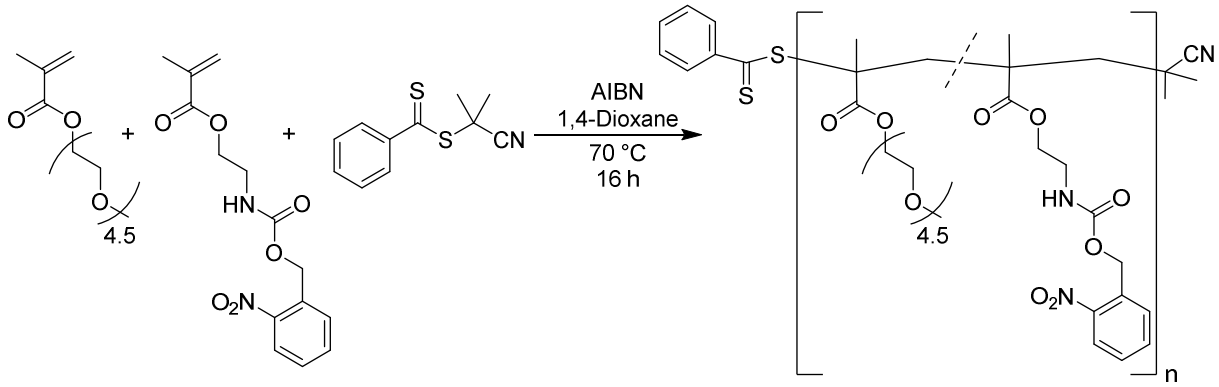

P3/P3'

10.0 mg of the RAFT agent 2-cyano-2-propyl benzodithioate (45.2 µmol, 1.00 eq.) and 1.48 mg azobisisobutyronitrile (AIBN, 9.04 µmol, 0.200 eq.) were dissolved in 5.5 mL of 1,4-dioxane and 2.75 mL of poly(ethylene glycol) methyl ether methacrylate (PEGMEMA, M_n = 300 g·mol^{-1}, 2.89 g, 9.63 mmol, 214 eq.) and 419 mg of 2-((((2-nitrobenzyl)oxy)carbonyl)amino)ethyl methacrylate (*o*NBMA, 1.36 mmol, 30.1 eq.) were added. The solution was degassed by three consecutive freeze-pump-thaw cycles and subsequently heated to 70 °C for 16 h. The reaction was stopped by cooling the flask to room temperature and opening it to air. The polymer was precipitated three times in a mixture of diethyl ether and *n*-pentane (1:1 v/v). The precipitate was isolated by centrifugation and dried under reduced pressure to give **P3** as a pink oil (2.16 g). A second batch of the polymer (**P3'**) was prepared in the same way.

^{1}H NMR (600 MHz, CD_3CN, 298 K): δ / ppm = 8.20-7.45 (br, *o*NBMA-Aryl-*H*), 6.35-6.15 (br, *o*NBMA-N*H*), 5.52-5.38 (br, *o*NBMA-Benzyl-CH_2), 4.20-3.90 (br, PEGMEMA-COOCH_2), 4.00-3.86 (br, *o*NBMA-COOCH_2), 3.75-3.35 (br, PEGMEMA-OCH_2CH_2), 3.44-3.34 (br, *o*NBMA-CH_2NH), 3.34-3.24 (br, PEGMEMA-OCH_3), 2.05-0.70 (br, aliphatic backbone).

SEC (THF, RI, PMMA cal.): **P3**: M_n = 28200 g·mol^{-1}, M_w = 34600 g·mol^{-1}, M_p = 33500 g·mol^{-1}, $Đ$ = 1.23. **P3'**: M_n = 30900 g·mol^{-1}, M_w = 36500 g·mol^{-1}, M_p = 34500 g·mol^{-1}, $Đ$ = 1.18.

DLS (CH_3CN): **P3**: D_s = 6.42 nm. **P3'**: D_s = 6.66 nm.

DOSY (400 MHz, CD_3CN, 301 K): **P3**: D = 1.43·10^{-10} m^2·s^{-1}. **P3'**: D = 1.47·10^{-10} m^2·s^{-1}.

6.3.2.3 Synthesis of SCNP3-Cu-Batch

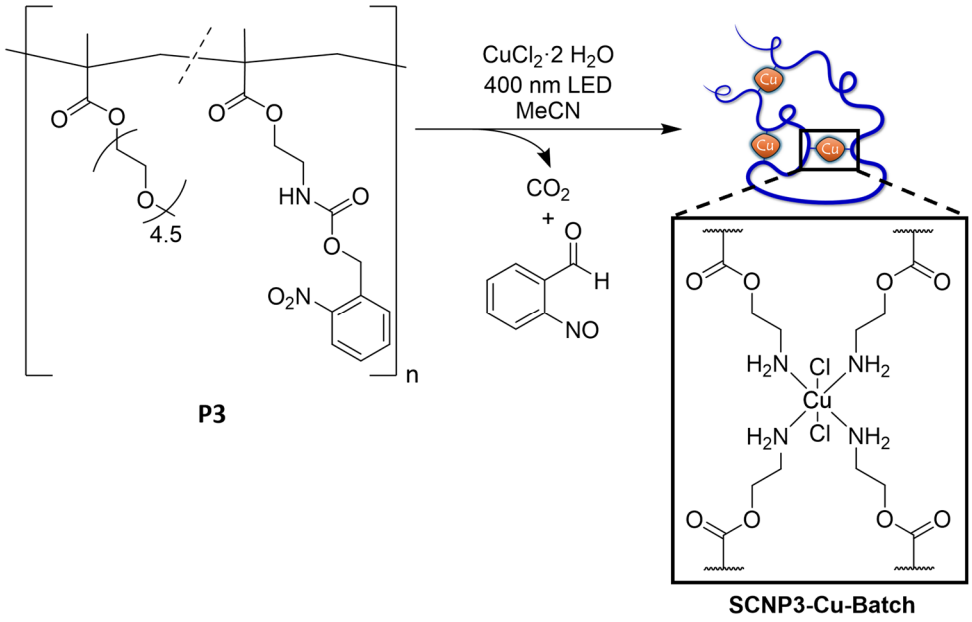

10.0 mg of **P3** (4.65 µmol, 1.00 eq. photoreactive unit) and 0.79 mg of $CuCl_2 \cdot 2\ H_2O$ (4.65 µmol, 1.00 eq.) were dissolved in 5 mL of acetonitrile. The resulting yellow solution was sparged with argon and subsequently irradiated using a 400 nm LED (10 W). After completion of the reaction (refer to **Figure 4.21a** for kinetics data), the solvent was evaporated under reduced pressure to give **SCNP3-Cu-Batch**. Note that this workup does not remove unreacted $CuCl_2 \cdot 2\ H_2O$.

^{1}H NMR (600 MHz, CD_3CN, 298 K): δ / ppm = 4.20-3.90 (br, PEGMEMA-COOCH_2), 3.75-3.40 (br, PEGMEMA-OCH_2CH_2), 3.38-3.20 (br, PEGMEMA-OCH_3), 2.00-0.65 (br, aliphatic backbone).

SEC (THF, RI, PMMA cal.): M_n = 9700 g·mol^{-1}, M_w = 15200 g·mol^{-1}, M_p = 18700 g·mol^{-1}, $Đ$ = 1.57.

DLS (CH_3CN): D_s = 3.05 nm.

DOSY (400 MHz, CD_3CN, 301 K): $D = 1.71 \cdot 10^{-10}$ m^2·s^{-1}.

Kinetics data (refer to **Figure 4.21a**) for the reaction were obtained in the following way: 10.0 mg of **P3** (4.65 µmol, 1.00 eq. photoreactive unit) and 0.79 mg of $CuCl_2 \cdot 2\ H_2O$ (4.65 µmol, 1.00 eq.) were dissolved in 5 mL of acetonitrile. The resulting yellow solution was sparged with argon and subsequently irradiated using a 400 nm LED (10 W). 0.1 mL of the reaction mixture were taken out 0, 2, 5, 10, 20, 30, 40 and 50 minutes, respectively, after starting the LED irradiation and each sample added to 0.3 mL of CD_3CN for NMR analysis.

To ensure that both, the presence of $CuCl_2 \cdot 2\ H_2O$ and light, are crucial for the formation of **SCNP3-Cu-Batch**, the following control reactions were conducted (refer to **Figure 4.21b**):

- **P3** + $CuCl_2 \cdot 2\ H_2O$, no irradiation:

10.0 mg of **P3** (4.65 µmol, 1.00 eq. photoreactive unit) and 0.79 mg of $CuCl_2 \cdot 2\ H_2O$ (4.65 µmol, 1.00 eq.) were dissolved in 5 mL of acetonitrile. The resulting yellow solution was sparged with argon and subsequently stirred for 50 minutes at room temperature.

- **P3**, irradiation, no $CuCl_2 \cdot 2\ H_2O$:

10.0 mg of **P3** (4.65 µmol, 1.00 eq. photoreactive unit) were dissolved in 5 mL of acetonitrile. The resulting yellow solution was sparged with argon and subsequently irradiated using a 400 nm LED (10 W) for 50 minutes.

- **P3**, $CuCl_2 \cdot 2\ H_2O$ added after irradiation:

10.0 mg of **P3** (4.65 µmol, 1.00 eq. photoreactive unit) were dissolved in 5 mL of acetonitrile. The resulting yellow solution was sparged with argon and subsequently irradiated using a 400 nm LED (10 W) for 50 minutes. Following irradiation, 0.79 mg of $CuCl_2 \cdot 2\ H_2O$ (4.65 µmol, 1.00 eq.) were added.

In all cases, the solvent was evaporated under reduced pressure and the resulting residue redissolved in THF for SEC analysis.

6.3.2.4 Synthesis of SCNP3-Cu-Flow

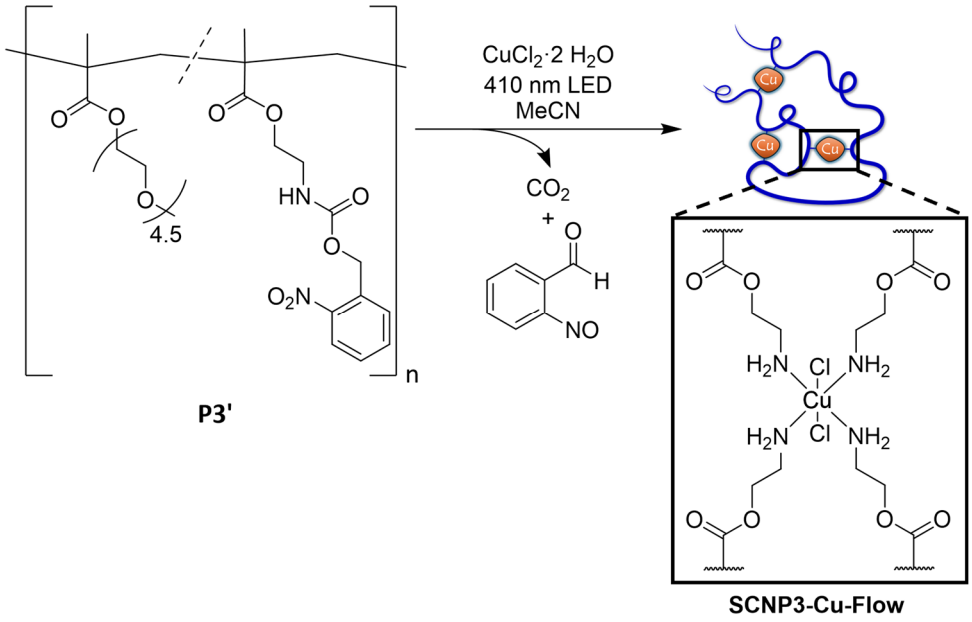

10.0 mg of **P3'** (4.98 µmol, 1.00 eq. photoreactive unit) and 0.84 mg of $CuCl_2 \cdot 2\ H_2O$ (4.98 µmol, 1.00 eq.) were dissolved in 5 mL of acetonitrile. The resulting yellow solution was sparged with argon and subsequently irradiated using a 410 nm LED (12 W) under photoflow conditions (flow rate 0.2 $mL \cdot min^{-1}$, refer to Chapter 6.2.9 for details regarding the photoflow reactor). The obtained yellow solution was directly loaded onto a preparative SEC column (Sephadex LH-20) and eluted with acetonitrile, resulting in a pale-yellow solution of **SCNP3-Cu-Flow**.

^{1}H NMR (600 MHz, CD_3CN, 298 K): δ / ppm = 4.20-3.90 (br, PEGMEMA-COOCH_2), 3.80-3.40 (br, PEGMEMA-OCH_2CH_2), 3.38-3.22 (br, PEGMEMA-OCH_3), 2.00-0.65 (br, aliphatic backbone).

SEC (THF, RI, PMMA cal.): M_n = 16000 $g \cdot mol^{-1}$, M_w = 22200 $g \cdot mol^{-1}$, M_p = 24600 $g \cdot mol^{-1}$, $Đ$ = 1.39.

DLS (CH_3CN): D_s = 4.65 nm.

DOSY (400 MHz, CD_3CN, 301 K): $D = 1.56 \cdot 10^{-10}$ $m^2 \cdot s^{-1}$.

Following the same general procedure as described above, the following experiments were conducted to investigate the influence of flow rate and polymer concentration:

- 10.0 mg of **P3'** (4.98 µmol, 1.00 eq. photoreactive unit) and 0.84 mg of $CuCl_2 \cdot 2\ H_2O$ (4.98 µmol, 1.00 eq.) were dissolved in 5 mL of acetonitrile and the solution sparged with argon. 1 mL aliquots were taken out of this solution and irradiated under photoflow conditions at flow rates of 0.2, 0.3, 0.4, 0.5 and 1 $mL \cdot min^{-1}$, respectively (refer to **Figure 4.25a** and **b**).

- 1 mL of acetonitrile solutions with the following amounts of **P3'** and $CuCl_2 \cdot 2\ H_2O$ were prepared from a stock solution and irradiated under photoflow conditions at a flow rate of 0.2 $mL \cdot min^{-1}$ (refer to **Figure 4.25c** and **d**):

  - 2.0 mg of **P3'** (0.996 µmol, 1.00 eq. photoreactive unit) and 0.17 mg of $CuCl_2 \cdot 2\ H_2O$ (0.996 µmol, 1.00 eq.)
  - 5.0 mg of **P3'** (2.49 µmol, 1.00 eq. photoreactive unit) and 0.42 mg of $CuCl_2 \cdot 2\ H_2O$ (2.49 µmol, 1.00 eq.)
  - 10.0 mg of **P3'** (4.98 µmol, 1.00 eq. photoreactive unit) and 0.84 mg of $CuCl_2 \cdot 2\ H_2O$ (4.98 µmol, 1.00 eq.)
  - 20.0 mg of **P3'** (9.96 µmol, 1.00 eq. photoreactive unit) and 1.69 mg of $CuCl_2 \cdot 2\ H_2O$ (9.96 µmol, 1.00 eq.)
  - 50.0 mg of **P3'** (24.9 µmol, 1.00 eq. photoreactive unit) and 4.24 mg of $CuCl_2 \cdot 2\ H_2O$ (24.9 µmol, 1.00 eq.)

For NMR analysis, 0.1 mL of each solution obtained after irradiation were added to 0.3 mL of CD_3CN. For SEC analysis, 0.1 mL of each solution obtained after irradiation were mixed with 0.2 mL of THF and SEC measurements performed with the resulting solutions.

6.3.2.5 Synthesis of [(2-Phenylethylamine)$_4$CuCl$_2$]

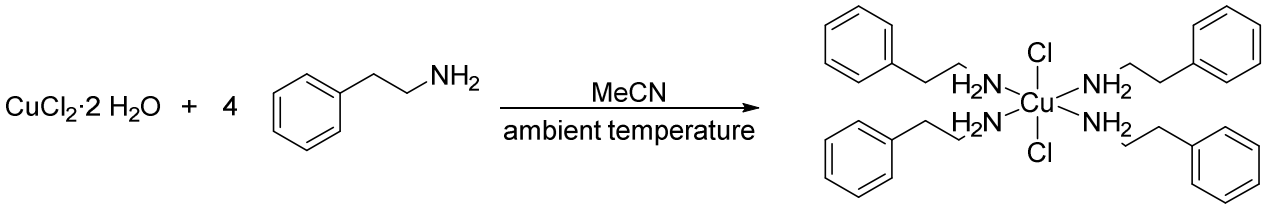

0.500 g of $CuCl_2 \cdot 2\ H_2O$ (2.93 mmol, 1.00 eq.) were dissolved in 10 mL of acetonitrile. To the resulting yellow solution, 0.737 mL of 2-phenylethylamine (0.711 g, 5.87 mmol, 2.00 eq.) were added, leading to an immediate color change to dark blue. The solution was subsequently concentrated to approximately 6 mL. After storage at ambient temperature overnight, pale blue needles suitable for single crystal X-ray diffraction experiments were obtained.

^{1}H NMR: No meaningful NMR data could be obtained due to the paramagnetism of the compound.

FT-IR (ATR): $\tilde{\nu}$ / cm^{-1} = 3336 (w), 3277 (w), 3207 (w), 3187 (w), 3116 (m), 3020 (w), 3000 (w), 2944 (w), 2913 (w), 2879 (w), 2851 (w), 1600 (m), 1496 (m), 1450 (s), 1445 (m), 1360 (m), 1247 (w), 1224 (w), 1151 (m), 1123 (m), 1078 (m), 1052 (s), 1035 (s), 999 (m), 939 (m), 920 (m), 753 (vs), 699 (vs), 671 (s), 634 (m), 578 (m), 516 (w), 490 (m).

Elemental analysis: [%] calculated for [$C_{36}H_{50}Cl_2CuN_6$] (701.28 g·mol^{-1}): C 62.07, H 7.16, N 9.05; found: C 61.30, H 6.59, N 9.72.

XRD: Refer to **Figure 4.24** and **Table 6.13**.

Table 6.13 Summary of crystal data and structure refinement of [(2-phenylethylamine)$_4$CuCl$_2$].

Identification code	SG114
Empirical formula	$C_{36}H_{50}Cl_2CuN_6$
Formula weight	701.26
Temperature/K	100
Crystal system	Monoclinic
Space group	$P2_1/n$
a/Å	14.4097(15)
b/Å	5.8858(7)
c/Å	21.876(3)
β/°	92.905(9)
Volume/Å^3	1853.0(4)
Z	2
ρ_{calc}/g·cm^{-3}	1.257
μ/mm^{-1}	0.766
F(000)	742.0
Crystal size/mm^3	0.231 × 0.106 × 0.043
Radiation	Mo-K_α (λ = 0.71073)
2Θ range for data collection/°	3.728 to 60.468
Index ranges	$-19 \leq h \leq 16$, $-8 \leq k \leq 7$, $-27 \leq l \leq 29$
Reflections collected	11145
Independent reflections	4550 [R_{int} = 0.0477, R_{sigma} = 0.0718]
Data/restraints/parameters	4550/0/206
Goodness-of-fit on F^2	1.032
Final R indexes [I>=2σ (I)]	R_1 = 0.0511, wR_2 = 0.1100
Final R indexes [all data]	R_1 = 0.0976, wR_2 = 0.1297
Largest diff. peak/hole / e Å^{-3}	0.53/-0.91

6.3.2.6 Synthesis of Poly(PEGMEMA)

Poly(PEGMEMA)

10.0 mg of the RAFT agent 2-cyano-2-propyl benzodithioate (45.2 µmol, 1.00 eq.) and 1.48 mg azobisisobutyronitrile (AIBN, 9.04 µmol, 0.200 eq.) were dissolved in 5.5 mL of 1,4-dioxane and 2.75 mL of poly(ethylene glycol) methyl ether methacrylate (PEGMEMA, M_n = 300 g·mol^{-1}, 2.89 g, 9.63 mmol, 214 eq.) were added. The solution was degassed by three consecutive freeze-pump-thaw cycles and subsequently heated to 70 °C for 16 h. The reaction was stopped by cooling the flask to room temperature and opening it to air. The polymer was precipitated three times in a mixture of diethyl ether and *n*-pentane (1:1 v/v). The precipitate was isolated by centrifugation and dried under reduced pressure to give Poly(PEGMEMA) as a pink oil (2.15 g).

^{1}H NMR (600 MHz, CD_3CN, 298 K): δ / ppm = 4.14-4.00 (br, COOCH_2), 3.74-3.42 (br, OCH_2CH_2), 3.34-3.24 (br, OCH_3), 2.04-0.70 (br, aliphatic backbone).

SEC (THF, RI, PMMA cal.): M_n = 35000 g·mol^{-1}, M_w = 39100 g·mol^{-1}, M_p = 36900 g·mol^{-1}, $Đ$ = 1.12.

6.3.2.7 Catalytic Reactions

Decarboxylation-Oxygenation of Xanthene-9-carboxylic acid

(I) SCNP3-Cu-Flow

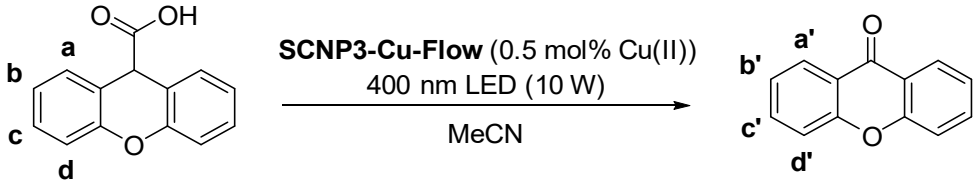

For reactions employing **SCNP3-Cu-Flow** as the catalyst, 10.0 mg of polymer **P3'** (4.98 µmol, 0.100 eq. photoreactive unit) and 0.84 mg $CuCl_2 \cdot 2\ H_2O$ (4.98 µmol, 0.100 eq.) were dissolved in 5 mL of acetonitrile. The resulting yellow solution was sparged with argon and subsequently irradiated using a 410 nm LED (12 W) under photoflow conditions (flow rate 0.2 $mL \cdot min^{-1}$). The obtained yellow solution was directly loaded onto a preparative SEC column (Sephadex LH-20) and eluted with acetonitrile, resulting in 5 mL of a pale-yellow solution of **SCNP3-Cu-Flow** (Cu(II) concentration about 0.05 $mmol \cdot L^{-1}$, refer to Chapter 4.2.4). The solution was transferred into a 20 mL crimp vial and 11.3 mg xanthene-9-carboxylic acid (49.8 µmol, 1.00 eq.) were added. After sparging with oxygen, an oxygen-filled balloon was fitted on top of the vial and the solution was irradiated using a 400 nm LED (10 W). 0.1 mL of the reaction solution were taken out before irradiation (t_0) and after 30, 60, 90 and 120 minutes, respectively, and 0.3 mL of CD_3CN added to each sample for NMR analysis. The reaction was performed in triplicate (refer to **Figure 6.5**).

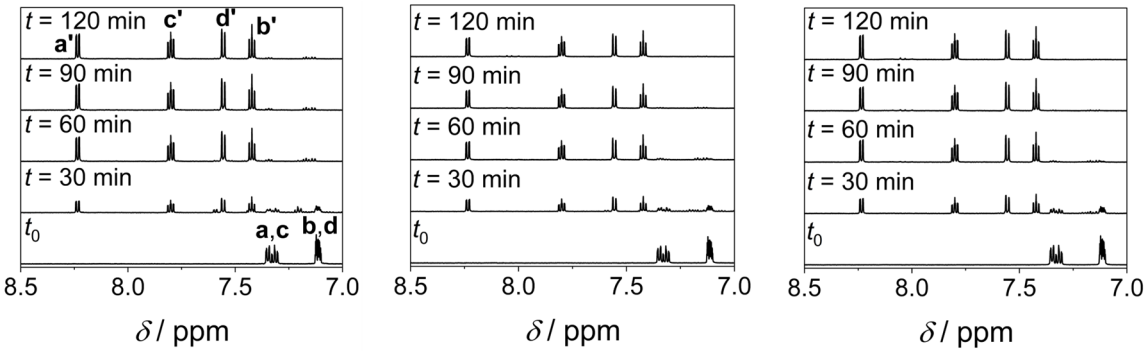

Figure 6.5 ^1H NMR spectra (600 MHz, CD_3CN, 298 K) of the reaction mixture of xanthene-9-carboxylic acid and **SCNP3-Cu-Flow** before (t_0) and at different times after starting the irradiation with a 400 nm LED (10 W) under oxygen atmosphere. Labels refer to reaction scheme on top of page. The experiment was performed in triplicate.

(II) SCNP3-Cu-Batch

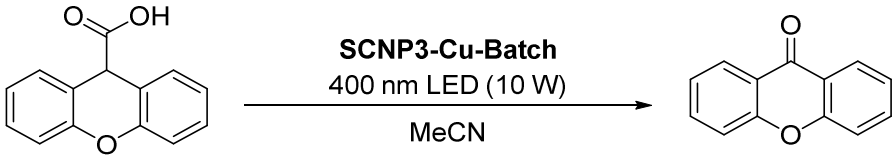

For reactions employing **SCNP3-Cu-Batch** as the catalyst, 10.0 mg of **P3'** (4.98 µmol, 0.100 eq. photoreactive unit) and 0.84 mg of $CuCl_2 \cdot 2\ H_2O$ (4.98 µmol, 0.100 eq.) were dissolved in 5 mL of acetonitrile. The resulting yellow solution was sparged with argon and subsequently irradiated using a 400 nm LED (10 W) for 50 minutes. The obtained yellow solution was directly loaded onto a preparative SEC column (Sephadex LH-20) and eluted with acetonitrile, resulting in a pale-yellow solution of **SCNP3-Cu-Batch**. The solution was transferred into a 20 mL crimp vial and 11.3 mg xanthene-9-carboxylic acid (49.8 µmol, 1.00 eq.) were added. After sparging with oxygen, an oxygen-filled balloon was fitted on top of the vial and the solution was irradiated using a 400 nm LED (10 W). 0.1 mL of the reaction solution were taken out before irradiation (t_0) and after 30, 60, 90 and 120 minutes, respectively, and 0.3 mL of CD_3CN added to each sample for NMR analysis (refer to **Figure 6.6**).

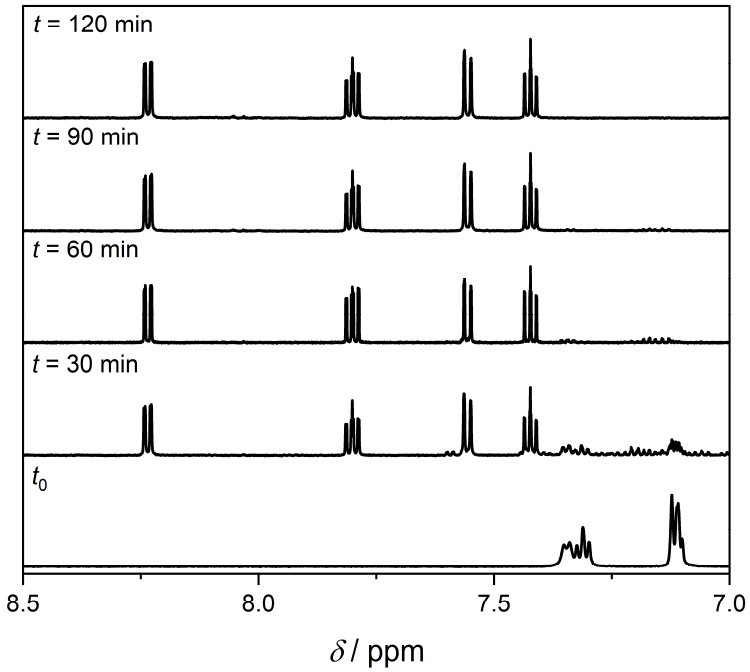

Figure 6.6 ^{1}H NMR spectra (600 MHz, CD_3CN, 298 K) of the reaction mixture of xanthene-9-carboxylic acid and **SCNP3-Cu-Batch** before (t_0) and at different times after starting the irradiation with a 400 nm LED (10 W) under oxygen atmosphere.

(III) 0.5 mol% $CuCl_2 \cdot 2\ H_2O$

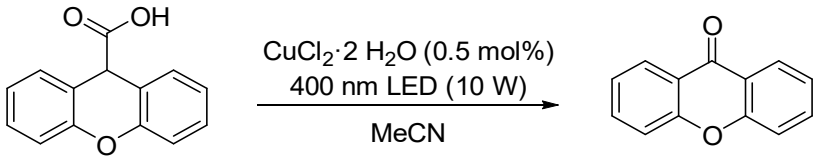

For reactions employing 0.5 mol% of $CuCl_2 \cdot 2\ H_2O$ as the catalyst, 11.3 mg xanthene-9-carboxylic acid (49.8 µmol, 1.00 eq.) were dissolved in 5 mL of a 0.01 $mg \cdot mL^{-1}$ $CuCl_2 \cdot 2\ H_2O$ stock solution (0.293 µmol, 0.00588 eq.) in acetonitrile in a 10 mL crimp vial. The resulting yellow solution was sparged with oxygen and an oxygen-filled balloon was fitted on top of the vial. The solution was irradiated using a 400 nm LED (10 W). 0.1 mL of the reaction solution were taken out before irradiation (t_0) and after 30, 60 and 90 minutes, respectively, and 0.3 mL of CD_3CN added to each sample for NMR analysis. The reaction was performed in triplicate (refer to **Figure 6.7**).

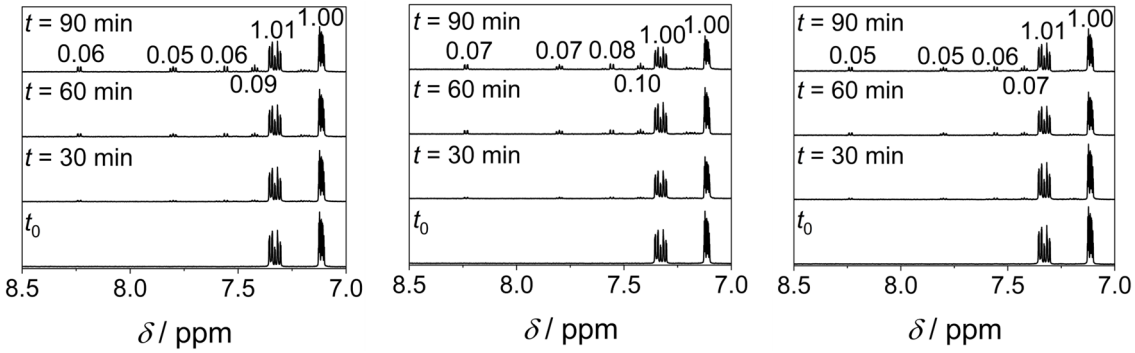

Figure 6.7 ^1H NMR spectra (600 MHz, CD_3CN, 298 K) of the reaction mixture of xanthene-9-carboxylic acid and 0.5 mol% $CuCl_2 \cdot 2\ H_2O$ before (t_0) and at different times after starting the irradiation with a 400 nm LED (10 W) under oxygen atmosphere. Numbers on peaks denote integral values. The experiment was performed in triplicate.

(IV) 10 mol% $CuCl_2 \cdot 2\ H_2O$

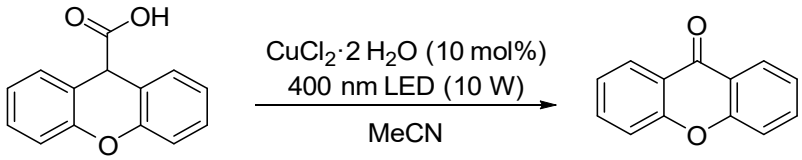

For reactions employing 10 mol% of $CuCl_2 \cdot 2\ H_2O$ as the catalyst, 11.3 mg xanthene-9-carboxylic acid (49.8 µmol, 1.00 eq.) and 0.84 mg $CuCl_2 \cdot 2\ H_2O$ (4.98 µmol, 0.100 eq.) were dissolved in 5 mL of acetonitrile in a 20 mL crimp vial. The resulting yellow solution was sparged with oxygen and an oxygen-filled balloon was fitted on top of the vial. The solution was irradiated using a 400 nm LED (10 W). 0.1 mL of the reaction solution were taken out before irradiation (t_0) and after 30, 60 and 90 minutes, respectively, and 0.3 mL of CD_3CN added to each sample for NMR analysis. The reaction was performed in triplicate (refer to **Figure 6.8**).

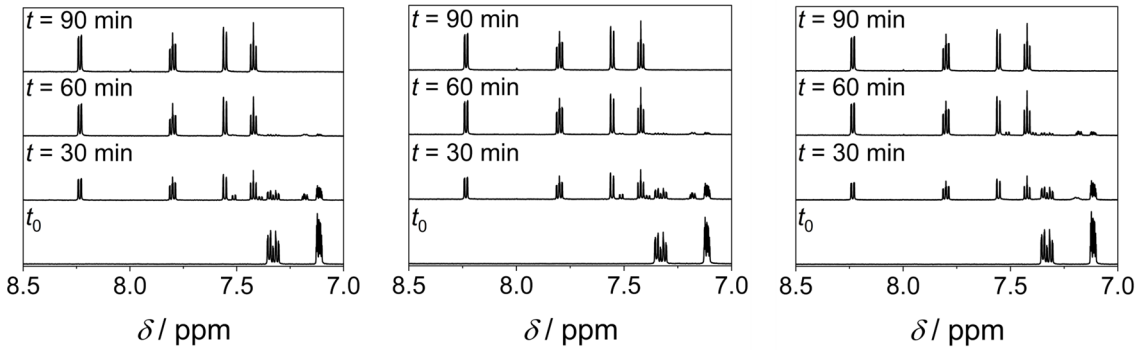

Figure 6.8 ^1H NMR spectra (600 MHz, CD_3CN, 298 K) of the reaction mixture of xanthene-9-carboxylic acid and 10 mol% $CuCl_2 \cdot 2\ H_2O$ before (t_0) and at different times after starting the irradiation with a 400 nm LED (10 W) under oxygen atmosphere. The experiment was performed in triplicate.

(V) $CuCl_2 \cdot 2\ H_2O$ + Poly(PEGMEMA)

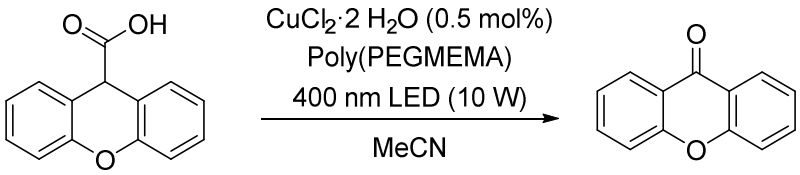

11.3 mg xanthene-9-carboxylic acid (49.8 µmol, 1.00 eq.) and 10.0 mg Poly(PEGMEMA) were dissolved in 5 mL of a 0.01 $mg \cdot mL^{-1}$ $CuCl_2 \cdot 2\ H_2O$ stock solution (0.293 µmol, 0.00588 eq.) in acetonitrile in a 10 mL crimp vial. The resulting slightly yellow solution was sparged with oxygen and an oxygen-filled balloon was fitted on top of the vial. The solution was irradiated using a 400 nm LED (10 W). 0.1 mL of the reaction solution were taken out before irradiation (t_0) and after 30, 60 and 90 minutes, respectively, and 0.3 mL of CD_3CN added to each sample for NMR analysis (refer to **Figure 6.9**).

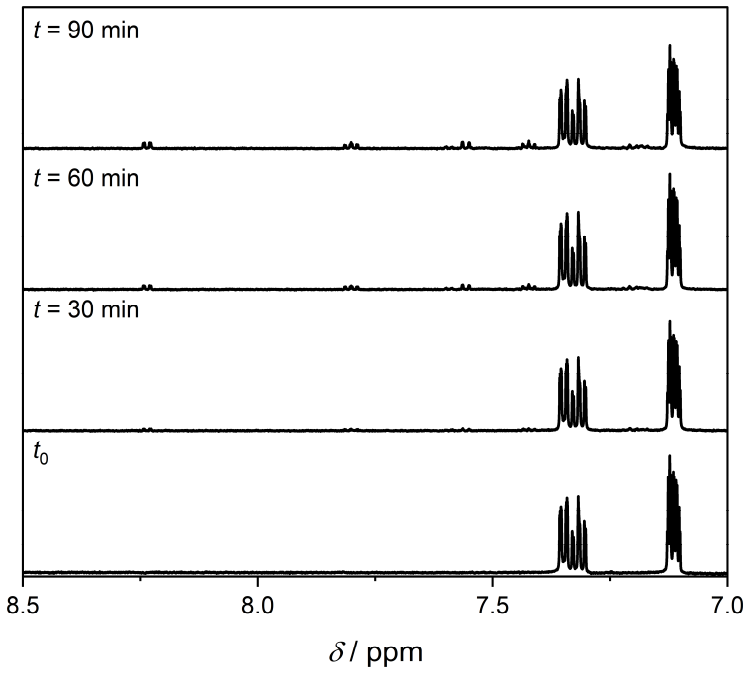

Figure 6.9 ^1H NMR spectra (600 MHz, CD_3CN, 298 K) of the reaction mixture of xanthene-9-carboxylic acid, 0.5 mol% $CuCl_2 \cdot 2\ H_2O$ and Poly(PEGMEMA) before (t_0) and at different times after starting the irradiation with a 400 nm LED (10 W) under oxygen atmosphere.

(VI) $CuCl_2$·2 H_2O + *n*-butylamine

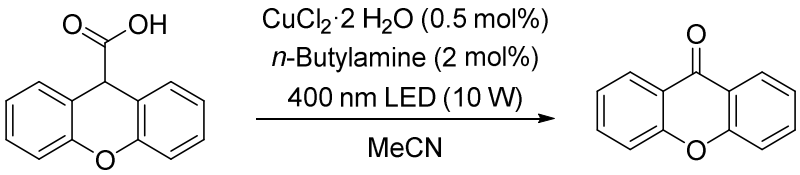

A stock solution containing 0.01 mg·mL^{-1} of $CuCl_2$·2 H_2O and 17.2 µg·mL^{-1} *n*-butylamine in acetonitrile was prepared. 11.3 mg xanthene-9-carboxylic acid (49.8 µmol, 1.00 eq.) were dissolved in 5 mL of this acetonitrile solution (0.293 µmol, 0.00588 eq. $CuCl_2$·2 H_2O; 1.18 µmol, 0.0235 eq. *n*-butylamine) in a 10 mL crimp vial. The resulting slightly blue solution was sparged with oxygen and an oxygen-filled balloon was fitted on top of the vial. The solution was irradiated using a 400 nm LED (10 W). 0.1 mL of the reaction solution were taken out before irradiation (t_0) and after 30, 60, 90 and 120 minutes, respectively, and 0.3 mL of CD_3CN added to each sample for NMR analysis (refer to **Figure 6.10**).

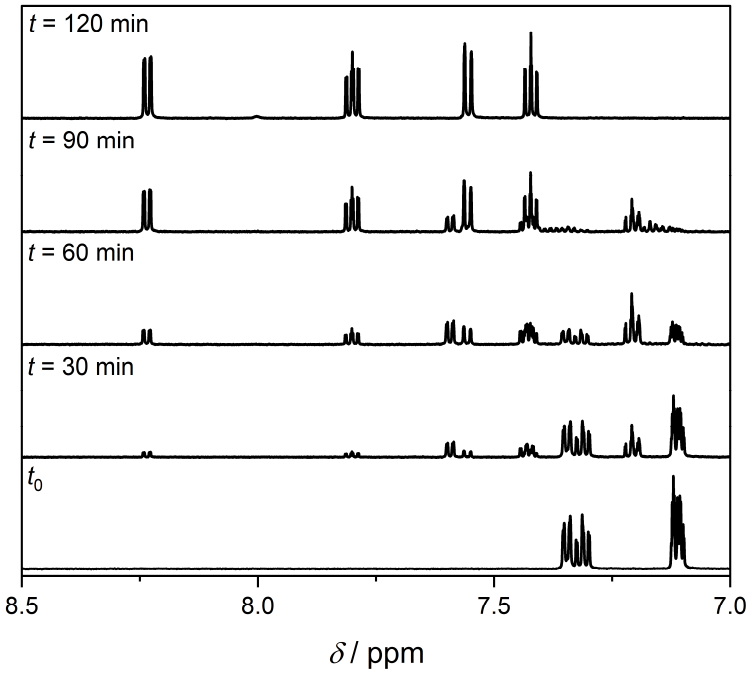

Figure 6.10 ^{1}H NMR spectra (600 MHz, CD_3CN, 298 K) of the reaction mixture of xanthene-9-carboxylic acid, 0.5 mol% $CuCl_2$·2 H_2O and 2 mol% *n*-butylamine before (t_0) and at different times after starting the irradiation with a 400 nm LED (10 W) under oxygen atmosphere.

(VII) P3'

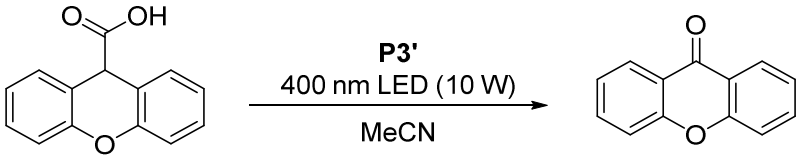

11.3 mg xanthene-9-carboxylic acid (49.8 µmol, 1.00 eq.) and 10.0 mg **P3'** (4.98 µmol, 0.10 eq. photoreactive unit) were dissolved in 5 mL of acetonitrile in a 20 mL crimp vial. The resulting colorless solution was sparged with oxygen and an oxygen-filled balloon was fitted on top of the vial. The solution was irradiated using a 400 nm LED (10 W). 0.1 mL of the reaction solution were taken out before irradiation (t_0) and after 120 minutes, respectively, and 0.3 mL of CD_3CN added to each sample for NMR analysis (refer to **Figure 6.11**).

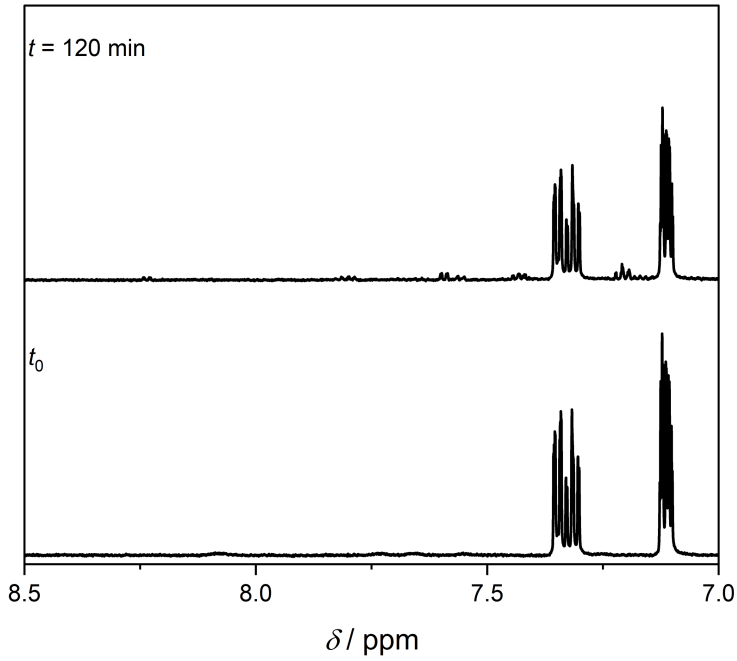

Figure 6.11 ^{1}H NMR spectra (600 MHz, CD_3CN, 298 K) of the reaction mixture of xanthene-9-carboxylic acid and **P3'** before (t_0) and after 120 minutes of irradiation with a 400 nm LED (10 W) under oxygen atmosphere.

(VIII) Mixture of P3' and $CuCl_2 \cdot 2\ H_2O$ subjected to preparative SEC

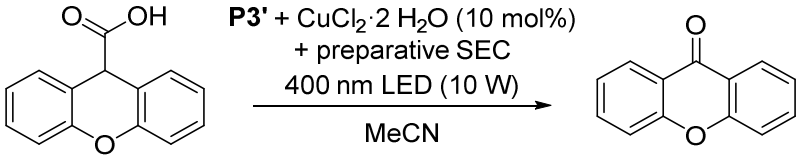

10.0 mg of polymer **P3'** (4.98 µmol, 0.100 eq. photoreactive unit) and 0.84 mg $CuCl_2 \cdot 2\ H_2O$ (4.98 µmol, 0.100 eq.) were dissolved in 5 mL of acetonitrile. The resulting yellow solution was directly loaded onto a preparative SEC column (Sephadex LH-20) and eluted with acetonitrile, resulting in a colorless solution of **P3'**. The solution was transferred into a 20 mL crimp vial and 11.3 mg xanthene-9-carboxylic acid (49.8 µmol, 1.00 eq.) were added. After sparging with oxygen, an oxygen-filled balloon was fitted on top of the vial and the solution irradiated using a 400 nm LED (10 W). 0.1 mL of the reaction solution were taken out before irradiation (t_0) and after 120 minutes, respectively, and 0.3 mL of CD_3CN added to each sample for NMR analysis (refer to **Figure 6.12**).

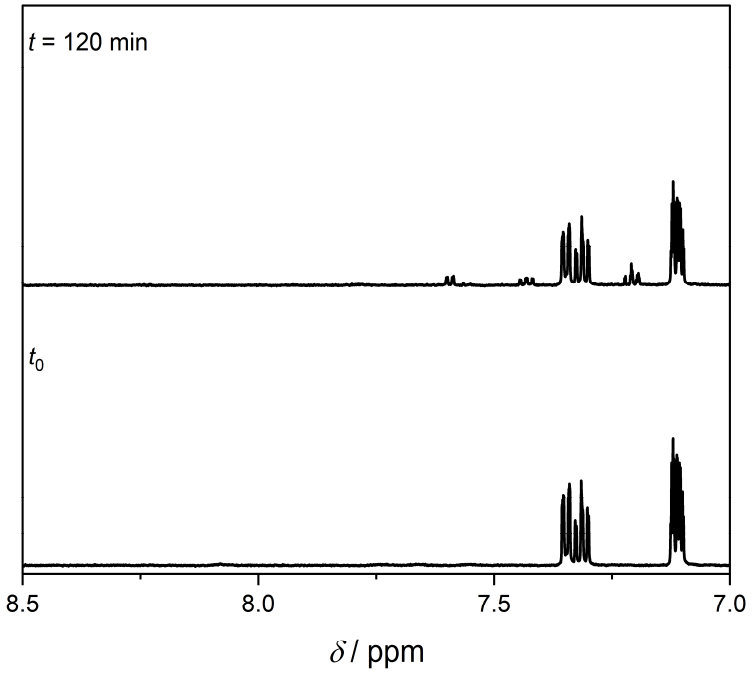

Figure 6.12 ^{1}H NMR spectra (600 MHz, CD_3CN, 298 K) of the reaction mixture of xanthene-9-carboxylic acid and **P3'** before (t_0) and after 120 minutes of irradiation with a 400 nm LED (10 W) under oxygen atmosphere. For that, **P3'** and $CuCl_2 \cdot 2\ H_2O$ were first mixed and subsequently subjected to preparative size-exclusion chromatography (Sephadex LH-20) in acetonitrile, demonstrating that catalytically active $CuCl_2 \cdot 2\ H_2O$ is effectively removed by this purification technique.

(IX) $CuCl_2 \cdot 2\ H_2O$ without LED irradiation

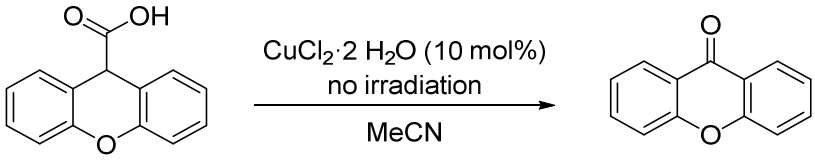

11.3 mg xanthene-9-carboxylic acid (49.8 µmol, 1.00 eq.) and 0.84 mg $CuCl_2 \cdot 2\ H_2O$ (4.98 µmol, 0.100 eq.) were dissolved in 5 mL of acetonitrile in a 20 mL crimp vial. The resulting yellow solution was sparged with oxygen and an oxygen-filled balloon was fitted on top of the vial. The solution was stirred at room temperature without irradiation. 0.1 mL of the reaction solution were taken out immediately (t_0) and after 120 minutes, respectively, and 0.3 mL of CD_3CN added to each sample for NMR analysis (refer to **Figure 6.13**).

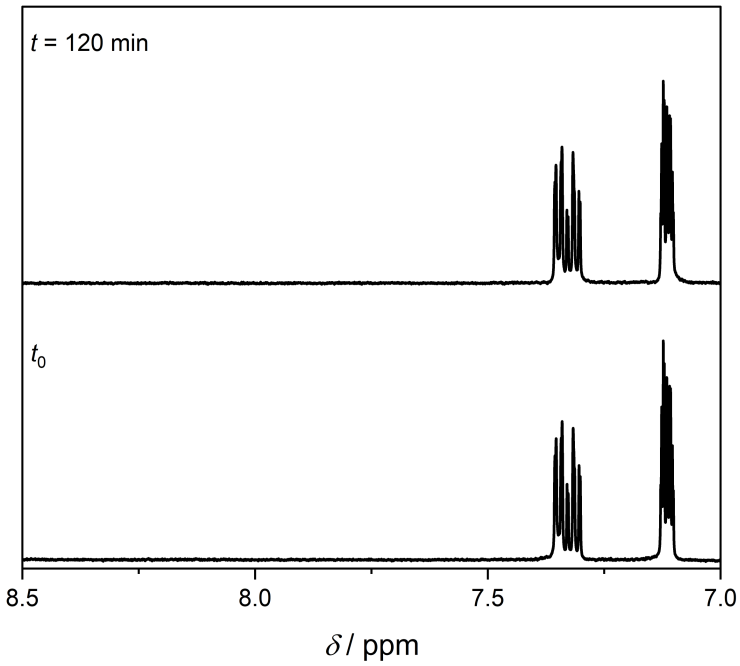

Figure 6.13 ^1H NMR spectra (600 MHz, CD_3CN, 298 K) of the reaction mixture of xanthene-9-carboxylic acid and 10 mol% $CuCl_2 \cdot 2\ H_2O$ before (t_0) and after 120 minutes of stirring at room temperature without irradiation under oxygen atmosphere.

(X) SCNP3-Cu-Flow without LED irradiation

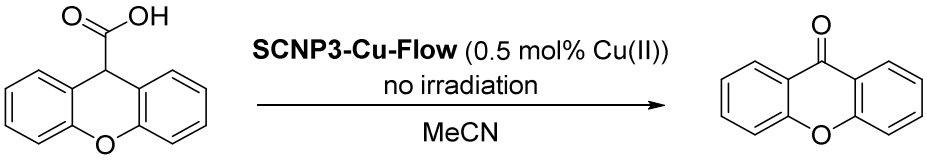

10.0 mg of polymer **P3'** (4.98 µmol, 0.100 eq. photoreactive unit) and 0.84 mg $CuCl_2 \cdot 2\ H_2O$ (4.98 µmol, 0.100 eq.) were dissolved in 5 mL of acetonitrile. The resulting yellow solution was sparged with argon and subsequently irradiated using a 410 nm LED (12 W) under photoflow conditions (flow rate 0.2 $mL \cdot min^{-1}$). The obtained yellow solution was directly loaded onto a preparative SEC column (Sephadex LH-20) and eluted with acetonitrile, resulting in a pale-yellow solution of **SCNP3-Cu-Flow**. The solution was transferred into a 20 mL crimp vial and 11.3 mg xanthene-9-carboxylic acid (49.8 µmol, 1.00 eq.) were added. After sparging with oxygen, an oxygen-filled balloon was fitted on top of the vial and the solution stirred at room temperature without irradiation. 0.1 mL of the reaction solution were taken out immediately (t_0) and after 120 minutes, respectively, and 0.3 mL of CD_3CN added to each sample for NMR analysis (refer to **Figure 6.14**).

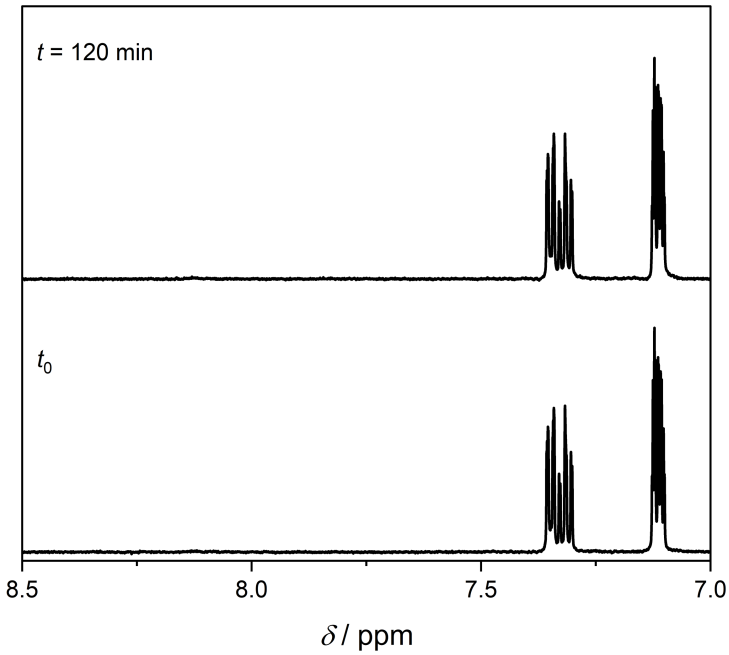

Figure 6.14 ^1H NMR spectra (600 MHz, CD_3CN, 298 K) of the reaction mixture of xanthene-9-carboxylic acid and **SCNP3-Cu-Flow** before (t_0) and after 120 minutes of stirring at room temperature without irradiation under oxygen atmosphere.

(XI) LED irradiation without catalyst

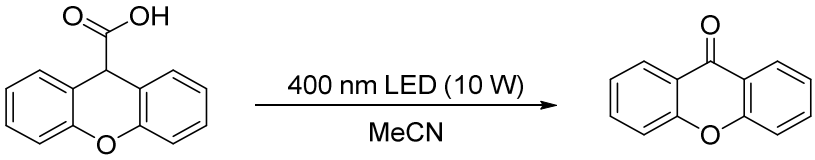

11.3 mg xanthene-9-carboxylic acid (49.8 µmol, 1.00 eq.) were dissolved in 5 mL of acetonitrile in a 20 mL crimp vial. The resulting colorless solution was sparged with oxygen and an oxygen-filled balloon was fitted on top of the vial. The solution was irradiated using a 400 nm LED (10 W). 0.1 mL of the reaction solution were taken out before irradiation (t_0) and 120 minutes after starting the irradiation, respectively, and 0.3 mL CD_3CN added to each sample for NMR analysis (refer to **Figure 6.15**).

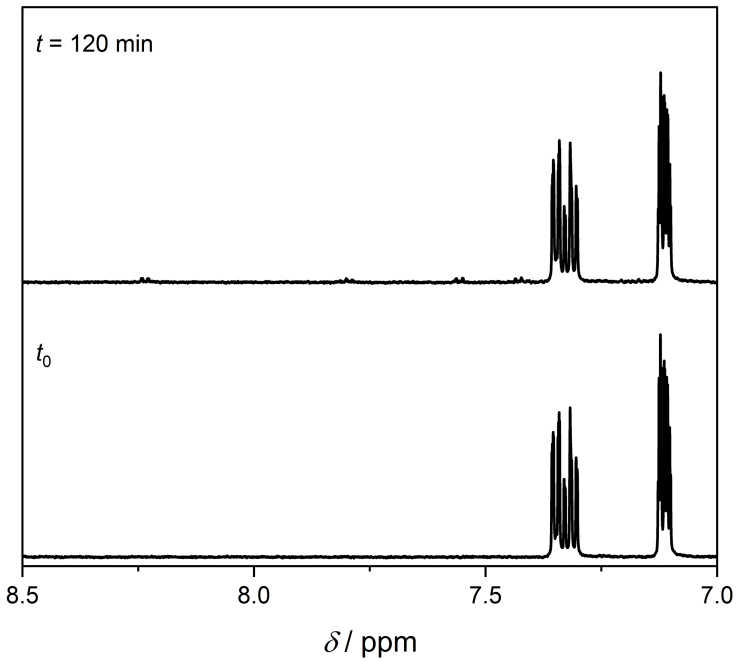

Figure 6.15 ^{1}H NMR spectra (600 MHz, CD_3CN, 298 K) of xanthene-9-carboxylic acid before (t_0) and after 120 minutes of irradiation with a 400 nm LED (10 W) under oxygen atmosphere.

Oxidative Double Bond Cleavage of Oleic acid

(I) SCNP3-Cu-Flow

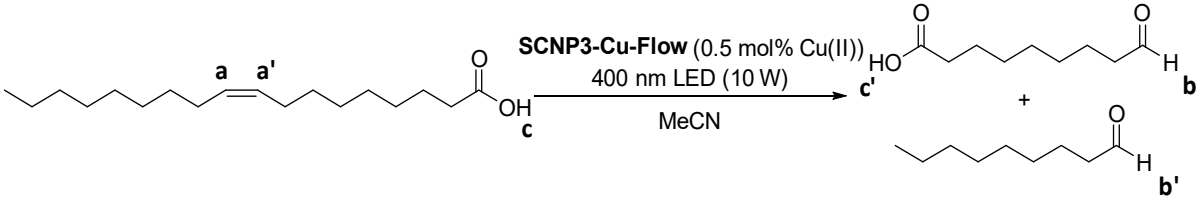

For reactions employing **SCNP3-Cu-Flow** as the catalyst, 10.0 mg of polymer **P3'** (4.98 µmol, 0.100 eq. photoreactive unit) and 0.84 mg $CuCl_2 \cdot 2\ H_2O$ (4.98 µmol, 0.100 eq.) were dissolved in 5 mL of acetonitrile. The resulting yellow solution was sparged with argon and subsequently irradiated using a 410 nm LED (12 W) under photoflow conditions (flow rate 0.2 $mL \cdot min^{-1}$). The obtained yellow solution was directly loaded onto a preparative SEC column (Sephadex LH-20) and eluted with acetonitrile, resulting in 5 mL of a pale-yellow solution of **SCNP3-Cu-Flow** (Cu(II) concentration about 0.05 $mmol \cdot L^{-1}$, refer to Chapter 4.2.4). The solution was transferred into a 20 mL crimp vial and 15.6 µL oleic acid (14.1 mg, 49.8 µmol, 1.00 eq.) were added. After sparging with oxygen, an oxygen-filled balloon was fitted on top of the vial and the solution irradiated using a 400 nm LED (10 W). 0.1 mL of the reaction solution were taken out before irradiation (t_0) and after 1, 3, 5 and 24 hours, respectively, and 0.3 mL of CD_3CN added to each sample for NMR analysis. The reaction was performed in triplicate (refer to **Figure 6.16**). In one case, irradiation was continued and the sample additionally analyzed by NMR after 96 hours of irradiation.

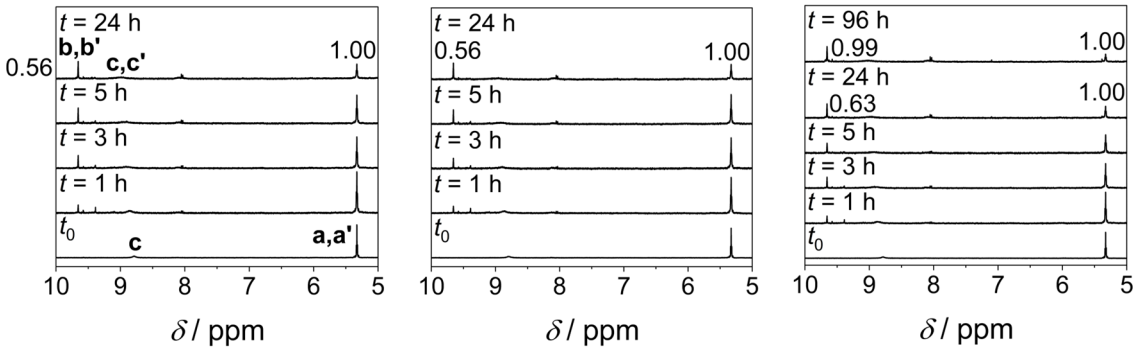

Figure 6.16 ^1H NMR spectra (600 MHz, CD_3CN, 298 K) of the reaction mixture of oleic acid and **SCNP3-Cu-Flow** before (t_0) and at different times after starting the irradiation with a 400 nm LED (10 W) under oxygen atmosphere. Numbers on peaks denote integral values. Labels refer to reaction scheme on top of page. The experiment was performed in triplicate.

(II) SCNP3-Cu-Batch

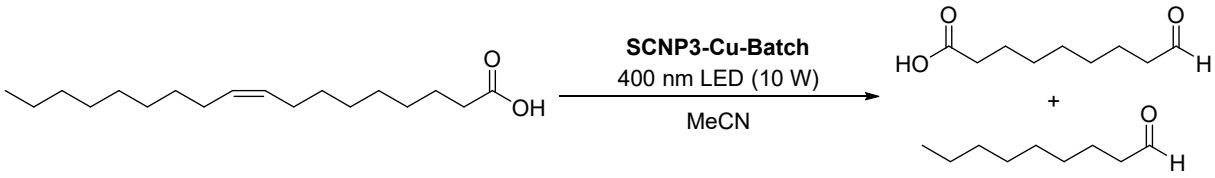

For reactions employing **SCNP3-Cu-Batch** as the catalyst, 10.0 mg of **P3'** (4.98 µmol, 0.100 eq. photoreactive unit) and 0.84 mg of $CuCl_2 \cdot 2\ H_2O$ (4.98 µmol, 0.100 eq.) were dissolved in 5 mL of acetonitrile. The resulting yellow solution was sparged with argon and subsequently irradiated using a 400 nm LED (10 W) for 50 minutes. The obtained yellow solution was directly loaded onto a preparative SEC column (Sephadex LH-20) and eluted with acetonitrile, resulting in a pale-yellow solution of **SCNP3-Cu-Batch**. The solution was transferred into a 20 mL crimp vial and 15.6 µL oleic acid (14.1 mg, 49.8 µmol, 1.00 eq.) were added. After sparging with oxygen, an oxygen-filled balloon was fitted on top of the vial and the solution irradiated using a 400 nm LED (10 W). 0.1 mL of the reaction solution were taken out before irradiation (t_0) and after 1, 3, 5 and 24 hours, respectively, and 0.3 mL of CD_3CN added to each sample for NMR analysis (refer to **Figure 6.17**).

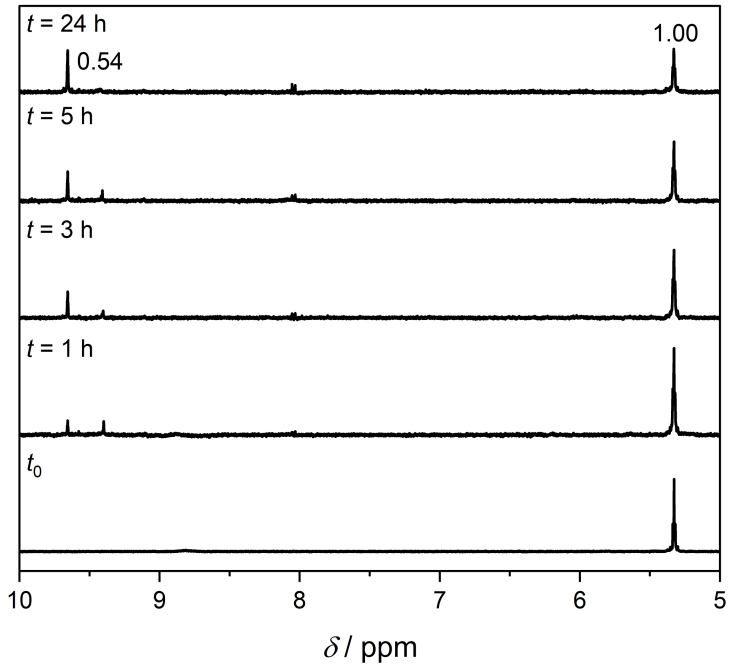

Figure 6.17 ^{1}H NMR spectra (600 MHz, CD_3CN, 298 K) of the reaction mixture of oleic acid and **SCNP3-Cu-Batch** before (t_0) and at different times after starting the irradiation with a 400 nm LED (10 W) under oxygen atmosphere. Numbers on peaks denote integral values.

(III) 0.5 mol% $CuCl_2 \cdot 2\ H_2O$

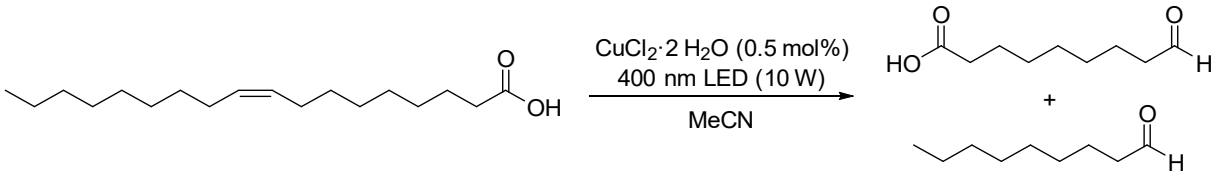

For reactions employing 0.5 mol% $CuCl_2 \cdot 2\ H_2O$ as the catalyst, 15.6 µL oleic acid (14.1 mg, 49.8 µmol, 1.00 eq.) were dissolved in 5 mL of a 0.01 $mg \cdot mL^{-1}$ $CuCl_2 \cdot 2\ H_2O$ stock solution (0.293 µmol, 0.00588 eq.) in acetonitrile in a 10 mL crimp vial. The resulting yellow solution was sparged with oxygen and an oxygen-filled balloon was fitted on top of the vial. The solution was irradiated using a 400 nm LED (10 W). 0.1 mL of the reaction solution were taken out before irradiation (t_0) and after 1, 3, 5 and 24 hours, respectively, and 0.3 mL of CD_3CN added to each sample for NMR analysis. The reaction was performed in triplicate (refer to **Figure 6.18**).

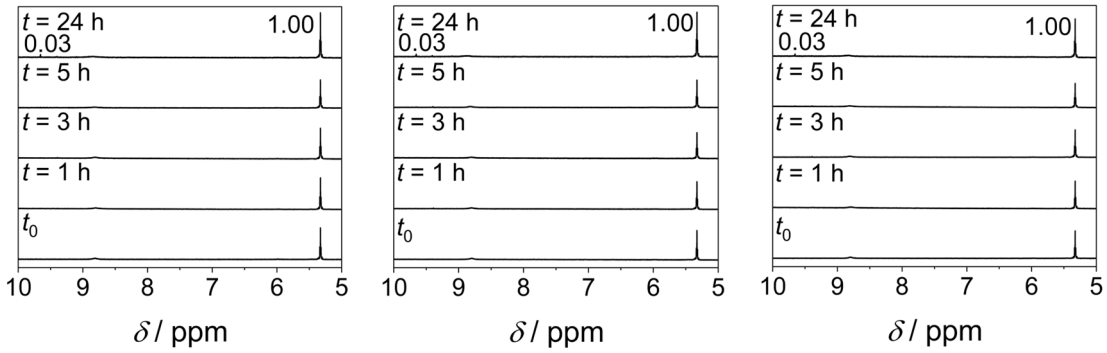

Figure 6.18 ^1H NMR spectra (600 MHz, CD_3CN, 298 K) of the reaction mixture of oleic acid and 0.5 mol% $CuCl_2 \cdot 2\ H_2O$ before (t_0) and at different times after starting the irradiation with a 400 nm LED (10 W) under oxygen atmosphere. Numbers on peaks denote integral values. The experiment was performed in triplicate.

(IV) 10 mol% $CuCl_2 \cdot 2\ H_2O$

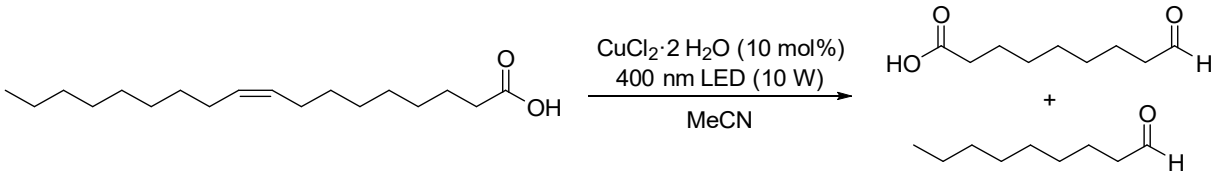

For reactions employing 10 mol% $CuCl_2 \cdot 2\ H_2O$ as the catalyst, 15.6 µL oleic acid (14.1 mg, 49.8 µmol, 1.00 eq.) and 0.84 mg $CuCl_2 \cdot 2\ H_2O$ (4.98 µmol, 0.100 eq.) were dissolved in 5 mL of acetonitrile in a 20 mL crimp vial. The resulting yellow solution was sparged with oxygen and an oxygen-filled balloon was fitted on top of the vial. The solution was irradiated using a 400 nm LED (10 W). 0.1 mL of the reaction solution were taken out before irradiation (t_0) and after 1, 3, 5 and 24 hours, respectively, and 0.3 mL of CD_3CN added to each sample for NMR analysis. The reaction was performed in triplicate (refer to **Figure 6.19**). In one case, irradiation was continued and the sample additionally analyzed by NMR after 48 hours of irradiation.

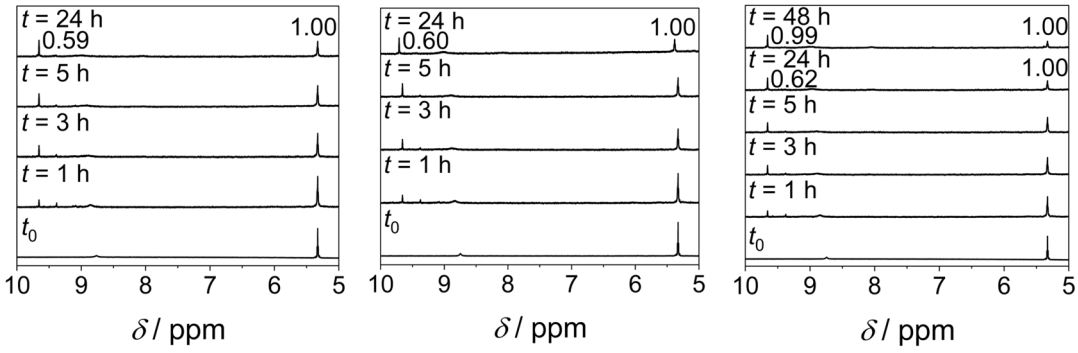

Figure 6.19 ^1H NMR spectra (600 MHz, CD_3CN, 298 K) of the reaction mixture of oleic acid and 10 mol% $CuCl_2 \cdot 2\ H_2O$ before (t_0) and at different times after starting the irradiation with a 400 nm LED (10 W) under oxygen atmosphere. Numbers on peaks denote integral values. The experiment was performed in triplicate.

To verify that the evolving resonance observed at δ = 9.66 ppm in the ^{1}H NMR spectra of the reaction mixture (refer to **Figure 6.19**) actually corresponds to the cleavage reaction of oleic acid to nonanal and 9-oxononanoic acid, the reaction progress was also monitored via LCMS, evidencing the formation of 9-oxanonanoic acid (refer to **Figure 6.20**).

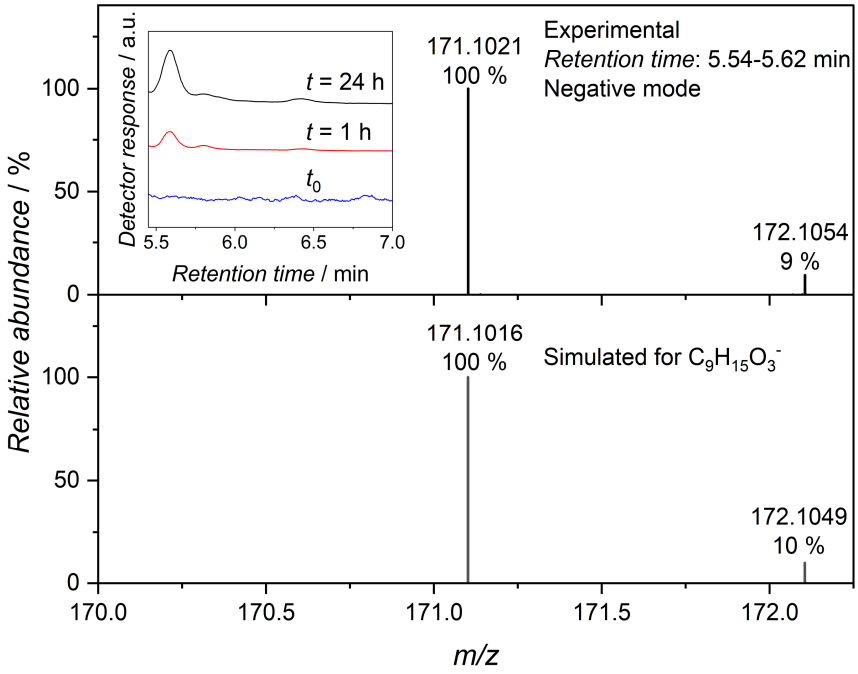

Figure 6.20 Expansion of the XIC for the *m/z* range 171.101-171.103 (insert) of the reaction mixture of oleic acid and 10 mol% $CuCl_2 \cdot 2\ H_2O$ before irradiation (t_0, blue) and after 1 hour (red) and 24 hours (black) of irradiation, respectively, with a 400 nm LED (10 W). Top: Expansion of the accumulated mass spectrum (negative mode) obtained from the XIC peak at 5.54-5.62 minutes elution time in the chromatogram of the reaction mixture of oleic acid and $CuCl_2 \cdot 2\ H_2O$. Bottom: Simulated mass spectrum for $C_9H_{15}O_3^-$, corresponding to deprotonated 9-oxononanoic acid, which is formed during the oxidative cleavage of the oleic acid double bond. A signal for nonanal could not be detected due to its low ionization tendency under the measurement conditions.

(V) $CuCl_2 \cdot 2\ H_2O$ + Poly(PEGMEMA)

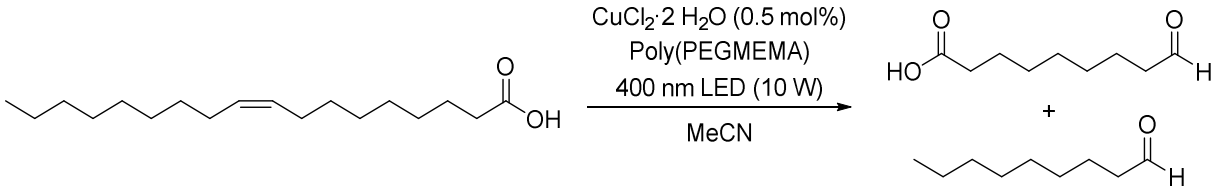

15.6 µL oleic acid (14.1 mg, 49.8 µmol, 1.00 eq.) and 10.0 mg Poly(PEGMEMA) were dissolved in 5 mL of a 0.01 mg·mL^{-1} $CuCl_2 \cdot 2\ H_2O$ stock solution (0.293 µmol, 0.00588 eq.) in acetonitrile in a 10 mL crimp vial. The resulting slightly yellow solution was sparged with oxygen and an oxygen-filled balloon was fitted on top of the vial. The solution was irradiated using a 400 nm LED (10 W). 0.1 mL of the reaction solution were taken out before irradiation (t_0) and after 1, 3, 5 and 24 hours, respectively, and 0.3 mL of CD_3CN added to each sample for NMR analysis (refer to **Figure 6.21**).

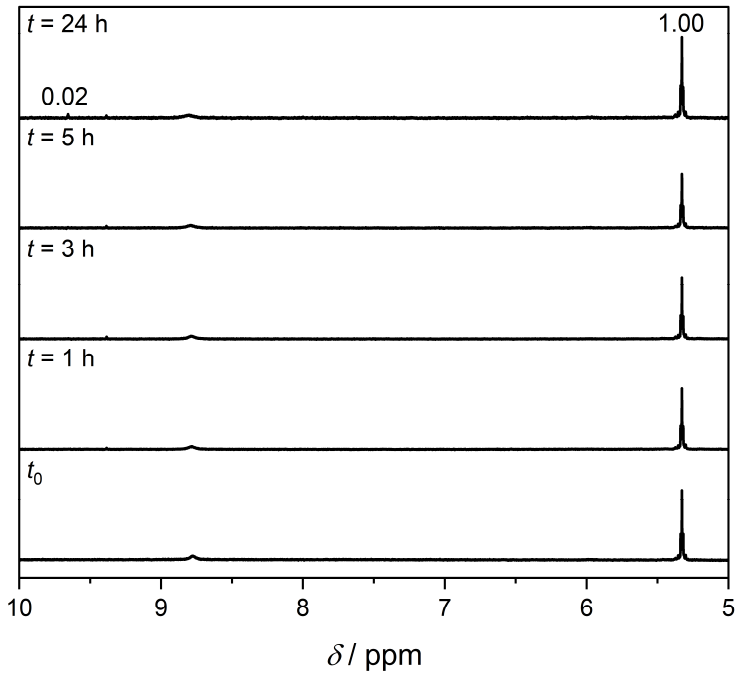

Figure 6.21 ^{1}H NMR spectra (600 MHz, CD_3CN, 298 K) of the reaction mixture of oleic acid, 0.5 mol% $CuCl_2 \cdot 2\ H_2O$ and Poly(PEGMEMA) before (t_0) and at different times after starting the irradiation with a 400 nm LED (10 W) under oxygen atmosphere. Numbers on peaks denote integral values.

(VI) $CuCl_2$·2 H_2O + *n*-butylamine

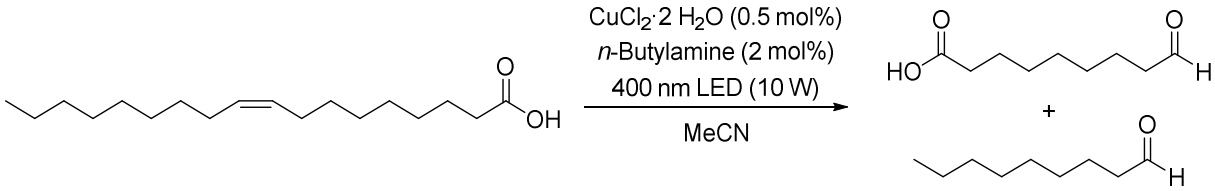

A stock solution containing 0.01 mg·mL^{-1} of $CuCl_2$·2 H_2O and 17.2 µg·mL^{-1} *n*-butylamine in acetonitrile was prepared. 15.6 µL oleic acid (14.1 mg, 49.8 µmol, 1.00 eq.) were dissolved in 5 mL of this acetonitrile solution (0.293 µmol, 0.00588 eq. $CuCl_2$·2 H_2O; 1.18 µmol, 0.0235 eq. *n*-butylamine) in a 10 mL crimp vial. The resulting yellow solution was sparged with oxygen and an oxygen-filled balloon was fitted on top of the vial. The solution was irradiated using a 400 nm LED (10 W). 0.1 mL of the reaction solution were taken out before irradiation (t_0) and after 1, 3, 5 and 24 hours, respectively, and 0.3 mL of CD_3CN added to each sample for NMR analysis (refer to **Figure 6.22**).

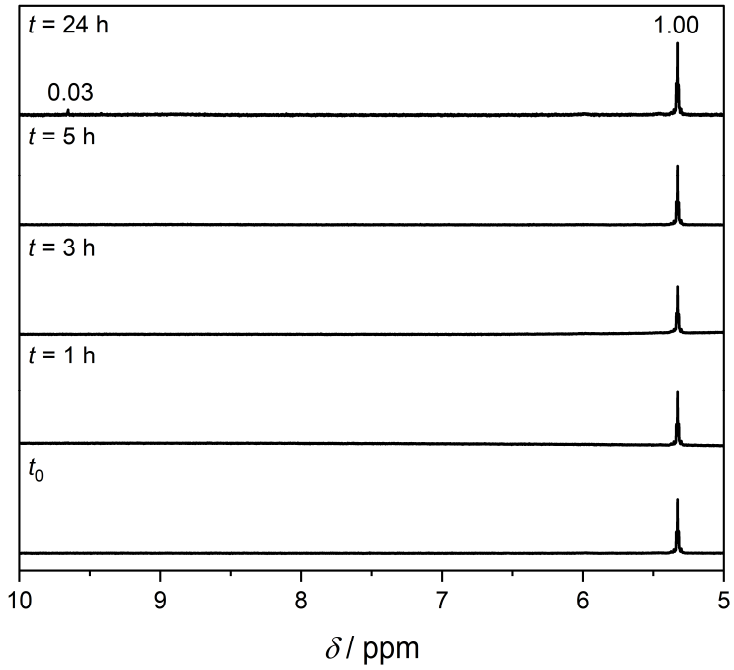

Figure 6.22 ^{1}H NMR spectra (600 MHz, CD_3CN, 298 K) of the reaction mixture of oleic acid, 0.5 mol% $CuCl_2$·2 H_2O and 2 mol% *n*-butylamine before (t_0) and at different times after starting the irradiation with a 400 nm LED (10 W) under oxygen atmosphere. Numbers on peaks denote integral values.

(VII) P3'

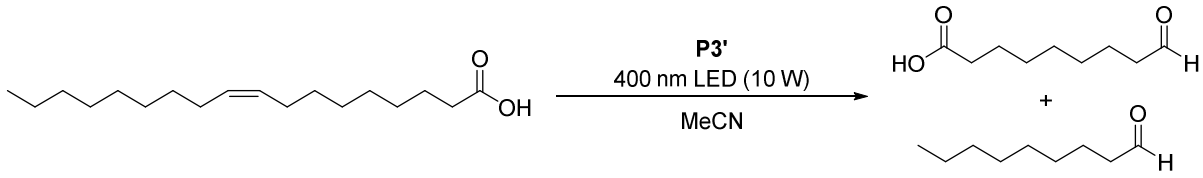

15.6 µL oleic acid (14.1 mg, 49.8 µmol, 1.00 eq.) and 10.0 mg **P3'** (4.98 µmol, 0.100 eq. photoreactive unit) were dissolved in 5 mL of acetonitrile in a 20 mL crimp vial. The resulting colorless solution was sparged with oxygen and an oxygen-filled balloon was fitted on top of the vial. The solution was irradiated using a 400 nm LED (10 W). 0.1 mL of the reaction solution were taken out before irradiation (t_0) and 1 hour and 24 hours after starting the irradiation, respectively, and 0.3 mL of CD_3CN added to each sample for NMR analysis (refer to **Figure 6.23**).

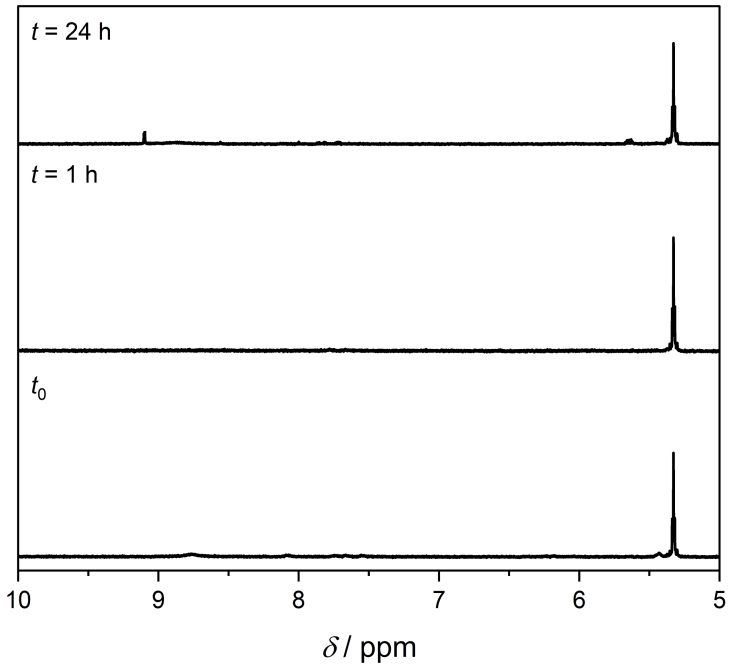

Figure 6.23 ^{1}H NMR spectra (600 MHz, CD_3CN, 298 K) of the reaction mixture of oleic acid and **P3'** before (t_0) and at 1 hour and 24 hours after starting the irradiation with a 400 nm LED (10 W) under oxygen atmosphere. Note that the additional resonance apparent after 24 hours is not isochronous to the one observed in the spectra of the catalyzed reactions.

(VIII) Mixture of P3' and $CuCl_2 \cdot 2\ H_2O$ subjected to preparative SEC

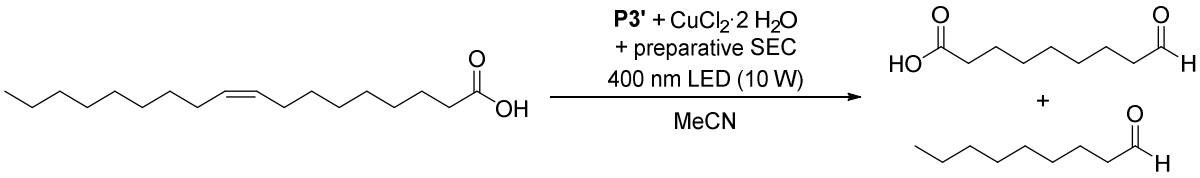

10.0 mg of polymer **P3'** (4.98 µmol, 0.100 eq. photoreactive unit) and 0.84 mg $CuCl_2 \cdot 2\ H_2O$ (4.98 µmol, 0.100 eq.) were dissolved in 5 mL of acetonitrile. The resulting yellow solution was directly loaded onto a preparative SEC column (Sephadex LH-20) and eluted with acetonitrile, resulting in a colorless solution of **P3'**. The solution was transferred into a 20 mL crimp vial and 15.6 µL oleic acid (14.1 mg, 49.8 µmol, 1.00 eq.) were added. After sparging with oxygen, an oxygen-filled balloon was fitted on top of the vial and the solution irradiated using a 400 nm LED (10 W). 0.1 mL of the reaction solution were taken out before irradiation (t_0) and after 1 hour and 24 hours, respectively, and 0.3 mL of CD_3CN added to each sample for NMR analysis (refer to **Figure 6.24**).

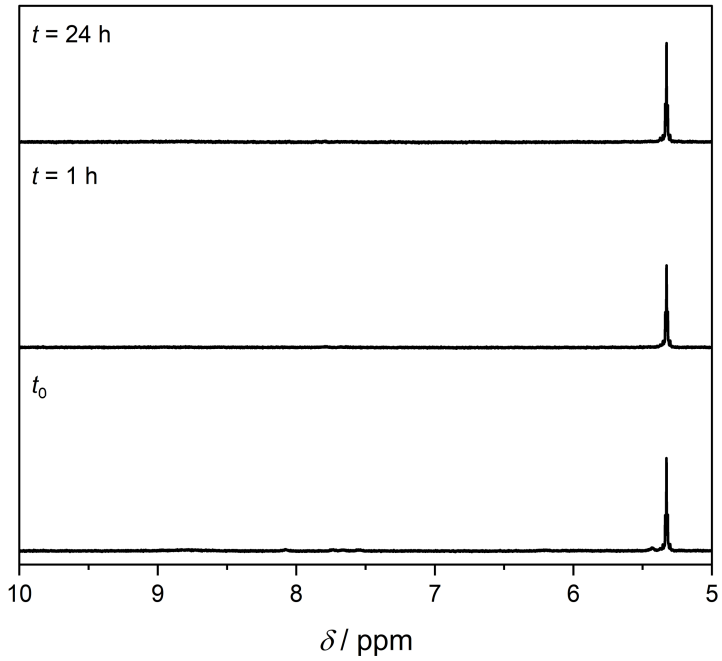

Figure 6.24 ^{1}H NMR spectra (600 MHz, CD_3CN, 298 K) of the reaction mixture of oleic acid and **P3'** before (t_0) and after 1 hour and 24 hours of irradiation with a 400 nm LED (10 W) under oxygen atmosphere. For that, **P3'** and $CuCl_2 \cdot 2\ H_2O$ were first mixed and subsequently subjected to preparative size-exclusion chromatography (Sephadex LH-20) in acetonitrile, demonstrating that catalytically active $CuCl_2 \cdot 2\ H_2O$ is effectively removed by this purification technique.

(IX) $CuCl_2 \cdot 2\ H_2O$ without LED irradiation

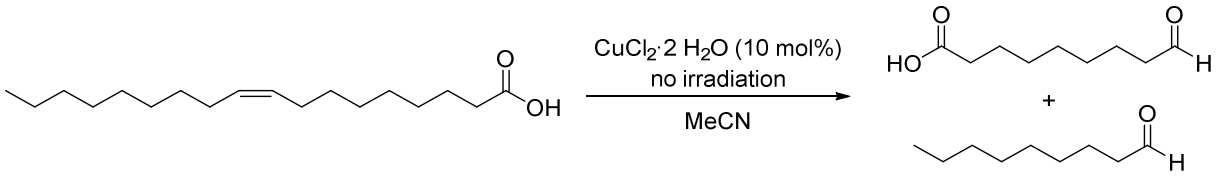

15.6 µL oleic acid (14.1 mg, 49.8 µmol, 1.00 eq.) and 0.84 mg $CuCl_2 \cdot 2\ H_2O$ (4.98 µmol, 0.100 eq.) were dissolved in 5 mL of acetonitrile in a 20 mL crimp vial. The resulting yellow solution was sparged with oxygen and an oxygen-filled balloon was fitted on top of the vial. The solution was stirred at room temperature without irradiation. 0.1 mL of the reaction solution were taken out immediately (t_0) and after 1 hour and 24 hours, respectively, and 0.3 mL of CD_3CN added to each sample for NMR analysis (refer to **Figure 6.25**).

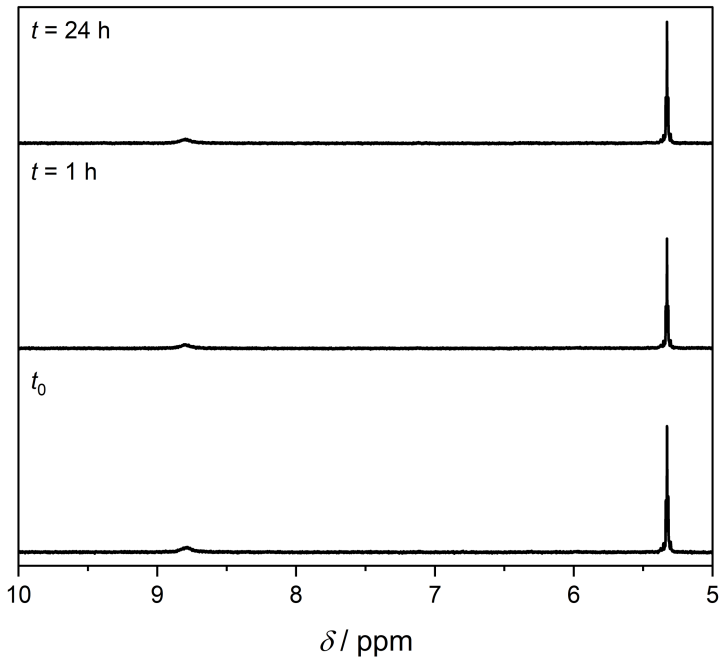

Figure 6.25 ^{1}H NMR spectra (600 MHz, CD_3CN, 298 K) of the reaction mixture of oleic acid and 10 mol% $CuCl_2 \cdot 2\ H_2O$ before (t_0) and after 1 hour and 24 hours of stirring at room temperature without irradiation under oxygen atmosphere.

(X) SCNP3-Cu-Flow without LED irradiation

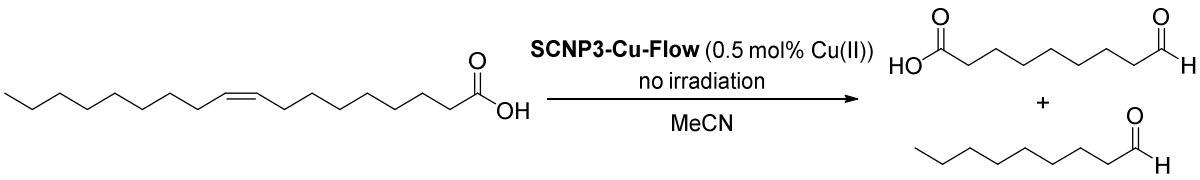

10.0 mg of polymer **P3'** (4.98 µmol, 0.100 eq. photoreactive unit) and 0.84 mg $CuCl_2 \cdot 2\ H_2O$ (4.98 µmol, 0.100 eq.) were dissolved in 5 mL of acetonitrile. The resulting yellow solution was sparged with argon and subsequently irradiated using a 410 nm LED (12 W) under photoflow conditions (flow rate 0.2 $mL \cdot min^{-1}$). The obtained yellow solution was directly loaded onto a preparative SEC column (Sephadex LH-20) and eluted with acetonitrile, resulting in a pale-yellow solution of **SCNP3-Cu-Flow**. The solution was transferred into a 20 mL crimp vial and 15.6 µL oleic acid (14.1 mg, 49.8 µmol, 1.00 eq.) were added. After sparging with oxygen, an oxygen-filled balloon was fitted on top of the vial and the solution was stirred at room temperature without irradiation. 0.1 mL of the reaction solution were taken out immediately (t_0) and after 1 hour and 24 hours, respectively, and 0.3 mL of CD_3CN added to each sample for NMR analysis (refer to **Figure 6.26**).

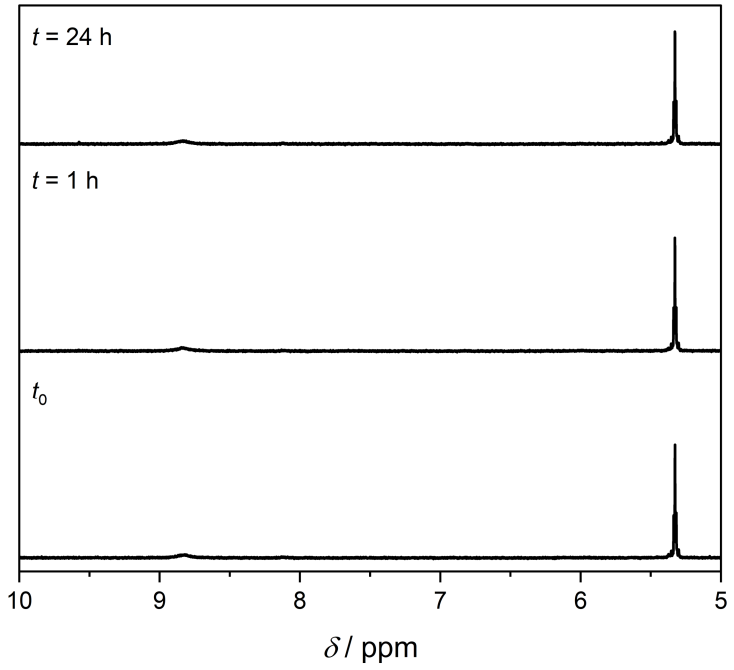

Figure 6.26 ^1H NMR spectra (600 MHz, CD_3CN, 298 K) of the reaction mixture of oleic acid and **SCNP3-Cu-Flow** before (t_0) and after 1 hour and 24 hours of stirring at room temperature without irradiation under oxygen atmosphere.

(XI) LED irradiation without catalyst

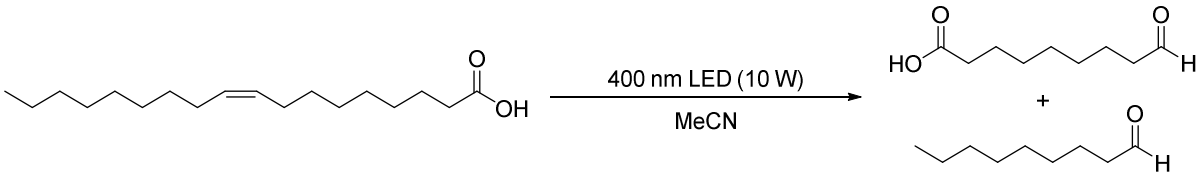

15.6 µL oleic acid (14.1 mg, 49.8 µmol, 1.00 eq.) were dissolved in 5 mL of acetonitrile in a 20 mL crimp vial. The resulting colorless solution was sparged with oxygen and an oxygen-filled balloon was fitted on top of the vial. The solution was irradiated using a 400 nm LED (10 W). 0.1 mL of the reaction solution were taken out before irradiation (t_0) and 1 hour and 24 hours after starting the irradiation, respectively, and 0.3 mL of CD_3CN added to each sample for NMR analysis (refer to **Figure 6.27**).

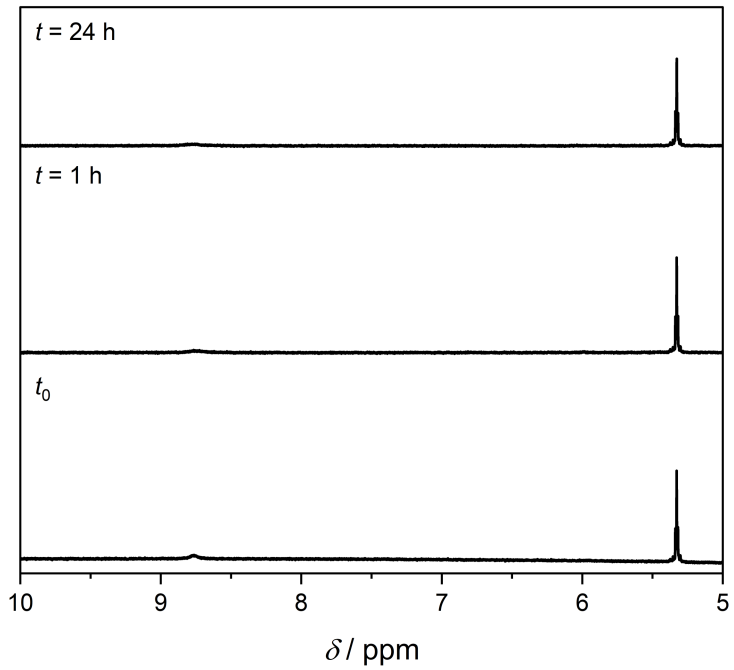

Figure 6.27 ^{1}H NMR spectra (600 MHz, CD_3CN, 298 K) of oleic acid before (t_0) and at 1 hour and 24 hours after starting the irradiation with a 400 nm LED (10 W) under oxygen atmosphere.

6.3.3 Ferrocene-Driven Single-Chain Polymer Compaction

Equivalents referring to polymers given in the synthetic procedures within Chapter 6.3.3 were calculated neglecting the influence of end groups, the chloromethyl moieties and SCNP crosslinking units on the molar mass. Hence, calculations were based on the molar mass of styrene alone. The given equivalents of phenanthroline units within **SCNP4-FcPhen** assumed the quantitative conversion of the chloromethyl styrene moieties of the precursor polymer **P4**. The palladium equivalents given for **SCNP4-FcPhen-Pd** assumed the quantitative palladium functionalization of all phenanthroline moieties. The latter values must therefore be considered as upper limits of the actual amounts of the respective functionalities.

6.3.3.1 Synthesis of P4

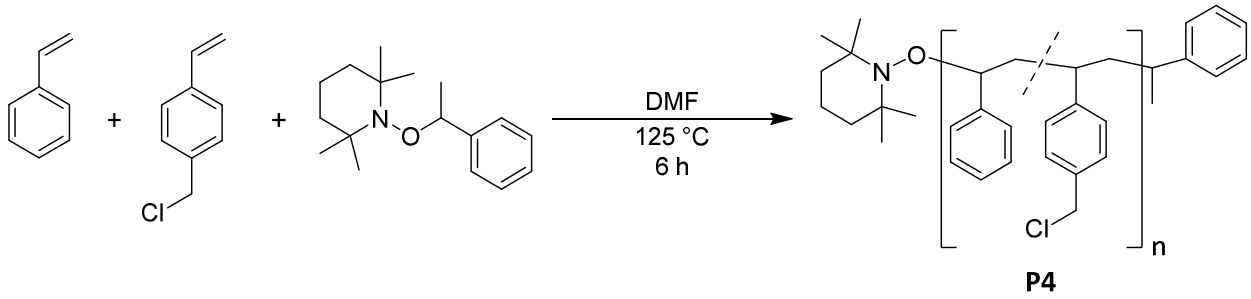

P4

46.6 mg of the NMP initiator 2,2,6,6-tetramethyl-1-(1-phenylethoxy)piperidine (0.178 mmol, 1.00 eq.) were dissolved in 4.20 mL of styrene (3.82 g, 36.9 mmol, 207 eq.) and 0.73 mL of 4-chloromethyl styrene (0.788 g, 5.16 mmol, 28.9 eq.) and 2 mL of DMF were added. The solution was degassed by three consecutive freeze-pump-thaw cycles and subsequently heated to 125 °C for 6 h. The reaction was stopped by cooling the flask with liquid nitrogen and opening it to air. THF was added and the polymer precipitated by dropwise addition of the solution to cold methanol. The precipitate was isolated by centrifugation and dried under reduced pressure to give **P4** as a colorless solid (2.27 g).

^{1}H NMR (400 MHz, THF-d_8, 298 K): δ / ppm = 7.40-6.26 (br, aromatic), 4.68-4.38 (br, CH_2Cl), 2.37-1.22 (br, aliphatic backbone).

SEC (DMAc, RI, PS cal.): M_n = 16300 g·mol^{-1}, M_w = 18700 g·mol^{-1}, M_p = 17900 g·mol^{-1}, $Đ$ = 1.15.

DLS (THF): D_s = 5.69 nm.

DOSY (400 MHz, THF-d_8, 298 K): D = 1.17·10^{-10} m^2·s^{-1}.

6.3.3.2 Synthesis of SCNP4-Fc

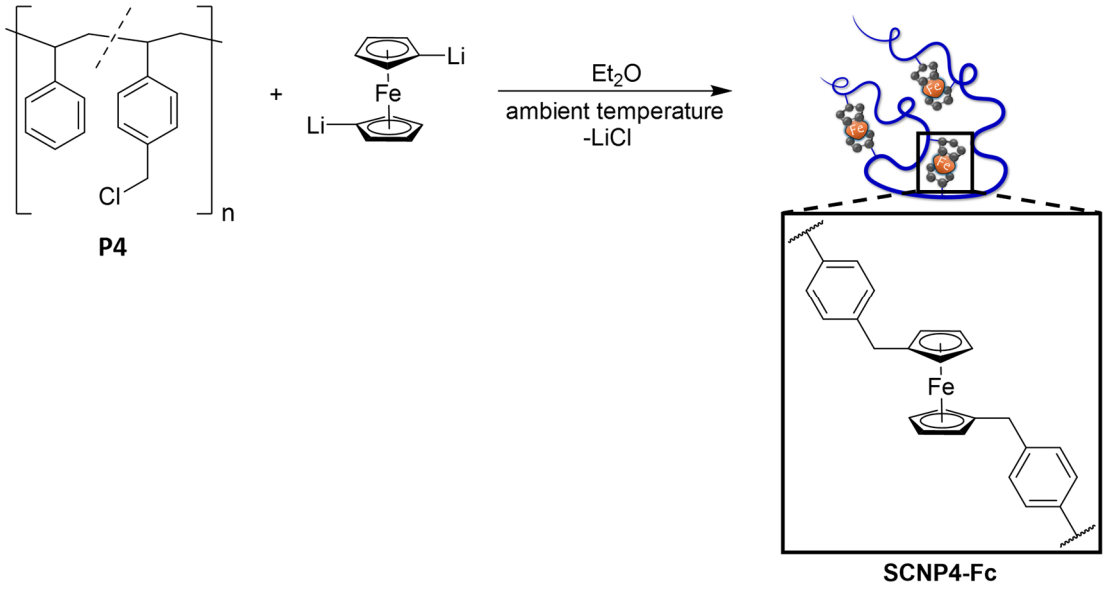

40.0 mg of ferrocene (0.215 mmol, 1.00 eq.) were dissolved in 4 mL of diethyl ether and 0.54 mL *n*-butyllithium (1.6 mol·L^{-1} in hexane, 0.860 mmol, 4.00 eq.) and 0.13 mL TMEDA (99.6 mg, 0.860 mol, 4.00 eq.) were added. After stirring the reaction mixture at room temperature overnight, an orange suspension was obtained which was diluted with 60 mL of diethyl ether. 60.0 mg of **P4** (80.7 µmol, 0.375 eq. chlorobenzyl functionalities) were dissolved in 20 mL of diethyl ether and slowly added to the reaction mixture using a syringe pump (2 mL·h^{-1}). After complete addition, an orange solution containing a colorless precipitate was obtained. The precipitate was removed by filtration and the solvent removed from the filtrate under reduced pressure. The resulting orange solid was washed with *n*-hexane (5 x 5 mL). After drying, **SCNP4-Fc** was obtained as an off-white solid (50 mg).

^{1}H NMR (400 MHz, THF-d_8, 298 K): δ / ppm = 7.40-6.26 (br, aromatic), 2.37-1.02 (br, aliphatic backbone).

SEC (DMAc, RI, PS cal.): M_n = 11900 g·mol^{-1}, M_w = 14100 g·mol^{-1}, M_p = 12400 g·mol^{-1}, $Đ$ = 1.19.

DLS (THF): D_s = 4.68 nm.

DOSY (400 MHz, THF-d_8, 298 K): D = 1.99·10^{-10} m^2·s^{-1}.

6.3.3.3 Synthesis of SCNP4-FcPhen

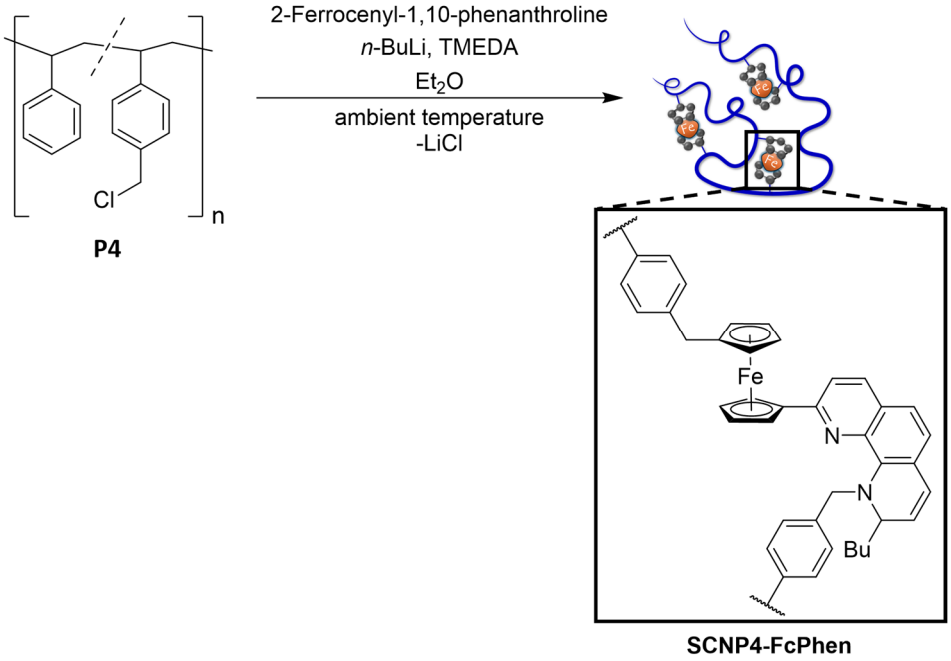

214 mg of 2-ferrocenyl-1,10-phenanthroline (0.588 mmol, 1.00 eq.) were dissolved in 40 mL of diethyl ether and 0.94 mL of *n*-butyllithium (2.5 mol·L^{-1} in hexane, 2.35 mmol, 4.00 eq.) and 0.35 mL of TMEDA (271 mg, 2.35 mmol, 4.00 eq.) were added. The solution was stirred at room temperature overnight and subsequently diluted with 40 mL of diethyl ether. 167 mg of **P4** (0.224 mmol, 0.382 eq. chlorobenzyl functionalities) were dissolved in 20 mL of diethyl ether and slowly added to the reaction mixture using a syringe pump (3 mL·h^{-1}). After complete addition, a dark red suspension was obtained. The precipitate was removed by filtration and the solvent removed from the filtrate under reduced pressure. The residue was washed with methanol until the washings were almost colorless (about 200 mL). After drying, **SCNP4-FcPhen** was obtained as an orange solid (80 mg, small molecule impurities included).

^{1}H NMR (400 MHz, THF-d_8, 298 K): δ / ppm = 7.40-6.26 (br, aromatic), 2.42-0.54 (br, aliphatic backbone).

SEC (DMAc, RI, PS cal.): M_n = 14800 g·mol^{-1}, M_w = 18800 g·mol^{-1}, M_p = 14200 g·mol^{-1}, $Đ$ = 1.27.

DLS (THF): D_s = 5.35 nm.

DOSY (400 MHz, THF-d_8, 298 K): D = 1.13·10^{-10} m^2·s^{-1}.

Note: The product contained unidentified small molecule impurities not considered in the given analytical data.

6.3.3.4 Synthesis of SCNP4-FcPhen-Pd

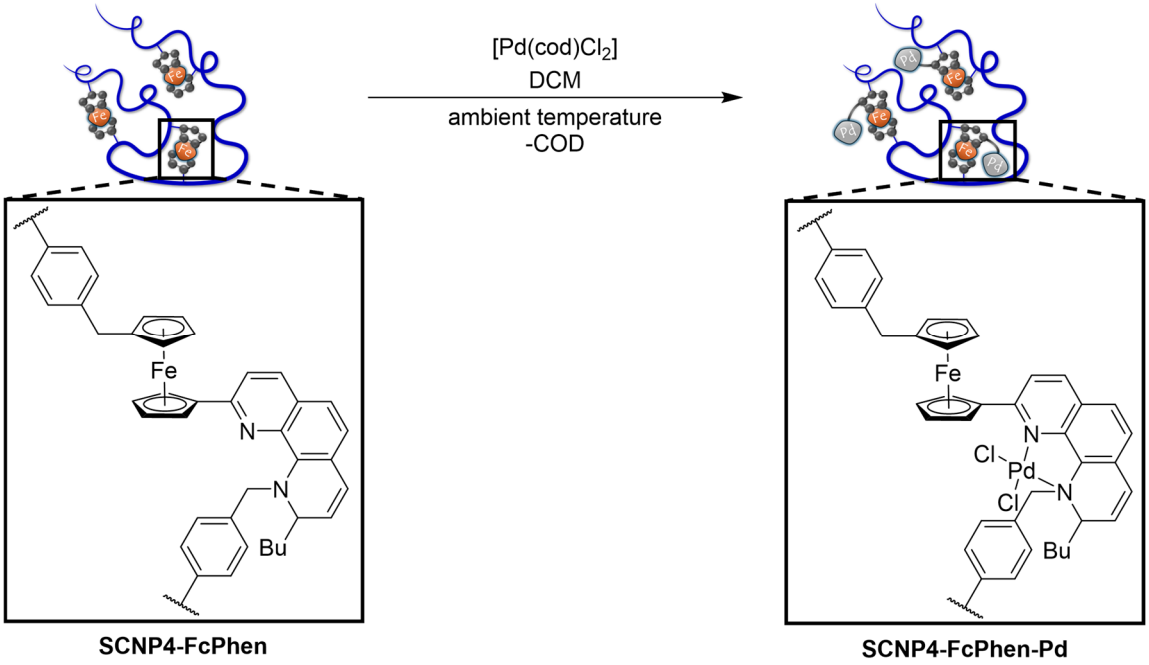

30.0 mg of **SCNP4-FcPhen** (mass includes small molecule impurities, Phen: 20.2 µmol, 1.00 eq.) were dissolved in 10 mL of DCM. 10.0 mg of dichloro(1,5-cyclooctadiene)palladium(II) (35.0 µmol, 1.74 eq.) were dissolved in DCM and added to the solution of **SCNP4-FcPhen**. The resulting orange solution was stirred at room temperature overnight to give a dark red solution. The solvent was removed under reduced pressure and the obtained dark red solid redissolved in a minimum quantity of DCM. Precipitation in cold methanol gave a dark solid which was collected by filtration and washed with methanol (3 x 5 mL). The residue was dried under reduced pressure to give **SCNP4-FcPhen-Pd** as a dark solid (20 mg).

^{1}H NMR (400 MHz, THF-d_8, 298 K): δ / ppm = 7.82-6.06 (br, aromatic), 4.54-4.15 (br, unassigned), 2.62-0.44 (br, aliphatic backbone).

SEC (DMAc, RI, PS cal.): M_n = 17700 g·mol^{-1}, M_w = 22800 g·mol^{-1}, M_p = 16600 g·mol^{-1}, $Đ$ = 1.29.

DOSY (400 MHz, THF-d_8, 298 K): D = 1.35·10^{-10} m^2·s^{-1}.

EDX: *Energy* / keV = 0.28 (C K$_\alpha$), 0.71 (Fe L$_\alpha$), 0.72 (Fe L$_\beta$), 2.62 (Cl K$_\alpha$), 2.81 (Cl K$_\beta$), 2.84 (Pd L$_\alpha$), 2.99 (Pd L$_\beta$), 6.41 (Fe K$_\alpha$), 7.06 (Fe K$_\beta$).

6.3.3.5 Catalytic Hydroamination of 2,2-Diphenyl-4-heptyn-1-amine

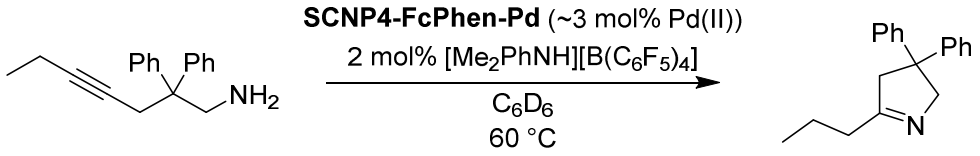

5.00 mg of **SCNP4-FcPhen-Pd** (Pd: 3.36 µmol, 0.0295 eq.) and 2.00 mg of dimethylanilinium tetrakis(pentafluorophenyl)borate (2.50 µmol, 0.0219 eq.) were dissolved in 0.5 mL of C_6D_6 in a NMR tube equipped with a J. Young valve. 30.0 mg of 2,2-diphenyl-4-heptyn-1-amine (0.114 mmol, 1.00 eq.) were added, and the tube immediately inserted into a Bruker Avance Neo 400 MHz spectrometer. The reaction mixture was heated to 60 °C inside the spectrometer using a Bruker Smart VT unit and ^{1}H NMR spectra recorded over a period of three hours (refer to **Figure 4.46**).

To ensure that the cocatalyst dimethylanilinium tetrakis(pentafluorophenyl)borate does not catalyze the reaction in the absence of **SCNP4-FcPhen-Pd**, an excess of the cocatalyst was added to 2,2-diphenyl-4-heptyn-1-amine in C_6D_6 and heated to 60 °C for three hours. No conversion of the starting material to the desired product was observed using ^{1}H NMR spectroscopy (refer to **Figure 6.28**).

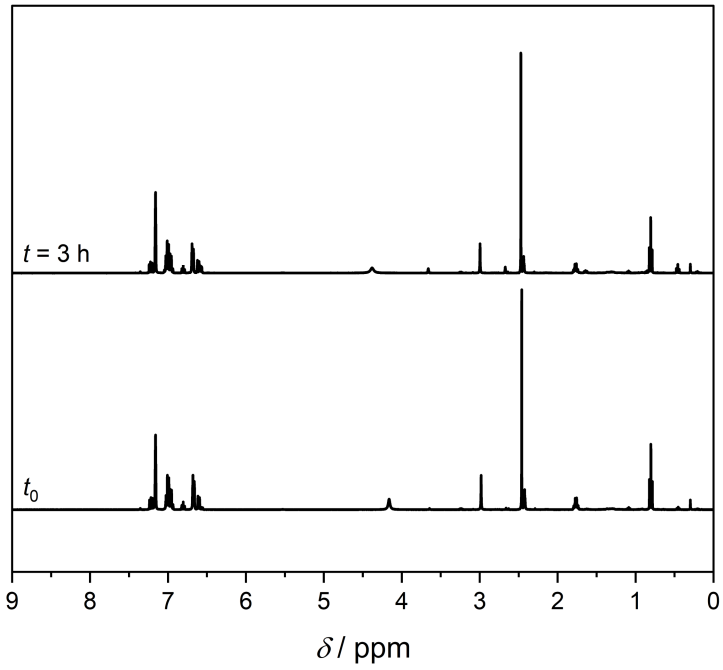

Figure 6.28 Stacked ^{1}H NMR spectra (400 MHz, C_6D_6, 298 K) of 2,2-diphenyl-4-heptyn-1-amine directly after the addition of dimethylanilinium tetrakis(pentafluorophenyl)borate (t_0) and after heating the mixture to 60 °C for three hours (t = 3 h).

6.3.3.6 Computational Details

Quantum chemical calculations at the density functional theory level relevant to Chapter 4.3 were performed with TURBOMOLE.[303-304] For all calculations, the PBE0 hybrid functional[305-306] was employed. dhf-TZVP basis sets[307-309] together with the effective core potential for Pd (ECP-28)[310] were used. The resolution of the identity approximation for the Coulomb part (RI-*J*) in combination with the corresponding auxiliary basis sets was employed in all cases.[311-312] Self-consistent field thresholds were set to 10^{-7} Hartree. For response calculations, the convergence criterion for the root mean square of the density matrix was set to 10^{-7} Hartree. Medium sized multigrids (gridsize m3)[313-314] were used for the numerical integration of the exchange-correlation terms. In all calculations, the D4 dispersion correction was employed.[315] Non-relaxed difference densities were analyzed using the python script PANAMA (Peak ANAlyzing MAchine).[316] Information concerning the ten lowest energy singlet vertical excitations of the small molecule model compounds **I** and **II** (refer to Chapter 4.3.4 for details) are provided in **Table 6.14** and **Table 6.15**. Cartesian coordinates of all optimized structures are provided in the literature.[7]

The nucleophilic attack of *n*-butyllithium to 2-ferrocenyl-1,10-phenanthroline gives rise to stereocenters on the 1,10-phenanthroline moiety. As no chiral auxiliary is added, racemic mixtures are obtained. Only one of the existing stereoisomers is considered in the calculations reported in Chapter 4.3. For all molecules, different conformations exist for which rapid interconversion is expected to take place in solution at ambient temperature. Only the energetically most favorable conformation in each case is reported. The latter was determined by performing geometry optimizations starting from several different chemically reasonable initial conformations. The TMEDA present in the reaction mixture throughout the synthesis of **SCNP4-FcPhen** is not considered in the calculations. While additional coordination of TMEDA to the lithium ions is expected to contribute to the overall stability of the structures, this should not lead to a qualitative change of the overall picture discussed in Chapter 4.3.

Table 6.14 Ten lowest energy singlet vertical excitations (PBE0/dhf-TZVP/D4) of the small molecule model compound **I** (refer to Chapter 4.3.4 for details).

Excitation number	Excitation energy / nm	Oscillator strength / Velocity representation	Contributions (> 10 %)	Orbital pair contributions
1	522.09	0.00113	HOMO-2-LUMO+7	23.6
			HOMO-1-LUMO+7	15.7
			HOMO-1-LUMO+6	11.7
2	520.83	0.00280	HOMO-1-LUMO+7	21.2
			HOMO-2-LUMO+7	16.4
			HOMO-2-LUMO+6	13.4
3	476.12	0.00128	HOMO-5-LUMO+7	22.5
			HOMO-2-LUMO+6	14.0
			HOMO-2-LUMO+5	10.3
4	466.30	0.00006	HOMO-5-LUMO+6	16.9
			HOMO-1-LUMO+6	13.8
			HOMO-1-LUMO+5	10.0
5	428.74	0.02769	HOMO-LUMO	96.5
6	370.79	0.00221	HOMO-5-LUMO+7	16.6
			HOMO-1-LUMO	11.8
			HOMO-2-LUMO+6	10.7
7	364.89	0.00050	HOMO-5-LUMO+6	16.6
			HOMO-2-LUMO	14.0
			HOMO-5-LUMO+5	9.8
8	361.91	0.05922	HOMO-LUMO+1	82.9
9	329.54	0.08866	HOMO-1-LUMO	54.2
			HOMO-1-LUMO+7	13.5
			HOMO-2-LUMO	9.5
10	327.20	0.03338	HOMO-2-LUMO	55.6
			HOMO-2-LUMO+7	18.6
			HOMO-1-LUMO	11.1

Table 6.15 Ten lowest energy singlet vertical excitations (PBE0/dhf-TZVP/D4) of the small molecule model compound **II** (refer to Chapter 4.3.4 for details).

Excitation number	Excitation energy / nm	Oscillator strength / Velocity representation	Contributions (> 10 %)	Orbital pair contributions
1	653.94	0.00220	HOMO-2-LUMO	42.7
			HOMO-5-LUMO	19.3
			HOMO-3-LUMO	18.7
2	595.03	0.00287	HOMO-3-LUMO	62.2
			HOMO-5-LUMO	15.5
3	553.65	0.00040	HOMO-1-LUMO	26.7
			HOMO-1-LUMO+2	14.8
			HOMO-1-LUMO+6	11.4
4	552.70	0.01440	HOMO-LUMO	29.0
			HOMO-5-LUMO	13.6
5	539.57	0.00688	HOMO-2-LUMO	16.7
			HOMO-5-LUMO	16.6
6	499.38	0.00477	HOMO-12-LUMO	19.8
			HOMO-6-LUMO	12.1
			HOMO-10-LUMO	9.7
7	487.65	0.00207	HOMO-1-LUMO+8	21.0
			HOMO-1-LUMO+6	13.4
8	476.13	0.00011	HOMO-LUMO+8	27.2
			HOMO-1-LUMO	18.7
			HOMO-LUMO+6	15.8
9	459.33	0.00717	HOMO-LUMO	52.4
10	451.01	0.00017	HOMO-1-LUMO	51.7

6.3.4 Photocatalysis Action Plots of Eosin Y Single-Chain Nanoparticles

6.3.4.1 Synthesis of P5

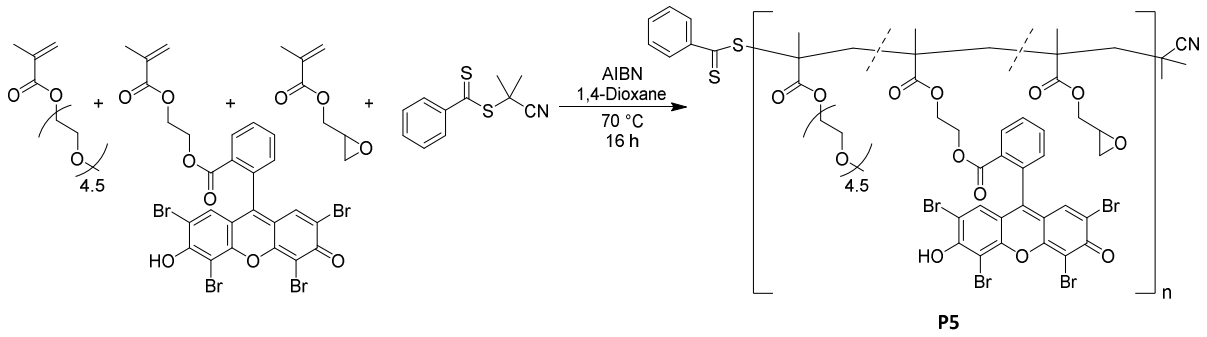

10.0 mg of the RAFT agent 2-cyano-2-propyl benzodithioate (45.2 µmol, 1.00 eq.) and 1.48 mg azobisisobutyronitrile (AIBN, 9.04 µmol, 0.200 eq.) were dissolved in 5.5 mL of 1,4-dioxane and 2.75 mL of poly(ethylene glycol) methyl ether methacrylate (PEGMEMA, M_n = 300 g·mol^{-1}, 2.89 g, 9.63 mmol, 214 eq.), 0.181 mL of glycidyl methacrylate (GMA, 193 mg, 1.36 mmol, 30.1 eq.) and 50.0 mg of 2-(methacryloyloxy)ethyl 2-(2,4,5,7-tetrabromo-6-hydroxy-3-oxo-3*H*-xanthen-9-yl)benzoate (EYMA, 65.8 µmol, 1.46 eq.) were added. The solution was degassed by three consecutive freeze-pump-thaw cycles and subsequently heated to 70 °C for 16 h. The reaction was stopped by cooling the flask to room temperature and opening it to air. The polymer was precipitated three times in a mixture of diethyl ether and *n*-pentane (1:1 v/v) and subsequently additionally purified by dialysis against THF (10 kDa molecular weight cutoff). After evaporation of the solvent under reduced pressure, **P5** was obtained as an orange oil (2.05 g).

^{1}H NMR (600 MHz, CD_3CN, 298 K): δ / ppm = 8.52-7.10 (br, Eosin Y-Aryl-*H*), 4.39-4.26 (br, GMA-COOCH_2), 4.22-3.90 (br, PEGMEMA-COOCH_2), 3.81-3.69 (br, GMA-COOCH_2), 3.72-3.38 (br, PEGMEMA-OCH_2CH_2), 3.35-3.24 (br, PEGMEMA-OCH_3), 3.24-3.14 (br, GMA-Epoxide-C*H*), 2.87-2.56 (br, GMA-Epoxide-CH_2), 2.07-0.65 (br, aliphatic backbone).

SEC (DMAc, RI, PMMA cal.): M_n = 45300 g·mol^{-1}, M_w = 54700 g·mol^{-1}, M_p = 49500 g·mol^{-1}, $Đ$ = 1.21.

DLS (CH_3CN): D_s = 7.80 nm.

DOSY (400 MHz, CD_3CN, 301 K): D = 1.09·10^{-10} m^2·s^{-1}.

6.3.4.2 Synthesis of SCNP5-EY

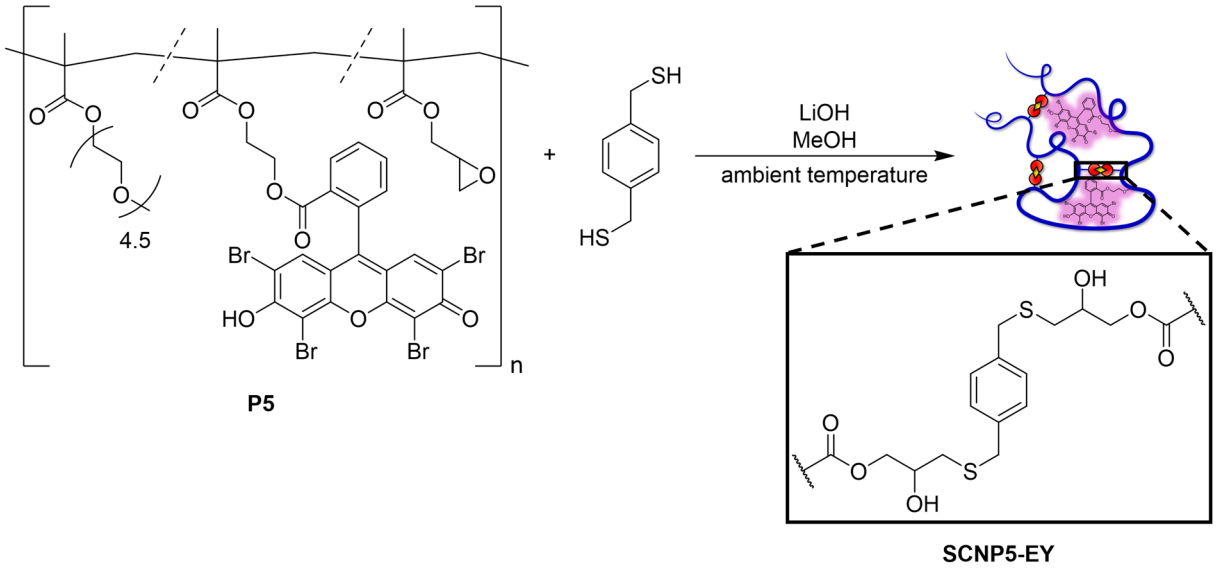

22.0 mg of 1,4-benzenedimethanethiol (0.129 mmol, 1.00 eq.) and 6.19 mg of lithium hydroxide (0.258 mol, 2.00 eq.) were dissolved in 50 mL of methanol and 50.0 mg of **P5** (about 27.1 µmol, 0.210 eq. epoxide functionalities), dissolved in 10 mL of methanol, slowly added using a syringe pump (1 mL·h^{-1}). After complete addition of the polymer solution, the volume was reduced by solvent evaporation under reduced pressure and the resulting solution subjected to preparative SEC (Sephadex LH-20) in methanol. Subsequently, an excess of acetonitrile was added and the methanol evaporated under reduced pressure. The resulting acetonitrile solution was further purified by preparative SEC (Sephadex LH-20) using acetonitrile as the eluent, resulting in a bright purple acetonitrile solution of **SCNP5-EY**.

^{1}H NMR (600 MHz, CD_3CN, 298 K): δ / ppm = 7.59-7.14 (br, aromatic), 4.26-3.94 (br, PEGMEMA-COOCH_2), 3.75-3.41 (br, PEGMEMA-OCH_2CH_2), 3.39-3.23 (br, PEGMEMA-OCH_3), 2.87-2.40 (br, unassigned), 1.63-0.54 (br, aliphatic backbone).

SEC (DMAc, RI, PMMA cal.): M_n = 40400 g·mol^{-1}, M_w = 50700 g·mol^{-1}, M_p = 44200 g·mol^{-1}, $Đ$ = 1.26.

DLS (CH_3CN): D_s = 7.22 nm.

DOSY (400 MHz, CD_3CN, 301 K): D = 1.52·10^{-10} m^2·s^{-1}.

6.3.4.3 Synthesis of P6

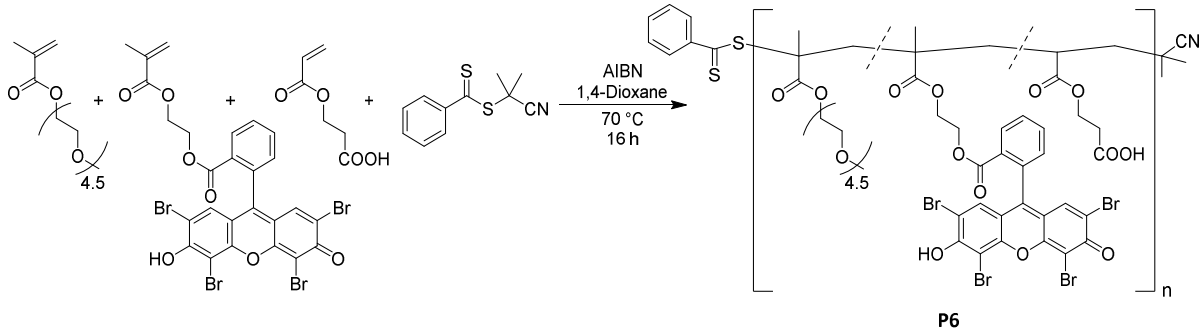

P6

10.0 mg of the RAFT agent 2-cyano-2-propyl benzodithioate (45.2 µmol, 1.00 eq.) and 1.48 mg azobisisobutyronitrile (AIBN, 9.04 µmol, 0.200 eq.) were dissolved in 5.5 mL of 1,4-dioxane and 2.75 mL of poly(ethylene glycol) methyl ether methacrylate (PEGMEMA, M_n = 300 g·mol^{-1}, 2.89 g, 9.63 mmol, 214 eq.), 0.161 mL of 2-carboxyethyl acrylate (2CEA, 196 mg, 1.36 mmol, 30.1 eq.) and 50.0 mg of 2-(methacryloyloxy)ethyl 2-(2,4,5,7-tetrabromo-6-hydroxy-3-oxo-3*H*-xanthen-9-yl)benzoate (EYMA, 65.8 µmol, 1.46 eq.) were added. The solution was degassed by three consecutive freeze-pump-thaw cycles and subsequently heated to 70 °C for 16 h. The reaction was stopped by cooling the flask to room temperature and opening it to air. The polymer was precipitated three times in a mixture of diethyl ether and *n*-pentane (1:1 v/v) and subsequently additionally purified twice by dialysis, first against THF and second against acetonitrile (10 kDa molecular weight cutoff). After evaporation of the solvent under reduced pressure, **P6** was obtained as a red oil (1.95 g).

^{1}H NMR (600 MHz, CD_3CN, 298 K): δ / ppm = 8.64-6.94 (br, Eosin Y-Aryl-*H*), 4.38-4.26 (br, 2CEA-COOC*H*$_2$), 4.24-3.91 (br, PEGMEMA-COOC*H*$_2$), 3.84-3.39 (br, PEGMEMA-OC*H*$_2$C*H*$_2$), 3.38-3.20 (br, PEGMEMA-OC*H*$_3$), 2.72-2.52 (br, 2CEA-C*H*$_2$COOH), 2.47-0.56 (br, aliphatic backbone).

SEC (DMAc, RI, PMMA cal.): M_n = 43900 g·mol^{-1}, M_w = 67800 g·mol^{-1}, M_p = 59600 g·mol^{-1}, $Đ$ = 1.54.

DLS (CH_3CN): D_s = 7.33 nm.

DOSY (400 MHz, CD_3CN, 301 K): D = 1.47·10^{-10} m^2·s^{-1}.

6.3.4.4 Photocatalysis Action Plots of Triphenylphosphine Oxidation

To reach a consistent dye concentration over all photochemical action plot experiments reported in Chapter 4.4, a calibration relating the 2-(propionyloxy)ethyl 2-(2,4,5,7-tetra-bromo-6-hydroxy-3-oxo-3*H*-xanthen-9-yl)benzoate (**EY**) concentration to the absorbance values in acetonitrile solution was initially established (refer to **Figure 6.29** and **Figure 6.30**).

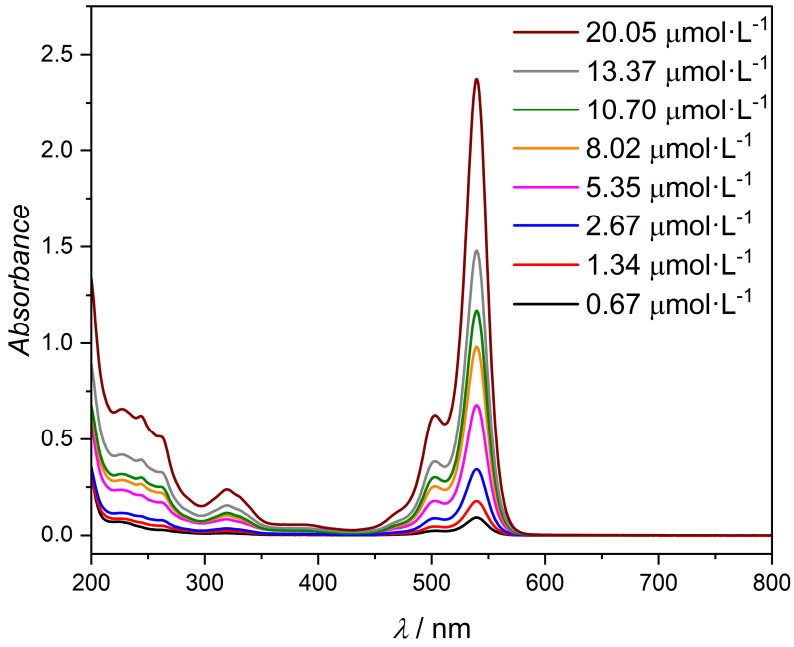

Figure 6.29 UV/Vis absorbance spectra (CH_3CN, 298 K) of **EY** at different concentrations.

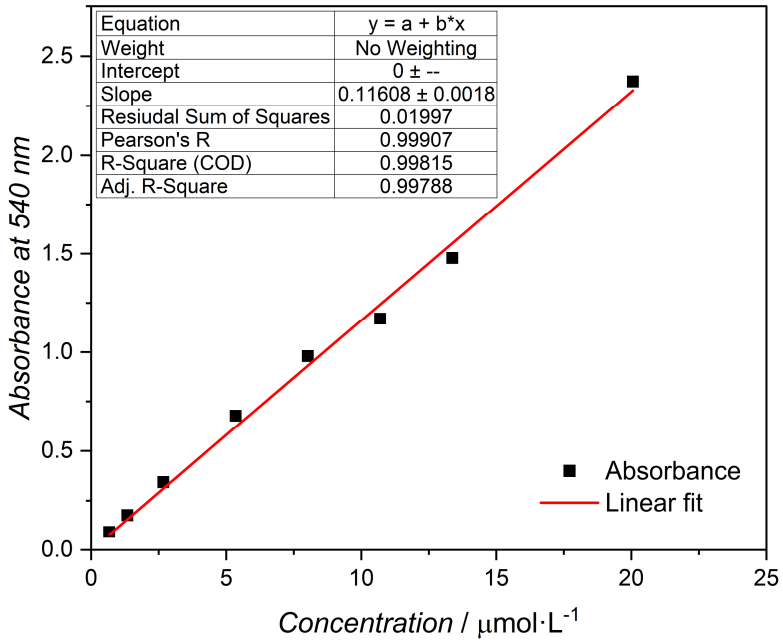

Figure 6.30 Plot of the 540 nm peak absorbance values in the UV/Vis spectrum (CH_3CN, 298 K) versus concentration of **EY**. Red line refers to linear fit to experimental data points performed with OriginPro 2023. Table provides details on linear fit parameters and derived data.

The described calibration enabled the estimation of the dye concentration within any solution of **EY**, **SCNP5-EY** or **P6**. It is noted that this approach assumes identical transition dipole moments of the relevant electronic excitations in the small molecule and polymeric systems, respectively, potentially limiting its reliability. However, given the good solvent conditions the experiments were conducted under, the differences in the transition dipole moments of the electronic excitations of the chromophore were expected to be negligible as the dye is presumably primarily surrounded by solvent molecules in each case. It is further noted that the optical absorption spectra of **EY**, **SCNP5-EY** and **P6** showed minor deviations in the absorbance profiles, however, these differences were considered negligible and their effect on the determined concentrations neglected.

Based on the calibration, all solutions employed in the photochemical action plot experiments were adjusted to a dye concentration of 13.4 $\mu mol \cdot L^{-1}$ in acetonitrile. For the action plots depicted in **Figure 4.52** and **Figure 4.54**, 200 equivalents of triphenylphosphine with respect to the dye were added. For the action plots depicted in **Figure 4.56**, 15 equivalents of zinc(II) triflate were initially added, causing a color change of the solutions from purple to yellow, followed by 200 equivalents of triphenylphosphine. For the action plots depicted in **Figure 4.57**, 60 equivalents of aqueous lithium hydroxide and 15 equivalents of zinc(II) triflate were initially added, followed by 200 equivalents of triphenylphosphine.

In each case, 0.4 mL of the resulting stock solutions were transferred to clear glass laser vials (0.8 mL, 7 mm x 40 mm) and irradiated with $1.10 \cdot 10^{18}$ photons within five minutes with a monochromatic nanosecond pulsed laser (refer to Chapter 6.2.8 for details). The energy per pulse was adjusted to keep the total number of photons at each wavelength the same with respect to the total irradiation time (refer to **Table 6.16** and Chapter 6.2.8 for details).

Subsequent to irradiation, the individual solutions were transferred to NMR tubes and 0.1 mL of CD_3CN added for ^1H NMR spectroscopic analysis. The distinct resonances of the aromatic protons of triphenylphosphine and the catalysis oxidation product triphenylphosphine oxide, respectively, could be integrated relative to each other, enabling the determination of the conversion of the substrate to the catalysis product. Each experiment was performed in triplicate, and the determined average, lowest and highest conversions plotted in the photocatalysis action plots depicted in Chapter 4.4 are summarized in **Table 6.17** to **Table 6.23**. It is noted that handling of the samples required rigorous protection from ambient light during sample preparation and analysis to avoid the determination of erroneous conversions.

Table 6.16 Photon energies, laser vial transmittance values and energies per pulse for the wavelengths reported in the photochemical action plots in Chapter 4.4.

Wavelength / nm	Photon energy / 10^{-19} J	Vial transmittance / %	Energy per pulse / µJ
360	5.52	67.7	149.4
380	5.23	68.3	140.3
400	4.97	68.6	132.8
420	4.73	68.7	126.3
440	4.51	68.7	120.5
460	4.32	68.7	115.2
480	4.14	68.7	110.4
500	3.97	68.7	106.0
520	3.82	68.7	101.9
540	3.68	68.7	98.1
560	3.55	68.7	94.6
580	3.42	68.7	91.4

Table 6.17 Average, lowest and highest conversion determined for each wavelength reported in the photochemical action plot depicted in **Figure 4.52a** and **Figure 4.54a**.

Wavelength / nm	Average conversion / %	Lowest conversion / %	Highest conversion / %
360	11	10	12
380	9	8	10
400	8	7	8
420	7	7	7
440	4	3	4
460	8	7	8
480	13	13	14
500	28	26	28
520	30	29	30
540	32	32	33
560	14	13	15
580	1	1	2

Table 6.18 Average, lowest and highest conversion determined for each wavelength reported in the photochemical action plot depicted in **Figure 4.52b**.

Wavelength / nm	Average conversion / %	Lowest conversion / %	Highest conversion / %
360	18	17	19
380	13	11	15
400	14	13	15
420	15	13	15
440	9	8	9
460	13	12	13
480	18	17	19
500	29	29	31
520	32	31	33
540	38	36	39
560	21	19	21
580	4	4	5

Table 6.19 Average, lowest and highest conversion determined for each wavelength reported in the photochemical action plot depicted in **Figure 4.54b**.

Wavelength / nm	Average conversion / %	Lowest conversion / %	Highest conversion / %
360	14	13	15
380	10	10	11
400	10	9	11
420	8	7	9
440	8	7	8
460	12	12	13
480	21	19	21
500	34	34	34
520	36	36	37
540	41	39	45
560	24	23	24
580	3	3	3

Table 6.20 Average, lowest and highest conversion determined for each wavelength reported in the photochemical action plot depicted in **Figure 4.56a**.

Wavelength / nm	Average conversion / %	Lowest conversion / %	Highest conversion / %
360	36	34	37
380	42	41	43
400	39	38	40
420	39	39	40
440	48	47	49
460	51	50	53
480	58	55	61
500	50	49	51
520	50	48	51
540	24	22	26
560	5	5	6
580	4	3	5

Table 6.21 Average, lowest and highest conversion determined for each wavelength reported in the photochemical action plot depicted in **Figure 4.56b**.

Wavelength / nm	Average conversion / %	Lowest conversion / %	Highest conversion / %
360	41	40	42
380	44	44	45
400	40	40	41
420	39	38	40
440	44	44	45
460	47	46	49
480	49	48	49
500	41	41	42
520	36	35	38
540	15	15	15
560	5	5	6
580	2	0	4

Table 6.22 Average, lowest and highest conversion determined for each wavelength reported in the photochemical action plot depicted in **Figure 4.57a**.

Wavelength / nm	Average conversion / %	Lowest conversion / %	Highest conversion / %
360	28	26	29
380	35	35	35
400	32	31	32
420	31	30	31
440	37	36	38
460	39	38	40
480	42	40	43
500	40	39	41
520	36	35	36
540	27	27	28
560	11	11	12
580	4	4	5

Table 6.23 Average, lowest and highest conversion determined for each wavelength reported in the photochemical action plot depicted in **Figure 4.57b**.

Wavelength / nm	Average conversion / %	Lowest conversion / %	Highest conversion / %
360	10	10	11
380	10	9	10
400	9	9	10
420	8	7	9
440	9	7	10
460	15	15	16
480	25	24	26
500	36	34	37
520	39	39	39
540	43	43	44
560	18	18	19
580	1	1	2

6.3.4.5 Switching of Catalytic Activity of EY and P6

To demonstrate the stimuli responsiveness of the photocatalysts **EY** and **P6** illustrated in **Figure 4.59**, a solution of **EY** or **P6**, respectively, in CD_3CN with a dye concentration of 13.4 µmol·L^{-1} was prepared. 200 equivalents of triphenylphosphine with respect to the dye were added and 0.4 mL of the resulting respective solution transferred to a clear glass laser vial (0.8 mL, 7 mm x 40 mm). After being kept in the dark for five minutes, the solution was irradiated at 440 nm with $1.10 \cdot 10^{18}$ photons within five minutes with a monochromatic nanosecond pulsed laser (refer to Chapter 6.2.8 for details). Subsequently, 15 equivalents of zinc(II) triflate were added and the solution again irradiated under identical conditions. After that, 60 equivalents of aqueous lithium hydroxide were added and the irradiation step was repeated. After each step, the solution was analyzed by ^{1}H NMR spectroscopy. The experiments were performed in triplicate and the determined conversions are summarized in **Table 6.24**.

Table 6.24 Conversions of triphenylphosphine to triphenylphosphine oxide upon the photosensitized oxidation catalyzed by **EY** or **P6** without irradiation, upon irradiation at 440 nm with $1.10 \cdot 10^{18}$ photons over five minutes and upon conducting the same irradiation procedure after consecutive addition of zinc(II) triflate and lithium hydroxide. The experiments were performed in triplicate.

	No irradiation	**440 nm**	**$ZnOTf_2$+440nm**	**$ZnOTf_2$+LiOH+440nm**
EY				
Experiment I	0 %	2 %	42 %	67 %
Experiment II	0 %	3 %	48 %	62 %
Experiment III	0 %	4 %	45 %	69 %
P6				
Experiment I	0 %	7 %	45 %	45 %
Experiment II	0 %	6 %	46 %	50 %
Experiment III	0 %	7 %	47 %	50 %

6.3.4.6 Computational Details

Quantum chemical calculations at the density functional theory level relevant to Chapter 4.4 were performed with TURBOMOLE.[303-304] For all calculations, the generalized gradient approximation functional BLYP[317-319] together with def2-TZVPP basis sets[307] was employed. The resolution of the identity approximation for the Coulomb part (RI-*J*) in combination with the corresponding auxiliary basis sets was used in all cases.[311-312] Self-consistent field thresholds were set to 10^{-8} Hartree and the convergence criterion for the root mean square of the density matrix was set to 10^{-7} Hartree. Large grids (gridsize 5)[313-314] were used for the numerical integration of the exchange-correlation terms. The conductor-like screening model (COSMO)[320] with Gaussian charge distributions,[321] a dielectric constant of 37.5 (corresponding to acetonitrile)[322] and otherwise default parameters was used to account for solvation effects. Information concerning the twenty lowest energy singlet vertical excitations of **EY-Na** and **EY-Zn** are given in **Table 6.25** and **Table 6.26**. Electronic excitation spectra shown in **Figure 4.55** were simulated based on the calculated singlet vertical excitation energies and oscillator strengths with a full width at half maximum of 15 nm (**EY-Na**) and 35 nm (**EY-Zn**), respectively. Non-relaxed difference densities were analyzed using the python script PANAMA (Peak ANAlyzing MAchine).[316] Cartesian coordinates of the optimized structures are provided in **Table 6.27** and **Table 6.28**.

It is noted that the calculations do not account for effects of triphenylphosphine or triflate ions, also present in the solutions corresponding to the experimental spectra depicted in **Figure 4.55**. It is further noted that the calculated excitation energies showed a pronounced dependence on the density functional chosen for the calculations.

Table 6.25 Twenty lowest energy singlet vertical excitations (BLYP/def2-TZVPP) of the model compound **EY-Na** (refer to Chapter 4.4.3 for details).

Excitation number	Excitation energy / nm	Oscillator strength / Velocity representation	Contributions (> 10 %)	Orbital pair contributions
1	506.22	0.21966	HOMO-LUMO+1 HOMO-LUMO	55.2 39.7
2	500.30	0.27294	HOMO-LUMO HOMO-LUMO+1	44.8 44.2
3	480.94	0.10419	HOMO-1-LUMO	86.9
4	465.36	0.00028	HOMO-2-LUMO	99.9
5	410.72	0.00352	HOMO-1-LUMO+1	99.3
6	409.85	0.00016	HOMO-4-LUMO	99.3
7	392.65	0.03770	HOMO-5-LUMO	97.5
8	387.61	0.04432	HOMO-3-LUMO	84.9
9	381.41	0.00264	HOMO-2-LUMO+1	98.6
10	375.29	0.01370	HOMO-LUMO+2	86.6
11	364.34	0.00857	HOMO-LUMO+3 HOMO-LUMO+4	84.8 11.0
12	362.69	0.00033	HOMO-6-LUMO	98.2
13	360.12	0.00025	HOMO-7-LUMO	93.7
14	353.94	0.00008	HOMO-8-LUMO	93.7
15	353.28	0.00036	HOMO-3-LUMO+1	95.3
16	342.89	0.00968	HOMO-LUMO+5 HOMO-LUMO+4	63.6 32.7
17	342.28	0.00031	HOMO-4-LUMO+1	98.7
18	338.12	0.01823	HOMO-9-LUMO	92.5
19	336.83	0.00358	HOMO-5-LUMO+1	98.6
20	335.65	0.00097	HOMO-10-LUMO	98.1

Table 6.26 Twenty lowest energy singlet vertical excitations (BLYP/def2-TZVPP) of the model compound **EY-Zn** (refer to Chapter 4.4.3 for details).

Excitation number	Excitation energy / nm	Oscillator strength / Velocity representation	Contributions (> 10 %)	Orbital pair contributions
1	854.39	0.00114	HOMO-LUMO	99.9
2	617.33	0.00064	HOMO-1-LUMO	99.9
3	606.56	0.00000	HOMO-2-LUMO	99.9
4	518.11	0.14529	HOMO-LUMO+1	43.9
			HOMO-3-LUMO	41.6
			HOMO-1-LUMO+1	12.3
5	516.59	0.08962	HOMO-3-LUMO	58.1
			HOMO-LUMO+1	30.3
6	487.90	0.00002	HOMO-2-LUMO+1	99.8
7	480.13	0.00021	HOMO-4-LUMO	99.4
8	470.98	0.00012	HOMO-5-LUMO	99.6
9	457.52	0.00253	HOMO-6-LUMO	98.8
10	454.18	0.30692	HOMO-1-LUMO+1	72.4
			HOMO-LUMO+1	18.7
11	449.24	0.00037	HOMO-7-LUMO	99.9
12	440.37	0.01669	HOMO-LUMO+2	97.3
13	423.64	0.00053	HOMO-8-LUMO	99.8
14	417.58	0.00358	HOMO-LUMO+3	99.1
15	412.13	0.00327	HOMO-9-LUMO	98.4
16	410.36	0.04195	HOMO-3-LUMO+1	61.3
			HOMO-5-LUMO+1	33.2
17	403.00	0.00208	HOMO-4-LUMO+1	71.9
			HOMO-5-LUMO+1	12.2
18	398.62	0.02056	HOMO-5-LUMO+1	47.9
			HOMO-6-LUMO+1	22.5
			HOMO-3-LUMO+1	18.6
19	396.11	0.00299	HOMO-10-LUMO	98.8
20	389.75	0.01088	HOMO-6-LUMO+1	48.8
			HOMO-7-LUMO+1	28.2

Table 6.27 Cartesian coordinates (xyz format, Å) of the optimized structure (BLYP/def2-TZVPP) of the model compound **EY-Na**.

52

Energy = -11947.56140059

C	-2.5586836	2.5402314	-0.7764962
C	-3.4062718	1.648559	-1.5629218
C	-3.1776464	0.2471657	-1.2899459
C	-2.2392554	-0.1996586	-0.3696898
C	-1.4273433	0.7150775	0.3718105
C	-1.6286456	2.1072655	0.1319707
O	-2.109065	-1.5538836	-0.1886214
C	-1.2104042	-2.0692088	0.7163414
C	-0.3697485	-1.1901259	1.4804342
C	-0.4722434	0.2030379	1.2891668
C	-1.1446014	-3.4436164	0.858851
C	-0.2290397	-4.1022823	1.7803911
C	0.6109366	-3.1561527	2.5318798
C	0.5484391	-1.7984026	2.3951529
C	0.3380835	1.1455649	2.1333409
C	1.5839208	1.7023318	1.7409084
C	2.2485646	2.5859552	2.6166238
C	1.7029384	2.9200485	3.8566478
C	0.4739945	2.3737596	4.2421959
C	-0.1977771	1.4960048	3.3852306
C	2.1933177	1.3505032	0.4160447
O	3.3217263	2.0652818	0.1590062
O	1.7425566	0.5174965	-0.3628685
C	3.9998587	1.7833898	-1.1117968
C	5.2099247	2.7114833	-1.1666786
C	6.0151897	2.5299971	-2.4451628
O	7.0662256	3.386153	-2.4719636
O	5.7534649	1.7274295	-3.3319544
C	7.9681928	3.3436191	-3.6440218
C	9.122991	2.3759975	-3.4134218
Br	-2.7919763	4.4405953	-1.0579641
O	-4.2606906	2.0715581	-2.4009753
Br	-4.2443651	-1.0307296	-2.2651561
Br	-2.2966707	-4.5801771	-0.1861392
O	-0.1609347	-5.34831	1.9212389
Br	1.8692547	-3.9270468	3.7835129
H	-1.0310989	2.8263623	0.6829922
H	1.2002746	-1.1596067	2.9823342

Table 6.27 continued

H	3.2029952	3.0071816	2.3182462
H	2.2345549	3.6017766	4.5168102
H	0.0360412	2.626204	5.2056765
H	-1.1541254	1.0739545	3.6862236
H	3.3017807	1.971399	-1.9333553
H	4.2906833	0.7283827	-1.12963
H	5.8756492	2.5298726	-0.3123799
H	4.8957277	3.7615397	-1.1017073
H	8.3188988	4.3753076	-3.7365805
H	7.3786702	3.0772736	-4.5255931
H	9.8071303	2.4244857	-4.2705349
H	8.7666881	1.3441659	-3.3177305
H	9.6854706	2.6434443	-2.5110988
Na	-5.7905726	1.3587078	-3.8639428

Table 6.28 Cartesian coordinates (xyz format, Å) of the optimized structure (BLYP/def2-TZVPP) of the model compound **EY-Zn**.

52

Energy = -13564.50778293

C	-2.7861256	2.5337293	-0.6589835
C	-3.5348934	1.6141664	-1.470867
C	-3.2130509	0.2430862	-1.2784151
C	-2.2393146	-0.1866126	-0.3761936
C	-1.5029805	0.7488242	0.394811
C	-1.8138148	2.1238873	0.226679
O	-2.022752	-1.5290975	-0.27214
C	-1.0877333	-2.0286486	0.6072892
C	-0.2949135	-1.1234309	1.4033935
C	-0.4840384	0.2577082	1.2788644
C	-0.9370875	-3.3960571	0.6864156
C	0.0321571	-4.0288872	1.5762368
C	0.8250405	-3.0623916	2.3650107
C	0.6751263	-1.7107891	2.2857295
C	0.2866096	1.221545	2.1334197
C	1.5015407	1.8362821	1.7306664
C	2.1459245	2.7274407	2.6121016
C	1.606743	3.0153023	3.8668928
C	0.4092386	2.4100785	4.2626512
C	-0.2418044	1.520721	3.400958
C	2.0861987	1.5406804	0.3819651
O	3.2850234	2.1475956	0.1876361

Table 6.28 continued

O	1.5521409	0.8319457	-0.465621
C	3.9252883	1.9258326	-1.1158807
C	5.2415622	2.6966354	-1.0858374
C	6.008927	2.5689999	-2.3942724
O	7.2084544	3.1938052	-2.3058982
O	5.5998517	1.9923575	-3.3940423
C	8.0916715	3.1774104	-3.4932454
C	9.0317056	1.9782081	-3.4610868
Br	-3.1698328	4.4120306	-0.8448349
O	-4.4408028	2.0698885	-2.3095625
Br	-4.1413155	-1.1164653	-2.3172367
Br	-2.0190762	-4.5579588	-0.3959623
O	0.1805846	-5.2665579	1.6644198
Br	2.136474	-3.8084855	3.5653909
H	-1.2720637	2.8633155	0.8074995
H	1.2890838	-1.0542075	2.8934387
H	3.0753722	3.1956697	2.3046233
H	2.1195443	3.707443	4.5309901
H	-0.0207497	2.6248347	5.2386739
H	-1.1718321	1.0499723	3.711752
H	3.2553251	2.287545	-1.9017741
H	4.0823708	0.8512626	-1.2517216
H	5.8825043	2.34046	-0.269143
H	5.0593991	3.7638168	-0.8998525
H	8.6388883	4.1212944	-3.419798
H	7.4670342	3.1857804	-4.3905887
H	9.7168053	2.0376592	-4.3167264
H	8.478491	1.0348915	-3.5304473
H	9.6306703	1.9729771	-2.542864
Zn	-5.2685844	0.8238688	-3.4998133

References

[1] R. Feynman, *Eng. Sci.* **1960**, *23*, 22-36.

[2] I. Khan, K. Saeed, I. Khan, *Arab. J. Chem.* **2019**, *12*, 908-931.

[3] *Single-Chain Polymer Nanoparticles,* Ed.: J. A. Pomposo, Wiley-VCH Verlag GmbH & Co. KGaA, Weinheim, Germany, **2017**.

[4] C. K. Lyon, A. Prasher, A. M. Hanlon, B. T. Tuten, C. A. Tooley, P. G. Frank, E. B. Berda, *Polym. Chem.* **2015**, *6*, 181-197.

[5] I. Asenjo-Sanz, T. Claros, E. González, J. Pinacho-Olaciregui, E. Verde-Sesto, J. A. Pomposo, *Mater. Lett.* **2021**, *304*, 130622.

[6] J. L. Bohlen, B. Kulendran, H. Rothfuss, C. Barner-Kowollik, P. W. Roesky, *Polym. Chem.* **2021**, *12*, 4016-4021.

[7] S. Gillhuber, J. O. Holloway, H. Frisch, F. Feist, F. Weigend, C. Barner-Kowollik, P. W. Roesky, *Chem. Commun.* **2023**, *59*, 4672-4675.

[8] A. E. Izuagbe, V. X. Truong, B. T. Tuten, P. W. Roesky, C. Barner-Kowollik, *Macromolecules* **2022**, *55*, 9242-9248.

[9] N. D. Knöfel, H. Rothfuss, C. Barner-Kowollik, P. W. Roesky, *Polym. Chem.* **2019**, *10*, 86-93.

[10] N. D. Knöfel, H. Rothfuss, P. Tzvetkova, B. Kulendran, C. Barner-Kowollik, P. W. Roesky, *Chem. Sci.* **2020**, *11*, 10331-10336.

[11] N. D. Knöfel, H. Rothfuss, J. Willenbacher, C. Barner-Kowollik, P. W. Roesky, *Angew. Chem. Int. Ed.* **2017**, *56*, 4950-4954.

[12] P. H. Maag, F. Feist, H. Frisch, P. W. Roesky, C. Barner-Kowollik, *Macromolecules* **2022**, *55*, 9918-9924.

[13] K. Mundsinger, A. Izuagbe, B. T. Tuten, P. W. Roesky, C. Barner-Kowollik, *Angew. Chem. Int. Ed.* **2024**, *63*, e202311734.

[14] J. Pinacho-Olaciregui, E. Verde-Sesto, D. Taton, J. A. Pomposo, *Nanoscale* **2024**, *16*, 9742-9747.

[15] H. Rothfuss, N. D. Knöfel, P. W. Roesky, C. Barner-Kowollik, *J. Am. Chem. Soc.* **2018**, *140*, 5875-5881.

[16] H. Rothfuss, N. D. Knöfel, P. Tzvetkova, N. C. Michenfelder, S. Baraban, A.-N. Unterreiner, P. W. Roesky, C. Barner-Kowollik, *Chem. Eur. J.* **2018**, *24*, 17475-17486.

[17] J. Rubio-Cervilla, E. González, J. A. Pomposo, *Nanomaterials* **2017**, *7*, 341.

[18] A. Sathyan, S. Croke, A. M. Pérez-López, B. F. M. de Waal, A. Unciti-Broceta, A. R. A. Palmans, *Mol. Syst. Des. Eng.* **2022**, *7*, 1736-1748.

[19] J. Willenbacher, O. Altintas, P. W. Roesky, C. Barner-Kowollik, *Macromol. Rapid Commun.* **2014**, *35*, 45-51.

[20] J. Willenbacher, O. Altintas, V. Trouillet, N. Knöfel, M. J. Monteiro, P. W. Roesky, C. Barner-Kowollik, *Polym. Chem.* **2015**, *6*, 4358-4365.

[21] T. M. Xiong, E. S. Garcia, J. Chen, L. Zhu, A. J. Alzona, S. C. Zimmerman, *Chem. Commun.* **2022**, *58*, 985-988.

[22] A. Sathyan, T. Loman, L. Deng, A. R. A. Palmans, *Nanoscale* **2023**, *15*, 12710-12717.

[23] B. F. Patenaude, E. B. Berda, S. Pazicni, *Polym. Chem.* **2022**, *13*, 677-683.

[24] S. Gillhuber, J. O. Holloway, K. Mundsinger, J. A. Kammerer, J. R. Harmer, H. Frisch, C. Barner-Kowollik, P. W. Roesky, *Chem. Sci.* **2024**, *15*, 15280-15290.

[25] W. Kuhn, G. Balmer, *J. Polym. Sci.* **1962**, *57*, 311-319.

[26] P. Longi, F. Greco, U. Rossi, *Makromol. Chem.* **1968**, *116*, 113-121.
[27] P. Longi, F. Greco, U. Rossi, *Makromol. Chem.* **1969**, *129*, 157-164.
[28] M. Antonietti, H. Sillescu, M. Schmidt, H. Schuch, *Macromolecules* **1988**, *21*, 736-742.
[29] M. Antonietti, H. Sillescu, *Macromolecules* **1986**, *19*, 798-803.
[30] J. E. Martin, B. E. Eichinger, *Macromolecules* **1983**, *16*, 1345-1350.
[31] J. E. Martin, B. E. Eichinger, *Macromolecules* **1983**, *16*, 1350-1358.
[32] V. W. Kuhn, H. Majer, *Makromol. Chem.* **1956**, *18*, 239-253.
[33] G. Allen, J. Burgess, S. F. Edwards, D. J. Walsh, *Proc. R. Soc. Lond. A* **1973**, *334*, 453-463.
[34] D. Mecerreyes, V. Lee, C. J. Hawker, J. L. Hedrick, A. Wursch, W. Volksen, T. Magbitang, E. Huang, R. D. Miller, *Adv. Mater.* **2001**, *13*, 204-208.
[35] M. Szwarc, *Living Polymers and Mechanisms of Anionic Polymerization* in *Advances in Polymer Science, Vol. 49*, Springer, Berlin, Heidelberg, Germany, **1983**, pp. 1-177.
[36] K. Matyjaszewski, *Macromolecules* **2012**, *45*, 4015-4039.
[37] R. B. Grubbs, *Polym. Rev.* **2011**, *51*, 104-137.
[38] J. Chiefari, Y. K. Chong, F. Ercole, J. Krstina, J. Jeffery, T. P. T. Le, R. T. A. Mayadunne, G. F. Meijs, C. L. Moad, G. Moad, E. Rizzardo, S. H. Thang, *Macromolecules* **1998**, *31*, 5559-5562.
[39] S. Perrier, *Macromolecules* **2017**, *50*, 7433-7447.
[40] J.-F. Lutz, M. Ouchi, D. R. Liu, M. Sawamoto, *Science* **2013**, *341*, 1238149.
[41] M. A. Gauthier, M. I. Gibson, H. A. Klok, *Angew. Chem. Int. Ed.* **2009**, *48*, 48-58.
[42] O. Altintas, C. Barner-Kowollik, *Macromol. Rapid Commun.* **2016**, *37*, 29-46.
[43] V. A. Davankov, M. M. Ilyin, M. P. Tsyurupa, G. I. Timofeeva, L. V. Dubrovina, *Macromolecules* **1996**, *29*, 8398-8403.
[44] E. Harth, B. V. Horn, V. Y. Lee, D. S. Germack, C. P. Gonzales, R. D. Miller, C. J. Hawker, *J. Am. Chem. Soc.* **2002**, *124*, 8653-8660.
[45] A. Tuteja, M. E. Mackay, C. J. Hawker, B. Van Horn, D. L. Ho, *J. Polym. Sci. Part B: Polym. Phys.* **2006**, *44*, 1930-1947.
[46] J. N. Dobish, S. K. Hamilton, E. Harth, *Polym. Chem.* **2012**, *3*, 857-860.
[47] T. E. Dukette, M. E. Mackay, B. Van Horn, K. L. Wooley, E. Drockenmuller, M. Malkoch, C. J. Hawker, *Nano Lett.* **2005**, *5*, 1704-1709.
[48] O. Altintas, J. Willenbacher, K. N. R. Wuest, K. K. Oehlenschlaeger, P. Krolla-Sidenstein, H. Gliemann, C. Barner-Kowollik, *Macromolecules* **2013**, *46*, 8092-8101.
[49] I. Perez-Baena, I. Loinaz, D. Padro, I. García, H. J. Grande, I. Odriozola, *J. Mater. Chem.* **2010**, *20*, 6916-6922.
[50] A. R. de Luzuriaga, N. Ormategui, H. J. Grande, I. Odriozola, J. A. Pomposo, I. Loinaz, *Macromol. Rapid Commun.* **2008**, *29*, 1156-1160.
[51] N. Ormategui, I. García, D. Padro, G. Cabañero, H. J. Grande, I. Loinaz, *Soft Matter* **2012**, *8*, 734-740.
[52] A. R. de Luzuriaga, I. Perez-Baena, S. Montes, I. Loinaz, I. Odriozola, I. García, J. A. Pomposo, *Macromol. Symp.* **2010**, *296*, 303-310.
[53] H. Frisch, J. P. Menzel, F. R. Bloesser, D. E. Marschner, K. Mundsinger, C. Barner-Kowollik, *J. Am. Chem. Soc.* **2018**, *140*, 9551-9557.
[54] A. E. Cherian, F. C. Sun, S. S. Sheiko, G. W. Coates, *J. Am. Chem. Soc.* **2007**, *129*, 11350-11351.
[55] A. Sanchez-Sanchez, D. A. Fulton, J. A. Pomposo, *Chem. Commun.* **2014**, *50*, 1871-1874.
[56] L. Buruaga, J. A. Pomposo, *Polymers* **2011**, *3*, 1673-1683.
[57] J. B. Beck, K. L. Killops, T. Kang, K. Sivanandan, A. Bayles, M. E. Mackay, K. L. Wooley, C. J. Hawker, *Macromolecules* **2009**, *42*, 5629-5635.

[58] J. Wen, L. Yuan, Y. Yang, L. Liu, H. Zhao, *ACS Macro Lett.* **2013**, *2*, 100-106.
[59] B. T. Tuten, D. Chao, C. K. Lyon, E. B. Berda, *Polym. Chem.* **2012**, *3*, 3068-3071.
[60] J.-H. Ryu, R. T. Chacko, S. Jiwpanich, S. Bickerton, R. P. Babu, S. Thayumanavan, *J. Am. Chem. Soc.* **2010**, *132*, 17227-17235.
[61] O. Altintas, E. Lejeune, P. Gerstel, C. Barner-Kowollik, *Polym. Chem.* **2012**, *3*, 640-651.
[62] O. Altintas, T. Rudolph, C. Barner-Kowollik, *J. Polym. Sci. Part A: Polym. Chem.* **2011**, *49*, 2566-2576.
[63] O. Altintas, P. Gerstel, N. Dingenouts, C. Barner-Kowollik, *Chem. Commun.* **2010**, *46*, 6291-6293.
[64] R. Scott Lokey, B. L. Iverson, *Nature* **1995**, *375*, 303-305.
[65] J. C. Nelson, J. G. Saven, J. S. Moore, P. G. Wolynes, *Science* **1997**, *277*, 1793-1796.
[66] D. D. Prabhu, K. Aratsu, Y. Kitamoto, H. Ouchi, T. Ohba, M. J. Hollamby, N. Shimizu, H. Takagi, R. Haruki, S.-i. Adachi, S. Yagai, *Sci. Adv.* **2018**, *4*, eaat8466.
[67] P. Wu, A. Pietropaolo, M. Fortino, S. Shimoda, K. Maeda, T. Nishimura, M. Bando, N. Naga, T. Nakano, *Angew. Chem. Int. Ed.* **2022**, *61*, e202210556.
[68] S. Wijker, L. Deng, F. Eisenreich, I. K. Voets, A. R. A. Palmans, *Macromolecules* **2022**, *55*, 6220-6230.
[69] A. Blazquez-Martín, E. Verde-Sesto, A. J. Moreno, A. Arbe, J. Colmenero, J. A. Pomposo, *Polymers (Basel)* **2021**, *13*, 293.
[70] M. Gonzalez-Burgos, A. Latorre-Sanchez, J. A. Pomposo, *Chem. Soc. Rev.* **2015**, *44*, 6122-6142.
[71] H. Frisch, B. T. Tuten, C. Barner-Kowollik, *Isr. J. Chem.* **2020**, *60*, 86-99.
[72] O. Galant, H. B. Donmez, C. Barner-Kowollik, C. E. Diesendruck, *Angew. Chem. Int. Ed.* **2021**, *60*, 2042-2046.
[73] E. H. H. Wong, S. J. Lam, E. Nam, G. G. Qiao, *ACS Macro Lett.* **2014**, *3*, 524-528.
[74] J. A. Pomposo, D. Arena, E. Verde-Sesto, J. Maiz, P. M. de Molina, A. J. Moreno, *Macromol. Rapid Commun.* **2024**, *45*, 2400453.
[75] J. He, L. Tremblay, S. Lacelle, Y. Zhao, *Soft Matter* **2011**, *7*, 2380-2386.
[76] D. E. Bergbreiter, Y.-C. Yang, *J. Org. Chem.* **2010**, *75*, 873-878.
[77] Y. Zhao, L. Tremblay, Y. Zhao, *J. Polym. Sci. Part A: Polym. Chem.* **2010**, *48*, 4055-4066.
[78] P. G. Frank, B. T. Tuten, A. Prasher, D. Chao, E. B. Berda, *Macromol. Rapid Commun.* **2014**, *35*, 249-253.
[79] P. H. Maag, F. Feist, H. Frisch, P. W. Roesky, C. Barner-Kowollik, *Chem. Sci.* **2024**, *15*, 5218-5224.
[80] J. Steinkoenig, H. Rothfuss, A. Lauer, B. T. Tuten, C. Barner-Kowollik, *J. Am. Chem. Soc.* **2017**, *139*, 51-54.
[81] T. Nitsche, S. J. Blanksby, J. P. Blinco, C. Barner-Kowollik, *Polym. Chem.* **2020**, *11*, 1696-1701.
[82] T. Terashima, T. Mes, T. F. A. De Greef, M. A. J. Gillissen, P. Besenius, A. R. A. Palmans, E. W. Meijer, *J. Am. Chem. Soc.* **2011**, *133*, 4742-4745.
[83] H. G. Barth, C. Jackson, B. E. Boyes, *Anal. Chem.* **1994**, *66*, 595-620.
[84] J. A. Pomposo, I. Perez-Baena, L. Buruaga, A. Alegría, A. J. Moreno, J. Colmenero, *Macromolecules* **2011**, *44*, 8644-8649.
[85] E. Blasco, B. T. Tuten, H. Frisch, A. Lederer, C. Barner-Kowollik, *Polym. Chem.* **2017**, *8*, 5845-5851.
[86] C. M. Maguire, M. Rösslein, P. Wick, A. Prina-Mello, *Sci. Technol. Adv. Mater.* **2018**, *19*, 732-745.
[87] G. Mie, *Ann. Phys.* **1908**, *330*, 377-445.

[88] A. Einstein, *Ann. Phys.* **1905**, *322*, 549-560.
[89] C. C. Miller, J. Walker, *Proc. R. Soc. Lond. A* **1924**, *106*, 724-749.
[90] Y. Cohen, L. Avram, L. Frish, *Angew. Chem. Int. Ed.* **2005**, *44*, 520-554.
[91] P. Groves, *Polym. Chem.* **2017**, *8*, 6700-6708.
[92] E. O. Stejskal, J. E. Tanner, *J. Chem. Phys.* **1965**, *42*, 288-292.
[93] B. Antalek, *Concepts Magn. Reson.* **2002**, *14*, 225-258.
[94] J. Jeong, Y.-J. Lee, B. Kim, B. Kim, K.-S. Jung, H.-j. Paik, *Polym. Chem.* **2015**, *6*, 3392-3397.
[95] E. J. Foster, E. B. Berda, E. W. Meijer, *J. Am. Chem. Soc.* **2009**, *131*, 6964-6966.
[96] J. Engelke, B. T. Tuten, R. Schweins, H. Komber, L. Barner, L. Plüschke, C. Barner-Kowollik, A. Lederer, *Polym. Chem.* **2020**, *11*, 6559-6578.
[97] A. Arbe, J. A. Pomposo, A. J. Moreno, F. LoVerso, M. González-Burgos, I. Asenjo-Sanz, A. Iturrospe, A. Radulescu, O. Ivanova, J. Colmenero, *Polymer* **2016**, *105*, 532-544.
[98] M. Doi, S. F. Edwards, *The Theory of Polymer Dynamics*, Clarendon Press, Oxford, UK, **1988**.
[99] J. A. Pomposo, I. Perez-Baena, F. Lo Verso, A. J. Moreno, A. Arbe, J. Colmenero, *ACS Macro Lett.* **2014**, *3*, 767-772.
[100] A. J. Moreno, F. Lo Verso, A. Sanchez-Sanchez, A. Arbe, J. Colmenero, J. A. Pomposo, *Macromolecules* **2013**, *46*, 9748-9759.
[101] I. Perez-Baena, I. Asenjo-Sanz, A. Arbe, A. J. Moreno, F. Lo Verso, J. Colmenero, J. A. Pomposo, *Macromolecules* **2014**, *47*, 8270-8280.
[102] S. Basasoro, M. Gonzalez-Burgos, A. J. Moreno, F. L. Verso, A. Arbe, J. Colmenero, J. A. Pomposo, *Macromol. Rapid Commun.* **2016**, *37*, 1060-1065.
[103] A. Arbe, J. Rubio, P. Malo de Molina, J. Maiz, J. A. Pomposo, P. Fouquet, S. Prevost, F. Juranyi, M. Khaneft, J. Colmenero, *J. Appl. Phys.* **2020**, *127*, 044305.
[104] I. Berkovich, S. Mavila, O. Iliashevsky, S. Kozuch, N. G. Lemcoff, *Chem. Sci.* **2016**, *7*, 1773-1778.
[105] F. Lo Verso, J. A. Pomposo, J. Colmenero, A. J. Moreno, *Soft Matter* **2015**, *11*, 1369-1375.
[106] F. Lo Verso, J. A. Pomposo, J. Colmenero, A. J. Moreno, *Soft Matter* **2016**, *12*, 9039-9046.
[107] X. Wang, R. McHale, *Macromol. Rapid Commun.* **2010**, *31*, 331-350.
[108] Z. Wei, H. Duan, G. Weng, J. He, *J. Mater. Chem. C* **2020**, *8*, 15956-15980.
[109] Y. Lu, N. Yeung, N. Sieracki, N. M. Marshall, *Nature* **2009**, *460*, 855-862.
[110] H. J. Davis, T. R. Ward, *ACS Cent. Sci.* **2019**, *5*, 1120-1136.
[111] F. Schwizer, Y. Okamoto, T. Heinisch, Y. Gu, M. M. Pellizzoni, V. Lebrun, R. Reuter, V. Köhler, J. C. Lewis, T. R. Ward, *Chem. Rev.* **2018**, *118*, 142-231.
[112] S. Mavila, C. E. Diesendruck, S. Linde, L. Amir, R. Shikler, N. G. Lemcoff, *Angew. Chem. Int. Ed.* **2013**, *52*, 5767-5770.
[113] M. A. J. Gillissen, I. K. Voets, E. W. Meijer, A. R. A. Palmans, *Polym. Chem.* **2012**, *3*, 3166-3174.
[114] A. Sanchez-Sanchez, A. Arbe, J. Colmenero, J. A. Pomposo, *ACS Macro Lett.* **2014**, *3*, 439-443.
[115] A. Sanchez-Sanchez, A. Arbe, J. Kohlbrecher, J. Colmenero, J. A. Pomposo, *Macromol. Rapid Commun.* **2015**, *36*, 1592-1597.
[116] Z. Zhu, N. Xu, Q. Yu, L. Guo, H. Cao, X. Lu, Y. Cai, *Macromol. Rapid Commun.* **2015**, *36*, 1521-1527.

[117] Y. Bai, X. Feng, H. Xing, Y. Xu, B. K. Kim, N. Baig, T. Zhou, A. A. Gewirth, Y. Lu, E. Oldfield, S. C. Zimmerman, *J. Am. Chem. Soc.* **2016**, *138*, 11077-11080.
[118] H. Cao, Z. Cui, P. Gao, Y. Ding, X. Zhu, X. Lu, Y. Cai, *Macromol. Rapid Commun.* **2017**, *38*, 1700269.
[119] S. Thanneeru, S. S. Duay, L. Jin, Y. Fu, A. M. Angeles-Boza, J. He, *ACS Macro Lett.* **2017**, *6*, 652-656.
[120] J. Chen, J. Wang, Y. Bai, K. Li, E. S. Garcia, A. L. Ferguson, S. C. Zimmerman, *J. Am. Chem. Soc.* **2018**, *140*, 13695-13702.
[121] Z. Cui, L. Huang, Y. Ding, X. Zhu, X. Lu, Y. Cai, *ACS Macro Lett.* **2018**, *7*, 572-575.
[122] Y. Liu, P. Turunen, B. F. M. de Waal, K. G. Blank, A. E. Rowan, A. R. A. Palmans, E. W. Meijer, *Mol. Syst. Des. Eng.* **2018**, *3*, 609-618.
[123] J. Chen, K. Li, S. E. Bonson, S. C. Zimmerman, *J. Am. Chem. Soc.* **2020**, *142*, 13966-13973.
[124] Z. Hu, H. Pu, *Eur. Polym. J.* **2021**, *143*, 110194.
[125] Y. Liu, T. Pauloehrl, S. I. Presolski, L. Albertazzi, A. R. A. Palmans, E. W. Meijer, *J. Am. Chem. Soc.* **2015**, *137*, 13096-13105.
[126] A. E. Izuagbe, B. T. Tuten, P. W. Roesky, C. Barner-Kowollik, *Polym. Chem.* **2024**, *15*, 1955-1961.
[127] K. Freytag, S. Säfken, K. Wolter, J. C. Namyslo, E. G. Hübner, *Polym. Chem.* **2017**, *8*, 7546-7558.
[128] A. Blazquez-Martín, E. Verde-Sesto, A. Arbe, J. A. Pomposo, *Angew. Chem. Int. Ed.* **2023**, *62*, e202313502.
[129] Y. Zhang, L. Zhou, B. Han, B. Li, L. Wang, J. Wang, X. Wang, L. Zhu, *Catal. Lett.* **2022**, *152*, 106-115.
[130] J. Chen, J. Wang, K. Li, Y. Wang, M. Gruebele, A. L. Ferguson, S. C. Zimmerman, *J. Am. Chem. Soc.* **2019**, *141*, 9693-9700.
[131] Y. Zhang, W. Wang, W. Fu, M. Zhang, Z. Tang, R. Tan, D. Yin, *Chem. Commun.* **2018**, *54*, 9430-9433.
[132] W. Wang, C. Li, Y. Pi, J. Wang, R. Tan, D. Yin, *Catal. Sci. Technol.* **2019**, *9*, 5626-5635.
[133] Y. Li, J. Wen, M. Qin, Y. Cao, H. Ma, W. Wang, *ACS Biomater. Sci. Eng.* **2017**, *3*, 979-989.
[134] W. Wang, J. Wang, S. Li, C. Li, R. Tan, D. Yin, *Green Chem.* **2020**, *22*, 4645-4655.
[135] K. J. Rodriguez, A. M. Hanlon, C. K. Lyon, J. P. Cole, B. T. Tuten, C. A. Tooley, E. B. Berda, S. Pazicni, *Inorg. Chem.* **2016**, *55*, 9493-9496.
[136] C. A. Tooley, S. Pazicni, E. B. Berda, *Polym. Chem.* **2015**, *6*, 7646-7651.
[137] F. Wang, H. Pu, M. Jin, D. Wan, *Macromol. Rapid Commun.* **2016**, *37*, 330-336.
[138] F. Wang, H. Pu, X. Che, *Chem. Commun.* **2016**, *52*, 3516-3519.
[139] T. H. Galow, F. Ilhan, G. Cooke, V. M. Rotello, *J. Am. Chem. Soc.* **2000**, *122*, 3595-3598.
[140] F. Wang, H. Pu, Y. Ding, R. Lin, H. Pan, Z. Chang, M. Jin, *Polymer* **2018**, *141*, 86-92.
[141] O. I. H. Zebari, K. Demirelli, S. Y. Sharaf Zeebaree, H. Tuncer, *J. Thermoplast. Compos. Mater.* **2024**, *37*, 1957-1990.
[142] S. Thanneeru, J. K. Nganga, A. S. Amin, B. Liu, L. Jin, A. M. Angeles-Boza, J. He, *ChemCatChem* **2017**, *9*, 1157-1162.
[143] M. A. Reith, S. Kardas, C. Mertens, M. Fossépré, M. Surin, J. Steinkoenig, F. E. Du Prez, *Polym. Chem.* **2021**, *12*, 4924-4933.
[144] G. Qian, B. Zhu, Y. Wang, S. Deng, A. Hu, *Macromol. Rapid Commun.* **2012**, *33*, 1393-1398.
[145] M. Artar, T. Terashima, M. Sawamoto, E. W. Meijer, A. R. A. Palmans, *J. Polym. Sci. Part A: Polym. Chem.* **2014**, *52*, 12-20.

[146] M. Artar, E. R. J. Souren, T. Terashima, E. W. Meijer, A. R. A. Palmans, *ACS Macro Lett.* **2015**, *4*, 1099-1103.
[147] J. Chen, K. Li, J. S. L. Shon, S. C. Zimmerman, *J. Am. Chem. Soc.* **2020**, *142*, 4565-4569.
[148] E. S. Garcia, T. M. Xiong, A. Lifschitz, S. C. Zimmerman, *Polym. Chem.* **2021**, *12*, 6755-6760.
[149] S. Mavila, I. Rozenberg, N. G. Lemcoff, *Chem. Sci.* **2014**, *5*, 4196-4203.
[150] A. Levy, R. Feinstein, C. E. Diesendruck, *J. Am. Chem. Soc.* **2019**, *141*, 7256-7260.
[151] V. Kobernik, R. S. Phatake, J. Tzadikov, O. Reany, N. G. Lemcoff, *React. Funct. Polym.* **2021**, *165*, 104971.
[152] V. Kobernik, I. Berkovich, A. Levy, N. G. Lemcoff, C. E. Diesendruck, *Chem. Eur. J.* **2020**, *26*, 15835-15838.
[153] L. Greb, H. Mutlu, C. Barner-Kowollik, J.-M. Lehn, *J. Am. Chem. Soc.* **2016**, *138*, 1142-1145.
[154] Y. Shao, Y.-L. Wang, Z. Tang, Z. Wen, C. Chang, C. Wang, D. Sun, Y. Ye, D. Qiu, Y. Ke, F. Liu, Z. Yang, *Angew. Chem. Int. Ed.* **2022**, *61*, e202205183.
[155] R. Lambert, A.-L. Wirotius, S. Garmendia, P. Berto, J. Vignolle, D. Taton, *Polym. Chem.* **2018**, *9*, 3199-3204.
[156] S. Garmendia, S. B. Lawrenson, M. C. Arno, R. K. O'Reilly, D. Taton, A. P. Dove, *Macromol. Rapid Commun.* **2019**, *40*, 1900071.
[157] D. Arena, E. Verde-Sesto, I. Rivilla, J. A. Pomposo, *J. Am. Chem. Soc.* **2024**, *146*, 14397-14403.
[158] Z.-Y. Hu, H.-T. Pu, J.-G. Wu, *Chin. J. Polym. Sci.* **2021**, *39*, 441-446.
[159] A. Latorre-Sanchez, J. A. Pomposo, *Chem. Commun.* **2015**, *51*, 15736-15738.
[160] J. Pinacho-Olaciregui, E. Verde-Sesto, D. Taton, J. A. Pomposo, *Polymers* **2024**, *16*, 378.
[161] A. B. Benito, M. K. Aiertza, M. Marradi, L. Gil-Iceta, T. Shekhter Zahavi, B. Szczupak, M. Jiménez-González, T. Reese, E. Scanziani, L. Passoni, M. Matteoli, M. De Maglie, A. Orenstein, M. Oron-Herman, G. Kostenich, L. Buzhansky, E. Gazit, H.-J. Grande, V. Gómez-Vallejo, J. Llop, I. Loinaz, *Biomacromolecules* **2016**, *17*, 3213-3221.
[162] Z. Lu, J. Zhang, W. Yin, C. Guo, M. Lang, *Macromol. Rapid Commun.* **2022**, *43*, 2200156.
[163] C.-C. Cheng, D.-J. Lee, Z.-S. Liao, J.-J. Huang, *Polym. Chem.* **2016**, *7*, 6164-6169.
[164] Y. Zhang, H. Zhao, *Polymer* **2015**, *64*, 277-284.
[165] M. E. Mackay, T. T. Dao, A. Tuteja, D. L. Ho, B. Van Horn, H.-C. Kim, C. J. Hawker, *Nat. Mater.* **2003**, *2*, 762-766.
[166] R. Zeng, L. Chen, Q. Yan, *Angew. Chem. Int. Ed.* **2020**, *59*, 18418-18422.
[167] R. Lambert, A.-L. Wirotius, D. Taton, *ACS Macro Lett.* **2017**, *6*, 489-494.
[168] S. Garmendia, A. P. Dove, D. Taton, R. K. O'Reilly, *Polym. Chem.* **2019**, *10*, 2282-2289.
[169] S. Garmendia, A. P. Dove, D. Taton, R. K. O'Reilly, *Polym. Chem.* **2018**, *9*, 5286-5294.
[170] J. J. Piane, S. Huss, L. T. Alameda, S. J. Koehler, L. E. Chamberlain, M. J. Schubach, A. C. Hoover, E. Elacqua, *J. Polym. Sci.* **2021**, *59*, 2867-2877.
[171] K. Mundsinger, B. T. Tuten, L. Wang, K. Neubauer, C. Kropf, M. L. O'Mara, C. Barner-Kowollik, *Angew. Chem. Int. Ed.* **2023**, *62*, e202302995.
[172] J. J. Piane, L. E. Chamberlain, S. Huss, L. T. Alameda, A. C. Hoover, E. Elacqua, *ACS Catal.* **2020**, *10*, 13251-13256.
[173] F. Eisenreich, E. W. Meijer, A. R. A. Palmans, *Chem. Eur. J.* **2020**, *26*, 10355-10361.
[174] I. Perez-Baena, F. Barroso-Bujans, U. Gasser, A. Arbe, A. J. Moreno, J. Colmenero, J. A. Pomposo, *ACS Macro Lett.* **2013**, *2*, 775-779.
[175] L. Deng, L. Albertazzi, A. R. A. Palmans, *Biomacromolecules* **2022**, *23*, 326-338.
[176] K. M. Fromm, *Coord. Chem. Rev.* **2008**, *252*, 856-885.

[177] D. Banerjee, J. B. Parise, *Cryst. Growth Des.* **2011**, *11*, 4704-4720.
[178] A. Suwansoontorn, K. Yamamoto, S. Nagano, J. Matsui, Y. Nagao, *Electrochemistry* **2021**, *89*, 401-408.
[179] G. B. Deacon, R. J. Phillips, *Coord. Chem. Rev.* **1980**, *33*, 227-250.
[180] N. Hosono, A. M. Kushner, J. Chung, A. R. A. Palmans, Z. Guan, E. W. Meijer, *J. Am. Chem. Soc.* **2015**, *137*, 6880-6888.
[181] N. Wedler-Jasinski, T. Lueckerath, H. Mutlu, A. S. Goldmann, A. Walther, M. H. Stenzel, C. Barner-Kowollik, *Chem. Commun.* **2017**, *53*, 157-160.
[182] T. S. Fischer, D. Schulze-Sünninghausen, B. Luy, O. Altintas, C. Barner-Kowollik, *Angew. Chem. Int. Ed.* **2016**, *55*, 11276-11280.
[183] T. Mes, R. van der Weegen, A. R. A. Palmans, E. W. Meijer, *Angew. Chem. Int. Ed.* **2011**, *50*, 5085-5089.
[184] T. S. Fischer, S. Spann, Q. An, B. Luy, M. Tsotsalas, J. P. Blinco, H. Mutlu, C. Barner-Kowollik, *Chem. Sci.* **2018**, *9*, 4696-4702.
[185] P. H. Maag, F. Feist, V. X. Truong, H. Frisch, P. W. Roesky, C. Barner-Kowollik, *Angew. Chem. Int. Ed.* **2023**, *62*, e202309259.
[186] S. Babaoglu, D. Karaca Balta, G. Temel, *J. Polym. Sci. Part A: Polym. Chem.* **2017**, *55*, 1998-2003.
[187] D. Kodura, H. A. Houck, F. R. Bloesser, A. S. Goldmann, F. E. Du Prez, H. Frisch, C. Barner-Kowollik, *Chem. Sci.* **2021**, *12*, 1302-1310.
[188] A. Alexander-Katz, H. Wada, R. R. Netz, *Phys. Rev. Lett.* **2009**, *103*, 028102.
[189] Z. Han, S. L. Hilburg, A. Alexander-Katz, *Macromolecules* **2022**, *55*, 1295-1309.
[190] H. J. C. Berendsen, J. R. Grigera, T. P. Straatsma, *J. Phys. Chem.* **1987**, *91*, 6269-6271.
[191] L. F. F. Corrêa, J. Hao, R. Neerup, S. Almeida, M. Shi, K. Thomsen, P. L. Fosbøl, *Geothermics* **2022**, *104*, 102465.
[192] P. E. Batson, N. Dellby, O. L. Krivanek, *Nature* **2002**, *418*, 617-620.
[193] M. P. Oxley, A. R. Lupini, S. J. Pennycook, *Rep. Prog. Phys.* **2017**, *80*, 026101.
[194] L. Packman, B. Philippa, A. Pivrikas, P. L. Burn, I. R. Gentle, *Small Methods* **2024**, *8*, 2301305.
[195] A. A. Sousa, R. D. Leapman, *J. Microsc.* **2007**, *228*, 25-33.
[196] M. B. Plutschack, B. Pieber, K. Gilmore, P. H. Seeberger, *Chem. Rev.* **2017**, *117*, 11796-11893.
[197] D. T. McQuade, P. H. Seeberger, *J. Org. Chem.* **2013**, *78*, 6384-6389.
[198] L. D. Elliott, J. P. Knowles, P. J. Koovits, K. G. Maskill, M. J. Ralph, G. Lejeune, L. J. Edwards, R. I. Robinson, I. R. Clemens, B. Cox, D. D. Pascoe, G. Koch, M. Eberle, M. B. Berry, K. I. Booker-Milburn, *Chem. Eur. J.* **2014**, *20*, 15226-15232.
[199] D. J. Walsh, D. A. Schinski, R. A. Schneider, D. Guironnet, *Nat. Commun.* **2020**, *11*, 3094.
[200] M. H. Reis, F. A. Leibfarth, L. M. Pitet, *ACS Macro Lett.* **2020**, *9*, 123-133.
[201] M. Van De Walle, K. De Bruycker, J. P. Blinco, C. Barner-Kowollik, *Angew. Chem. Int. Ed.* **2020**, *59*, 14143-14147.
[202] O. Galant, C. E. Diesendruck, S. Spatari, *Org. Process Res. Dev.* **2024**, *28*, 1607-1617.
[203] H. Frisch, F. R. Bloesser, C. Barner-Kowollik, *Angew. Chem. Int. Ed.* **2019**, *58*, 3604-3609.
[204] J. A. Barltrop, P. Schofield, *Tetrahedron Lett.* **1962**, *3*, 697-699.
[205] D. H. R. Barton, Y. L. Chow, A. Cox, G. W. Kirby, *J. Chem. Soc.* **1965**, 3571-3578.
[206] D. H. R. Barton, Y. L. Chow, A. Cox, G. W. Kirby, *Tetrahedron Lett.* **1962**, *3*, 1055-1057.
[207] A. Patchornik, B. Amit, R. B. Woodward, *J. Am. Chem. Soc.* **1970**, *92*, 6333-6335.
[208] J. C. Sheehan, R. M. Wilson, *J. Am. Chem. Soc.* **1964**, *86*, 5277-5281.

[209] P. Klán, T. Šolomek, C. G. Bochet, A. Blanc, R. Givens, M. Rubina, V. Popik, A. Kostikov, J. Wirz, *Chem. Rev.* **2013**, *113*, 119-191.
[210] H. Zhao, E. S. Sterner, E. B. Coughlin, P. Theato, *Macromolecules* **2012**, *45*, 1723-1736.
[211] I. M. Irshadeen, S. L. Walden, M. Wegener, V. X. Truong, H. Frisch, J. P. Blinco, C. Barner-Kowollik, *J. Am. Chem. Soc.* **2021**, *143*, 21113-21126.
[212] S. L. Walden, J. A. Carroll, A.-N. Unterreiner, C. Barner-Kowollik, *Adv. Sci.* **2024**, *11*, 2306014.
[213] J. Bachmann, C. Petit, L. Michalek, Y. Catel, E. Blasco, J. P. Blinco, A.-N. Unterreiner, C. Barner-Kowollik, *ACS Macro Lett.* **2021**, *10*, 447-452.
[214] J.-M. Mewes, A. Dreuw, *Phys. Chem. Chem. Phys.* **2013**, *15*, 6691-6698.
[215] C. Petit, J. Bachmann, L. Michalek, Y. Catel, E. Blasco, J. P. Blinco, A.-N. Unterreiner, C. Barner-Kowollik, *Chem. Commun.* **2021**, *57*, 2911-2914.
[216] X. Wang, G. Liu, J. Hu, G. Zhang, S. Liu, *Angew. Chem. Int. Ed.* **2014**, *53*, 3138-3142.
[217] Z. Tao, H. Fan, J. Huang, T. Sun, T. Kurokawa, J. P. Gong, *ACS Appl. Mater. Interfaces* **2019**, *11*, 37139-37146.
[218] H. A. Jahn, E. Teller, F. G. Donnan, *Proc. R. Soc. Lond. A* **1937**, *161*, 220-235.
[219] S. Li, D. Tian, X. Zhao, Y. Yin, R. Lee, Z. Jiang, *Org. Chem. Front.* **2022**, *9*, 6229-6239.
[220] J. A. Pomposo, A. J. Moreno, A. Arbe, J. Colmenero, *ACS Omega* **2018**, *3*, 8648-8654.
[221] S. Tshepelevitsh, A. Kütt, M. Lõkov, I. Kaljurand, J. Saame, A. Heering, P. G. Plieger, R. Vianello, I. Leito, *Eur. J. Org. Chem.* **2019**, *2019*, 6735-6748.
[222] A. Kütt, I. Leito, I. Kaljurand, L. Sooväli, V. M. Vlasov, L. M. Yagupolskii, I. A. Koppel, *J. Org. Chem.* **2006**, *71*, 2829-2838.
[223] A. Kütt, S. Tshepelevitsh, J. Saame, M. Lõkov, I. Kaljurand, S. Selberg, I. Leito, *Eur. J. Org. Chem.* **2021**, *2021*, 1407-1419.
[224] J. F. Coetzee, *Ionic Reactions in Acetonitrile* in *Prog. Phys. Org. Chem.* (Eds.: A. Streitwieser, R. W. Taft), **1967**, pp. 45-92.
[225] A.-L. Fameau, T. Zemb, *Adv. Colloid Interface Sci.* **2014**, *207*, 43-64.
[226] D. Astruc, *Eur. J. Inorg. Chem.* **2017**, *2017*, 6-29.
[227] K. Heinze, H. Lang, *Organometallics* **2013**, *32*, 5623-5625.
[228] U. Rauf, G. Shabir, S. Bukhari, F. Albericio, A. Saeed, *Molecules* **2023**, *28*, 5765.
[229] R. Pietschnig, *Chem. Soc. Rev.* **2016**, *45*, 5216-5231.
[230] F. S. Arimoto, A. C. Haven, Jr., *J. Am. Chem. Soc.* **1955**, *77*, 6295-6297.
[231] C. D'Silva, S. Afeworki, O. L. Parri, P. K. Baker, A. E. Underhill, *J. Mater. Chem.* **1992**, *2*, 225-230.
[232] K. L. Robinson, N. S. Lawrence, *Anal. Sci.* **2008**, *24*, 339-343.
[233] M. H. George, G. F. Hayes, *J. Polym. Sci. Polym. Chem. Ed.* **1975**, *13*, 1049-1070.
[234] C. U. Pittman, Jr., J. C. Lai, D. P. Vanderpool, M. Good, R. Prado, *Macromolecules* **1970**, *3*, 746-754.
[235] C. U. Pittman, Jr., R. L. Voges, W. R. Jones, *Macromolecules* **1971**, *4*, 291-297.
[236] O. Nuyken, V. Burkhardt, C. Hübsch, *Macromol. Chem. Phys.* **1997**, *198*, 3353-3363.
[237] M. Gallei, R. Klein, M. Rehahn, *Macromolecules* **2010**, *43*, 1844-1854.
[238] M. Gallei, B. V. K. J. Schmidt, R. Klein, M. Rehahn, *Macromol. Rapid Commun.* **2009**, *30*, 1463-1469.
[239] M. Gallei, S. Tockner, R. Klein, M. Rehahn, *Macromol. Rapid Commun.* **2010**, *31*, 889-896.
[240] D. Albagli, G. Bazan, M. S. Wrighton, R. R. Schrock, *J. Am. Chem. Soc.* **1992**, *114*, 4150-4158.

[241] A. S. Gamble, J. T. Patton, J. M. Boncella, *Makromol. Chem., Rapid Commun.* **1992**, *13*, 109-115.
[242] C. Feng, Z. Shen, D. Yang, Y. Li, J. Hu, G. Lu, X. Huang, *J. Polym. Sci. Part A: Polym. Chem.* **2009**, *47*, 4346-4357.
[243] B. Y. Kim, E. L. Ratcliff, N. R. Armstrong, T. Kowalewski, J. Pyun, *Langmuir* **2010**, *26*, 2083-2092.
[244] Z.-P. Xiao, Z.-H. Cai, H. Liang, J. Lu, *J. Mater. Chem.* **2010**, *20*, 8375-8381.
[245] C. G. Hardy, L. Ren, T. C. Tamboue, C. Tang, *J. Polym. Sci. Part A: Polym. Chem.* **2011**, *49*, 1409-1420.
[246] T. Sakakiyama, H. Ohkita, M. Ohoka, S. Ito, Y. Tsujii, T. Fukuda, *Chem. Lett.* **2005**, *34*, 1366-1367.
[247] M. Shi, A.-L. Li, H. Liang, J. Lu, *Macromolecules* **2007**, *40*, 1891-1896.
[248] C. Herfurth, D. Voll, J. Buller, J. Weiss, C. Barner-Kowollik, A. Laschewsky, *J. Polym. Sci. Part A: Polym. Chem.* **2012**, *50*, 108-118.
[249] S. A. Merchant, M. T. Meredith, T. O. Tran, D. B. Brunski, M. B. Johnson, D. T. Glatzhofer, D. W. Schmidtke, *J. Phys. Chem. C* **2010**, *114*, 11627-11634.
[250] H. Li, A. Sundararaman, T. Pakkirisamy, K. Venkatasubbaiah, F. Schödel, F. Jäkle, *Macromolecules* **2011**, *44*, 95-103.
[251] K. Parab, F. Jäkle, *Macromolecules* **2009**, *42*, 4002-4007.
[252] I. Tomatsu, A. Hashidzume, A. Harada, *Macromol. Rapid Commun.* **2006**, *27*, 238-241.
[253] M. A. Hempenius, C. Cirmi, F. L. Savio, J. Song, G. J. Vancso, *Macromol. Rapid Commun.* **2010**, *31*, 772-783.
[254] H. Ritter, B. E. Mondrzik, M. Rehahn, M. Gallei, *Beilstein J. Org. Chem.* **2010**, *6*, 60.
[255] R. H. Staff, M. Gallei, M. Mazurowski, M. Rehahn, R. Berger, K. Landfester, D. Crespy, *ACS Nano* **2012**, *6*, 9042-9049.
[256] M. Mazurowski, M. Gallei, J. Li, H. Didzoleit, B. Stühn, M. Rehahn, *Macromolecules* **2012**, *45*, 8970-8981.
[257] P. S. Borchers, I. Anufriev, J. Vitz, H. Görls, J. Elbert, I. Nischang, M. D. Hager, U. S. Schubert, *Macromolecules* **2022**, *55*, 1576-1589.
[258] A. Botana, J. A. Aguilar, M. Nilsson, G. A. Morris, *J. Magn. Reson.* **2011**, *208*, 270-278.
[259] T. Wang, F. Chen, J. Qin, Y.-M. He, Q.-H. Fan, *Angew. Chem. Int. Ed.* **2013**, *52*, 7172-7176.
[260] W. Yang, T. Nakano, *Chem. Commun.* **2015**, *51*, 17269-17272.
[261] O. Moudam, F. Ajamaa, A. Ekouaga, H. Mamlouk, U. Hahn, M. Holler, R. Welter, J.-F. Nierengarten, *Eur. J. Org. Chem.* **2007**, *2007*, 417-419.
[262] I. R. Butler, *Organometallics* **1992**, *11*, 74-83.
[263] A. E. Reed, R. B. Weinstock, F. Weinhold, *J. Chem. Phys.* **1985**, *83*, 735-746.
[264] T. Li, C. Zhou, M. Jiang, *Polym. Bull.* **1991**, *25*, 211-216.
[265] T. E. Müller, K. C. Hultzsch, M. Yus, F. Foubelo, M. Tada, *Chem. Rev.* **2008**, *108*, 3795-3892.
[266] J.-W. Pissarek, D. Schlesiger, P. W. Roesky, S. Blechert, *Adv. Synth. Catal.* **2009**, *351*, 2081-2085.
[267] H. Zhang, L. Peng, Y. Xin, Q. Yan, J. Yuan, *Macromol. Symp.* **2013**, *329*, 66-69.
[268] Y. Liu, S. Pujals, P. J. M. Stals, T. Paulöhrl, S. I. Presolski, E. W. Meijer, L. Albertazzi, A. R. A. Palmans, *J. Am. Chem. Soc.* **2018**, *140*, 3423-3433.
[269] M. Spicuzza, S. P. Gaikwad, S. Huss, A. A. Lee, C. V. Craescu, A. Griggs, J. Joseph, M. Puthenpurayil, W. Lin, C. Matarazzo, S. Baldwin, V. Perez, D. A. Rodriguez-Acevedo, J. R. Swierk, E. Elacqua, *Polym. Chem.* **2024**, *15*, 1833-1838.

[270] F. Eisenreich, A. R. A. Palmans, *Chem. Eur. J.* **2022**, *28*, e202201322.
[271] D. P. Hari, B. König, *Chem. Commun.* **2014**, *50*, 6688-6699.
[272] A. Bosveli, T. Montagnon, D. Kalaitzakis, G. Vassilikogiannakis, *Org. Biomol. Chem.* **2021**, *19*, 3303-3317.
[273] N. A. Romero, D. A. Nicewicz, *Chem. Rev.* **2016**, *116*, 10075-10166.
[274] G. R. Fleming, A. W. E. Knight, J. M. Morris, R. J. S. Morrison, G. W. Robinson, *J. Am. Chem. Soc.* **1977**, *99*, 4306-4311.
[275] A. Penzkofer, A. Beidoun, M. Daiber, *J. Lumin.* **1992**, *51*, 297-314.
[276] I. Mohamed Irshadeen, V. X. Truong, H. Frisch, C. Barner-Kowollik, *Chem. Commun.* **2023**, *59*, 11959-11962.
[277] J. J. Lessard, G. M. Scheutz, A. B. Korpusik, R. A. Olson, C. A. Figg, B. S. Sumerlin, *Polym. Chem.* **2021**, *12*, 2205-2209.
[278] A. Brändle, A. Khan, *Polym. Chem.* **2012**, *3*, 3224-3227.
[279] A. Khan, *Chem. Commun.* **2023**, *59*, 11028-11044.
[280] M. C. Stuparu, A. Khan, *J. Polym. Sci. Part A: Polym. Chem.* **2016**, *54*, 3057-3070.
[281] Y. Zhang, C. Ye, S. Li, A. Ding, G. Gu, H. Guo, *RSC Adv.* **2017**, *7*, 13240-13243.
[282] S. H. Park, C. H. Choi, S. Y. Lee, S. I. Woo, *ACS Comb. Sci.* **2017**, *19*, 81-84.
[283] I. R. Butler, J.-L. Roustan, *Can. J. Chem.* **1990**, *68*, 2212-2215.
[284] N. De Alwis Watuthanthrige, P. N. Kurek, D. Konkolewicz, *Polym. Chem.* **2018**, *9*, 1557-1561.
[285] R. A. Olson, J. S. Levi, G. M. Scheutz, J. J. Lessard, C. A. Figg, M. N. Kamat, K. B. Basso, B. S. Sumerlin, *Macromolecules* **2021**, *54*, 4880-4888.
[286] G. Sheldrick, *Acta Cryst. A* **2008**, *64*, 112-122.
[287] G. Sheldrick, *Acta Cryst. C* **2015**, *71*, 3-8.
[288] O. V. Dolomanov, L. J. Bourhis, R. J. Gildea, J. A. K. Howard, H. Puschmann, *J. Appl. Cryst.* **2009**, *42*, 339-341.
[289] M. J. Abraham, T. Murtola, R. Schulz, S. Páll, J. C. Smith, B. Hess, E. Lindahl, *SoftwareX* **2015**, *1-2*, 19-25.
[290] S. Pronk, S. Páll, R. Schulz, P. Larsson, P. Bjelkmar, R. Apostolov, M. R. Shirts, J. C. Smith, P. M. Kasson, D. van der Spoel, B. Hess, E. Lindahl, *Bioinformatics* **2013**, *29*, 845-854.
[291] D. Van Der Spoel, E. Lindahl, B. Hess, G. Groenhof, A. E. Mark, H. J. C. Berendsen, *J. Comput. Chem.* **2005**, *26*, 1701-1718.
[292] N. Schmid, A. P. Eichenberger, A. Choutko, S. Riniker, M. Winger, A. E. Mark, W. F. van Gunsteren, *Eur. Biophys. J.* **2011**, *40*, 843-856.
[293] A. K. Malde, L. Zuo, M. Breeze, M. Stroet, D. Poger, P. C. Nair, C. Oostenbrink, A. E. Mark, *J. Chem. Theory Comput.* **2011**, *7*, 4026-4037.
[294] M. Stroet, B. Caron, K. M. Visscher, D. P. Geerke, A. K. Malde, A. E. Mark, *J. Chem. Theory Comput.* **2018**, *14*, 5834-5845.
[295] X. Pan, H. Wang, C. Li, J. Z. H. Zhang, C. Ji, *J. Chem. Inf. Model.* **2021**, *61*, 3159-3165.
[296] G. Bussi, D. Donadio, M. Parrinello, *J. Chem. Phys.* **2007**, *126*, 014101.
[297] M. Parrinello, A. Rahman, *J. Appl. Phys.* **1981**, *52*, 7182-7190.
[298] S. Miyamoto, P. A. Kollman, *J. Comput. Chem.* **1992**, *13*, 952-962.
[299] B. Hess, H. Bekker, H. J. C. Berendsen, J. G. E. M. Fraaije, *J. Comput. Chem.* **1997**, *18*, 1463-1472.
[300] I. G. Tironi, R. Sperb, P. E. Smith, W. F. van Gunsteren, *J. Chem. Phys.* **1995**, *102*, 5451-5459.
[301] H. Grubmüller, H. Heller, A. Windemuth, K. Schulten, *Mol. Simul.* **1991**, *6*, 121-142.

[302] R. J. Gowers, M. Linke, J. Barnoud, T. J. E. Reddy, M. N. Melo, S. L. Seyler, J. Domanski, D. L. Dotson, S. Buchoux, I. M. Kenney, O. Beckstein, *MDAnalysis: A Python Package for the Rapid Analysis of Molecular Dynamics Simulations*, Austin, Texas, United States, **2019**.
[303] TURBOMOLE V7.7 2022, a development of University of Karlsruhe and Forschungszentrum Karlsruhe GmbH, 1989–2007, TURBOMOLE GmbH, since 2007.
[304] Y. J. Franzke, C. Holzer, J. H. Andersen, T. Begušić, F. Bruder, S. Coriani, F. Della Sala, E. Fabiano, D. A. Fedotov, S. Fürst, S. Gillhuber, R. Grotjahn, M. Kaupp, M. Kehry, M. Krstić, F. Mack, S. Majumdar, B. D. Nguyen, S. M. Parker, F. Pauly, A. Pausch, E. Perlt, G. S. Phun, A. Rajabi, D. Rappoport, B. Samal, T. Schrader, M. Sharma, E. Tapavicza, R. S. Treß, V. Voora, A. Wodyński, J. M. Yu, B. Zerulla, F. Furche, C. Hättig, M. Sierka, D. P. Tew, F. Weigend, *J. Chem. Theory Comput.* **2023**, *19*, 6859-6890.
[305] J. P. Perdew, K. Burke, M. Ernzerhof, *Phys. Rev. Lett.* **1996**, *77*, 3865-3868.
[306] C. Adamo, V. Barone, *J. Chem. Phys.* **1999**, *110*, 6158-6170.
[307] F. Weigend, R. Ahlrichs, *Phys. Chem. Chem. Phys.* **2005**, *7*, 3297-3305.
[308] F. Weigend, A. Baldes, *J. Chem. Phys.* **2010**, *133*, 174102.
[309] F. Weigend, M. Häser, H. Patzelt, R. Ahlrichs, *Chem. Phys. Lett.* **1998**, *294*, 143-152.
[310] K. A. Peterson, D. Figgen, M. Dolg, H. Stoll, *J. Chem. Phys.* **2007**, *126*, 124101.
[311] F. Weigend, *Phys. Chem. Chem. Phys.* **2006**, *8*, 1057-1065.
[312] K. Eichkorn, F. Weigend, O. Treutler, R. Ahlrichs, *Theor. Chem. Acc.* **1997**, *97*, 119-124.
[313] O. Treutler, R. Ahlrichs, *J. Chem. Phys.* **1995**, *102*, 346-354.
[314] O. Treutler, *Entwicklung und Anwendung von Dichtefunktionalmethoden*, Dissertation, Universität Karlsruhe (TH), Karlsruhe, **1995**.
[315] E. Caldeweyher, C. Bannwarth, S. Grimme, *J. Chem. Phys.* **2017**, *147*, 034112.
[316] X.-X. Yang, I. Issac, S. Lebedkin, M. Kühn, F. Weigend, D. Fenske, O. Fuhr, A. Eichhöfer, *Chem. Commun.* **2014**, *50*, 11043-11045.
[317] J. C. Slater, *Phys. Rev.* **1951**, *81*, 385-390.
[318] P. A. M. Dirac, R. H. Fowler, *Proc. R. Soc. Lond. A* **1929**, *123*, 714-733.
[319] C. Lee, W. Yang, R. G. Parr, *Phys. Rev. B* **1988**, *37*, 785-789.
[320] A. Schäfer, A. Klamt, D. Sattel, J. C. W. Lohrenz, F. Eckert, *Phys. Chem. Chem. Phys.* **2000**, *2*, 2187-2193.
[321] A. Pausch, *J. Chem. Theory Comput.* **2024**, *20*, 3169-3183.
[322] L. G. Gagliardi, C. B. Castells, C. Ràfols, M. Rosés, E. Bosch, *J. Chem. Eng. Data* **2007**, *52*, 1103-1107.